Harmonic Stability and Distortion in Offshore Wind Farms

Beloqui Larumbe, L.

DOI
10.4233/uuid:2d917deb-1a14-414a-b475-956455d9b4ce

Publication date
2024

Document Version
Final published version

Citation (APA)
Beloqui Larumbe, L. (2024). *Harmonic Stability and Distortion in Offshore Wind Farms*. [Dissertation (TU Delft), Delft University of Technology]. https://doi.org/10.4233/uuid:2d917deb-1a14-414a-b475-956455d9b4ce

Harmonic Stability and Distortion in Offshore Wind Farms

Harmonic Stability and Distortion in Offshore Wind Farms

Proefschrift

ter verkrijging van de graad van doctor aan de Technische Universiteit Delft,
op gezag van de Rector Magnificus Prof. dr. ir. T. H. J. J. van der Hagen,
voorzitter van het College voor Promoties,
in het openbaar te verdedigen op

vrijdag 1 november 2024 om 10:00 uur

door

Lucía BELOQUI LARUMBE

Master of Science in Industriële Techniek,
Specialisatie en Elektriciteit en Duurzame Energie,
Universidad Pública de Navarra, Pamplona, Spanje,
geboren te Pamplona, Spanje.

Dit proefschrift is goedgekeurd door de promotoren.

Samenstelling promotiecommissie bestaat uit:

Rector Magnificus,	voorzitter
Prof. dr. ir. P. Bauer,	Technische Universiteit Delft, promotor
Dr. Z. Qin,	Technische Universiteit Delft, copromotor
Onafhankelijke leden:	
Prof. dr. P. Rodríguez Cortés,	Luxembourg Institute of Science and Technology
Prof. dr. P. Sanchis Gurpide,	Universidad Pública de Navarra
Prof. ir. J. B. M. van Waes,	Technische Universiteit Eindhoven
Prof. ir. P. T. M. Vaessen,	Technische Universiteit Delft
Dr. ir. J. L. Rueda Torres,	Technische Universiteit Delft

This work was partially funded by TKI Wind op Zee under the project 'Large Offshore Wind Harmonics Mitigation (LOW-HarM)' by the Rijksdienst voor Ondernemend (RVO), The Netherlands.

Keywords: Stability, harmonics, wind turbine generator, impedance modelling, offshore wind energy.

Printed by: Ridderprint.

Front & Back: Cover designed by Andrea Santiago.

ISBN 978-94-6384-646-2
An electronic version of this dissertation is available at
http://repository.tudelft.nl/.

He buscado la luz todo este tiempo
y la he descubierto prendiendo fuego a todo

Andrea Santiago

To my sister, María

Summary

The green energy transition is underway. Numerous countries, companies, organizations and individuals are now committed to pursuing a sustainable future. While the exact composition of the future energy mix remains undecided, certain technologies, like offshore wind, are bound to play a prominent role.

Connecting renewable energies to the grid does not come without a challenge. In most cases, the energy produced by renewable generators needs to be transformed before being fed into the grid, for which power-electronic converters are typically used. These converters are a fundamental piece of the integration of renewables into the grid but, at the same time, pose a challenge due to their inherently different behaviour from traditional equipment.

As the population of converters increases, numerous complications have emerged. An instability phenomenon occurs when an electrical disturbance exceeds the capacity of the system to manage it, leaving insufficient margin to restore balance. As a result, an equilibrium point is not regained and the voltages and currents escalate uncontrollably. Among other consequences, losing stability may result in the undesired tripping of protections, damage to equipment, or in the worst case, system blackouts.

Due to the proliferation of converters, new mechanisms that trigger instability have appeared in recent years. Extensive research has been conducted into the role of Phase-Locked Loops (PLLs) in instability initiation. The PLL is an algorithm that, based on measurements, is able to estimate the grid frequency and phase angle ensuring the converter synchronization with the grid. When connected to a weak grid, the PLL has difficulties maintaining synchronism, impairing the ability of the converter to control the active and reactive power injected into the network. Even though some power grids are inherently weak in their normal operational state, weak grids are often a consequence of a grid reconfiguration due to a fault. When a fault or short-circuit occurs, it is usually isolated by disconnecting a section of the network. This alters the network structure, which may induce a weak grid state. One realization leading to the work in this thesis is that faults are typically unbalanced, and therefore, a weak grid condition often coincides with an unbalanced condition.

This thesis presents an analytical model of the PLL that reveals the time-periodic dynamics resulting from the imbalance. When embedded in an impedance-based model of the converter, the resulting equations can predict when the converter will become unstable in both weak and unbalanced conditions. Among other results, this thesis shows how the grid-voltage imbalance and the current-reference strategy considered during fault-ride through affect the stability margins of the converter.

Further, the expansion of grid-connected converters has led to a rise in the concerns about

harmonic generation. A harmonic is a distortion that appears in the voltage and/or current signals at frequencies other than the fundamental. These distortions have the capability of propagating through the system, leading to reduced efficiencies, accelerated insulation ageing, measurement inaccuracies, and other consequences. Power-electronic converters base their operation on the switching of semiconductors, which inevitably produces harmonic distortion.

Despite harmonics not being new phenomena, dealing with harmonics in modern power systems is challenging due to the difficulty of predicting distortion levels in converter-based power systems. Modelling-based distortion estimation is fundamental in the connection process of renewable energies to the grid, as a key requirement in the grid-code compliance procedures that precede the operation of the plant. Accurate prediction of distortion levels is also important in project planning, in order to estimate the need (or absence thereof) of harmonic-mitigation measures.

However, forecasting the summation or cancellation of harmonics in a system with several converters is difficult due to the randomness of the harmonic generation by converters, and typical methods used in the past have proven inaccurate when compared to distortion measurements. An emerging method to deal with the statistical variation of the harmonic emission is to apply Monte Carlo simulations. This thesis studies the importance of correlation and frequency-coupling effects in the results of offshore wind farm harmonic studies obtained with the Monte Carlo method. The results show that, while frequency-coupling effects due to converter control non-linearities do not significantly affect results, correlation effects can have an important impact on distortion estimation.

Samenvatting

De groene energietransitie is in volle gang. Talrijke landen, bedrijven, organisaties en individuen hebben zich gecommitteerd aan een duurzame toekomst. Ook al ligt de exacte samenstelling van de toekomstige energiemix nog niet vast, zullen bepaalde technologieën, zoals wind op zee, een belangrijke rol spelen.

Het verbinden van hernieuwbare energie aan het elektriciteitsnet is niet zonder uitdaging. In de meeste gevallen moet de door hernieuwbare bronnen opgewekte energie worden getransformeerd voordat het kan worden aangesloten op het net. Hiervoor worden typisch vermogenselektronische omvormers gebruikt. Deze omvormers zijn een fundamenteel onderdeel van de integratie van hernieuwbare bronnen met het net, maar tegelijkertijd vormen ze een uitdaging vanwege hun afwijkend gedrag van traditionele apparatuur.

Terwijl de populatie van omvormers toeneemt zijn er vele complicaties verschenen. Een fenomeen van instabiliteit vindt plaats als er een kleine of grote verstoring is en het systeem niet genoeg marge heeft om hiermee om te gaan. Het resultaat hiervan is dat het evenwichtspunt niet wordt teruggevonden en spanningen en stromen zich ongecontroleerd kunnen ontwikkelen. Het verlies aan stabiliteit kan onder andere leiden tot het ongewenst afschakelen van beveiligingen, schade aan apparatuur of, in het ergste geval, systeemuitval.

Vanwege de toename van omvormers, zijn er in de afgelopen jaren nieuwe mechanismen ontstaan die instabiliteit kunnen veroorzaken. Er is veel onderzoek gedaan naar de rol van zogenaamde ‘Phase-Locked Loops’ (PLLs) als initiator van instabiliteit. De PLL is een algoritme dat, gebaseerd op meetdata, in staat is om de netfrequentie en fasehoek in te schatten, zodat de omvormer gesynchroniseerd blijft met het net. Wanneer het verbonden is aan een zwak net heeft de PLL moeite om synchroon te blijven, waardoor de omvormer niet in staat is om het actieve en reactieve vermogen dat op het net geïnjecteerd wordt te beheersen. Hoewel sommige elektriciteitsnetwerken inherent zwak zijn in hun normale operationele toestand, zijn zwakke netten vaak het gevolg van het herconfigureren van het netwerk door een storing. Als een storing of kortsluiting plaatsvindt, wordt de storing meestal geïsoleerd door het loskoppelen van een deel van het netwerk, waardoor de netstructuur wordt aangepast en soms in een verzwakte toestand raakt. Eén realisatie die heeft geleid tot het werk in deze scriptie is dat storingen typisch niet in balans zijn en daarom een zwakke toestand van het net vaak samen lijkt te vallen met een ongebalanceerde toestand.

Deze scriptie presenteert een analytisch model van de PLL dat de tijd-periodieke dynamica laat zien die ontstaan als gevolg van een imbalans. Wanneer ingebed in een impedantiegebaseerd model van de omvormer, kunnen de resulterende vergelijkingen voorspellen wanneer de omvormer instabiel zal worden onder zowel zwakke als ongebalanceerde omstandighe-

den. Onder andere resultaten toont deze scriptie dat de netspanningsonbalans en de stroomreferentiestrategie die tijdens de fault-ride through wordt toegepast, de stabiliteitsmarges van de omvormer beïnvloeden.

Bovendien heeft de uitbreiding van netgekoppelde omvormers geleid tot een toename van zorgen over harmonische generatie. Een harmonische is een vervorming die optreedt in de spanning- en/of stroomsignalen op andere frequenties dan de grondfrequentie. Deze vervormingen zijn in staat om door het systeem te propageren, wat leidt tot inefficiënties, het verouderen van isolatie, en andere gevolgen. Vermogenselektronische omvormers baseren hun werking op het schakelen van halfgeleiders, wat onvermijdelijk harmonische vervorming veroorzaakt.

Ondanks dat harmonischen niet een nieuw fenomeen zijn, is het omgaan met harmonischen in moderne netsystemen uitdagend vanwege de moeilijkheid om het niveau van vervorming in omvormergebaseerde netsystemen te voorspellen. Modelgebaseerde schatting van vervorming is fundamenteel in het aansluitingsproces van hernieuwbare energiebronnen op het net, als een sleutelvoorwaarde bij de netcode-nalevingsprocedures die voorafgaan aan de ingebruikname van een energiecentrale. Nauwkeurige voorspelling van vervormingsniveaus is ook belangrijk in de planning van een project, om de behoefte (of het ontbreken daarvan) aan harmonische mitigatiemaatregelen te kunnen inschatten.

Het voorspellen van de som of opheffing van harmonischen in een systeem met meerdere omvormers is echter moeilijk vanwege de willekeurigheid van de harmonische generatie door omvormers. De gangbare methoden die in het verleden werden gebruikt bleken onnauwkeurig vergeleken met vervormingsmetingen. Een opkomende methode voor het omgaan met statistische variatie van de harmonische emissie is het toepassen van Monte Carlo-simulaties. Deze scriptie onderzoekt het belang van correlatie en frequentiekoppelingseffecten in de resultaten van harmonischen bij windparken op zee verkregen door de Monte Carlo-methode. De resultaten laten zien dat, hoewel frequentiekoppelingseffecten als gevolg van niet-lineariteiten in de omvormerbesturing de resultaten niet significant beïnvloeden, correlatie-effecten een belangrijke impact kunnen hebben op de voorspelling van een vervorming.

Acknowledgements

This thesis is the result of the work of many years. Many people have helped me through this journey; some by providing guidance, some by directly contributing to the technical work, and some by supporting me or celebrating with me during the ups and downs. All of you have been essential in this process. I want to thank you all.

To Professor Bauer, thank you for giving me the opportunity to do the MSc Thesis and the PhD in your group. On top of being a PhD candidate, in all these years in the group, you also gave me the chance to become the unofficial corona-quizz master :) I am sure that our paths will cross again in the future.

To Zian, thank you so much for everything you have done in the past years. You gave me direction in this journey, a critical look of my work, and much technical input that was very valuable to complete this thesis. On top of that, I want to stress the personal support as well: thank you for believing in me all this time; one cannot say that you haven't had patience.

To the members of the committee, thank you for your comments and critical questions. I am looking forward to more discussions in the future. To the rest of the Electrical Sustainable Energy Department of TUDelft; Margot, Ellen, Carla, Mark, Marieke, and the rest, thank you. Especially, I want to thank Sharmila, you have always taken such good care of all of us. To the current and past members of the EEMCS Diversity and Inclusion Team (EDIT), let's keep up the good work! I truly believe that change is possible.

To Arjen Kremers and Mohammad Alhayek, thank you for trusting me in supervising your MSc thesis. Your inputs are all throughout this work.

To the old gang of DCES: Pavel, Udai, Nils, Soumya, Laurens, Aditya and Mladen. Some of you stayed, some of you left, but I think we can all agree that we will remember the stories. Let's keep in touch.

To my other colleagues during the PhD: Gautham, Jianning, Mohammad, Thiago, Laura, Yunhe, Lu, Wiljan, Wenli, Sachin, Marco, Lyu, Yang, Calvin, Nishant, Victor, Pierpaolo, Alejandro, Joel, Dario, Miad, Nikos, Alvaro, Zhengzhao, Reza, Farshid, Guillermo, Christian, Luis, Fabio, Djurre, Armando, Minos, Prasanth, Tsegay, and many others; and to the lab technicians, Joris, Harrie and Bart, thank you for all your help and for all those coffee breaks. Both coffee and breaks are essential parts of a PhD :)

I want to thank as well Erik van Iperen, Paul Donnellan and Yin Sun, who gave me the opportunity to join their team at Shell. Songda, thank you for being the best onboarding buddy one could have ever asked for, it has been an amazing journey since, in and out of the office. Also to my team lead Jackie Lava and the rest of the grid connection technologies

team: Dhana, Digvijay, Saran, Robert, Dan, Ben, Redouane, Roozbeh, Reza, Renata, Vinay and David; to the hydrogen team: Toshi, Martijn; and to the rest of the renewable power generation group; I have enjoyed so much these past 2 years together and I am looking forward to keep working with you to make the world every day a tiny bit more sustainable.

I have always believed in the importance of looking forward but, recently, I have started to appreciate also the value of reflecting back. I want to thank the people that helped me on my path to where I am today. To my university back in Spain, the Public University of Navarre, and especially the Electrical Engineering Department, thank you for everything that you taught me. Prof. Pablo Sanchis, it is a true statement when I say that I would not be here without you, thank you so much. To Marcos Lafoz and everyone else at the CIEMAT in Madrid, thank you for letting me do my bachelor thesis with you. From that first experimental set up I learnt things that I still apply today.

To Ibra and Franci: wow, it has been a journey, and probably nobody has witnessed it as close as you. I can't even begin to say thank you for all your support in and out of the faculty. I always have a blast with you and I love every bit of our spontaneous trips together. Anika, you came to my life later than these two, but I am sure that many trips and stories together await (looking forward!).

To all the debate club crew: Tanya, Aman, Fons, Jorino, Wessel, Karan, Aida, Lars, Daniel and Abhi, you were such a find. I feel so lucky that I came to the Netherlands and was able to surround myself by trustworthy, honest, smart and fun people like you. It has been 8 years together already, and we are growing closer every day. I have enjoyed every part of the journey: our times at Wijnhaven, the countless dinners at each other's houses, our trips to India, and many more. Let's keep making memories together :)

Aurora, I still remember the first time we met outside one of our master courses. I am so glad we became friends and maintained all throughout. Today we are in the Netherlands, tomorrow hopefully in Alcala ;) Alicia, you really tried to avoid me for months, but I guess that you were not lucky enough to succeed hahah I am so happy that we connected; I have a blast with our games and your *tortilla de patata* dinners are legendary :) Michelle, I am very glad Alicia introduced us. I think we both have quite the pottery touch hahah ;) Priya, I am so glad that Francesca brought us together, you are a truly great flatmate and living with you is super easy. Tess, thank you for helping me to start listening to my body; you helped me realize my own limits at a time when I was about to crash.

To all my people in Spain: Pati, Pitu, Isa, Irina, Clau, Paloma, Julia, Pat, Pilar, Ale and Maria, we have been friends for 20+ years already, and I know that I can still count on you at all times. Be it for fun, partying and laughter; or for comfort, advice and understanding. You are such an important pillar in my life. Let's go for the next 20 ;) To Gade, Sebas, Jaio, Celia and Myri, you are the absolute proof that engineers can also be flexible, lively and fun. Thank you for all the amazing times we spent during the uni years, sometimes suffering together but always helping each other out. Many years have passed since, and yet here we are. I can't wait to keep fighting forward together ;)

Elisa, you came into my life at a moment where nothing was easy for me nor for you, and despite everything you managed to really be there for me. I will never forget that, nor the amazing times we have spent together. For all, thank you.

And of course, to my family. *Mama y papa*, you taught us not only the principle of perseverance and hard work, but also the importance of ethics and honesty. You have sup-

ported us unconditionally during all our lives, giving us always everything you had. This thesis is as much mine as it is yours. I love you immensely. Cristina, I am so happy you came into this family, you are for me an absolute example of principles, competence, and hard work; while at the same time being an equally super fun and good person :) I am so proud of being your sister-in-law. And to my sister, Maria, I dedicate this thesis to you. Not only because you were my inspiration for studying engineering, but also because you have always been my inspiration to uphold my values and stand for what I believe in. I know for sure that we will always have each other backs. And finally, Maria, I hope that you realize that, after all, *parece que la moco igual es doctora jajaja* ;)

Contents

Notation

Space vectors and complex transfer functions

This thesis uses space vectors and complex transfer functions for the majority of the mathematical derivations. Both elements are noted with an overhead arrow, as for example: $\overrightarrow{v_{\mathrm{dq}}} = v_{\mathrm{d}} + jv_{\mathrm{q}}$; $\overrightarrow{v_{\alpha\beta}} = v_{\alpha} + jv_{\beta}$; $\overrightarrow{H_{\mathrm{dq}}(s)} = H_{\mathrm{d}}(s) + jH_{\mathrm{q}}(s)$; and $\overrightarrow{H_{\alpha\beta}(s)} = H_{\alpha}(s) + jH_{\beta}(s)$. The upper index * denotes complex conjugate as in: $\overrightarrow{v^*_{\mathrm{dq}}} = v_{\mathrm{d}} - jv_{\mathrm{q}}$ and $\overrightarrow{H^*_{\mathrm{dq}}(s)} = H_{\mathrm{d}}(s) - jH_{\mathrm{q}}(s)$. The upper index $^{\mathrm{ref}}$ is used for references to control loops.

A complex transfer function is a transfer function with complex coefficients [124]. Complex transfer functions are very useful for representing Two Input Two Output (TITO) systems. An example of a TITO system is shown below:

$$\begin{bmatrix} V_{2\mathrm{d}} \\ V_{2\mathrm{q}} \end{bmatrix} = \begin{bmatrix} H_{\mathrm{dd}}(s) & H_{\mathrm{dq}}(s) \\ H_{\mathrm{qd}}(s) & H_{\mathrm{qq}}(s) \end{bmatrix} \begin{bmatrix} V_{1\mathrm{d}} \\ V_{1\mathrm{q}} \end{bmatrix} \tag{1}$$

If the input and output voltages are represented as a space vector ($\overrightarrow{v_{1\mathrm{dq}}} = v_{1\mathrm{d}} + jv_{1\mathrm{q}}$ and $\overrightarrow{v_{2\mathrm{dq}}} = v_{2\mathrm{d}} + jv_{2\mathrm{q}}$, respectively), and if the transfer function matrix complies with certain symmetry conditions (i.e. $H_{\mathrm{dd}}(s) = H_{\mathrm{qq}}(s)$ and $H_{\mathrm{qd}}(s) = -H_{\mathrm{dq}}(s)$), then the system can be represented with only one complex transfer function as:

$$\overrightarrow{v_{2\mathrm{dq}}} = \overrightarrow{H_{\mathrm{dq}}(s)}\overrightarrow{v_{1\mathrm{dq}}} \tag{2}$$

where $\overrightarrow{H_{\mathrm{dq}}(s)} = H_{\mathrm{dd}}(s) + jH_{\mathrm{qd}}(s)$. These symmetry conditions are met by a lot of systems, including certain converter controllers. If these symmetry conditions are not met, then the TITO system can be represented with two complex transfer functions, as in:

$$\overrightarrow{v_{2\mathrm{dq}}} = \overrightarrow{H_{+}(s)}\overrightarrow{v_{1\mathrm{dq}}} + \overrightarrow{H_{-}(s)}\overrightarrow{v^*_{1\mathrm{dq}}} \tag{3}$$

where $\overrightarrow{H_{+}(s)} = \frac{1}{2}[H_{\mathrm{dd}}(s) + H_{\mathrm{qq}}(s) + j(H_{\mathrm{qd}}(s) - H_{\mathrm{dq}}(s))]$ and $\overrightarrow{H_{-}(s)} = \frac{1}{2}[H_{\mathrm{dd}}(s) - H_{\mathrm{qq}}(s) + j(H_{\mathrm{qd}}(s) + H_{\mathrm{dq}}(s))]$. One advantage of this notation is that the space vectors $\overrightarrow{v_{1\mathrm{dq}}}$ and $\overrightarrow{v^*_{1\mathrm{dq}}}$ can be interpreted as a rotating vector at a certain frequency and its conjugate, which rotates at the same frequency but in the opposite direction (or sequence).

Further, the main advantage of using complex transfer functions in converter modelling is the easiness of performing frame transformations. A transformation from the dq frame to the $\alpha\beta$ frame can be performed with a simple frequency shift [125]; for example: if $\overrightarrow{v_{2\mathrm{dq}}} = \overrightarrow{H_{\mathrm{dq}}(s)}\overrightarrow{v_{1\mathrm{dq}}}$, then the voltages in the $\alpha\beta$ frame are: $\overrightarrow{v_{2\alpha\beta}} = e^{j\omega t}\overrightarrow{v_{2\mathrm{dq}}}$ and $\overrightarrow{v_{1\alpha\beta}} =$

$e^{j\omega t}\overrightarrow{v_{1\mathrm{dq}}}$. The relationship between them can be easily found as: $\overrightarrow{v_{2\alpha\beta}} = \overrightarrow{H_{\alpha\beta}(s)}\overrightarrow{v_{1\alpha\beta}}$, with $\overrightarrow{H_{\alpha\beta}(s)} = \overrightarrow{H_{\mathrm{dq}}(s - j\omega)}$ where ω is the frequency at which the dq frame rotates.

Phasors

Additionally, phasor notation is used in certain parts of the thesis, especially in Chapter 4. This is identified with bold notation e.g., $\mathbf{I_{WT}} = I\angle\phi$. Note that phasors are different from space vectors in that space vectors are dynamic (usually, space vectors rotate at a certain frequency) whereas phasors are static.

Chapter 1

Introduction

1.1 Motivation

1.1.1 Offshore wind power plant development

By the end of 2021, there was approximately 236 GW of wind energy capacity installed in Europe: 207 GW onshore and 28 GW offshore (see Fig. 1.1) [1]. If the promises made by European governments are kept, it is expected that, in the period 2022-2026, another 116 GW of new wind farms will be installed on the continent. Around 25 % of this should be offshore wind. This means that, between 2022-2026, the European wind offshore capacity is expected to double.

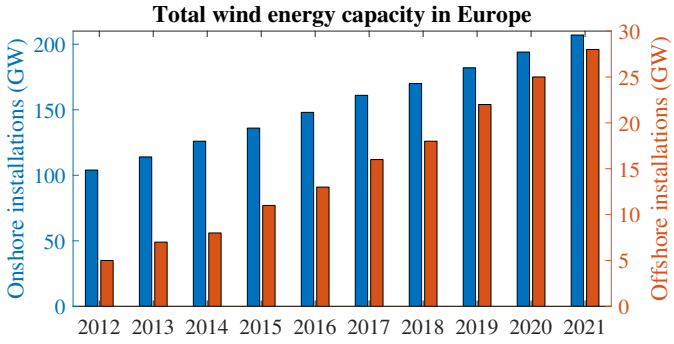

Figure 1.1: Total installed wind energy capacity in Europe [1].

Further ahead, the European Green Deal sets the target of making the EU carbon-neutral by 2050 [2]. In order to achieve this goal, in 2018, the European Commission envisioned an installed offshore wind capacity between 230 and 450 GW by 2050 [3]. With 450 GW installed, offshore wind could provide around 30 % of Europe's electricity demand in 2050 [4]. Some reports argued then that, indeed, it is feasible to deploy 450 GW by 2050 [4]. Later, in 2020, the European Commission estimated that an installed capacity of 300 GW of offshore wind by 2050 was realistic and achievable [5]. In parallel, the International Energy Agency (IEA) calculated in 2019 that offshore wind could become the number one source of power

generation in Europe around 2040, and that high capacity installations are expected in the upcoming years in China, the United States, Korea, Japan, and others [6]. A recent analysis made by the International Renewable Energy Agency (IRENA) indicated that offshore wind could have, globally, an installed capacity of 380 GW by 2030 and more than 2000 GW by 2050 [7].

Despite variations in the exact installation predictions by different organizations, nowadays, it is undoubted that offshore wind will become a fundamental pillar in the future energy mix. As such, offshore wind power plants must operate in a safe, efficient and resilient manner, which includes ensuring the stability and power quality of the farms. However, as a Power Electronic Converter (PEC)-based system, this is not always straightforward.

1.1.2 Stability, harmonics and voltage imbalance in offshore wind power plants

The stability and power quality properties of offshore wind farms depend, among other things, on the type of HV connection to shore. A schematic of both HVAC and HVDC configurations, with some of the nomenclature used in this thesis, is shown in Fig. 1.2.

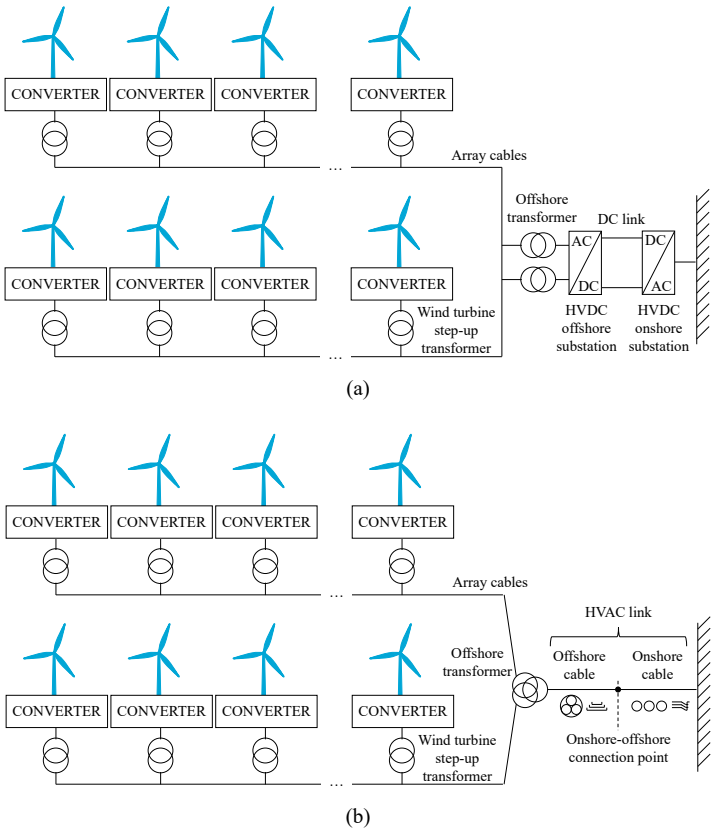

Figure 1.2: Offshore wind farm schematic with a) HVDC connection; b) HVAC connection.

Nowadays, the preferred choice for wind turbine systems is variable-speed generators [8], which may be: full converter technology (also called type IV wind turbine), or Doubly Fed Induction Generator (DFIG) technology (also called type III wind turbine). The focus of this thesis is type IV wind turbines, since they are more common in offshore wind farm applications. If an instability or power quality problem appears in a type IV wind turbine, the grid-side inverter (see Fig. 1.3) might be the culprit, since it is the one directly facing and interacting with the grid. Thus, much of the effort of this thesis is focused on modelling and analysing this converter.

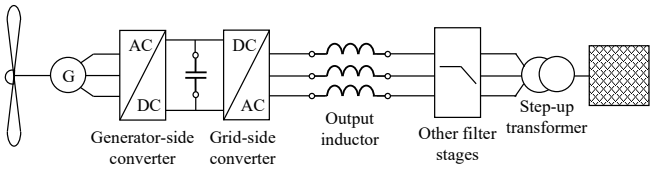

Figure 1.3: Schematic of a type IV (full converter) wind turbine.

(a) Harmonic stability

Instability related to converter control loops may happen in both HVDC and HVAC connected offshore wind power plants. An HVDC connection implies a small system offshore that operates relatively independently from the rest of the power grid and in which PECs manage virtually 100 % of the power. Apart from issues originated from the low inertia in the offshore system, harmonic stability interactions may appear between the PECs in the wind turbines and the PEC in the HVDC substation. One of the particularities of HVDC-connected wind farms is that the impedance of the offshore HVDC converter highly influences the grid impedance seen by the wind turbine converters. The impedance of HVDC converters is quite complex compared to the passive impedance of overhead lines and cables. At some frequency ranges, its real part can even be negative, making the system more prone to resonant phenomena [9]. Further, to increase efficiency, offshore wind power plants are usually designed to minimize resistive losses, which lowers the damping in the system. Fig. 1.4 summarizes some of the main harmonic instability challenges in HVDC-connected offshore wind farms.

In contrast, HVAC-connected wind farms may be vulnerable due to the long HV link to shore. There is abundant literature that reports that there is a break-even distance after which using HVDC transmission is more financially efficient than the HVAC counterpart. However, some papers argue that, if innovative reactive power compensation schemes are considered, the break-even distance might be higher than what it is usually assumed [10,11]. In fact, there are a lot of offshore wind farms connected via long HVAC cables, like the Gemini wind farm in the Netherlands (which has an export HVAC cable of around 100 km [12]), the Horns Rev B wind farm in Denmark (which has a 100 km AC cable connection divided between 42 km of subsea cable and 58 km of onshore cable [13]), or the recently built Hornsea One project in the UK (which consists of 145 km offshore plus 38 km onshore [14]).

Therefore, offshore wind farms with long HVAC connections are common. This pro-

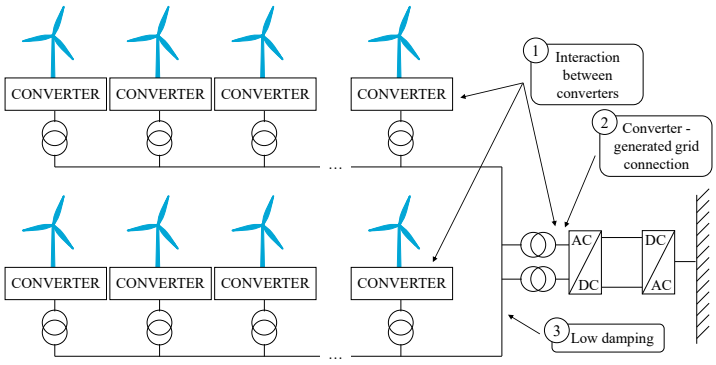

Figure 1.4: Harmonic instability challenges in HVDC-connected offshore wind farms.

duces some harmonic instability challenges, as summarized in Fig. 1.5. From the point of view of the wind farm, a long HVAC cable makes the grid connection weaker, which, apart from several frequency and voltage stability challenges, it might make synchronization challenging for converters after a big disturbance [15]. In particular, in a weak grid, a disturbance might make the voltage at the Point of Common Coupling (PCC) to oscillate significantly, making it challenging for the PLL in the converter to synchronize. The estimated phase-angle by the PLL might be oscillatory or might take a long time to converge, which influences the currents injected by the converter, affecting the voltage at the PCC and further degrading the stability of the system. Also, when multiple converters are connected in parallel to the grid (like each string in a wind farm), the grid impedance causes their dynamics to be coupled, since the current injected by one converter affects the voltage at the PCC that is followed by another converter (and vice-versa), which might affect the harmonic stability of the system [16].

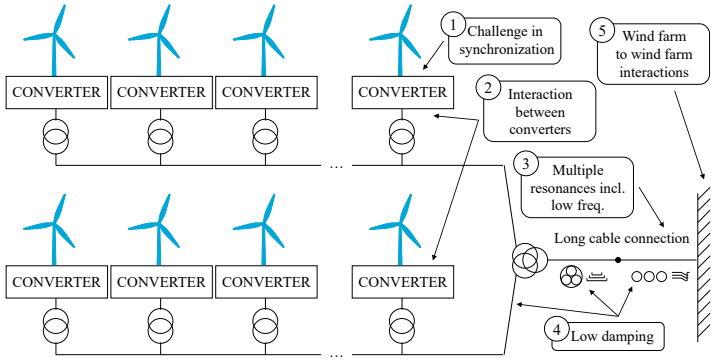

Figure 1.5: Harmonic instability challenges in HVAC-connected offshore wind farms.

In addition, due to the distributed nature of the cable shunt capacitance and series inductance, the cable creates multiple resonant frequencies in a wide frequency range. Further, due to the large capacitance of the long HVAC connection, some of these resonances can

appear at lower frequencies, even between the second and the third harmonic order [17]. These might overlap with the converter control loops in the wind turbines, which might create stability problems. Further, the HV transmission in offshore wind farms has very low damping by design, which makes the resonances in the system to have high-quality factors [17], further increasing the risk of undamped or poorly damped oscillations. Finally, offshore wind farms are usually constructed in designated areas in the sea, leading to many offshore wind farms being constructed close to each other (geographically). If these wind farms are connected to the grid at a nearby electrical connection point, interactions could occur [15][1].

Recent research has put much attention into harmonic stability, since it has caused significant oscillations and resonance problems in real applications; for example, in type IV onshore wind farms [18], in solar farms [16, 19], in data centers [20], in point-to-point HVDC links [21, 22], in STATCOM applications [23] or in railway systems [24, 25]. Some of these systems present oscillations in the sub-synchronous range, some in the super-synchronous frequency range, and some in both.

Concerning offshore wind farms specifically, a harmonic instability event occurred in the HVDC-connected BorWin1 plant in Germany in 2014 [26]. After increasing the output power level of the plant to its rated capacity, the plant started to interact with the offshore HVDC rectifier substation, resulting in stability oscillations in the super-synchronous frequency range. These oscillations damaged the filters at the HVDC station, which left the plant out of operation for several months. The loss of revenue due to this disruption was calculated to amount to hundreds of millions of euros approximately [27].

TenneT Germany has reported another harmonic stability phenomenon in an HVDC-connected wind farm [28]. During normal grid operation, an AC cable was energised in the offshore grid in order to connect another wind farm to the same HVDC offshore substation. This led to a variation of the resonant frequency seen by the wind turbine converters, driving the converters to instability. Immediately after the cable connection, high oscillations occurred, which led to a trip of the HVDC system. In this case, the resonant frequency was found to be around 451 Hz. The distorted voltage waveform is shown in Fig. 1.6 a) and b).

Another example is the disruption that occurred in August 2019 in the HVAC-connected Hornsea offshore wind power plant in the UK. A remote phase-to-earth fault caused an unbalanced voltage dip at the point of connection of the wind farm with the grid. This led to the wind farm to inject reactive power for voltage support, but in an oscillatory manner [29] (see Fig. 1.6 c)). As a result, the over-current protection systems in most wind turbines tripped, causing the de-loading of the wind farm from 799 MW to 62 MW. The sudden loss of wind generation contributed to cause a wide black-out in the UK power system [27]. It was later determined that, during the incident, the turbine controllers reacted incorrectly due to an insufficiently damped electrical resonance in the sub-synchronous frequency range [30]. The Hornsea wind farm has type IV wind turbine generators installed.

As a final example, [31] focuses on a sub-synchronous oscillation that happened in an HVAC-connected offshore wind farm that uses type IV wind turbine generators. When one of the two exporting offshore cables was taken out of service, the Short Circuit Ratio (SCR)

[1] Some TSOs try to prevent this from happening by connecting wind farms at different points of the HV grid, even if that means significantly de-routing the offshore transmission cable. In an HVAC-connected wind farm, this would materialize in an even weaker (longer) cable connection.

of the connection reduced to an extremely low value ($1.2 - 1.5$ at the MV terminal of the turbine transformer approximately). It was observed that an 8.5 Hz oscillation gradually appeared when the total active power injection was increased to one third of the total active power capacity (see Fig. 1.6 d) and e)). The total export power of the farm had to be curtailed to avoid oscillations. After the incident, a number of converter control parameters were tuned to stabilize the system.

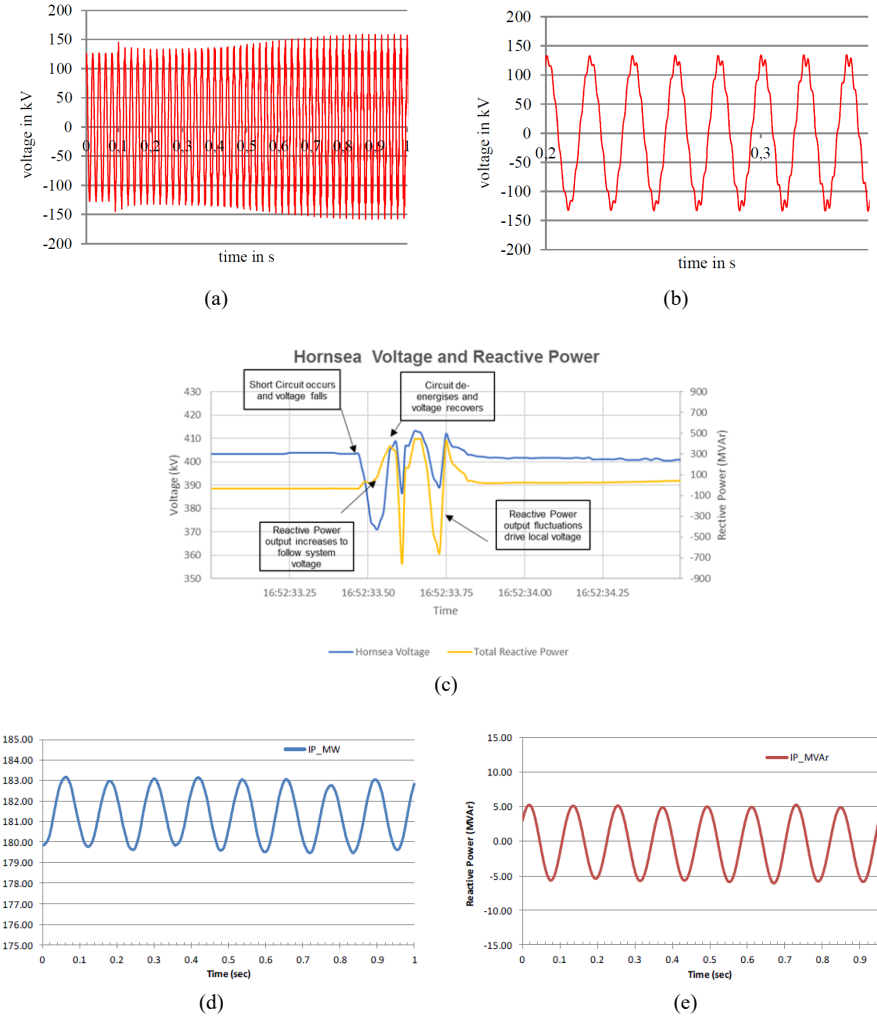

Figure 1.6: Examples of harmonic instability events in offshore wind farms. Example 1: HVDC-connected wind farm with high-frequency oscillation a) measured voltage; b) zoom version of the voltage [28]. Example 2: HVAC-connected Hornsea wind farm during the August 2019 event c) reactive power oscillations due to a sub-synchronous resonance [30]. Example 3: HVAC-connected wind farm with low-frequency oscillation d) measured active power; e) measured reactive power [31].

(b) Steady-state harmonic distortion

The issue of harmonic distortion in offshore wind farms has attracted much attention for many years [32]. Offshore wind farms are prone to high harmonic distortion due to several reasons. One reason could be that wind farms are PEC-dominated systems, and therefore they are systems with high penetration of harmonic sources. However, this is not necessarily the leading cause of harmonic problems in wind farms. An example of the harmonic spectrum obtained from different commercial wind turbines is shown in Fig.1.7. Despite the different manufacturers and topologies of the wind turbines (in this image, two have a DFIG topology while the other has full conversion) it is clear that the harmonic distortion from the wind turbine is relatively low. Other authors also agree that the characteristic emission of wind is small if they are well-designed and, therefore, that this is usually not the cause of system harmonic problems [9].

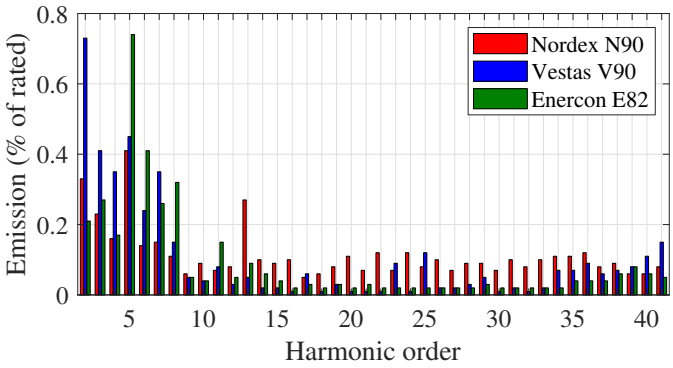

Figure 1.7: Example of the current harmonic spectrum from commercial wind turbines [33].

In a wind farm with HVDC interconnection, another possible source of harmonics is the HVDC offshore converter. However, in a similar way to wind turbine converters, the HVDC rectifier needs to comply with strict harmonic limits. Therefore, it is not expected to be a high harmonic source. For HVAC-connected wind farms, apart from wind turbine converters, the other main harmonic source is the background harmonics present in the grid (i.e., the harmonics created by other users of the grid that provoke background harmonic distortion at the Point of Common Coupling of the farm). However, this source is also relatively low, since system operators make sure to comply with harmonic limits in order to deliver high power quality to their customers. The harmonic limits may vary from country to country depending on their grid codes [34], but in general, the limits on harmonics are quite low (always below 5 %, and the majority of the times below 3 %), as shown in Fig. 1.8. As put in [9] about the grid background distortion, these harmonics can vary over time and depend on the power system configurations, but are relatively small.

Therefore, the risk of having high harmonic distortion in offshore wind farms is not due to emission but, rather, due to amplification. Note that, as mentioned before when discussing stability, the cable systems in offshore wind farms (transmission and collection) have very low damping by design, which makes the resonances in the system to have high-quality factors [17]. Also, the resonant profiles in offshore wind farms might be especially prone to

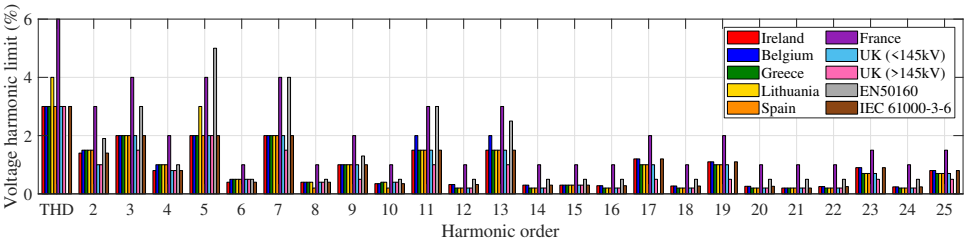

Figure 1.8: Voltage harmonic limits in HV networks in different countries [35].

harmonic amplification. This may happen in both HVDC-connected and HVAC-connected wind farms.

HVDC-connected wind farms are analysed in [26]. The authors express concern for possible harmonic amplification, since the impedances in the offshore grid have multiple resonance peaks, as seen in Fig. 1.9. The resonant peaks change with the switching configuration, meaning that there is a risk of overlapping with typical emission orders (e.g., the 5^{th} or 7^{th} harmonic orders).

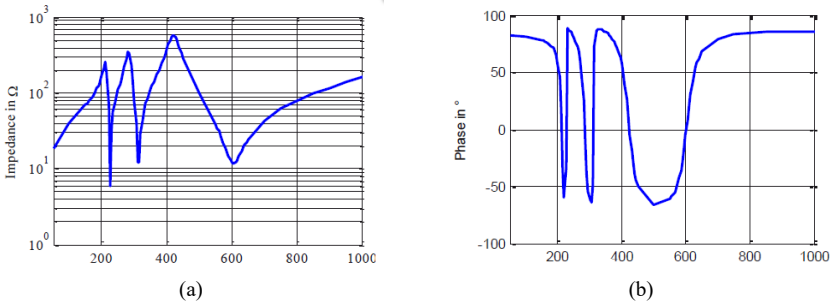

Figure 1.9: Example of grid impedance in an offshore grid of an HVDC-connected wind farm [26].

In the case of HVAC-connected wind farms, there is a risk of harmonic amplification due to the long HVAC cable. This long cable introduces resonances in a wide frequency range, increasing the likelihood of harmonic amplification. Fig. 1.10 shows an example of the impedance seen from the offshore transformer in an HVAC-connected wind farm considering offshore and onshore cable.

Indeed, recent studies [36] have shown that the main reason for the high harmonic measurements in HVAC-connected offshore wind farms is not the high emission sources but, rather, the amplification of the harmonics in the transmission cables. Fig. 1.11 shows voltage and current harmonic measurements performed at the Anholt offshore wind farm in Denmark. In Fig. 1.11 a) it can be seen how the current harmonic distortion is high at the onshore-offshore cable connection point. However, in Fig. 1.11 b), it is shown that the current distortion at the offshore substation is even higher, indicating amplification of the harmonic distortion through the offshore cable.

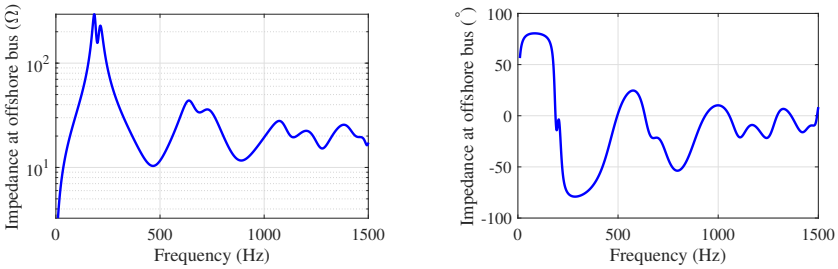

Figure 1.10: Impedance seen from the offshore transformer in an HVAC-connected wind farm considering offshore and onshore cable.

(c) Voltage imbalance

This section addresses voltage imbalance. In HVAC-connected wind farms, from a steady-state perspective, there might be three sources of voltage imbalance, which are summarized in Fig. 1.12.

The first source is the background imbalance that is present in the HV grid (due to, for example, railway connections). This source is expected to be low, since system operators take great care in maintaining the imbalance below specified limits. For example, IEC 61000-3-13 suggests a planning level limit of 1.4% for HV networks. Another example is the measurement campaign in different onshore wind farms connected to an HV weak grid presented in [38]. Here, voltage imbalance levels at the PCC range from $0.5 - 2\,\%$ (with 10 min averaging).

It is worth mentioning that international standards are often customized to local grid conditions and can be tighter or looser [39]. Also, to be precise, it is important to clarify that voltage imbalance measurements are aggregated over a certain period. In particular, imbalance assessment is based on 95% quantiles of the 10 min mean values for one week [40]. These values are appropriate to address long-term (thermal) effects [40]. However, they might mask higher imbalance values that might appear in a shorter time period, which might be detrimental for certain equipment (for example, commutation failure in LCC HVDC converters). This means that, even if a certain HV busbar is compliant with standards (imbalance lower than 1.4%), the imbalance can be higher on a short-term basis. In fact, in [41], it is argued that in weak networks (e.g., rural areas and heavily populated residential areas), the voltage unbalance in distribution grids can reach 10% for short durations of time like tens of seconds (while the limit is usually 2%). Therefore, the background voltage imbalance level is expected to be low, although the limit of 1.4% can be potentially misleading.

The second source of imbalance in offshore wind farms is the network and equipment asymmetries in the offshore wind farm. In particular, the HV connection to the grid typically has two parts: the offshore cable and the onshore cable. The HV offshore connection is typically designed with three-core cables, which means that the conductors, within the same armour, are in symmetrical trefoil formation. In contrast, the HV onshore connection is

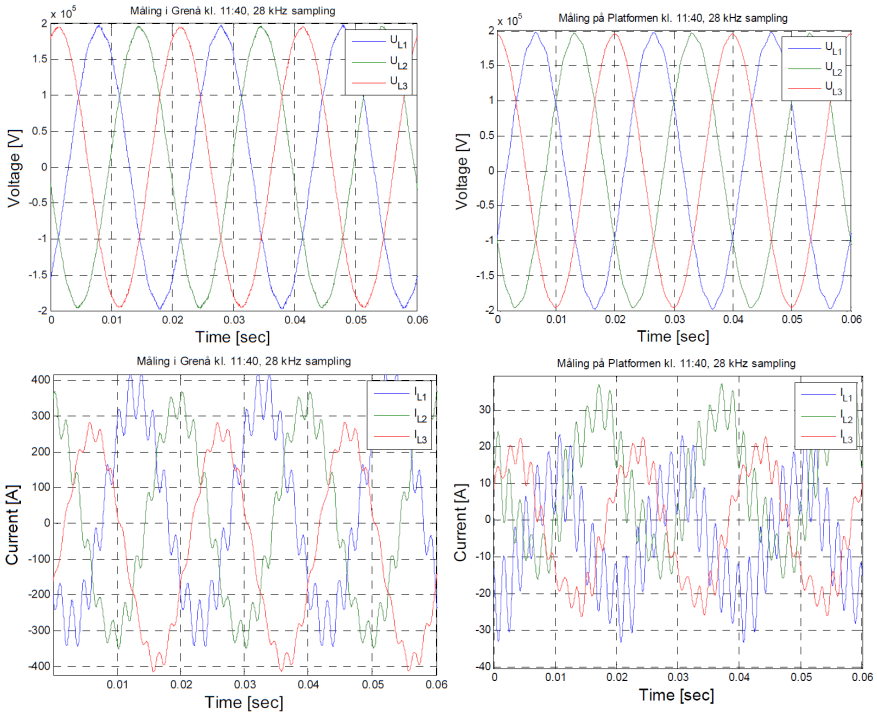

Figure 1.11: Voltage and current harmonic measurements in Anholt wind farm at (a) onshore-offshore cable connection point (b) offshore substation [37].

frequently made with single-core cables in flat formation, which generates asymmetries due to unequal mutual coupling between phases. An example would be the Anholt wind farm in Denmark, with approximately 60 km of onshore cable in flat formation [36]. Other equipment asymmetries might also contribute to the imbalance. For example, wind turbine step-up transformers are usually three-phase transformers with three limbs (e.g. [42]), which is a similar transformer architecture to the one used in many distribution systems. In this type of transformers, the centre leg of the three phases has a different magnetizing current than the outer legs, creating asymmetry.

The third possible source of imbalance in HVAC-connected wind farms is power electronic converters. The PEC behaviour is not necessarily the same in both sequences, depending significantly on the converter controls. As an example, this can be seen in the asymmetrical impedance presented by two-level converters with dq-based current control [43]. In a dq-based current control, the PI controller generates an infinite gain at 0 Hz in the dq frame, which translates to an infinite impedance at 50 Hz in the $\alpha\beta$ or abc frame. However, this 0 Hz in the dq frame does not translate as an infinite gain at 50 Hz in the negative sequence, which means that an imbalanced voltage at the terminals of the converter might induce the converter to create negative-sequence current, even if the current reference is

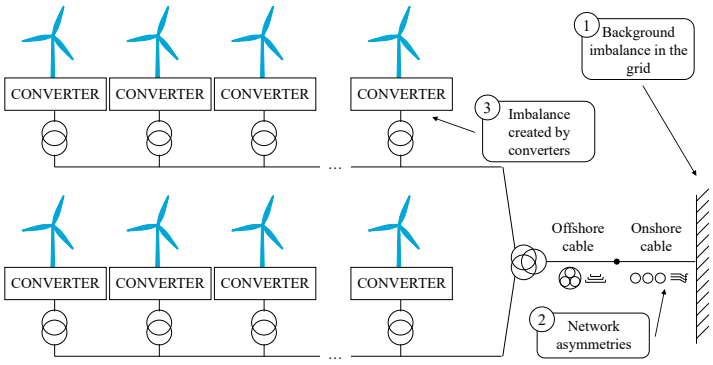

Figure 1.12: Possible sources of imbalance in HVAC-connected offshore wind farms.

purely positive sequence.

In contrast, other control loops have similar behaviour in the positive and negative sequences and can present high gain at 50 Hz in both sequences. For example, this is the case for PR control in the $\alpha\beta$ frame or the double synchronous reference frame current control [44]. Since the offshore wind turbines are increasingly required to control positive and negative sequence currents during faults [45], it is expected that the wind turbine converter controls are designed in such a way that both sequences are fully controllable, and thus, that these converters do not contribute to imbalance levels in the farm in normal operation.

Therefore, the leading causes for steady-state voltage imbalance in HVAC-connected wind farms are considered here to be the (low) background voltage imbalance in the grid, and the network imbalance, primarily due to the onshore cable in flat formation. In order to show the significance of these two imbalance sources, several power flows are conducted in PowerFactory. The onshore cable is modelled as a flat formation cable with cross-bonding with a variable length, the grid as a voltage source with variable voltage imbalance level, and the wind farm simply as a current source that inputs the nominal current of the combined wind turbines (with power factor PF $= 1$). A schematic of the simulation and the results are shown in Fig. 1.13.

Fig. 1.13 shows that, even when the background distortion in the grid is low, the imbalance at the onshore-offshore connection point can be higher due to the onshore cable. Despite this, the actual value depends on whether the voltage imbalance limits apply in the offshore network or not, which might depend, among other factors, on the ownership of the cable.

In HVDC-connected offshore wind farms, the voltage at the offshore network is controlled by the HVDC converter. Therefore, neither the grid nor an HV asymmetrical export cable connection are possible sources of imbalance in these systems. Thus, the expectation is that the voltage imbalance is kept low in steady-state, as opposed to faulty conditions in which high voltage imbalance might also appear.

Indeed, the voltage imbalance in offshore wind farms might be very high during asymmetrical fault conditions. For example, [46] simulates several types of faults at an HVAC-connected wind farm, and the negative-phase-sequence voltage at the system bus bar is 46.2 %, 19.6 % and 44.7 %, depending on the fault. In [47], the simulation results of sev-

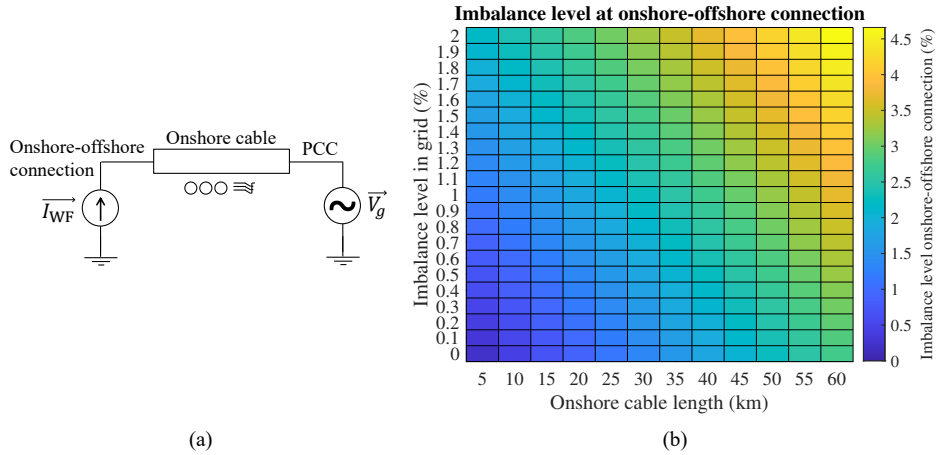

(a) (b)

Figure 1.13: Voltage imbalance level at the offshore substation as a function of onshore cable length and grid voltage background imbalance.

eral faults at the offshore grid in an HVDC-connected wind farm are shown. At the wind turbine terminals, the imbalance level can be even higher.

Voltage imbalance may become a power quality issue in offshore wind farms in a similar sense as harmonics: if the wind turbine injects high unbalanced currents or if the network amplifies/creates unbalanced currents (e.g., due to network asymmetry), the voltage imbalance may become significant, which may affect the operation of other equipment connected to the power grid. To the author's knowledge, however, real examples of such events have not been reported in the literature.

However, another issue is whether the presence of imbalance may affect the operation of the wind farm. Voltage imbalance may significantly affect wind turbine operation during faulty conditions, and as a consequence, Low Voltage Ride Through (LVRT) capabilities have been well researched in the literature. In addition, during normal operation, steady-state voltage imbalance, despite its low levels, may still have a significant impact on the operation of wind farms if the type III wind turbine technology is used. This is due to the fact that DFIG wind turbines have their stator directly connected to the grid, and that voltage imbalance has a great impact on rotating machinery. One example is the Sanmenxia onshore wind farm in China. The voltage imbalance created by a nearby railway system affects the wind turbines, which start to create high negative sequence currents to the point that their protections have tripped on several occasions [48, 49]. Other events are reported in [50]. Consequently, the influence of railway-generated voltage imbalance in DFIG-based wind farms has been studied in the literature [51–54]. In general, the effect of background voltage imbalance on DFIG wind turbines has been a concern for many years [41, 55].

1.2 State of the art

1.2.1 Scope

The topics of stability and power quality in offshore wind farms are very broad subjects that encompass multiple phenomena (see Fig. 1.14). In this section, the state of the art is reviewed focusing on the topics that are dealt with in this thesis: harmonic stability, harmonic distortion, and voltage imbalance. As this section portrays, these three topics have been well researched in the literature, although usually from the perspective of considering them separate issues. In contrast to the state of the art presented here, in this thesis, the relationship between them is explored. In particular, the focus is on the influence of voltage imbalance on the harmonic stability and harmonic distortion of wind turbine converters in offshore wind farms.

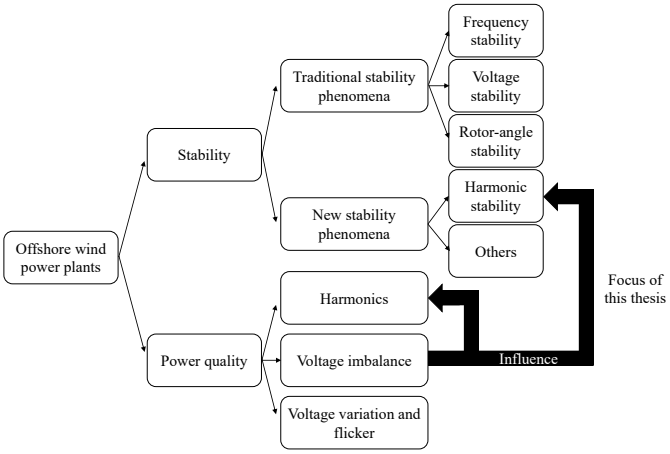

Figure 1.14: Topics and sub-topics within stability and power quality in offshore wind farms.

Note that power system stability is a complex problem that involves multiple phenomena. While stability is a global condition of the system, past literature has classified instability into different types of problems, in an attempt to separate the different possible dynamics involved in the instability, the analysis tools for predicting the potential occurrence of an unstable situation, and the possible remedial measures. In the past, a widely accepted classification of power system stability was the one given in [56], encompassing rotor-angle stability, frequency stability, and voltage stability.

However, the growing penetration of power-electronic converters is changing the dynamics of the electric power system, which has led to the appearance of new stability phenomena that were not observed in traditional power systems. As a consequence, a new stability classification has been recently proposed in [57][2]. In this new classification, two new types of stability appear: “resonance stability” and “converter-driven stability”. In parallel, recent literature has also focused on a new concept called “harmonic stability” [59]. The

[2] A summary of this report can be found in [58].

differences, similarities, and overlaps between these concepts are subsequently explained to clarify the scope of this thesis.

In the new stability classification [57], "resonance stability" does not refer to any power system unstable situation that involves a resonance. Instead, it refers to the resonant situations in which rotating machines directly participate in provoking the instability. This type of resonance usually happens at sub-synchronous frequencies; thus, it is usually named Sub-Synchronous Resonance, or SSR. This phenomenon can appear due to: a) a resonance between a series-compensated electrical network and the mechanical torsional frequencies of the turbine-generator shaft (this would be an electromechanical resonance, named "torsional" in [57]); and b) due to a resonance between series compensation and the electrical characteristics of the generator (this would be an entirely electrical resonance, named "electrical" in [57]). This distinction is shown in Fig. 1.15.

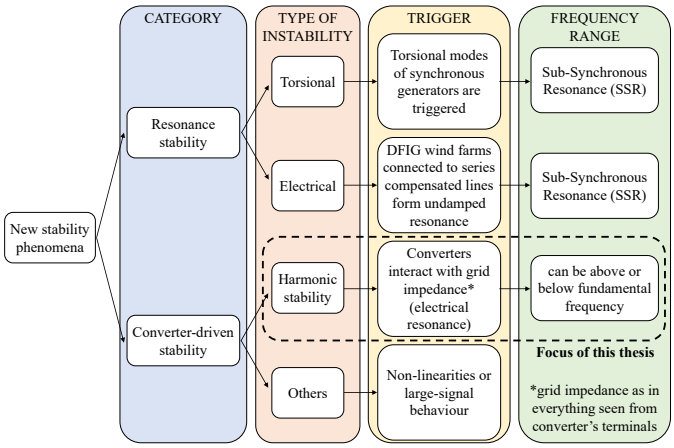

Figure 1.15: New stability phenomena in converter-based power systems, including the typical mechanism by which they are triggered, and their usual frequency range.

Torsional resonance has happened in traditional power systems[3] with little or no presence of power-electronic conversion [60]. With the connection of PECs to the grid, the torsional resonance of existing synchronous generators can be negatively affected, but also positively affected if the PEC controls are adequately designed [61]. In contrast, electrical SSR has never occurred in traditional power systems [58]. It has only been since the connection of PECs that this phenomenon has been observed.

In particular, electrical SSR has occurred in situations in which Doubly-Fed Induction Generator (DFIG) based wind turbines are connected to series-compensated lines. In this instability, the inductance of the stator (which is directly connected to the grid) forms a resonance with the series (capacitive) compensation in the network. This resonance typically appears at sub-synchronous frequencies, where the DFIG wind turbine can create a negative resistance behaviour due to, partly, the induction generator effect (IGE), and partly,

[3]Thus, torsional resonance is not a new stability phenomena, although it is new in the classification. According to [58], this instability type was not included in the previous classification because the time scale in which SSR occurs was not considered in [56].

due to the converter controls. This phenomenon has been observed on several occasions; for example, in Texas (USA) [62], in Minnesota (USA) [63], and in the North-China Power Grid [64]. A detailed explanation of the phenomenon is found in [65].

Electrical resonance can also appear without the involvement of rotating machines. In particular, it has been observed in systems with power-electronic converters. This occurs when the converter faces a resonance in the grid[4], and the converter provokes the amplification of the resonance oscillations (usually, voltage and current oscillations) by lowering the damping of the system in that specific frequency range.

The phenomenon of electrical resonance triggered by power-electronic converters is, in the classification in [57], within the label "converter-driven instability". It is worth pointing out that, in the electrical SSR phenomenon (which, as mentioned before, usually involves a DFIG wind turbine connected to a series-compensated network), the power-electronic converter connected to the rotor might also participate in destabilizing the resonance. However, in this case, the induction-generator effect also reduces the damping in the system and, therefore, the electrical SSR is usually classified separately from "converter-driven instability".

Also, note that resonance is not the only way in which converters can become unstable. Thus, the label "converter-driven instability" encompasses also other instability mechanisms other than resonance; for example, converter transient (large signal) instability due to a loss of synchronism in the presence of large disturbances [66], or instabilities related to converter current or voltage limiting strategies [67].

The term "harmonic stability" has two interpretations in the literature. In [57], it is considered that harmonic stability occurs only when the inner fast control loops of the converter interact with passive grid components, generating oscillations in the range of hundreds of hertz to several kilohertz (like the phenomenon described in [68]). In contrast, in [59], it is considered that "harmonic stability" consists of any event in which a power-electronic converter lowers the damping in the system, creating oscillations in which any control loop in the converter might be involved, and which can appear at above and below the fundamental frequency. This thesis follows the interpretation given in [59]. This means that, in this thesis, the term "harmonic stability" encompasses all the phenomena that the label "converter-driven instability" in [57] groups, except the instabilities caused by certain nonlinearities and large signal behaviour in the converter. This is shown in Fig. 1.15. In this sense, it is worth mentioning as well that, in [69], the harmonic instability phenomenon is called composite instability, in order to emphasize that the resonant frequency of the interconnected system depends on all the components, including converters and their control.

Finally, another ambiguous term is SSR. In a literal interpretation, the term should encompass all resonances that happen below the fundamental. However, in practice, this is not the case. The term Sub-Synchronous Oscillation (SSO) is usually used to encompass all resonance events below the fundamental; whereas SSR is usually used only for torsional resonance or for the resonance that may happen when DFIG-based wind farms are connected to series-compensated lines [65] (see Fig. 1.15). Under this understanding, SSR is a type of SSO. Note that it is possible to have an electrical resonance in the sub-fundamental frequency range for reasons other than SSR. Sub-synchronous oscillations have happened

[4]From the converter's perspective, everything else in the power system is part of the grid and, therefore, from this perspective, a resonance in the grid might be caused by a cable, a filter (sometimes, even the converter's own filter), by other power-electronic converters, or others.

in data centers [70, 71], in electric railways [72] and, according to [65], they can happen in both DFIG-based (type III) wind farms and full-converter (type IV) wind farms when connected to weak grids. For example, type IV onshore wind farms have had sub-synchronous oscillation issues in Xinjiang (China) [18] and in Texas (USA) [73] when connected to grids with low Short Circuit Ratio (SCR). A review of SSO events related to wind farms is found in [65], where it is concluded that a lot of real-world SSO events in these systems can be classified as either "series capacitor SSO" (for type III wind farms interacting with series compensation) or "weak grid SSO" (for type III or type IV wind farms interacting with weak grids). A more thorough review, that includes both wind farms and PV farms is found in [74], and it supports the conclusion of using the terms "series capacitor SSO" or "weak grid SSO". Nonetheless, it is worth remembering that there are other mechanisms for the appearance of SSOs other than "series capacitor SSO" and "weak grid SSO", like torsional resonance. In any case, according to the classification in [57], the SSR (torsional or electrical) falls under "resonance stability", whereas the events related to converter interactions in weak grids fall under "converter-driven stability", albeit that both of them can be SSOs.

No matter the exact terminology, it is clear that new stability phenomena have appeared in power systems in the presence of PECs. One that has attracted much research in recent years is the harmonic stability issue, which is a small-signal oscillatory instability that appears when the converter interacts with the grid impedance or with other converters, unleashing an electrical resonance phenomenon at a wide range of frequencies. This is the type of instability addressed in this thesis.

Finally, the issue of stability and harmonics can be confused since, sometimes, stability oscillations can be so poorly damped that are almost sustained. When the voltage or current waveforms are measured, these oscillations might appear to be steady-state harmonics. These oscillations are what some literature calls "resonance-induced harmonics" [9, 75]. An example of these harmonics, with frequency at 289 Hz, is shown in Fig. 1.16.

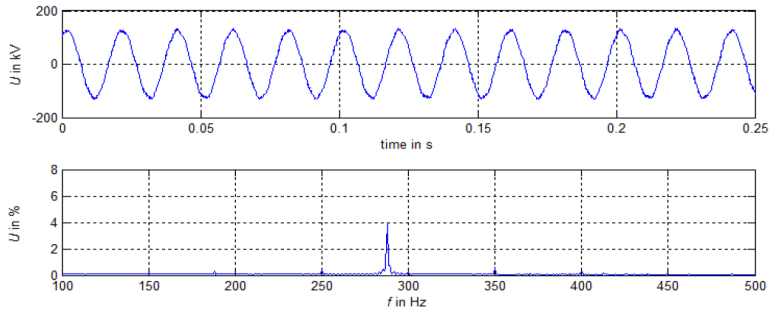

Figure 1.16: Measured resonance-induced harmonic (i.e., a sustained stability oscillation) in a real system [9].

From the signal processing perspective, it is true that a sustained stability oscillation and a steady-state harmonic are indistinguishable. However, in this thesis, both phenomena are differentiated, since the underlying causes are different.

1.2.2 Modelling and analysis

Generally speaking, a PEC can interact with the electromechanical dynamics of machines and the electromagnetic transients of the network due to the wide time scale of its controls. However, the exact matching in between grid stability phenomena and the converter control loops that might influence them, is very case dependent.

On the grid side, stability phenomena such as, for example, rotor-angle stability, may happen in narrower or wider frequency ranges depending on the characteristics of the network (e.g., probably wider in weak grid scenarios). For example, the transients that occur in MV and LV grids with dispersed distributed generation are usually expected to be faster than in HV transmission grids with high levels of inertia [76]. On the converter side, depending on the specific application under consideration (including the voltage and power level, grid-connection requirements, and other specifications), the power-electronic converter might present very different architectures: topology selection, semiconductor choice, switching-frequency decision, control-layout implementation, passive component sizing, etc. The effect that all these converter elements have in different frequency ranges depends on how they have been designed to match the application requirements. Therefore, there is not a unique answer as to which converter controls influence which stability phenomena. However, looking at a specific application, it is useful to regard the frequency as a matching translator between the two, as illustrated in Fig. 1.17.

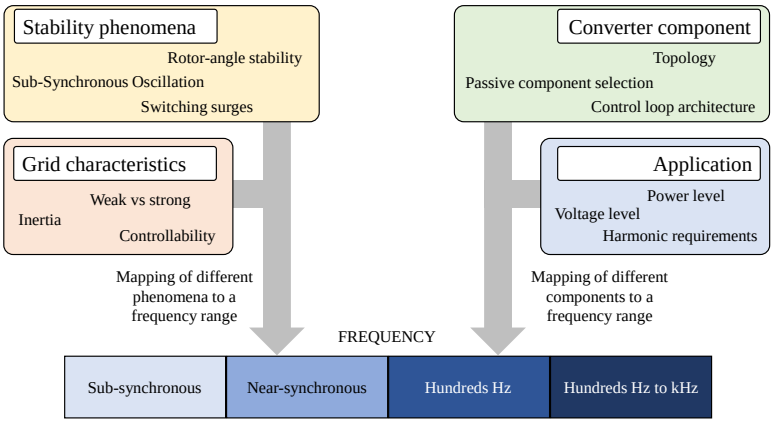

Figure 1.17: Frequency as a translator in between stability phenomena in a specific grid to a certain converter component designed for a specific application.

When modelling a PEC, three key elements are to be considered : (1) the controls, which can be represented to full extent (with the details of the PI controllers, etc.) or by the use of a transfer function of a certain order to represent the main dynamics; (2) the semiconductor power stage, which can be represented with different levels of complexity: thermal model, ideal switch, via an equivalent model (e.g., a voltage source), etc.; and (3) the passive hardware components; i.e., the capacitors, inductors, etc. which are usually represented as pure inductances and capacitances (or perhaps with a small resistor to represent losses).

With respect to the first element, for many converter topologies and modulation strategies, the selection of the switching frequency imposes an upper limit in the control bandwidth design. Especially in the case of medium-voltage MW-level applications, optimized designs typically lead to the choice of semiconductors with high blocking voltages that are operated at low switching frequencies ($f_{\text{sw}} < 3\,\text{kHz}$). For the specific case study of PECs in offshore wind turbines, the switching frequency can indeed be assumed to be limited to $1-2\,\text{kHz}$ (or below) and, thus, the current control bandwidth presents and upper limit of a few hundreds of hertz (see Fig. 1.18).

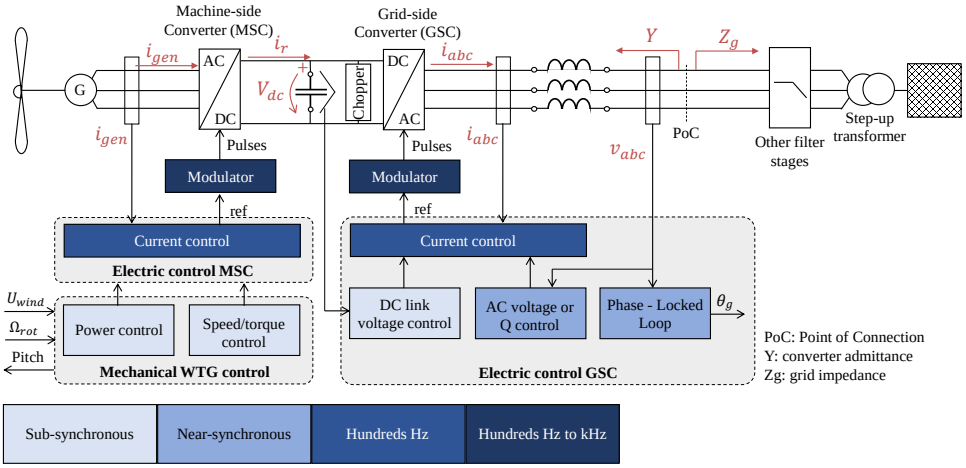

Figure 1.18: Typical control layers in a grid-following type IV wind turbine generator and their relevance in different frequency ranges.

Given the nested control architecture typically implemented in WTG converters, the upper control loops (e.g., reactive-power controller or AC voltage controller) are limited to a smaller bandwidth. The Phase-Locked Loop (PLL) has been shown in the literature to pose harmonic stability problems if designed too fast, and as such its bandwidth is typically limited below 50 Hz, sometimes even below 30 Hz. The main function of the DC link voltage controller is to ensure power balance in the DC link. When there is a wind speed change, the incoming power from the machine-side converter is modified, and thus maintaining a constant voltage (i.e., constant energy accumulated in the DC capacitor) ensures that the incoming power is pushed towards the grid-side converter. Since these dynamics are relatively slow, the bandwidth of the DC voltage controller is typically limited to only a few tens of hertz, or less. Note that certain control loops are implemented in the dq frame (e.g., PLL, DC link voltage controller), and therefore have their effect concentrated around 50 Hz (being their effect narrower or wider depending mostly on their bandwidth). Further, note that the current control in the Machine-Side Converter (MSC) might have a high bandwidth, but from the grid perspective, it can be ignored in many studies due to the effect of the DC voltage loop, as proven in [77, 78].

With respect to the second element, the switching stage, for studies limited to only a few

hundreds of hertz, an average model of the converter that uses controlled-voltage sources may be used. If it is desired to extend the range of the study up until frequencies near the switching frequency (roughly, $\frac{f_{sw}}{2}$ and above), then the switching and modulation strategies together with the switching devices must be explicitly modelled.

With respect to the third element, the passive hardware devices, certain elements may be ignored selectively depending on the frequency range (e.g., the capacitor in the DC link may be relevant for modelling 100 Hz oscillations in single-phase power systems or three-phase unbalanced systems, but perhaps not in other studies [76]).

Since different control loops and converter components might be involved in different events, harmonic instability can manifest in very different ways. Consequently, the PEC model needed to reproduce and analyse different instabilities might vary, having to include more or fewer details of different control loops [76]. For the specific case of Type IV wind turbine generators in weak offshore networks, a modelling recommendation is provided in Fig. 1.19.

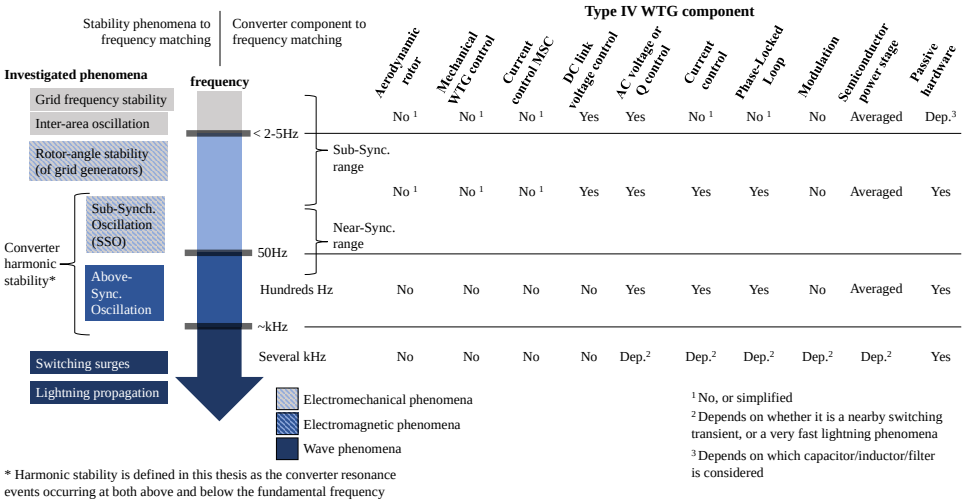

Figure 1.19: WTG modelling recommendation for different stability phenomena in the power grid.

Note that the control architecture shown in Fig. 1.18 and the approximated matching stability phenomena shown in Fig. 1.19 are valid in the case of Type IV WTGs, but may not be valid in other cases of grid-connected converters (e.g., HVDC Modular Multilevel Converters, where other control loops, like the ones in charge of circulating currents or capacitor balancing, may be relevant in certain frequency ranges). Also, note that Fig. 1.19 is focused in stability studies, although many other power system studies may be done considering converters. For example, in the context of scheduling, optimization and planning studies, many power flow problems are typically carried out, in which PECs are usually represented in steady-state as a constant current source. In these studies, attention must be paid to the correct modelling of the consumption/generation pattern by the converter: e.g., constant power behaviour, constant current behaviour, etc. In order to properly represent this be-

haviour, certain outer control loops of the converter might have to be modelled. Finally, the frequency ranges shown in Fig. 1.19 might need to be narrowed or widened depending on the power system to which the WTG is connected. In general, a suitable model for studying transient stability of a converter in strong grids might not be detailed enough to study the same phenomenon in a weak grid.

Since the dynamics involved depend on the specific instability event, the remedial measures to attenuate the problem might also differ (e.g., the control parameters to modify or the filter resonant frequency to adjust). Thus, each harmonic event might involve different dynamics, require different models for its analysis, and involve different remedial measures. This is an important reason why, even though the fundamental mechanism as to how harmonic instability occurs is by now understood (i.e., electrical resonance), much research has been devoted and is still devoted to this phenomenon. Note that, when a specific control loop is involved in an instability situation, it is not necessarily with a detrimental effect. There are certain frequency ranges in which the converter can help to stabilize the system (Fig. 1.20).

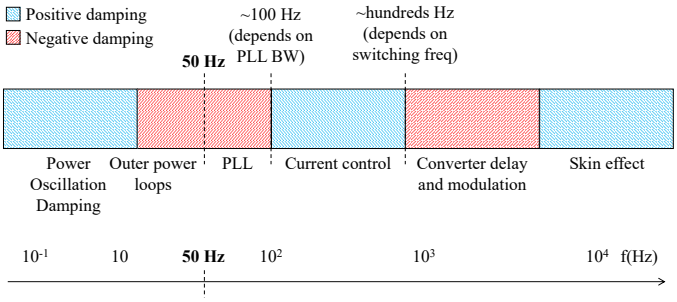

Figure 1.20: Different stability phenomena occur in different frequency ranges [79].

Some of the instability mechanisms modelled and studied in the literature include converter interactions: with its own filter [80], with other parallel inverters and their filters [81], with other converters connected in a meshed network [68], with a lengthy cable [82], between the PLL and the grid [83–86], with the negative resistance behaviour of constant power loads [87], due to the outer control loops [88], due to the PWM modulator [89, 90], due to the sampling process [91], and others. Traditionally, grid-following inverters have been screened for possible harmonic instability mechanisms; however, recent efforts have also focused on grid-forming converters, showing that they are also susceptible to this type of instabilities (e.g. [92, 93]).

In recent years, extensive research has been performed for finding the best method to study harmonic stability for converter systems. Since this instability type is a small-signal phenomenon, linear methods have gathered considerable attention. On the one hand, a small-signal approach can not guarantee global stability of a non-linear system; however, it informs about local stability. In fact, according to [94], most instabilities seen in converter-based power systems can be detected by applying linear control system theory. Two system-level linear-analysis methods have gathered the most attention: the impedance-based method in the frequency domain, and the state-space eigenvalue analysis in the time

domain. Several papers compare the advantages and disadvantages of both methods [59,95]. On the one hand, the impedance-based method is usually praised because of its black-box capabilities. An impedance model of a converter can be derived: analytically, if all the details of the controls and parameters are known; numerically, with detailed time-domain simulations; or with measurements of the real system. The analytical approach is interesting because it reveals the relation of different parameters and control loops. The measurement in the real system is interesting because it provides the highest confidence in the accuracy of the model with respect to the real system; although this confidence is subject to performing the measurements correctly, which can sometimes be a challenge. The numerical method usually provides sufficient accuracy, and does not present the difficulties of measurements in the real system. Once the impedance model is obtained, it can be given to third parties to perform system-wide stability studies, without having to reveal details of the control design, which are usually proprietary. In wind farm systems specifically, this black-box characteristic is very appealing, since they are usually multi-vendor systems. In an HVAC-connected wind farm, the supplier of the wind turbines and a possible STATCOM can be different; and in an HVDC-connected wind farm, this happens with the supplier of the wind turbines and the HVDC system.

The base of eigenvalue analysis is finding the state-matrix of the system, and calculating its eigenvalues. The disadvantage lies in the fact that the eigenvalue calculation is an ill-conditioned problem, so for high-order systems, the accuracy quickly decays. In traditional power systems with synchronous generators, the rotor-angle stability was often studied using the eigenvalue method. However, in that specific case, the frequency range of interest was the low-frequency range, where the network transients can be ignored. Under this assumption, the passive network can be modelled as a set of algebraic equations (as opposed to differential equations), which reduces significantly the order of the system to analyse. PECs, however, can interact in many frequency ranges. If the eigenvalue method is to be used to study a wide frequency range, measures should be taken to guarantee the accuracy of the eigenvalue calculation, like increasing the precision of the computer calculations (e.g., increasing double precision to quadruple, or more). If the eigenvalue method is used in the lower frequency range, perhaps some network simplifications can be performed, depending on the system. For example, [31] uses the eigenvalue method to model a sub-synchronous oscillation in an HVAC-connected wind farm. Alternatively, the wind turbines and the collector cable can be aggregated to help in performing such studies. This is done, for example, in [94][5]. Another disadvantage of the eigenvalue method is its difficulty in considering the frequency dependence of assets [26] (e.g., skin effect).

On the other hand, one weakness of the impedance method is that it does not provide participation factors like the eigenvalue method. However, some techniques have been recently developed to identify the converter or converters that participate more in a particular oscillation mode using impedance models (e.g. [97, 98]). Further, another disadvantage of the impedance method is the limited observability of certain states, given its dependence on the definition of local source-load sub-systems, which makes it necessary to investigate the stability at different sub-system interfaces [95]. Nonetheless, the evaluation of stability with the impedance-based method is very time efficient, and therefore this is not a signifi-

[5] Any kind of aggregation must be dealt with great care, because the aggregation process might mask internal unstable modes of the system (i.e., provoke an undesired pole-zero cancellation) [96].

cant disadvantage.

As a result, many authors are now considering to use the impedance method for system-level stability studies. In real multi-vendor systems, this might be the most practical solution to preserve the intellectual property of manufacturers. Once it is decided to apply the impedance-based method, a question arises as to whether using the Nyquist stability criterion, bode-based criteria, or others. This question has also been addressed in the literature [99–102].

In addition, it is worth mentioning that, at first, the impedance models developed were SISO models [43], where the impedance represents the current that a converter creates at a specific frequency, as a result of a voltage at its terminals at the same frequency. Later, it was found that certain dynamics in the converter create frequency couplings, in the sense that a single perturbation frequency in the voltage can create two (or more) frequencies in the current (e.g., [89, 91, 103, 104]).

The interest in frequency coupling dynamics appeared from real-life experiences. Usually, when a harmonic instability phenomenon occurs, an oscillation with a relatively constant frequency starts to enlarge (see the examples in Fig. 1.6). However, sometimes it has occurred that two coupled frequencies start to grow. For example, the current that appeared in an SSO event in an onshore wind farm zone in North China is shown in Fig. 1.21 a) and b) [65]. The current measured contains one main oscillation of 50% of the fundamental and a coupled frequency. Another example of an instability event involving coupling frequencies is shown in [105, 106], where a type III wind turbine started to interact with the inductive grid, creating oscillations at 37 and 63 Hz. The voltage spectrum of this event is shown in Fig. 1.21 c), and the current spectrum of a STATCOM connected to the farm in Fig. 1.21 d) [74].

A third example happened in West China in 2015. The specific zone has a lot of onshore wind farm connections and long lines, making the SCR small. On July 1st 2015, a type IV wind farm started to oscillate. The oscillations occurred around 77 Hz with a coupled frequency of approximately 23 Hz [94] (see Fig. 1.21 e)). The frequency coupling, which appeared in the sub-synchronous range, coincided at times with the torsional frequencies of a nearby synchronous-generator-based power plant, thus triggering a strong torsional interaction. According to [65], the oscillation was caused by the interaction between the weak AC grid and the type IV wind generators, and is confirmed to be due to an inappropriate Phase-Locked Loop (PLL) design. Changing the wind turbine control mitigated the problem.

Therefore, increasing research has been done for developing more accurate converter models that incorporate frequency coupling dynamics, and other dynamics, to accurately represent and understand the mechanisms that drive converters into instability. As a consequence, not only Linear Time Invariant (LTI) but also Linear Time Periodic (LTP) [107] models are becoming increasingly common.

In any case, both LTI and LTP models are linearised versions of a non-linear system and, therefore, can only guarantee local stability. In a real application, impedance-based analysis (based on LTI or LTP converter models) can be performed to detect the situations in which the system presents a low stability margin. In this sense, the number of potentially-problematic situations can be narrowed down, after which time-domain EMT simulations are recommended for further screening [28, 94].

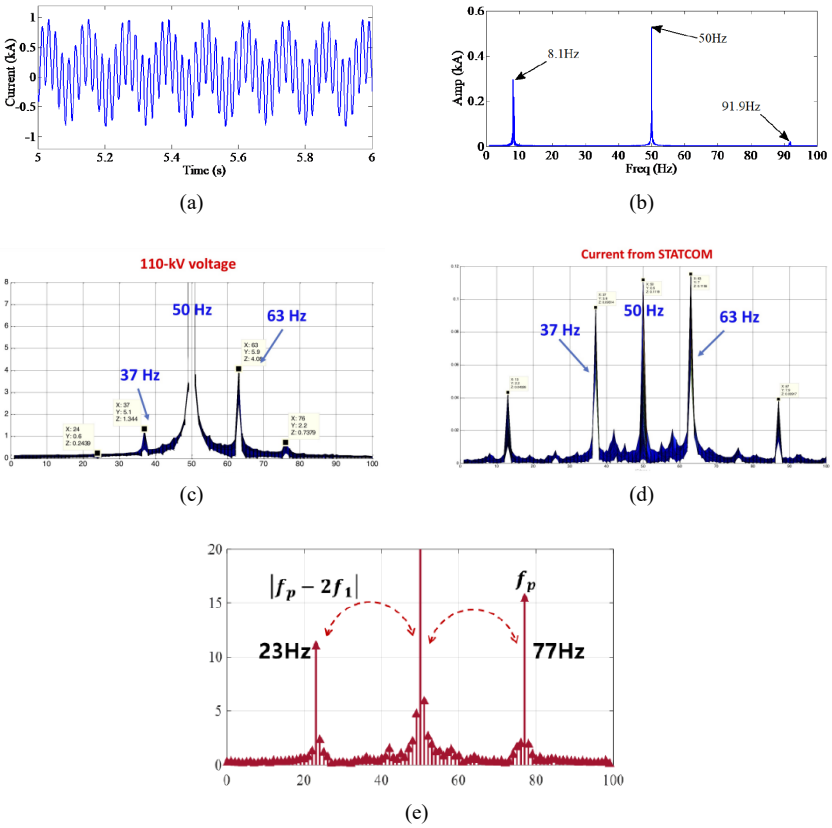

Figure 1.21: Examples of harmonic instability with frequency coupling dynamics. Example 1: SSO measured in an onshore wind farm zone in North China a) current waveform; b) current spectrum [65]. Example 2: oscillations measured in an onshore type III wind farm with weak grid interconnection c) voltage spectrum; d) current spectrum from a connected STATCOM [74]. Example 3: Event in West China e) spectrum of the oscillating current output from type IV WTs [94].

For harmonic studies, in order to model a distortion-generator device, a current source with the specific harmonic distortion can sometimes be used. However, in order to model PECs specifically, literature has shown that it is better to model the converter as a Norton (or Thevenin) equivalent [32]. In this equivalent, the current source represents the characteristic emission of the converter (i.e., the emission that the converter generates in normal operating conditions, when confronted to a perfectly balanced and undistorted voltage), while the impedance represents the distortion that the converter generates as a response to background distortion in the voltage at its Point of Connection (PoC). Therefore, the impedance used for stability studies can also become practical in harmonic studies. Recent literature proposes more advanced harmonic models of PECs in which the statistical variability of the harmonic emission is considered. However, considering an MIMO model for the impedance, that includes frequency couplings, has not been done in the literature.

Sometimes, the distortion at a particular busbar is of interest. For example, this can be the case at the point of interface of a particular new or planned installation with the grid. In these cases, aggregation of the new installation elements and aggregation of the grid can be helpful to address the role of each sub-system in the overall distortion at the interface. In the case of offshore wind farms, the aggregation of the whole wind farm can be performed as a Norton equivalent, while the grid can be aggregated as a Thevenin equivalent, as shown in Fig. 1.22. From this figure, (1.1) can be derived.

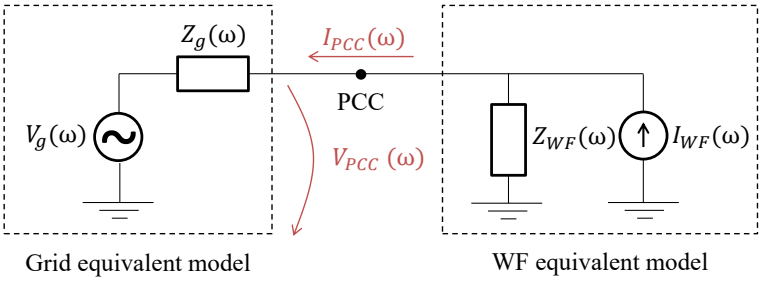

Figure 1.22: Schematic of Wind Farm (WF) to grid connection at the PCC.

$$V_{\mathrm{PCC}}(\omega) = \underbrace{\frac{Z_{\mathrm{WF}}(\omega)Z_{\mathrm{g}}(\omega)}{Z_{\mathrm{WF}}(\omega)+Z_{\mathrm{g}}(\omega)}}_{Z_{\mathrm{post}}(\omega)} I_{\mathrm{WF}}(\omega) + \underbrace{\frac{Z_{\mathrm{WF}}(\omega)}{Z_{\mathrm{WF}}(\omega)+Z_{\mathrm{g}}(\omega)}}_{\mathrm{HG}(\omega)} V_{\mathrm{g}}(\omega) \tag{1.1}$$

In (1.1), the influence of both harmonic sources (wind farm harmonics I_{WF}, coming from the wind turbines, and background harmonics V_{g}) is shown. Also, (1.1) shows how their amplification depends on the relation between the grid equivalent impedance Z_{g} and the aggregated wind farm impedance Z_{WF}. The amplification factors of the harmonic sources are usually called Harmonic Gain (HG) and post-connection impedance (Z_{post}). It can clearly be seen in (1.1) that, if $Z_{\mathrm{WF}} + Z_{\mathrm{g}} \approx 0$ (i.e., if there is a series resonance in between the wind farm and the grid), the amplification can be very high [9]. In the Netherlands and several other countries [34,108], the methodology for addressing steady-state harmonic compliance in OWPPs is inspired by this schematic (Fig. 1.22).

Two useful tools for harmonic analysis at the system level are the harmonic power flow (which is a power flow performed at different frequencies) and the impedance frequency scan (in which the frequency-dependent impedance of the network is obtained, which helps to reveal possible resonance points). Finding the possible resonance points is also relevant from the stability point of view.

If a resonant frequency in the power system is undamped or poorly damped, and if a harmonic source (e.g., a converter or other device) injects harmonic currents at that frequency, very high oscillations can appear in the system. In the end, these are just amplified steady-state harmonics. Sometimes, the harmonics are not injected in steady state but in a transient manner. A typical example is the harmonics injected at twice the fundamental frequency (and other frequencies) when energizing a transformer. This process has excited some low-frequency cable resonances in the past; for example, in HVAC-connected offshore wind

farms [109]. In any case, no matter whether the harmonic injection mechanism is steady or transient, if there is a resonant frequency in the power system that is undamped or poorly damped, the system is not strictly unstable; however, if the resonance is stimulated, the consequences may be equally destructive.

In general, resonant phenomena are more pronounced if the system is unloaded (i.e., no active power is transmitted). This can happen, for example, during the system energization or when some wind turbines are out of service and the cable network is unloaded. The overall damping is higher when the system is loaded [110].

For imbalance propagation studies, a similar approach as the one for harmonic studies can be applied, except that, in this case, only the 50 Hz frequency is addressed. This means that, for modelling PECs, the network, and other power system elements, the frequency dependency of elements has no impact as long as the 50 Hz characteristics are accurately represented. For the wind turbine converter models in particular, as mentioned before, the converter controls are expected to be designed so that full controllability of positive and negative sequence currents is achieved. Therefore, the control gain is expected to be infinite at 50 Hz in both sequences, which means that the impedance is infinite at 50 Hz and that the converter behaves like a perfect current source (with both sequences) at this frequency. Therefore, a Norton equivalent is not necessary for modelling the wind turbines in imbalance propagation studies. Note that, in this case, a harmonic power flow is not needed but only a normal power flow.

It is worth clarifying that there are different definitions of imbalance although, usually, the degree of imbalance is expressed as the ratio of the negative- and zero-sequence components to the positive-sequence component. In particular, the appearance of negative-sequence voltage is usually the primary concern due to its impact on three-phase rotating machinery. Hence imbalance usually refers to negative-sequence imbalance [111]. In the specific case of offshore wind farms, zero sequence components (at 50 Hz or other frequencies) are not expected to propagate throughout the farm since the wind turbine step-up transformers and the offshore transformers both usually have one side of the transformer connected in delta configuration. Therefore, in this thesis, when addressing voltage imbalance issues, the focus is exclusively on negative-sequence voltage.

1.2.3 Remedial measures

Stability and harmonics are sometimes treated in parallel when addressing remedial measures. Usually, passive filtering and active filtering techniques are considered when thinking about solving harmonic issues. Passive filtering consists of installing passive filters as shunt elements to decrease voltage distortion at the point of interest [112]. These filters work by providing a low impedance path to the harmonic currents. In offshore wind power plants, they might be installed: at the wind turbine level, at the offshore substation, or at the onshore substation.

Active filtering, however, is a term that is usually used when power-electronic devices measure a specific distortion in a voltage or current signal, and generate the necessary opposite waveform to cancel out the harmonic (i.e., a distortion with opposite phase angle). In this way, the PEC absorbs/suppresses the harmonic. Usually, this is performed with a PEC connected in a shunt manner to the distortion [113]. Active filtering is a term also used when the objective is to eliminate a current or voltage harmonic generated by the converter

itself; which might involve a total or partial cancellation of the harmonic. For example, the distortion can be separated in the part due to the characteristic emission of the converter, and in the part that the converter generates due to the background distortion (non-characteristic emission), and one or both can be compensated [114].

Another approach is to modify the controller in the power-electronic converter in order to shape its output impedance, changing the resonant profile of the network and reducing the harmonic amplification. This approach can include damping an existing resonance, or moving a resonance to another frequency where there are no significant harmonic sources. This method is sometimes called active damping, and some articles consider it a type of active filtering [115]. An example of real application is given in [115, 116], where active filtering (in particular, active damping) was installed in the wind turbine converters of Anholt offshore wind farm (Denmark) in order to damp a resonance that was provoking harmonic amplification.

These active filtering functions can be implemented in various power-electronic converter devices in a wind farm, for example, in the wind turbine grid-side converter [115], the STATCOM in an HVAC-connected wind farm [117–119], or the HVDC converter in an HVDC-connected farm. The control function can be implemented to correct the harmonics at a local bus to which the PEC connects, or at a remote bus [113].

Both active and passive filtering have advantages and disadvantages, as discussed in the literature [112]. The main advantage of active filtering is that it has the potential to be adapted to cope with the changing network configurations[6], and that the same device can be used to compensate several frequency components [121]. The main disadvantage of active filtering is that the frequency bandwidth of action is limited. In any case, the solution to harmonic problems in complex wind farm systems might be a combination of all types of solutions [112].

Changing the resonant profile of the network can also be beneficial in terms of stability, which is why damping techniques are usually discussed also within this field. This applies to both active damping and passive damping techniques. For example, [122] discusses an active damping technique for wind turbine converters in HVDC-connected wind farms to improve stability. Also, [94] shows an example in which installing a passive filter in the low-voltage side of the offshore transformers, which is tuned at a specific frequency where the wind farm is non-passive, can help to increase the passivity of the system.

Further, some solutions apply to harmonic problems only. In particular, some solutions try to increase harmonic cancellation at the wind farm level. For example, the carrier of different close-by wind turbines can be synchronized with a specific phase-angle displacement to promote harmonic cancellation [32]. Another solution could be to modify the vector group of the wind turbine step-up transformers. Sometimes, these measures have been called “active filtering in groups of wind turbines” [112]. These measures are more or less effective depending on the frequency range. Also, different modulation techniques have different emission profiles, so that could be another degree of freedom to reduce or modify the harmonic emission of PECs [113].

Further, apart from passive and active damping, other methods can be applied to address stability issues. Some other methods that have been applied in real wind or solar farms are

[6]For example, due to different configuration topologies of the network or due to different number of wind turbines in operation, the resonances in the network can significantly vary [120].

reviewed in [94], which include: internal operational scenarios (which consist in analysing the different network topologies that may happen within a farm and trying to avoid the topologies that lead to worse resonance conditions), external operational scenarios (which is the same as the one before, but considering the different topologies in the external grid), converter set-point adjustment (which, for example, might be reducing the output power of the wind turbine converters under certain operating conditions), converter control adjustment (i.e., control tuning), and system fault level increase (in order to increase the SCR of the grid, different measures can be applied, e.g., the installation of synchronous condensers).

Voltage imbalance in offshore wind farms can also be compensated using power electronic devices like STATCOMs. Also, certain papers have discussed the possibility of using the wind turbine converters themselves to compensate the voltage imbalance created by the asymmetrical HV connection [111] or by other connectees at other nodes in the grid [123].

1.3 Research objective and research questions

Stability, steady-state harmonics, and voltage imbalance are all issues that appear in offshore wind farms. As it has been reviewed, there is abundant literature that explores: the origin and causes of these issues, the modelling of power-electronic converters (and other devices) for studying and predicting the appearance of these phenomena, and the possible solutions to these problems. Thus, significant effort has been paid to study these problems independently.

However, the links between these issues have not been thoroughly addressed. This thesis explores a specific relationship between these issues: the effect of voltage imbalance on stability and harmonic performance. Since voltage imbalance exists in offshore wind farms in normal operation and, also, at much higher levels, during faulty conditions, it is a problem with a wide range of characterizations that may affect the converter steady-state and dynamic operation. Therefore, the research objective of this thesis is:

> Research Objective
> To investigate offshore wind turbine converters and their stability and harmonic generation in the presence of voltage imbalance.

In order to achieve this objective, several research questions have been defined, which have been answered in the different chapters of the thesis.

Chapter 2. *How does the grid voltage imbalance affect the stability and harmonic rejection capability of the PLL?*
Grid voltage synchronization is one of the main challenges for grid-connected converters in the presence of imbalance. In order to study the stability and harmonic amplification/rejection of the PLL, small-signal methods are often utilized. However, typical Linear Time Invariant (LTI) models of PLL are not sufficient to characterize the issue. In this thesis, Linear Time Periodic (LTP) models of PLLs are derived and used to characterize the stability and harmonic properties of PLLs. The study of the transient characteristics of PLLs is out of the scope of this thesis.

Chapter 3. *How does the grid voltage imbalance affect the stability and harmonic generation of the wind-turbine converter?*
At the converter level, several sources might generate LTP behaviour. Literature has often focused on the LTP dynamics that the control dq asymmetries can create, which induce the converter to generate frequency couplings. This thesis develops models to characterize the periodic dynamics of converters due to voltage imbalance and the control dq asymmetries due to the PLL, and shows that even voltage imbalance dynamics alone can drive the converter to instability. The study of the transient response of converters is out of the scope of this thesis.

Chapter 4. *How do the converter frequency couplings affect the harmonic compliance of the wind farm?*
The LTP dynamics generated by the voltage imbalance and other reasons induce the converter to have frequency coupling dynamics. That is to say, for a specific voltage harmonic at the terminals of the converter, the converter generates more than one harmonic (at different frequencies) in the output current. This effect is not taken into consideration nowadays in wind farm harmonic studies. This thesis analyses the impact of this phenomenon.

1.4 Methodology

The methodology followed to answer the research questions in Section 1.3 is shown in Fig. 1.23. An iterative process has been implemented, in which, starting from the concept and analytical modelling, the verification/validation is performed either with computer simulations only or with simulations and experiments combined (depending on the chapter in question). After being verified/validated, the models can be used for further analysis and to obtain the conclusions for the research question.

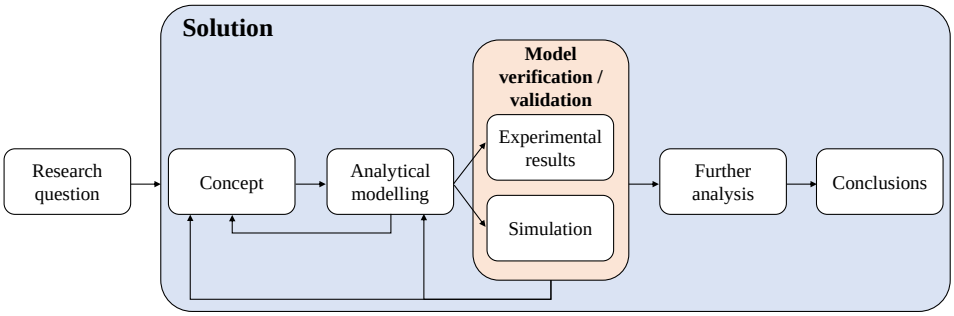

Figure 1.23: Thesis methodology.

1.5 Contributions

The main contributions of this thesis relate to the study of harmonic stability and steady-state harmonics in offshore wind farms, and are summarized below:

- An LTP model of the PLL for the study of the effect of voltage imbalance on the stability and harmonics (Chapter 2)
- The quantification of the reduction of the PLL stability damping with increasing voltage imbalance, and a method to overturn this effect (Chapter 2)
- A model of the whole converter that includes the LTP dynamics induced by the voltage imbalance and by the dq asymmetries in the PLL (Chapter 3)
- The uncovering of the relationship between PLL dynamics and current-reference generation strategies and their influence in the converter passivity (Chapter 3)
- The analysis of the effect of frequency coupling dynamics on the harmonic studies at the wind farm level (Chapter 4)

During the duration of this thesis, several publications have been made, which are listed at the end of this thesis. The relation between the different chapters and the publications is as shown in Fig. 1.24.

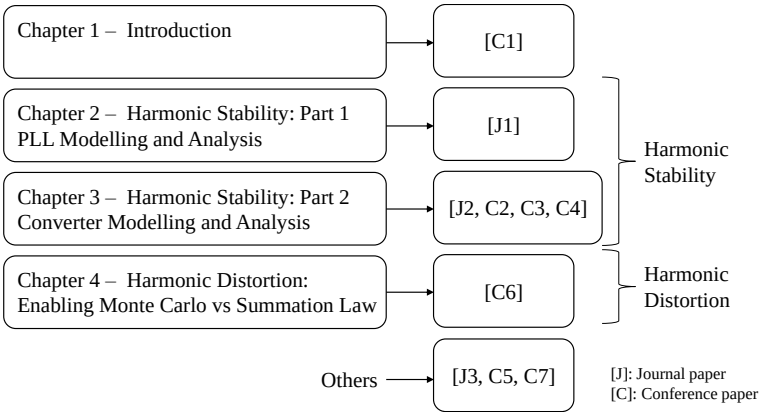

Figure 1.24: Relation between thesis chapters and publications.

1.6 Thesis outline

The thesis outline is shown in Fig. 1.25, starting with the introduction in Chapter 1, that provides input to the rest of the document. Since the final chapter are the conclusions, the rest of the document constitutes the body of the thesis, where the majority of the work is summarized.

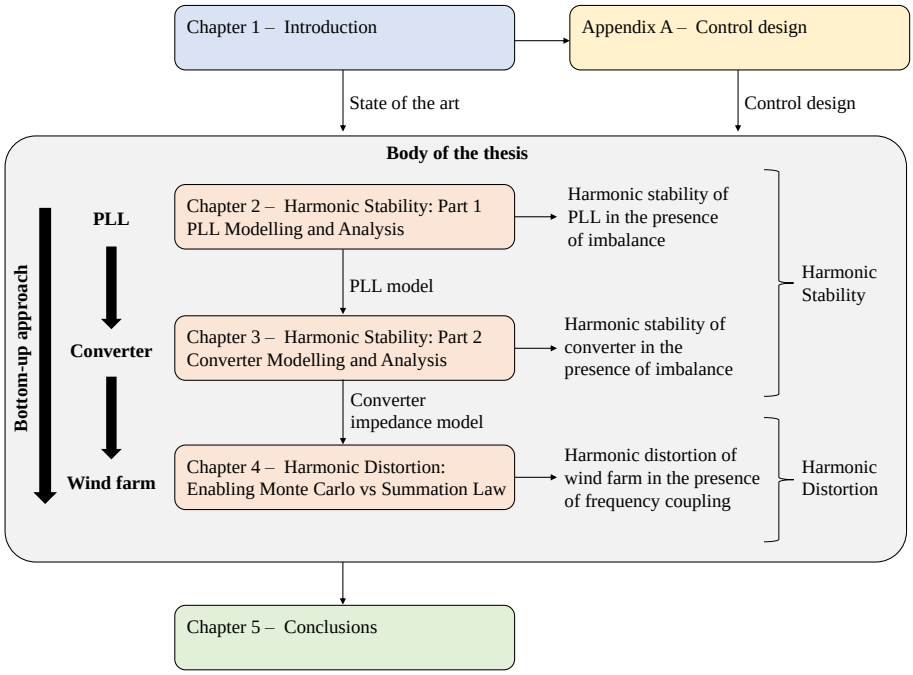

Figure 1.25: Thesis outline.

The body of the thesis is organized in a bottom-up approach from the converter controls' perspective: Chapter 2 analyses one of the most critical control loops in the presence of imbalance, the PLL. Then, the PLL models generated in Chapter 2 are fed into Chapter 3, that analyses the dynamics of the full converter. Finally, the impedance-based model of the converter serves as input to Chapter 4, where the whole wind farm perspective is adopted.

In Chapter 2 and Chapter 3, both harmonic stability and harmonic distortion at the PLL and converter-level, respectively, are addressed. However, since the focus is more on the former, it is considered that Chapter 2 and Chapter 3 form one unity that addresses the topic of harmonic stability. In Chapter 4, the model of the wind turbine converter generated in Chapter 3 is advanced further and then used for the analysis of steady-state harmonics at the wind farm level. Thus, the focus of Chapter 4 is on the topic of harmonic distortion exclusively, and forms a second unity that addresses the second main topic of the thesis: harmonic distortion in offshore wind farms. Finally, Chapter 5 gives conclusions and recommendations for future work.

Chapter 2

Harmonic Stability Part 1 – PLL Modelling and Analysis

Wind energy converters are required to ensure an adequate Low-Voltage Ride Through (LVRT) response. In order to achieve this, it is necessary that the converter keeps synchronism with the grid even in the presence of significant levels of voltage imbalance. This is especially challenging under weak grid conditions, like in offshore wind farms. In order to ensure synchronism in the case of a fault, several advanced Phase-Locked Loop (PLL) methods have been developed in the literature, like for example, the Decoupled Double Synchronous Reference Frame PLL (DDSRF-PLL). However, their modelling and stability analysis is usually performed without taking into account the effect that the imbalance has on the PLL dynamics. In particular, this chapter shows that the typical model used for analysis in literature, a Linear Time Invariant (LTI) model, can be inaccurate in predicting the stability limit of the PLL. In contrast, this chapter develops a Linear Time Periodic (LTP) model that is able to predict exactly the stability limit for all levels of imbalance. Further, this chapter shows that the DDSRF-PLL has frequency coupling dynamics in the presence of voltage imbalance, and that only the LTP model is able to capture them. In certain frequency ranges, these coupling dynamics might be very relevant, which is important for estimating the harmonic rejection capability of the phase tracking system.

This chapter is based on:

- L. Beloqui Larumbe, Z. Qin and P. Bauer, "Guidelines for Stability Analysis of the DDSRF-PLL Using LTI and LTP Modelling in the Presence of Imbalance," in IEEE Open Journal of the Industrial Electronics Society, vol. 3, pp. 339-352, 2022.

2.1 Introduction

Numerous papers have been published about small-signal modelling of Phase-Locked Loops (PLLs). In the particular case of single-phase PLLs or Frequency-Locked Loops (FLLs), the Linear Time Invariant (LTI) models have been recently challenged, as they are not capable of modelling the double-frequency oscillation typical in these structures. Several articles [126–128] have recently shown that the LTI models of different single-phase PLLs or FLLs are not able to predict the stability boundaries for different parameter variations, in comparison to the Linear Time Periodic (LTP) models which perform the task. In order to model more accurately the dynamic effect of certain non-linearities in Second-Order Generalized Integrators (SOGI)-based PLLs/FLLs, [129] proposes also the use of LTP theory. Further, [130] recommends the use of signal-flow graphs for easier understanding of the harmonic propagation in LTP systems, with the application example of single-phase PLLs.

With respect to three-phase PLLs, recent literature shows that LTP modelling might be necessary in the presence of a DC component in the input voltage [131] or in the presence of imbalance[1] [132, 133]. Specifically, [132] focuses on a SRF-PLL and shows that the 100 Hz oscillations that are caused by voltage imbalance in this type of PLL, brings LTP dynamics to the system. When the positive-sequence voltage phase-angle detected by the PLL ($\theta_{\mathrm{PLL}+}$) signal is fed back in the SRF-PLL, if the negative-sequence voltage (V_{n}) is high enough, the 100 Hz component in the PLL dq signals will inter-modulate with any perturbation $f_{\mathrm{p}}^{\mathrm{dq}+}$ that may be present in the $\theta_{\mathrm{PLL}+}$. This means that, if the voltage has a perturbation at $f_{\mathrm{p}}^{\mathrm{dq}+}$ (defined in the dq frame), the frequencies $f_{\mathrm{p}}^{\mathrm{dq}+}$ and $f_{\mathrm{p}}^{\mathrm{dq}+} \pm 2f_1$ will appear at $\theta_{\mathrm{PLL}+}$ (where f_1 is the fundamental frequency). In turn, these frequencies are part of the signal ($\theta_{\mathrm{PLL}+}$) which is fed back, so inter-modulation happens again and, therefore, in the end, $\theta_{\mathrm{PLL}+}$ will have the frequencies $f_{\mathrm{p}}^{\mathrm{dq}+} \pm 2f_1$, $f_{\mathrm{p}}^{\mathrm{dq}+} \pm 4f_1$, etc. The presence of (infinite) frequency couplings is typical in LTP systems [134].

In the case of single-phase or three-phase PLLs in the presence of imbalance, the chosen approach for LTP analysis is usually to develop a Harmonic Transfer Function (HTF) model in the frequency domain (e.g. [126–128, 131, 132]). Alternatively, [133] proposes a state-space in the time domain, with which stability can be assessed with the eigenvalues of the monodromy matrix. This chapter contributes to the topic by developing a HTF LTP model of the Decoupled Double Synchronous Reference Frame PLL (DDSRF-PLL) in the presence of imbalance. In particular, two different DDSRF-PLL implementations are modelled, and it is shown that the LTP approach predicts accurately the stability boundaries of the PLLs. Depending on the specific implementation, it is shown here that the LTP dynamics might appear at $f_{\mathrm{p}}^{\mathrm{dq}} \pm 2f_1$ (and beyond) or at $f_{\mathrm{p}}^{\mathrm{dq}} \pm 4f_1$ (and beyond).

This chapter starts by describing the two DDSRF-PLL implementations (or methods) under study. Among many possibilities for three-phase PLLs, the reason for choosing the DDSRF-PLL in this thesis is that it is a commonly implemented technique that has been shown to present good performance under imbalance conditions [135]. Subsequently, the LTI and LTP models are derived for both DDSRF-PLL methods in Section 2.3 – 2.6, which are verified in Section 2.8. An explanation of the LTI and LTP model differences is shown in Section 2.9. Later, Section 2.10 compares the LTI and LTP models for stability studies,

[1] It is worth to observe that, from a mathematical perspective, a single-phase voltage is equivalent to a three-phase voltage with considerable imbalance.

concluding that the LTP model is accurate in all imbalance levels, whereas the LTI model is not. With respect to harmonic studies, the suitability of both models is tested in Section 2.11, concluding that the LTP model is also better than the LTI model. Therefore, using the LTP model derived, this chapter finishes by analysing the impact of the grid voltage imbalance in the stability margins and harmonic rejection performance of the DDSRF-PLL.

2.2 Description of DDSRF-PLL methods

In this thesis, the PLL follows the phase-angle of the positive-sequence voltage ($\theta_{1+} = \omega_1 t + \phi_{vp}$) and of the negative-sequence voltage ($\theta_{1-} = -\omega_1 t - \phi_{vn}$)[2], defined in (2.1). The outputs of the PLL are θ_{PLL+} and θ_{PLL-}, which might not be exactly accurate, having some error as: $\theta_{PLL+} = \theta_{1+} + \Delta\theta_{1+}$ and $\theta_{PLL-} = \theta_{1-} + \Delta\theta_{1-}$ [136].

$$\begin{aligned} v_a(t) &= V_p \cos(\omega_1 t + \phi_{vp}) + V_n \cos(\omega_1 t + \phi_{vn}) \\ v_b(t) &= V_p \cos(\omega_1 t + \phi_{vp} - \frac{2\pi}{3}) + V_n \cos(\omega_1 t + \phi_{vn} + \frac{2\pi}{3}) \\ v_c(t) &= V_p \cos(\omega_1 t + \phi_{vp} - \frac{4\pi}{3}) + V_n \cos(\omega_1 t + \phi_{vn} + \frac{4\pi}{3}) \end{aligned} \tag{2.1}$$

2.2.1 Method 1: Direct tracking of θ_{1-}

Fig. 2.1 shows the schematic of method 1 (M1). This method uses two separate SRF-PLLs, one for tracking the positive sequence and one for the negative sequence. The logic behind this design is to try to make the PLL symmetrical. This method is called direct tracking since it uses a SRF-PLL to directly track the negative sequence. The phase angle obtained by this SRF-PLL, θ_{PLL-}, is used within the decoupling network of the DDSRF-PLL, which means that, in steady state, the negative-sequence frame in the decoupling network rotates perfectly with $\theta_{1-} = -\omega_1 t - \phi_{vn}$. Thus, $\overrightarrow{V^{fil}_{dq-}}$ has, in steady state, V_n in the d channel and 0 in the q channel.

Usually, the nominal voltage (V_{nom}) is used for designing the parameters for the positive-sequence SRF-PLL (details in Appendix A). The input to the negative-sequence SRF-PLL, however, varies a lot, since V_n ranges from being very low in normal operating conditions to being very high during certain faults. For minimizing this effect, normalization can be performed as:

$$V^{norm}_{q-} = \frac{V^{dec}_{q-}}{\sqrt{(V^{dec}_{d-})^2 + (V^{dec}_{q-})^2}}. \tag{2.2}$$

Thus, if V^{norm}_{q-} is multiplied by V_{nom}, the same PLL constants can be used for the positive- and negative-sequence SRF-PLL.

[2]Note that, in a three-phase system, it is mathematically equivalent to analyse a three-phase signal in the positive sequence with a negative frequency ($f < 0$) to analysing a three-phase signal with positive frequency ($f > 0$) in the negative sequence. Also, if the voltage is expressed as a space vector in the $\alpha\beta$-frame, the negative-sequence vector rotates at $-\omega_1 t - \phi_{vn}$.

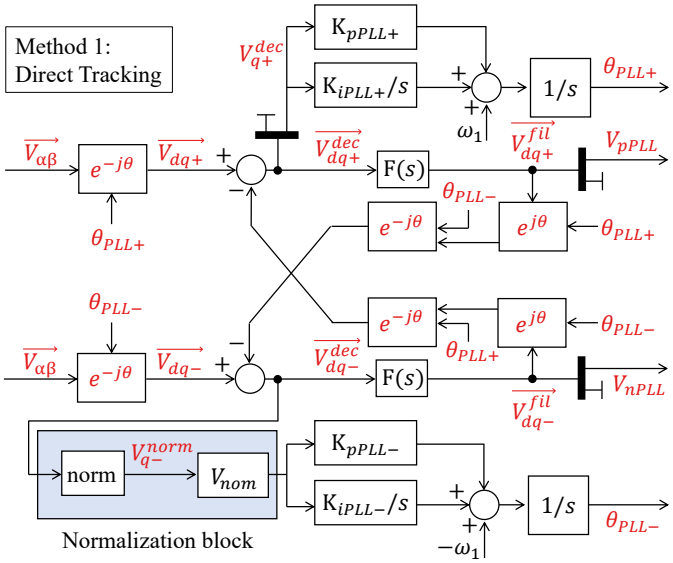

Figure 2.1: Method 1 (M1) for DDSRF-PLL implementation: Direct tracking of negative-sequence voltage phase-angle.

2.2.2 Method 2: Indirect tracking of θ_{1-}

The schematic of method 2 (M2) is shown in Fig. 2.2. This method uses only a positive-sequence SRF-PLL, and uses the phase-angle it creates, $\theta_{\mathrm{PLL}+}$ in all the decoupling network transformations. This means that, in steady state, the negative-sequence frame in the decoupling network does not rotate with $\theta_{1-} = -\omega_1 t - \phi_{\mathrm{vn}}$, but rather with $-\theta_{1+} = -\omega_1 t - \phi_{\mathrm{vp}}$. When representing the negative-sequence voltage in such a frame, the space vector has the form $V_{\mathrm{n}} e^{j(\phi_{\mathrm{vp}} - \phi_{\mathrm{vn}})}$. Note that, unless $\phi_{\mathrm{vp}} = \phi_{\mathrm{vn}}$, the signal that serves as input to the $atan2$ function does not have a q channel equal to 0. Therefore, the output of the $atan2$ function in Fig. 2.2 is, in steady state, equal to $\phi_{\mathrm{vp}} - \phi_{\mathrm{vn}}$. The $\theta_{\mathrm{PLL}-}$, then, can be obtained by subtracting $\theta_{\mathrm{PLL}+}$ from the output of the $atan2$ function.

This method is the traditional DDSRF-PLL shown in [137] but with additional blocks to calculate $\theta_{\mathrm{PLL}-}$ and V_{n}. This method is called indirect tracking since it only tracks directly the positive-sequence phase angle, while the negative-sequence phase angle is derived from the signals in the network.

2.3 LTP model of method 1

In this thesis, the dq frame rotating with θ_{1+} is called ideal positive-sequence dq frame whereas the non-ideal one rotates at $\theta_{\mathrm{PLL}+}$. Similarly occurs for the negative sequence. In order to derive the model, the first step is to analyse the rotational transformations shown in Fig. 2.1. This is explained in detail in [J1]. As an example, if the phase-angle error is considered sufficiently small, the impact of the phase-angle error in one of the transformations in Fig. 2.1 is given by:

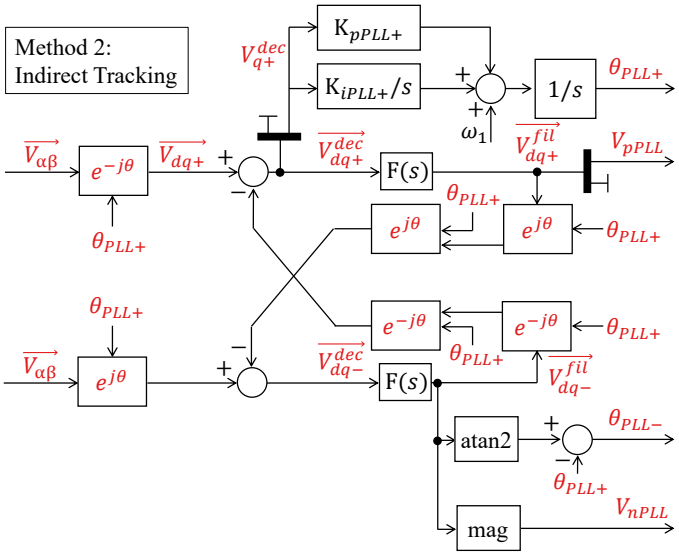

Figure 2.2: Method 2 (M2) for DDSRF-PLL implementation: Indirect tracking of negative-sequence voltage phase-angle.

$$\begin{aligned}\overrightarrow{V_{\text{nonidealdq+}}} &= \overrightarrow{V_{\text{idealdq+}}}e^{-j\Delta\theta_{1+}} \approx \overrightarrow{V_{\text{idealdq+}}}(1-j\Delta\theta_{1+}) \\ &= \overrightarrow{V_{\text{idealdq+}}} - jV_{\text{p}}\Delta\theta_{1+} - jV_{\text{n}}e^{-j(2\omega_1 t+\phi_{\text{vp}}+\phi_{\text{vn}})}\Delta\theta_{1+}.\end{aligned} \tag{2.3}$$

Taking into account all transformations, it can be found:

$$\overrightarrow{V_{\text{dq+}}^{\text{dec}}} = \overrightarrow{G_{\text{dq+}}(s)}(\overrightarrow{V_{\text{idealdq+}}} - jV_{\text{p}}\Delta\theta_{1+} - jV_{\text{n}}e^{-j(\phi_{\text{vp}}+\phi_{\text{vn}})}\Delta\theta_{1-}e^{-j2\omega_1 t}) \tag{2.4}$$

$$\overrightarrow{V_{\text{dq-}}^{\text{dec}}} = \overrightarrow{G_{\text{dq+}}^{*}(s)}(\overrightarrow{V_{\text{idealdq-}}} - jV_{\text{n}}\Delta\theta_{1-} - jV_{\text{p}}e^{+j(\phi_{\text{vp}}+\phi_{\text{vn}})}\Delta\theta_{1+}e^{+j2\omega_1 t}) \tag{2.5}$$

where

$$\overrightarrow{G_{\text{dq+}}(s)} = \frac{1-F(s+j2\omega_1)}{1-F(s)F(s+j2\omega_1)}. \tag{2.6}$$

$\overrightarrow{G_{\text{dq+}}(s)}$ only depends on one parameter, ω_{f}, which is usually set as $\omega_{\text{f}} = K\omega_1$. The effect of K is analysed later in this chapter. $\overrightarrow{G_{\text{dq+}}(s)}$ has a real and an imaginary part as $\overrightarrow{G_{\text{dq+}}(s)} = G_{\text{re}}(s) + jG_{\text{im}}(s)$ defined as:

$$G_{\text{re}}(s) = \frac{(s+\omega_{\text{f}})(s^3 + 2\omega_{\text{f}}s^2 + 4{\omega_1}^2 s + 4\omega_{\text{f}}{\omega_1}^2)}{s^4 + 4\omega_{\text{f}}s^3 + 4({\omega_1}^2 + {\omega_{\text{f}}}^2)s^2 + 8{\omega_1}^2\omega_{\text{f}}s + 4{\omega_1}^2{\omega_{\text{f}}}^2} \tag{2.7}$$

$$G_{\text{im}}(s) = \frac{2\omega_1\omega_{\text{f}}s^2 + 2\omega_1{\omega_{\text{f}}}^2 s}{s^4 + 4\omega_{\text{f}}s^3 + 4({\omega_1}^2 + {\omega_{\text{f}}}^2)s^2 + 8{\omega_1}^2\omega_{\text{f}}s + 4{\omega_1}^2{\omega_{\text{f}}}^2}. \tag{2.8}$$

Additionally, if it is defined $H_{\mathrm{PLL+}}(s) = [K_{\mathrm{pPLL+}} + \frac{K_{\mathrm{iPLL+}}}{s}]\frac{1}{s}$ (and similarly for the negative sequence) from the schematic in Fig. 2.1, it is straightforward to find[3]:

$$\Delta\theta_{1+} = V_{\mathrm{q+}}^{\mathrm{dec}} H_{\mathrm{PLL+}}(s) = \frac{1}{2j}(\overrightarrow{V_{\mathrm{dq+}}^{\mathrm{dec}}} - \overrightarrow{V_{\mathrm{dq+}}^{\mathrm{dec*}}})H_{\mathrm{PLL+}}(s) \tag{2.9}$$

$$\Delta\theta_{1-} = V_{\mathrm{q-}}^{\mathrm{dec}} H_{\mathrm{PLL-}}(s) = \frac{1}{2j}(\overrightarrow{V_{\mathrm{dq-}}^{\mathrm{dec}}} - \overrightarrow{V_{\mathrm{dq-}}^{\mathrm{dec*}}})H_{\mathrm{PLL-}}(s). \tag{2.10}$$

Combining (2.9) and (2.10) with (2.4) and (2.5) is not simple since both (2.4) and (2.5) depend on both $\Delta\theta_{1+}$ and $\Delta\theta_{1-}$. The procedure is not included here for brevity, but it is explained in [J1].

2.3.1 Positive-sequence phase-angle model

When combining these expressions, it can be found for the positive sequence:

$$\begin{aligned}\Delta\theta_{1+} = \overrightarrow{T_5}[&\overrightarrow{V_{\mathrm{idealdq+}}}\overrightarrow{T_1} - \overrightarrow{V_{\mathrm{idealdq+}}^{*}}\overrightarrow{T_1^{*}} + \overrightarrow{V_{\mathrm{idealdq+}}^{*}}e^{-j4\omega_1 t}\overrightarrow{T_3} \\ &-\overrightarrow{V_{\mathrm{idealdq+}}}e^{+j4\omega_1 t}\overrightarrow{T_3^{*}} + \Delta\theta_{1+}e^{-j4\omega_1 t}\overrightarrow{T_4} - \Delta\theta_{1+}e^{+j4\omega_1 t}\overrightarrow{T_4^{*}}]\end{aligned} \tag{2.11}$$

where $\overrightarrow{T_1}$–$\overrightarrow{T_5}$ are complex transfer functions defined in [J1]. The expression (2.11) clearly reveals the LTP dynamics of the PLL. If the voltage (in the positive dq frame) has a component at a frequency ω, then the $\Delta\theta_{1+}$ will have the components[4] $\pm\omega$, which in turn will create in a feedback loop through $\overrightarrow{T_4}$ and $\overrightarrow{T_4^{*}}$ the frequencies $\pm\omega \pm 4\omega_1$. Note that this is a theoretically infinite procedure, in which $\pm\omega \pm 4\omega_1$ will create also a new frequencies at $\pm\omega \pm 8\omega_1$; etc. In Fig. 2.3 the main frequency paths (i.e., at the frequencies $\pm\omega$, $\pm\omega \pm 4\omega_1$) are shown.

If other frequency components are neglected (this is further discussed in Section 2.10), then the following equations are obtained:

$$\begin{aligned}\Delta\theta_{1+}|_{\omega+4\omega_1} &= \big(-\overrightarrow{V_{\mathrm{idealdq+}}}e^{j4\omega_1 t}\overrightarrow{T_3}^{*} - \Delta\theta_{1+}|_{\omega}e^{j4\omega_1 t}\overrightarrow{T_4^{*}}\big)\overrightarrow{T_5} \\ \Delta\theta_{1+}|_{\omega-4\omega_1} &= \Delta\theta_{1+}|_{\omega}e^{-j4\omega_1 t}\overrightarrow{T_4}\overrightarrow{T_5} \\ \Delta\theta_{1+}|_{\omega} &= \big(\overrightarrow{V_{\mathrm{idealdq+}}}\overrightarrow{T_1} + \Delta\theta_{1+}|_{\omega+4\omega_1}e^{-j4\omega_1 t}\overrightarrow{T_4} - \Delta\theta_{1+}|_{\omega-4\omega_1}e^{j4\omega_1 t}\overrightarrow{T_4^{*}}\big)\overrightarrow{T_5}\end{aligned} \tag{2.12}$$

Similarly, for the conjugate frequencies, another set of three equations that are related to each other can be obtained:

$$\begin{aligned}\Delta\theta_{1+}|_{-\omega-4\omega_1} &= \big(\overrightarrow{V_{\mathrm{idealdq+}}^{*}}e^{-j4\omega_1 t}\overrightarrow{T_3} + \Delta\theta_{1+}|_{-\omega}e^{-j4\omega_1 t}\overrightarrow{T_4}\big)\overrightarrow{T_5} \\ \Delta\theta_{1+}|_{-\omega+4\omega_1} &= -\Delta\theta_{1+}|_{-\omega}e^{+j4\omega_1 t}\overrightarrow{T_4^{*}}\overrightarrow{T_5} \\ \Delta\theta_{1+}|_{-\omega} &= \big(-\overrightarrow{V_{\mathrm{idealdq+}}^{*}}\overrightarrow{T_1^{*}} + \Delta\theta_{1+}|_{-\omega+4\omega_1}e^{-j4\omega_1 t}\overrightarrow{T_4} - \Delta\theta_{1+}|_{-\omega-4\omega_1}e^{j4\omega_1 t}\overrightarrow{T_4^{*}}\big)\overrightarrow{T_5}\end{aligned} \tag{2.13}$$

[3] The normalization block is ignored for now but it is included later.

[4] As an example, a component $A\cos(\omega t)$ in $\Delta\theta_{1+}$ can be represented in space vector form as $\frac{A}{2}e^{j\omega t} + \frac{A}{2}e^{-j\omega t}$.

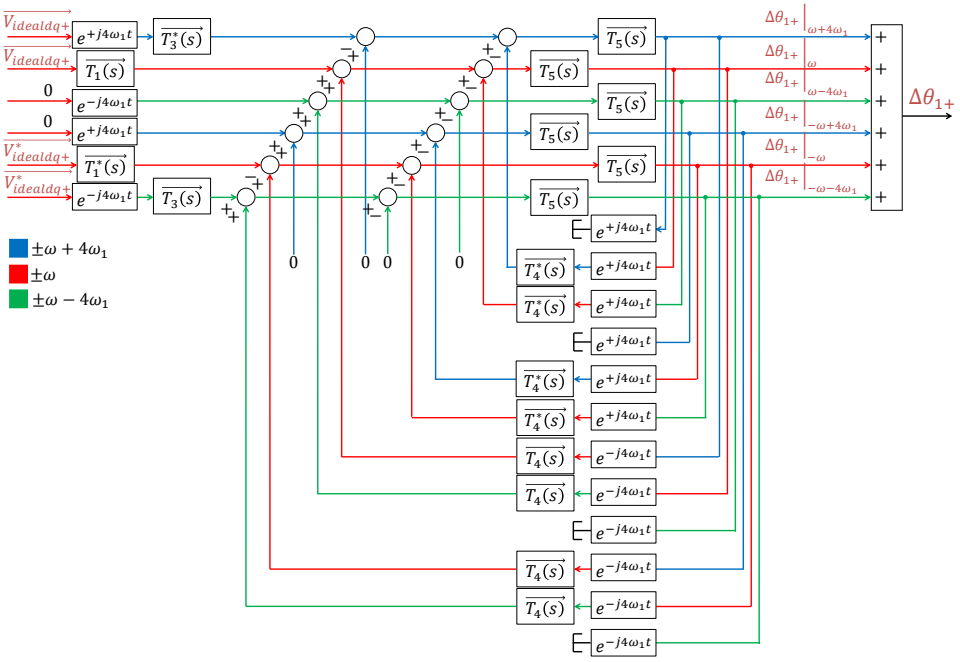

Figure 2.3: Schematic of equation (2.11), which clearly reveals the LTP dynamics of the PLL.

Solving for the direct path (at frequency ω) leads to:

$$\Delta\theta_{1+}|_{\omega} = \overrightarrow{TF_{\text{PLL1+}}(s)V_{\text{idealdq+}}} \tag{2.14}$$

with

$$\overrightarrow{TF_{\text{PLL1+}}(s)} = \frac{\overrightarrow{T_1T_5} - \overrightarrow{T_3^*(s+j4\omega_1)T_5(s+j4\omega_1)T_4T_5}}{1 + \overrightarrow{T_4^*(s+j4\omega_1)T_5(s+j4\omega_1)T_4T_5} + \overrightarrow{T_4(s-j4\omega_1)T_5(s-j4\omega_1)T_4^*T_5}}. \tag{2.15}$$

Solving the equations in (2.13) for $\Delta\theta_{1+}|_{-\omega}$ leads to:

$$\Delta\theta_{1+}|_{-\omega} = \overrightarrow{TF_{\text{PLL2+}}(s)V^*_{\text{idealdq+}}} \tag{2.16}$$

with

$$\overrightarrow{TF_{\text{PLL2+}}(s)} = \frac{-\overrightarrow{T_1^*T_5} - \overrightarrow{T_3(s-j4\omega_1)T_5(s-j4\omega_1)T_4^*T_5}}{1 + \overrightarrow{T_4^*(s+j4\omega_1)T_5(s+j4\omega_1)T_4T_5} + \overrightarrow{T_4(s-j4\omega_1)T_5(s-j4\omega_1)T_4^*T_5}}. \tag{2.17}$$

The other frequencies in $\Delta\theta_{1+}$ can be solved now:

$$\begin{aligned}
\Delta\theta_{1+}|_{\omega+4\omega_1} &= \underbrace{\left(-\overrightarrow{T_3^*} - \overrightarrow{T_4^* TF_{\text{PLL1+}}(s-j4\omega_1)}\right)\overrightarrow{T_5}}_{\overrightarrow{TF_{\text{PLL3+}}(s)}} \overrightarrow{V_{\text{idealdq+}}} e^{j4\omega_1 t} \\
\Delta\theta_{1+}|_{-\omega-4\omega_1} &= \underbrace{\left(\overrightarrow{T_3} + \overrightarrow{T_4 TF_{\text{PLL2+}}(s+j4\omega_1)}\right)\overrightarrow{T_5}}_{\overrightarrow{TF_{\text{PLL4+}}(s)}} \overrightarrow{V^*_{\text{idealdq+}}} e^{-j4\omega_1 t} \\
\Delta\theta_{1+}|_{\omega-4\omega_1} &= \underbrace{\overrightarrow{T_4 T_5 TF_{\text{PLL1+}}(s+j4\omega_1)}}_{\overrightarrow{TF_{\text{PLL5+}}(s)}} \overrightarrow{V_{\text{idealdq+}}} e^{-j4\omega_1 t} \\
\Delta\theta_{1+}|_{-\omega+4\omega_1} &= \underbrace{-\overrightarrow{T_4^* T_5 TF_{\text{PLL2+}}(s-j4\omega_1)}}_{\overrightarrow{TF_{\text{PLL6+}}(s)}} \overrightarrow{V^*_{\text{idealdq+}}} e^{j4\omega_1 t}
\end{aligned} \tag{2.18}$$

Thus, the final model for the positive-sequence phase-angle is shown in (2.19).

$$\begin{aligned}
\Delta\theta_{1+} \approx\ & \overrightarrow{V_{\text{idealdq+}}}\overrightarrow{TF_{\text{PLL1+}}} + \overrightarrow{V^*_{\text{idealdq+}}}\overrightarrow{TF_{\text{PLL2+}}} \\
&+\overrightarrow{V_{\text{idealdq+}}} e^{j4\omega_1 t}\overrightarrow{TF_{\text{PLL3+}}} + (\overrightarrow{V_{\text{idealdq+}}} e^{j4\omega_1 t})^*\overrightarrow{TF_{\text{PLL4+}}} \\
&+\overrightarrow{V_{\text{idealdq+}}} e^{-j4\omega_1 t}\overrightarrow{TF_{\text{PLL5+}}} + (\overrightarrow{V_{\text{idealdq+}}} e^{-j4\omega_1 t})^*\overrightarrow{TF_{\text{PLL6+}}}
\end{aligned} \tag{2.19}$$

(2.19) uses an approximate sign, since in reality there are an infinite number of couplings in the PLL. Here, only the first round of couplings is shown. The question as to how many couplings must be included in the model is answered in Section 2.10.6. Also, it can be shown that $\overrightarrow{TF_{\text{PLL2+}}(s)} = \overrightarrow{TF^*_{\text{PLL1+}}(s)}$, $\overrightarrow{TF_{\text{PLL4+}}(s)} = \overrightarrow{TF^*_{\text{PLL3+}}(s)}$ and $\overrightarrow{TF_{\text{PLL6+}}(s)} = \overrightarrow{TF^*_{\text{PLL5+}}(s)}$.

2.3.2 Negative-sequence phase-angle model

The final model for the negative-sequence phase-angle can be similarly derived and it is shown in (2.20).

$$\begin{aligned}
\Delta\theta_{1-} \approx\ & \overrightarrow{V_{\text{idealdq–}}}\overrightarrow{TF_{\text{PLL1–}}} + \overrightarrow{V^*_{\text{idealdq–}}}\overrightarrow{TF_{\text{PLL2–}}} \\
&+\overrightarrow{V_{\text{idealdq–}}} e^{-j4\omega_1 t}\overrightarrow{TF_{\text{PLL3–}}} + (\overrightarrow{V_{\text{idealdq–}}} e^{-j4\omega_1 t})^*\overrightarrow{TF_{\text{PLL4–}}} \\
&+\overrightarrow{V_{\text{idealdq–}}} e^{j4\omega_1 t}\overrightarrow{TF_{\text{PLL5–}}} + (\overrightarrow{V_{\text{idealdq–}}} e^{j4\omega_1 t})^*\overrightarrow{TF_{\text{PLL6–}}}
\end{aligned} \tag{2.20}$$

It can be shown that $\overrightarrow{TF_{\text{PLL2–}}(s)} = \overrightarrow{TF^*_{\text{PLL1–}}(s)}$, that $\overrightarrow{TF_{\text{PLL4–}}(s)} = \overrightarrow{TF^*_{\text{PLL3–}}(s)}$ and that $\overrightarrow{TF_{\text{PLL6–}}(s)} = \overrightarrow{TF^*_{\text{PLL5–}}(s)}$.

2.3.3 Including normalization

For including the normalization block shown in Fig. 2.1, it is necessary to linearise (2.2) through a Taylor series expansion (around the steady-state point $(V_{\text{n}}, 0)$). The result is:

$$V^{\text{norm}}_{\text{q–}} \approx \frac{V^{\text{dec}}_{\text{q–}}}{V_{\text{n}}}. \tag{2.21}$$

Thus, for including the normalization block, the only step is to substitute $H_{\text{PLL–}}(s)$ by $\frac{V_{\text{nom}} H_{\text{PLL–}}(s)}{V_{\text{n}}}$ in all equations.

2.4 LTI model of method 1

For developing the LTI model, the time-varying coefficients are ignored. In method 1, this means that (2.4) and (2.5) become:

$$\overrightarrow{V_{\mathrm{dq+}}^{\mathrm{dec}}} = \overrightarrow{G_{\mathrm{dq+}}(s)}(\overrightarrow{V_{\mathrm{idealdq+}}} - jV_{\mathrm{p}}\Delta\theta_{1+}) \tag{2.22}$$

$$\overrightarrow{V_{\mathrm{dq-}}^{\mathrm{dec}}} = \overrightarrow{G_{\mathrm{dq+}}^{*}(s)}(\overrightarrow{V_{\mathrm{idealdq-}}} - jV_{\mathrm{n}}\Delta\theta_{1-}) \tag{2.23}$$

Combining these expressions with (2.9) and (2.10) is straightforward, and leads to the model in (2.24) and (2.25).

$$\begin{aligned}\Delta\theta_{1+} &= \overrightarrow{V_{\mathrm{idealdq+}}}\overrightarrow{TF_{\mathrm{PLL1+LTI}}} + \overrightarrow{V_{\mathrm{idealdq+}}^{*}}\overrightarrow{TF_{\mathrm{PLL2+LTI}}}\\ \Delta\theta_{1-} &= \overrightarrow{V_{\mathrm{idealdq-}}}\overrightarrow{TF_{\mathrm{PLL1-LTI}}} + \overrightarrow{V_{\mathrm{idealdq-}}^{*}}\overrightarrow{TF_{\mathrm{PLL2-LTI}}}\end{aligned} \tag{2.24}$$

$$\begin{aligned}\overrightarrow{TF_{\mathrm{PLL1+LTI}}} &= \frac{H_{\mathrm{PLL+}}(s)\overrightarrow{G_{\mathrm{dq+}}(s)}}{2j(1 + V_{\mathrm{p}}H_{\mathrm{PLL+}}(s)G_{\mathrm{re}}(s))}\\ \overrightarrow{TF_{\mathrm{PLL1-LTI}}} &= \frac{H_{\mathrm{PLL-}}(s)\overrightarrow{G_{\mathrm{dq+}}^{*}(s)}}{2j(1 + V_{\mathrm{n}}H_{\mathrm{PLL-}}(s)G_{\mathrm{re}}(s))}\end{aligned} \tag{2.25}$$

In this case, $\overrightarrow{TF_{\mathrm{PLL2+LTI}}} = \overrightarrow{TF_{\mathrm{PLL1+LTI}}^{*}}$, $\overrightarrow{TF_{\mathrm{PLL2-LTI}}} = \overrightarrow{TF_{\mathrm{PLL1-LTI}}^{*}}$. For including the normalization block, the same steps as explained for the LTP model (Section 2.3.3) should be taken.

2.5 LTP model of method 2

In a similar process as it is done with the method 1, the following equations can be obtained for the method 2:

$$\overrightarrow{V_{\mathrm{dq+}}^{\mathrm{dec}}} = \overrightarrow{G_{\mathrm{dq+}}(s)}(\overrightarrow{V_{\mathrm{idealdq+}}} - jV_{\mathrm{p}}\Delta\theta_{1+} + jV_{\mathrm{n}}e^{-j(\phi_{\mathrm{vp}}+\phi_{\mathrm{vn}})}\Delta\theta_{1+}e^{-j2\omega_1 t}) \tag{2.26}$$

$$\overrightarrow{V_{\mathrm{dq-}}^{\mathrm{dec}}} = \overrightarrow{G_{\mathrm{dq+}}^{*}(s)}e^{+j(\phi_{\mathrm{vp}}-\phi_{\mathrm{vn}})}(\overrightarrow{V_{\mathrm{idealdq-}}} + jV_{\mathrm{n}}\Delta\theta_{1+} - jV_{\mathrm{p}}e^{+j(\phi_{\mathrm{vp}}+\phi_{\mathrm{vn}})}\Delta\theta_{1+}e^{+j2\omega_1 t}) \tag{2.27}$$

In this case, $\Delta\theta_{1-}$ does not appear in (2.26) nor in (2.27), since the decoupling network only uses $\theta_{\mathrm{PLL+}}$. In (2.27) there is a new term, $e^{+j(\phi_{\mathrm{vp}}-\phi_{\mathrm{vn}})}$, that does not appear in the equations of M1. This term is here because, in M2, the $\overrightarrow{V_{\mathrm{dq-}}^{\mathrm{dec}}}$ is a signal that ideally rotates with $-\theta_{1+} = -\omega_1 t - \phi_{\mathrm{vp}}$, instead of rotating with $\theta_{1-} = -\omega_1 t - \phi_{\mathrm{vn}}$ as in method 1.

2.5.1 Positive-sequence phase-angle model

The expression (2.26) can be used in (2.9). Operating leads to:

$$\begin{aligned}\Delta\theta_{1+} = \overrightarrow{T_6}[\overrightarrow{V_{\text{idealdq+}}}\overrightarrow{G_{\text{dq+}}(s)} - \overrightarrow{V^*_{\text{idealdq+}}}\overrightarrow{G^*_{\text{dq+}}(s)} \\ +\Delta\theta_{1+}e^{+j2\omega_1 t}\overrightarrow{T_7} - \Delta\theta_{1+}e^{-j2\omega_1 t}\overrightarrow{T_7^*}].\end{aligned} \tag{2.28}$$

where $\overrightarrow{T_6}$ and $\overrightarrow{T_7}$ are defined in [J1]. Similarly as with method 1, the expression (2.28) reveals LTP dynamics, although this time they are dependent on $\pm 2\omega_1$ instead of $\pm 4\omega_1$. Performing similar operations and schematics as with method 1, the following LTP model can be obtained:

$$\begin{aligned}\Delta\theta_{1+} \approx \overrightarrow{V_{\text{idealdq+}}}\overrightarrow{TF_{\text{PLL1+}}} + \overrightarrow{V^*_{\text{idealdq+}}}\overrightarrow{TF_{\text{PLL2+}}} \\ +\overrightarrow{V_{\text{idealdq+}}}e^{j2\omega_1 t}\overrightarrow{TF_{\text{PLL3+}}} + (\overrightarrow{V_{\text{idealdq+}}}e^{j2\omega_1 t})^*\overrightarrow{TF_{\text{PLL4+}}} \\ +\overrightarrow{V_{\text{idealdq+}}}e^{-j2\omega_1 t}\overrightarrow{TF_{\text{PLL5+}}} + (\overrightarrow{V_{\text{idealdq+}}}e^{-j2\omega_1 t})^*\overrightarrow{TF_{\text{PLL6+}}}\end{aligned} \tag{2.29}$$

2.5.2 Negative-sequence phase-angle model

Here, it is necessary to linearise $atan(\frac{V^{\text{fil}}_{\text{q–}}}{V^{\text{fil}}_{\text{d–}}})$ around the steady-state operating point defined by $(\Im\{V_{\text{n}}e^{+j(\phi_{\text{vp}}-\phi_{\text{vn}})}\}, \Re\{V_{\text{n}}e^{+j(\phi_{\text{vp}}-\phi_{\text{vn}})}\})$. This results in:

$$\begin{aligned}atan(\frac{V^{\text{fil}}_{\text{q–}}}{V^{\text{fil}}_{\text{d–}}}) \approx \phi_{\text{vp}} - \phi_{\text{vn}} + \frac{(e^{+j(\phi_{\text{vp}}-\phi_{\text{vn}})} + e^{-j(\phi_{\text{vp}}-\phi_{\text{vn}})})}{2V_{\text{n}}}V^{\text{fil}}_{\text{q–}} \\ -\frac{(e^{+j(\phi_{\text{vp}}-\phi_{\text{vn}})} - e^{-j(\phi_{\text{vp}}-\phi_{\text{vn}})})}{j2V_{\text{n}}}V^{\text{fil}}_{\text{d–}}.\end{aligned} \tag{2.30}$$

Since $\theta_{\text{PLL–}} = -\theta_{\text{PLL+}} + atan(\frac{V^{\text{fil}}_{\text{q–}}}{V^{\text{fil}}_{\text{d–}}})$, and also $\theta_{\text{PLL+}} = \omega_1 t + \phi_{\text{vp}} + \Delta\theta_{1+}$ and $\theta_{\text{PLL–}} = -\omega_1 t - \phi_{\text{vn}} + \Delta\theta_{1–}$, then:

$$\Delta\theta_{1–} = -\Delta\theta_{1+} + \frac{(e^{+j(\phi_{\text{vp}}-\phi_{\text{vn}})} + e^{-j(\phi_{\text{vp}}-\phi_{\text{vn}})})}{2V_{\text{n}}}V^{\text{fil}}_{\text{q–}} - \frac{(e^{+j(\phi_{\text{vp}}-\phi_{\text{vn}})} - e^{-j(\phi_{\text{vp}}-\phi_{\text{vn}})})}{j2V_{\text{n}}}V^{\text{fil}}_{\text{d–}}. \tag{2.31}$$

Knowing that $\overrightarrow{V^{\text{fil}}_{\text{dq–}}} = F(s)\overrightarrow{V^{\text{dec}}_{\text{dq–}}}$, the terms $V^{\text{fil}}_{\text{d–}}$ and $V^{\text{fil}}_{\text{q–}}$ can be derived from (2.27), while $\Delta\theta_{1+}$ is shown in (2.29). The final LTP model for $\Delta\theta_{1–}$ for method 2 is:

$$\begin{aligned}\Delta\theta_{1–} \approx \overrightarrow{V_{\text{idealdq–}}}\overrightarrow{TF_{\text{PLL1–}}} + \overrightarrow{V^*_{\text{idealdq–}}}\overrightarrow{TF_{\text{PLL2–}}} \\ +\overrightarrow{V_{\text{idealdq–}}}e^{-j2\omega_1 t}\overrightarrow{TF_{\text{PLL3–}}} + (\overrightarrow{V_{\text{idealdq–}}}e^{-j2\omega_1 t})^*\overrightarrow{TF_{\text{PLL4–}}} \\ +\overrightarrow{V_{\text{idealdq–}}}e^{+j2\omega_1 t}\overrightarrow{TF_{\text{PLL5–}}} + (\overrightarrow{V_{\text{idealdq–}}}e^{+j2\omega_1 t})^*\overrightarrow{TF_{\text{PLL6–}}}\end{aligned} \tag{2.32}$$

2.6 LTI model of method 2

In here, the time-varying coefficients are ignored. Thus, (2.26) and (2.27) become:

$$\overrightarrow{V_{\mathrm{dq+}}^{\mathrm{dec}}} = \overrightarrow{G_{\mathrm{dq+}}(s)}(\overrightarrow{V_{\mathrm{idealdq+}}} - jV_{\mathrm{p}}\Delta\theta_{1+}) \tag{2.33}$$

$$\overrightarrow{V_{\mathrm{dq-}}^{\mathrm{dec}}} = \overrightarrow{G_{\mathrm{dq+}}^{*}(s)}e^{+j(\phi_{\mathrm{vp}}-\phi_{\mathrm{vn}})}(\overrightarrow{V_{\mathrm{idealdq-}}} + jV_{\mathrm{n}}\Delta\theta_{1+}) \tag{2.34}$$

Since (2.33) is the same as (2.22), the LTI model of $\Delta\theta_{1+}$ is the same in method 2 as in method 1. For $\Delta\theta_{1-}$, knowing that $\overrightarrow{V_{\mathrm{dq-}}^{\mathrm{fil}}} = F(s)\overrightarrow{V_{\mathrm{dq-}}^{\mathrm{dec}}}$, it is necessary to use (2.34) in (2.31) and, ignoring oscillating terms, the LTI model results in:

$$\Delta\theta_{1-} = \overrightarrow{V_{\mathrm{idealdq-}}}\overrightarrow{TF_{\mathrm{PLL1-LTI}}} + \overrightarrow{V_{\mathrm{idealdq-}}^{*}}\overrightarrow{TF_{\mathrm{PLL2-LTI}}} \tag{2.35}$$

where $\overrightarrow{TF_{\mathrm{PLL2-LTI}}} = \overrightarrow{TF_{\mathrm{PLL1-LTI}}^{*}}$ and

$$\overrightarrow{TF_{\mathrm{PLL1-LTI}}} = \frac{1}{2jV_{\mathrm{n}}}(F(s)\overrightarrow{G_{\mathrm{dq+}}^{*}(s)}). \tag{2.36}$$

2.7 Comparison of LTP model in this thesis with other LTP models

The LTP models presented in this chapter are slightly different from others in the literature. A generic LTP model is shown below [25, 138, 139]:

$$\begin{bmatrix} \vdots \\ Y(s+j\omega_0) \\ Y(s) \\ Y(s-j\omega_0) \\ \vdots \end{bmatrix} = \begin{bmatrix} \ddots & \vdots & \vdots & \vdots & \\ \cdots & H_0(s-j\omega_0) & H_{-1}(s) & H_{-2}(s+j\omega_0) & \cdots \\ \cdots & H_1(s-j\omega_0) & H_0(s) & H_{-1}(s+j\omega_0) & \cdots \\ \cdots & H_2(s-j\omega_0) & H_1(s) & H_0(s+j\omega_0) & \cdots \\ & \vdots & \vdots & \vdots & \ddots \end{bmatrix} \begin{bmatrix} \vdots \\ U(s+j\omega_0) \\ U(s) \\ U(s-j\omega_0) \\ \vdots \end{bmatrix} \tag{2.37}$$

where ω_0 is the fundamental frequency of the input and output. Note that $\mathcal{L}\{u(t)e^{j\omega_0 t}\} = U(s-j\omega_0)$. When modelling a converter ω_0 can be equal to, for example, the voltage fundamental frequency ω_1 [25, 138], or it can be equal to $2\omega_1$ if only the harmonics created due to the LTP dynamics of a SRF-PLL are to be included in the model [139]. When modelling only the PLL, several papers [126–128, 132] model an $\omega_0 = 2\omega_1$.

In any case, in a generic model, each of the elements in the input vector and the output vector is a harmonic. Thus, $H_0(s-j\omega_0)$ and $H_0(s+j\omega_0)$ are the transfer functions from two harmonics in the input ($U(s+j\omega_0)$ and $U(s-j\omega_0)$) to the two harmonics in the output at their same frequencies ($Y(s+j\omega_0)$ and $Y(s-j\omega_0)$). In this sense, the Harmonic Transfer Function (HTF) shown above is a MIMO model that relates the Fourier coefficients of the input to those of the output.

When developing the LTP model as a relationship between Fourier coefficients, it is necessary to have to separate the d and q components in the voltage:

$$\begin{bmatrix} \vdots \\ \Delta\theta_{1+}(s+j\omega_0) \\ \Delta\theta_{1+}(s) \\ \Delta\theta_{1+}(s-j\omega_0) \\ \vdots \end{bmatrix} = \begin{bmatrix} \ddots & \vdots & \vdots & \vdots & \vdots & \\ \cdots & H_{0,q}(s-j\omega_0) & H_{-1,d}(s) & H_{-1,q}(s) & H_{-2,d}(s+j\omega_0) & \cdots \\ \cdots & H_{1,q}(s-j\omega_0) & H_{0,d}(s) & H_{0,d}(s) & H_{-1,d}(s+j\omega_0) & \cdots \\ \cdots & H_{2,q}(s-j\omega_0) & H_{1,d}(s) & H_{1,q}(s) & H_{0,d}(s+j\omega_0) & \cdots \\ & \vdots & \vdots & \vdots & \vdots & \ddots \end{bmatrix} \begin{bmatrix} \vdots \\ V_q(s+j\omega_0) \\ V_d(s) \\ V_q(s) \\ V_d(s-j\omega_0) \\ \vdots \end{bmatrix} \tag{2.38}$$

In the model in (2.37), the middle column is very relevant (or, in (2.38), the middle two columns). The middle column $[\dots H_{-1}(s), H_0(s), H_1(s) \dots]$ represents the transfer from $U(s)$ to all output frequencies. All the other columns hold the same information as the middle column, but frequency-shifted and re-arranged.

The model in this thesis is different: all the information of the model is contained in the first row (i.e., in (2.19)), and the other rows contain the same information but frequency shifted and re-arranged. Also, the voltage $\overrightarrow{V_{\text{idealdq+}}}$ in (2.43), contains all the harmonics. This makes the interpretation of the model similar to such of an LTI model. Imagine an LTI model as: $Y(s) = TF(s)U(s)$. If the input $U(s)$ has two harmonics (e.g. $100\,\text{Hz}$ and $200\,\text{Hz}$), the output has two harmonics, and the transfer function needs to be evaluated at those two frequencies: $Y|_{100\text{Hz}} = TF(s = j2\pi 100)U|_{100\text{Hz}}$ and $Y|_{200\text{Hz}} = TF(s = j2\pi 200)U|_{200\text{Hz}}$. The variable $U(s)$ serves to represent all the harmonics in the input.

With the LTP model in this thesis, the procedure is similar. If the voltage has two frequencies (e.g., $100\,\text{Hz}$ and $200\,\text{Hz}$) then the output has, through $\overrightarrow{TF_{\text{PLL1+}}}$, two frequencies: $Y|_{100\text{Hz}} = TF_{\text{PLL1+}}(s = j2\pi 100)U|_{100\text{Hz}}$ and $Y|_{200\text{Hz}} = TF_{\text{PLL1+}}(s = j2\pi 200)U|_{200\text{Hz}}$. Thus, the LTP model in this thesis, can be interpreted exactly like an LTI model except that it also shows the couplings. In the example here, the couplings show that the output also has other frequency components, e.g.,: $Y|_{300\text{Hz}} = TF_{\text{PLL3+}}(s = j2\pi 300)U|_{100\text{Hz}}$ and $Y|_{400\text{Hz}} = TF_{\text{PLL3+}}(s = j2\pi 400)U|_{200\text{Hz}}$. In this sense, even the generic LTP model in (2.37) can be interpreted in this way: $U(s)$ has all the harmonics and the important information lies in the middle column of the HTF.

Thus, the interpretation of the input and output vectors (whether they contain one harmonic or several) is not relevant. The relevant difference is that the input and output of the model in this thesis are space vectors related by complex transfer functions, whereas in (2.37) the input and output are Fourier coefficients related by real transfer functions. However, there is an equivalence in between the two types of transfer functions. One example of the equivalences is:

$$\begin{aligned} H_{0,d}(s) &= 2\Re\{\overrightarrow{TF_{\text{PLL1+}}(s)}\} = \overrightarrow{TF_{\text{PLL1+}}(s)} + \overrightarrow{TF_{\text{PLL2+}}(s)} \\ H_{0,q}(s) &= -2\Im\{\overrightarrow{TF_{\text{PLL1+}}(s)}\} = \frac{1}{-j}(\overrightarrow{TF_{\text{PLL1+}}(s)} - \overrightarrow{TF_{\text{PLL2+}}(s)}) \end{aligned} \tag{2.39}$$

Thus, the HTF matrix in this thesis is a linear combination of the HTF matrix of the type shown in (2.38). Therefore, the HTF matrix in this thesis has the same stability properties and the same theorems apply to it as if it would have been represented as (2.38). Nonetheless, it was considered in this thesis that it was more practical to model the HTF with space vectors instead of Fourier coefficients, because then the integration with the rest of the converter model is direct, and notions such as the sequence of the input voltage are maintained.

2.8 Verification of LTI and LTP models

2.8.1 Time domain verification

The models are verified with time-domain simulations. The PLL parameters in Appendix A are used, and also $K = 1/\sqrt{2}$. Three tests are performed:

- Test 1: From a steady-state operating point with $V_n = 5\%$, V_n is increased 10% of its value (small-signal perturbation).
- Test 2: From a steady-state operating point with $V_n = 60\%$, V_n is increased 10% of its value (small-signal perturbation).
- Test 3: From a steady-state operating point with $V_n = 5\%$, V_n is increased until $V_n = 60\%$ (large-signal perturbation).

The results for the DDSRF-PLL method 1 are shown in Fig. 2.4. It can be seen that, for small-signal perturbations (Test 1 and Test 2), the LTI model fails to predict the oscillations that appear in the phase angles. As a consequence, the LTI model predicts a much cleaner and stable response than what the simulations show. The LTP model, however, perfectly predicts the trend for small-signal perturbations.

In the test 3, where there is a large-signal perturbation, the LTI model again is inaccurate. For the LTP model, the positive-sequence phase-angle transient is perfectly predicted, but not the negative-sequence phase-angle. This is due to the fact that, in this method 1 and when using normalization, the dynamics of the PLL when tracking the positive or negative phase angle do not depend on V_n (i.e., the location of the poles do not vary with V_n). However, the gain of the system when tracking θ_{1-} does vary with V_n[5]. Therefore, the LTP model predicts correctly the oscillations in $\Delta\theta_{1+}$ and $\Delta\theta_{1-}$, but in $\Delta\theta_{1-}$ they are wrongly scaled. In any case, this test shows that, even if periodic, the LTP model is still small-signal.

The results for the DDSRF-PLL method 2 are shown in Fig. 2.5. The results of Test 1 show that the LTI model can predict the transient of a small-signal perturbation if V_n is low (at least for $\Delta\theta_{1+}$). However, if V_n is increased (Test 2), the LTI model is no longer small-signal accurate. Just like in method 1, the LTI model underestimates the oscillations in the system. In contrast, the LTP model follows the transient after a small-signal perturbation no matter the imbalance level. With respect to Test 3, both models are inaccurate since both models are linearised.

2.8.2 Frequency domain verification

In this section, different frequency sweeps are performed for different V_n levels. The results are shown in Fig. 2.6 (method 1). Certain transfer functions are not shown since they are conjugates of the transfer functions displayed. The figure shows that the LTP model is perfectly accurate for different levels of voltage imbalance, while the LTI model does not have a perfect overlap with the frequency scan. Also, the LTI model only appears in the plots for $\overrightarrow{TF_{\text{PLL1+}}}$ and $\overrightarrow{TF_{\text{PLL1-}}}$ since the LTI model does not anticipate the existence of couplings. The model for method 2 is also verified (Fig. 2.7). Both figures use the PLL parameters in Appendix A.

[5] This is demonstrated in Section 2.12.

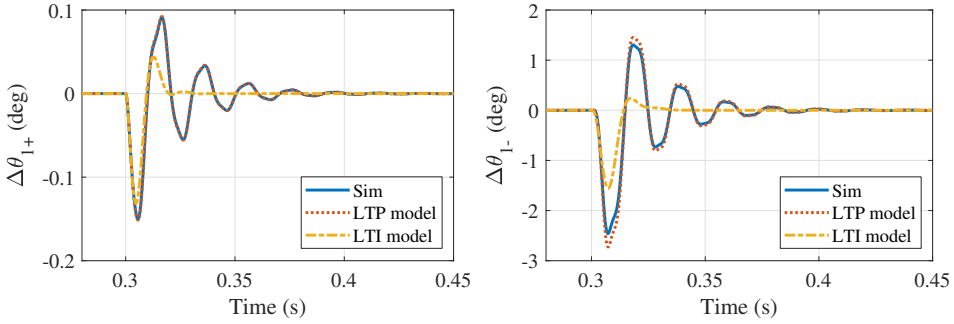

(a) Test 1: $\Delta\theta_{1+}$

(b) Test 1: $\Delta\theta_{1-}$

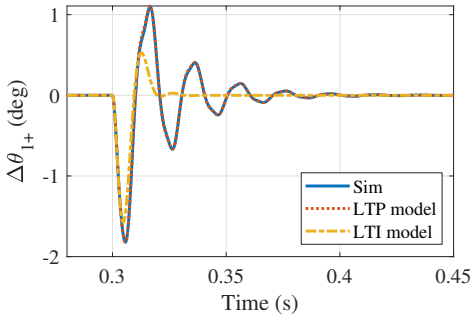

(c) Test 2: $\Delta\theta_{1+}$

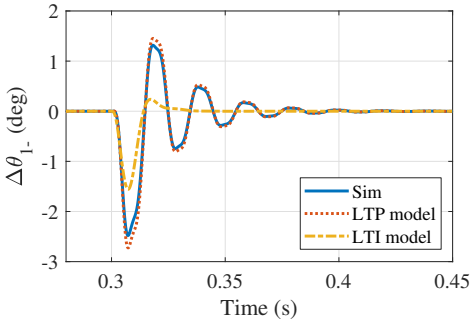

(d) Test 2: $\Delta\theta_{1-}$

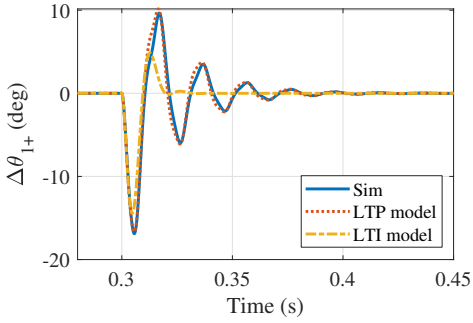

(e) Test 3: $\Delta\theta_{1+}$

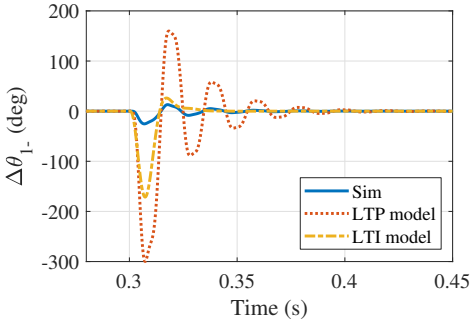

(f) Test 3: $\Delta\theta_{1-}$

Figure 2.4: Verification of LTI and LTP models for the DDSRF-PLL method 1 in the time domain. On the left, how the PLL tracks the positive-sequence phase angle; and on the right, the negative-sequence phase angle.

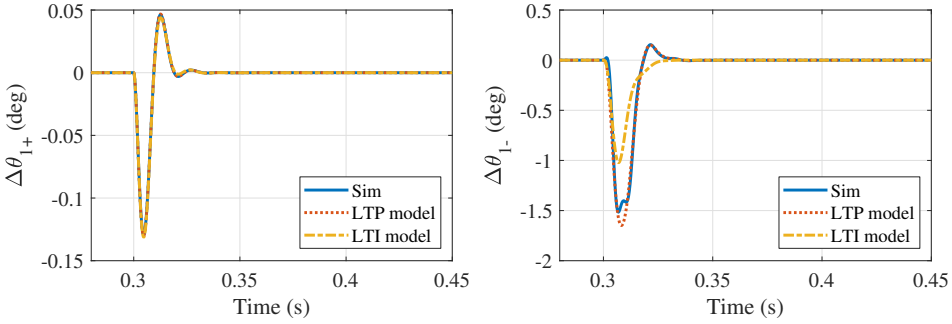

(a) Test 1: $\Delta\theta_{1+}$

(b) Test 1: $\Delta\theta_{1-}$

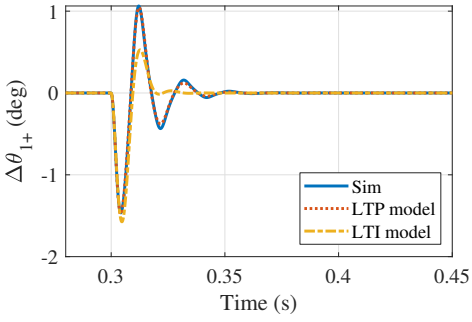

(c) Test 2: $\Delta\theta_{1+}$

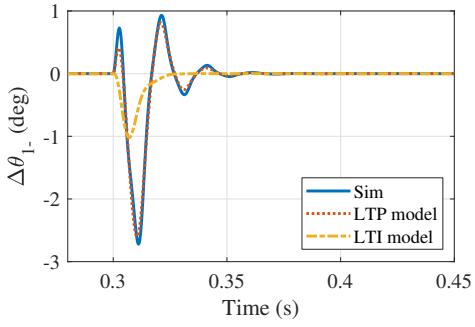

(d) Test 2: $\Delta\theta_{1-}$

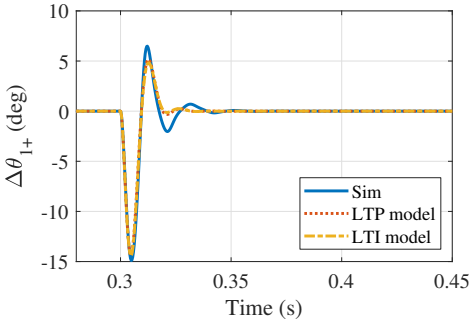

(e) Test 3: $\Delta\theta_{1+}$

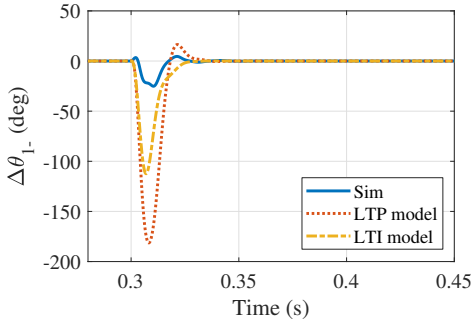

(f) Test 3: $\Delta\theta_{1-}$

Figure 2.5: Verification of LTI and LTP models for the DDSRF-PLL method 2 in the time domain. On the left, how the PLL tracks the positive-sequence phase angle; and on the right, the negative-sequence phase angle.

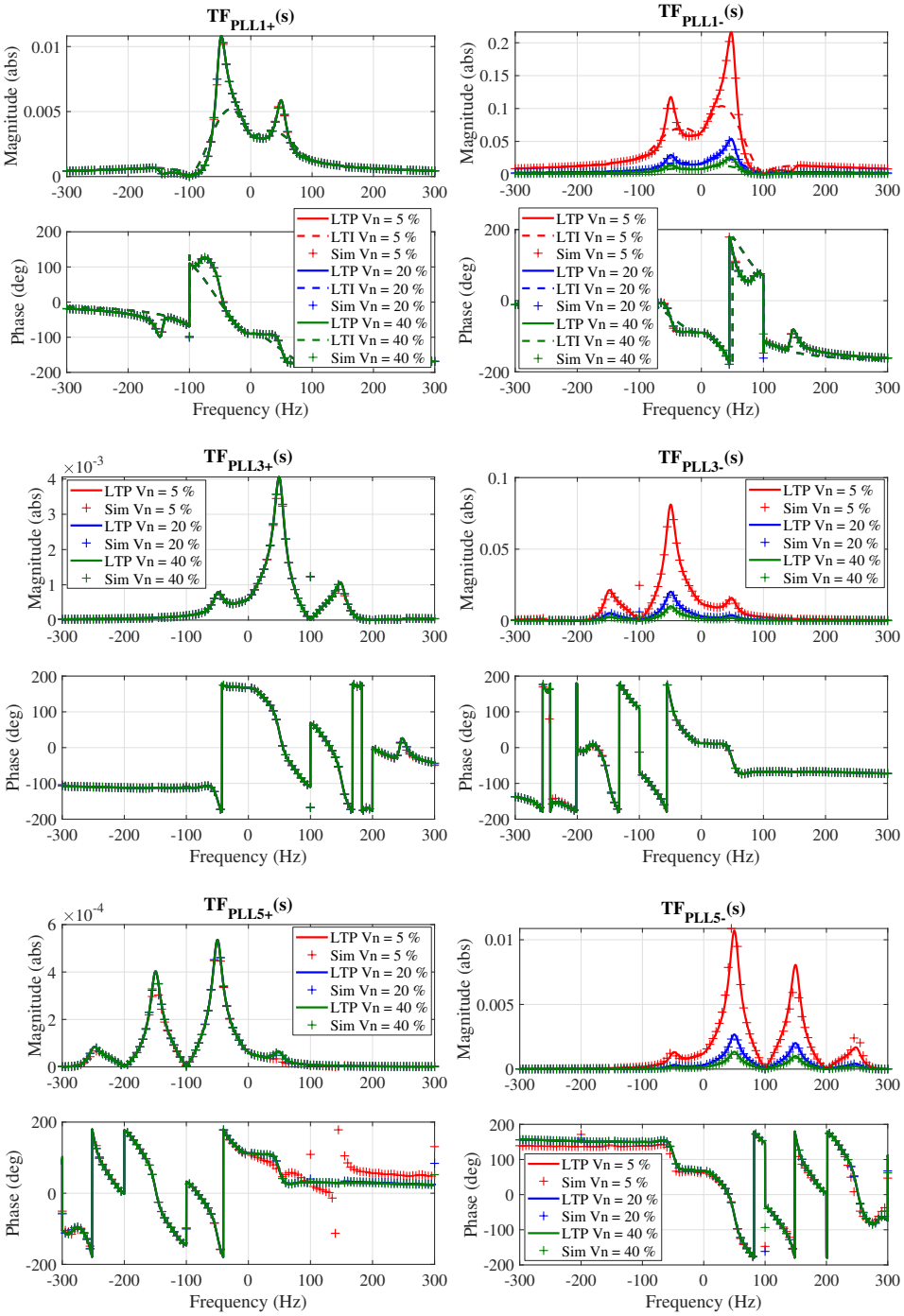

Figure 2.6: Verification of LTI and LTP models for the DDSRF-PLL method 1 in frequency domain. On the left and right, transfer functions related to the positive-sequence and negative-sequence phase angle, respectively.

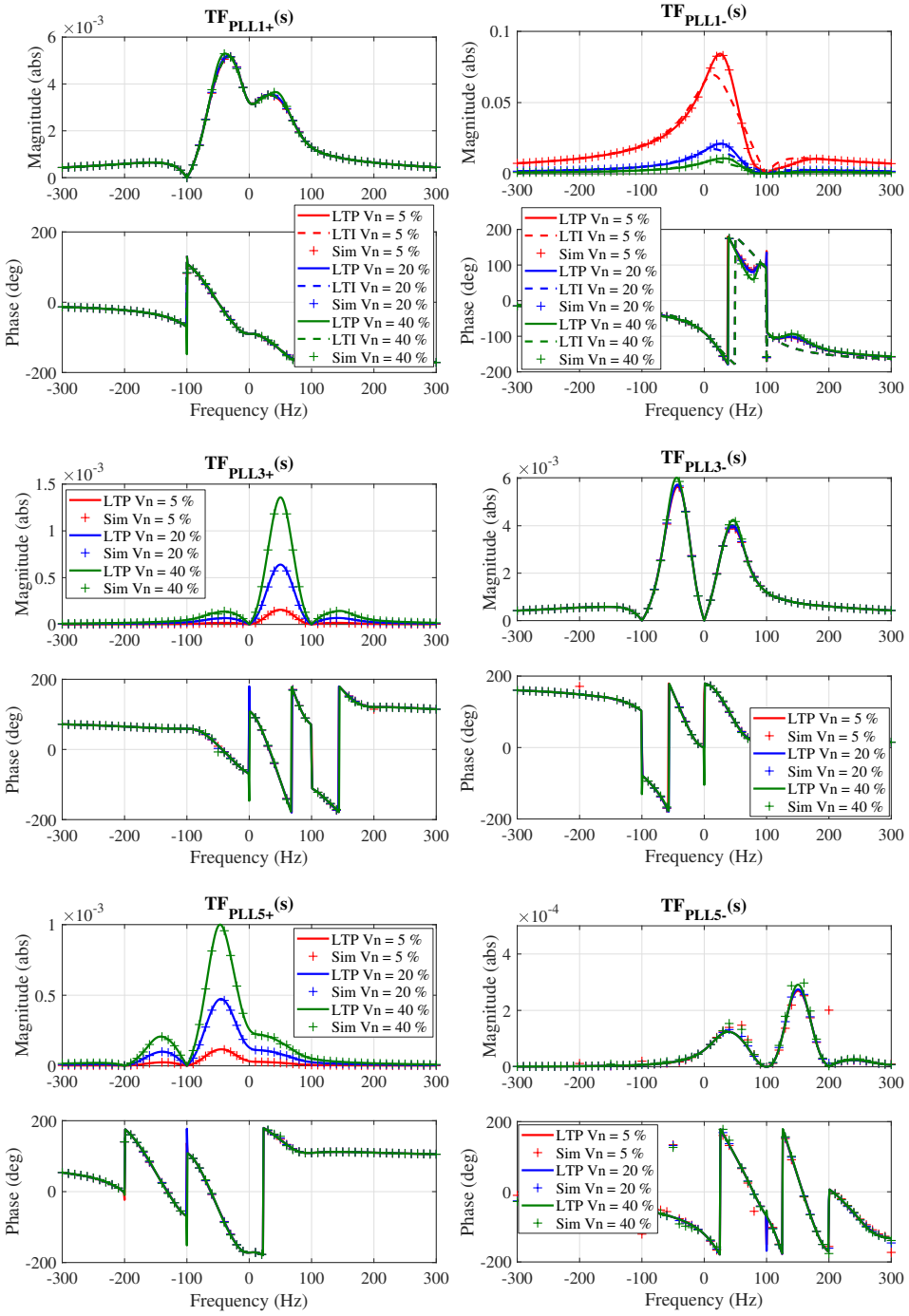

Figure 2.7: Verification of LTI and LTP models for the DDSRF-PLL method 2 in frequency domain. On the left and right, transfer functions related to the positive-sequence and negative-sequence phase angle, respectively.

2.9 Differences between the LTI and LTP models

When comparing the LTI and LTP model equations (for example, for the DDSRF-PLL method 1, the positive-sequence phase-angle equations would be (2.19) and (2.24)), it appears as if the only difference between the LTI and LTP model is that the LTP model predicts the couplings, while the LTI model does not. However, this is not the main difference.

For illustration purposes, the time-domain Test 1 results for method 1 are analysed in detail (i.e., Fig. 2.4 a) is further discussed). Fig. 2.8 shows the decomposition of the time-domain response of the LTP model, according to the contribution to the total response by each of its transfer functions. The black dotted line in Fig. 2.8 corresponds to the LTP line shown in Fig. 2.4 a). As it can be seen, the coupling transfer functions contribute to the response; however, the biggest contribution comes from $\overrightarrow{TF_{\text{PLL1+}}}$ and $\overrightarrow{TF_{\text{PLL2+}}}$, and in fact, the total response of the LTP model (summing the responses of all transfer functions) is relatively similar to the response that the model would give if only $\overrightarrow{TF_{\text{PLL1+}}}$ and $\overrightarrow{TF_{\text{PLL2+}}}$ would be considered.

Further, it is important to notice that the response given by $\overrightarrow{TF_{\text{PLL1+}}}$ and $\overrightarrow{TF_{\text{PLL2+}}}$ is not at all similar to such given by $\overrightarrow{TF_{\text{PLL1+LTI}}}$ and $\overrightarrow{TF_{\text{PLL2+LTI}}}$, which is shown in Fig. 2.4 a) (under the label LTI model). This is due to the fact that $\overrightarrow{TF_{\text{PLL1+}}}$ and $\overrightarrow{TF_{\text{PLL2+}}}$ are very different transfer functions than $\overrightarrow{TF_{\text{PLL1+LTI}}}$ and $\overrightarrow{TF_{\text{PLL2+LTI}}}$. This can be seen in the fact that the expression for $\overrightarrow{TF_{\text{PLL1+}}}$ (shown in (2.15)) is very different from the expression for $\overrightarrow{TF_{\text{PLL1+LTI}}}$ (shown in (2.25)). The transfer functions are different, and therefore they have different poles and stability properties. Therefore, the main difference between the LTI and LTP models is not that the LTP model predicts the couplings but that, through $\overrightarrow{TF_{\text{PLL1+}}}$ and $\overrightarrow{TF_{\text{PLL2+}}}$, the LTP model is able to predict important oscillatory behaviour that appears in the PLL in the presence of imbalance. Similar conclusions can be obtained by analysing in detail the time-domain waveforms of different tests, or when considering the DDSRF-PLL method 2.

2.10 Comparison of LTI and LTP models for stability studies

2.10.1 Procedure for stability analysis with the LTI model

The LTI and LTP models have two subsystems: one for the positive sequence and one for the negative sequence. In method 1, the LTI model for the positive sequence can be written as (2.40) and for the negative sequence as (2.41). $M_{\text{LTI1+}}$ is a 2x2 complex transfer function matrix derived from (2.24). $M_{\text{LTI1+}}$ is shown in (2.42). $M_{\text{LTI1–}}$ can be found analogously.

$$\begin{bmatrix} \Delta\theta_{1+} \\ \Delta\theta^*_{1+} \end{bmatrix} = [M_{\text{LTI1+}}]_{2x2} \begin{bmatrix} \overrightarrow{V_{\text{idealdq+}}} \\ \overrightarrow{V^*_{\text{idealdq+}}} \end{bmatrix} \tag{2.40}$$

$$\begin{bmatrix} \Delta\theta_{1-} \\ \Delta\theta^*_{1-} \end{bmatrix} = [M_{\text{LTI1–}}]_{2x2} \begin{bmatrix} \overrightarrow{V_{\text{idealdq–}}} \\ \overrightarrow{V^*_{\text{idealdq–}}} \end{bmatrix} \tag{2.41}$$

$$M_{\text{LTI1+}} = \begin{bmatrix} \overrightarrow{TF_{\text{PLL1+LTI}}(s)} & \overrightarrow{TF_{\text{PLL2+LTI}}(s)} \\ \overrightarrow{TF^*_{\text{PLL2+LTI}}(s)} & \overrightarrow{TF^*_{\text{PLL1+LTI}}(s)} \end{bmatrix} \tag{2.42}$$

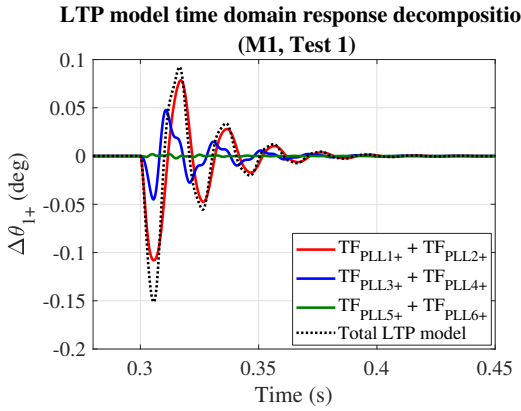

Figure 2.8: Decomposition of LTP model response (M1, Test 1).

According to multivariable stability theory, in order to evaluate the stability with a MIMO LTI model, the MIMO poles of $M_{\text{LTI1+}}$ and $M_{\text{LTI1–}}$ need to be found, and all should lay in the Left Half Plane (LHP) [140].[6]

2.10.2 Procedure for stability analysis with the LTP model

In the LTP model, the positive and negative sequence subsystems are shown in (2.43) and (2.44), respectively. $M_{\text{LTP1+}}$ is a complex transfer function matrix derived from (2.19). The resulting matrix is (2.45). $M_{\text{LTP1–}}$ can be found analogously.

$$\begin{bmatrix} \Delta\theta_{1+} \\ \Delta\theta^*_{1+} \\ \Delta\theta_{1+}e^{+j4\omega_1 t} \\ \Delta\theta^*_{1+}e^{-j4\omega_1 t} \\ \Delta\theta_{1+}e^{-j4\omega_1 t} \\ \Delta\theta^*_{1+}e^{+j4\omega_1 t} \end{bmatrix} = [M_{\text{LTP1+}}]_{6x6} \begin{bmatrix} \overrightarrow{V_{\text{idealdq+}}} \\ \overrightarrow{V^*_{\text{idealdq+}}} \\ \overrightarrow{V_{\text{idealdq+}}}e^{+j4\omega_1 t} \\ \overrightarrow{V^*_{\text{idealdq+}}}e^{-j4\omega_1 t} \\ \overrightarrow{V_{\text{idealdq+}}}e^{-j4\omega_1 t} \\ \overrightarrow{V^*_{\text{idealdq+}}}e^{+j4\omega_1 t} \end{bmatrix} \tag{2.43}$$

$$\begin{bmatrix} \Delta\theta_{1-} \\ \Delta\theta^*_{1-} \\ \Delta\theta_{1-}e^{-j4\omega_1 t} \\ \Delta\theta^*_{1-}e^{+j4\omega_1 t} \\ \Delta\theta_{1-}e^{+j4\omega_1 t} \\ \Delta\theta^*_{1-}e^{-j4\omega_1 t} \end{bmatrix} = [M_{\text{LTP1–}}]_{6x6} \begin{bmatrix} \overrightarrow{V_{\text{idealdq–}}} \\ \overrightarrow{V^*_{\text{idealdq–}}} \\ \overrightarrow{V_{\text{idealdq–}}}e^{-j4\omega_1 t} \\ \overrightarrow{V^*_{\text{idealdq–}}}e^{+j4\omega_1 t} \\ \overrightarrow{V_{\text{idealdq–}}}e^{+j4\omega_1 t} \\ \overrightarrow{V^*_{\text{idealdq–}}}e^{-j4\omega_1 t} \end{bmatrix} \tag{2.44}$$

[6] In a MIMO LTI system, there are two main ways of calculating the poles. The first one is to calculate the Smith-McMillan form of the transfer function matrix, a canonical form in which the poles are directly accessible [140]. Another option is to plot together all the poles of each individual transfer function in the matrix. This option gives the correct placement of the MIMO poles, although the multiplicities of the poles are unknown. The second option is used in this thesis since the computations are faster, and since the multiplicities of the poles are not relevant (i.e., it is not important to know the number of poles in the RHP, but only whether there is any pole there).

$$\begin{bmatrix} \overrightarrow{TF_{\text{PLL1+}}(s)} & \overrightarrow{TF_{\text{PLL2+}}(s)} & \overrightarrow{TF_{\text{PLL3+}}(s)} & \overrightarrow{TF_{\text{PLL4+}}(s)} & \overrightarrow{TF_{\text{PLL5+}}(s)} & \overrightarrow{TF_{\text{PLL6+}}(s)} \\ \overrightarrow{TF^{*}_{\text{PLL2+}}(s)} & \overrightarrow{TF^{*}_{\text{PLL1+}}(s)} & \overrightarrow{TF^{*}_{\text{PLL4+}}(s)} & \overrightarrow{TF^{*}_{\text{PLL3+}}(s)} & \overrightarrow{TF^{*}_{\text{PLL6+}}(s)} & \overrightarrow{TF^{*}_{\text{PLL5+}}(s)} \\ \overrightarrow{TF_{\text{PLL5+}}(s-j4\omega_1)} & \overrightarrow{TF_{\text{PLL4+}}(s-j4\omega_1)} & \overrightarrow{TF_{\text{PLL1+}}(s-j4\omega_1)} & 0 & 0 & \overrightarrow{TF_{\text{PLL2+}}(s-j4\omega_1)} \\ \overrightarrow{TF^{*}_{\text{PLL4+}}(s+j4\omega_1)} & \overrightarrow{TF^{*}_{\text{PLL5+}}(s+j4\omega_1)} & 0 & \overrightarrow{TF^{*}_{\text{PLL1+}}(s+j4\omega_1)} & \overrightarrow{TF^{*}_{\text{PLL2+}}(s+j4\omega_1)} & 0 \\ \overrightarrow{TF_{\text{PLL3+}}(s+j4\omega_1)} & \overrightarrow{TF_{\text{PLL6+}}(s+j4\omega_1)} & 0 & \overrightarrow{TF_{\text{PLL2+}}(s+j4\omega_1)} & \overrightarrow{TF_{\text{PLL1+}}(s+j4\omega_1)} & 0 \\ \overrightarrow{TF^{*}_{\text{PLL6+}}(s-j4\omega_1)} & \overrightarrow{TF^{*}_{\text{PLL3+}}(s-j4\omega_1)} & \overrightarrow{TF^{*}_{\text{PLL2+}}(s-j4\omega_1)} & 0 & 0 & \overrightarrow{TF^{*}_{\text{PLL1+}}(s-j4\omega_1)} \end{bmatrix} \tag{2.45}$$

The $M_{\text{LTP1+}}$ and $M_{\text{LTP1–}}$ shown in (2.43) and (2.44) are the HTF matrices of the system, and are 6x6. In reality, when an LTP system is represented in the frequency domain, the system (i.e., the HTF matrix) has an infinite order [134]. In here, the HTF matrix is 6x6 because only the first round of couplings are considered. $M_{\text{LTP1+}}$ could be 2x2 if this round of couplings was ignored (considering $\overrightarrow{TF_{\text{PLL3+}}}$–$\overrightarrow{TF_{\text{PLL6+}}}$ negligible). Alternatively, $M_{\text{LTP1+}}$ could be higher order than 6x6 if the second or more rounds of couplings are considered. A question arises as to what is the appropriate order to model. The issue of model truncation is explained subsequently.

Formally, the poles of an LTP system are the locations in the complex s-plane where the HTF is not analytic [141]. According to [141], the LTP poles appear in different strips. The horizontal strip confined by $y = \omega_{\text{p}}/2$ and $y = -\omega_{\text{p}}/2$ (with ω_{p} being the pumping frequency of the LTP system; i.e., $4\omega_1$ in M1 and $2\omega_1$ in M2) is called the fundamental strip. The poles that appear in this strip are then reflected to other strips (i.e., complementary strips) in such a way that only the imaginary part of the poles change, but not the real part. This is illustrated in Fig. 2.9.

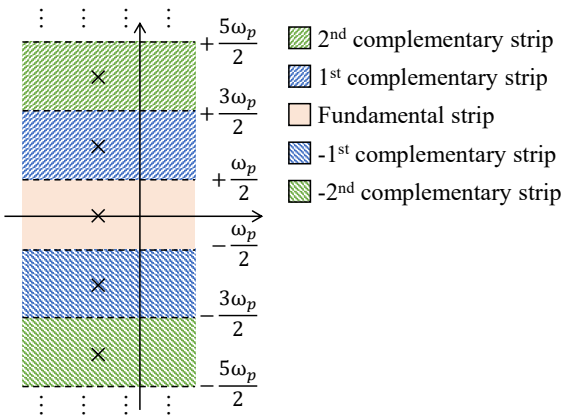

Figure 2.9: Infinite pole repetition in an LTP system [141].

This means that there are infinite LTP poles, but since the x-axis value of the poles does not change when comparing different strips, it is not necessary to look at all the poles of the system in order to assess stability, but only whether the poles in the fundamental strip fall entirely in the LHP or not. The relevance of the fundamental strip is shown also in the fact that some advanced concepts like the mode shapes or the time response of the modes can be defined in LTP systems using only the poles that lie on this strip [141].

In this thesis, it is considered that a certain HTF order is enough as long as the poles in the fundamental strip do not significantly change. In practice, this means that the conclusions of the stability study (the stability limit) remain unchanged if the order is increased. As it will be shown later, the $M_{\mathrm{LTP1+}}$ 2x2 HTF matrix predicts the same poles in the fundamental strip (and thus, the same stability limits) as the $M_{\mathrm{LTP1+}}$ 6x6 HTF matrix. Most importantly, as shown in Section 2.10.3 – 2.10.5, the stability results are correct.

Since the LTP model is approximated as an LTI MIMO model of a certain order, the poles can be determined in the same way as with MIMO LTI theory [25]. This means that the same method for pole determination will be used for the LTP system as for the LTI system, which is to plot the poles of each individual transfer function in the matrix. This method is also used in [142]. For method 2, the LTI and LTP MIMO matrices can be found in a similar way, leading to $M_{\mathrm{LTI2+}}$, $M_{\mathrm{LTI2-}}$, $M_{\mathrm{LTP2+}}$ and $M_{\mathrm{LTP2-}}$. In method 2, however, it is only necessary to check the poles of the positive-sequence sub-system, since only $\theta_{\mathrm{PLL+}}$ is used in the decoupling network.

2.10.3 LTI vs LTP stability results: DDSRF-PLL method 1

In this section, the parameter K that defines the cut-off frequency of the low-pass filter $F(s) = \frac{\omega_{\mathrm{f}}}{s+\omega_{\mathrm{f}}}$ (with $\omega_{\mathrm{f}} = K\omega_1$) is changed. According to simulations (one example is shown in Fig. 2.10), the DDSRF-PLL method 1 becomes unstable for K values higher than K_{lim}, being:

- $K_{\mathrm{lim}} = 1.05$ for $V_{\mathrm{n}} = 5\%$.
- $K_{\mathrm{lim}} = 1.05$ for $V_{\mathrm{n}} = 40\%$.

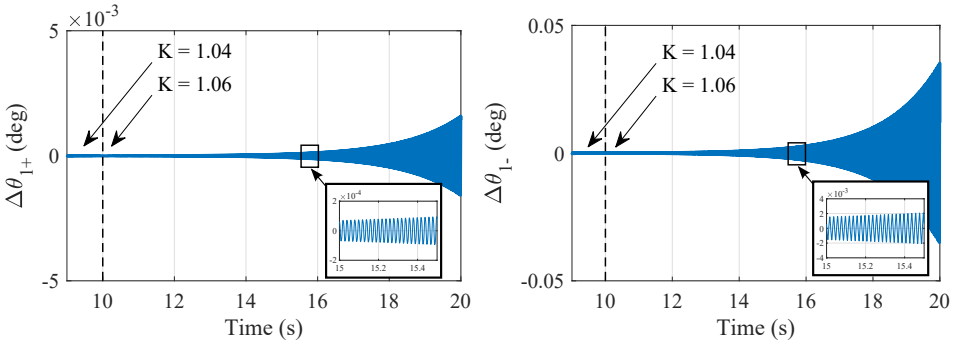

Figure 2.10: Method 1: Instability when changing K from 1.04 to 1.06 ($V_{\mathrm{n}} = 5\%$). On the left, the figure shows the positive-sequence phase angle calculation, and on the right, the negative-sequence phase angle calculation. One signal grows faster than the other, but both are unstable.

In Fig. 2.11 the pole maps[7] from $M_{\mathrm{LTI1+}}$ and $M_{\mathrm{LTI1-}}$ are shown for different K when $V_{\mathrm{n}} = 5\%$. As it can be seen, the LTI method predicts incorrectly the stability boundary,

[7]Only the poles close to the $x = 0$ line are shown.

since it predicts that, for $K = 1.15$ and $K = 1.35$, the system is still stable. The K has to be increased until $K = 2.45$ in order to predict instability (not shown in the figure). The pole maps of $M_{\mathrm{LTP1+}}$ and $M_{\mathrm{LTP1-}}$ are also shown in the same figure, and they correctly predict the stability boundary. Note that, no matter that the 2x2 or 6x6 LTP model is used, the stability limit is predicted accurately. In Fig. 2.12 the pole maps are shown for $V_{\mathrm{n}} = 40\%$. Again, the stability prediction of the LTI model is incorrect, whereas the LTP models are accurate.

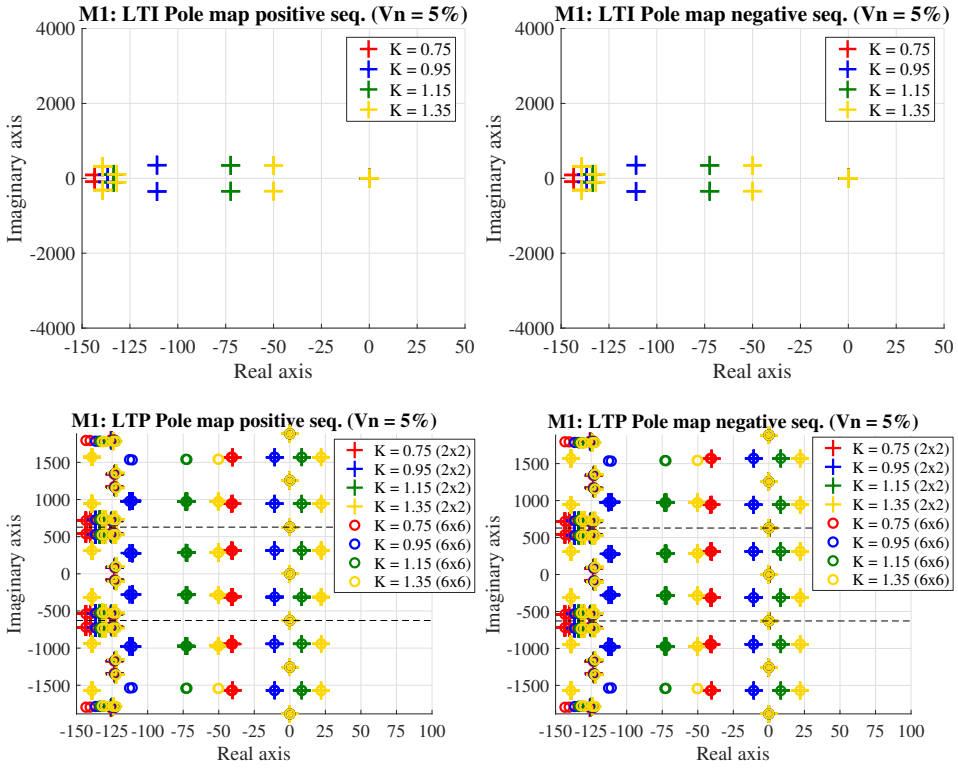

Figure 2.11: Stability results for method 1 ($V_{\mathrm{n}} = 5\%$). The LTP pole map shows the fundamental strip, and two complementary strips (y-axis: $[\frac{-3\omega_{\mathrm{p}}}{2}\ \frac{3\omega_{\mathrm{p}}}{2}]$ with $\omega_{\mathrm{p}} = 4\omega_1$).

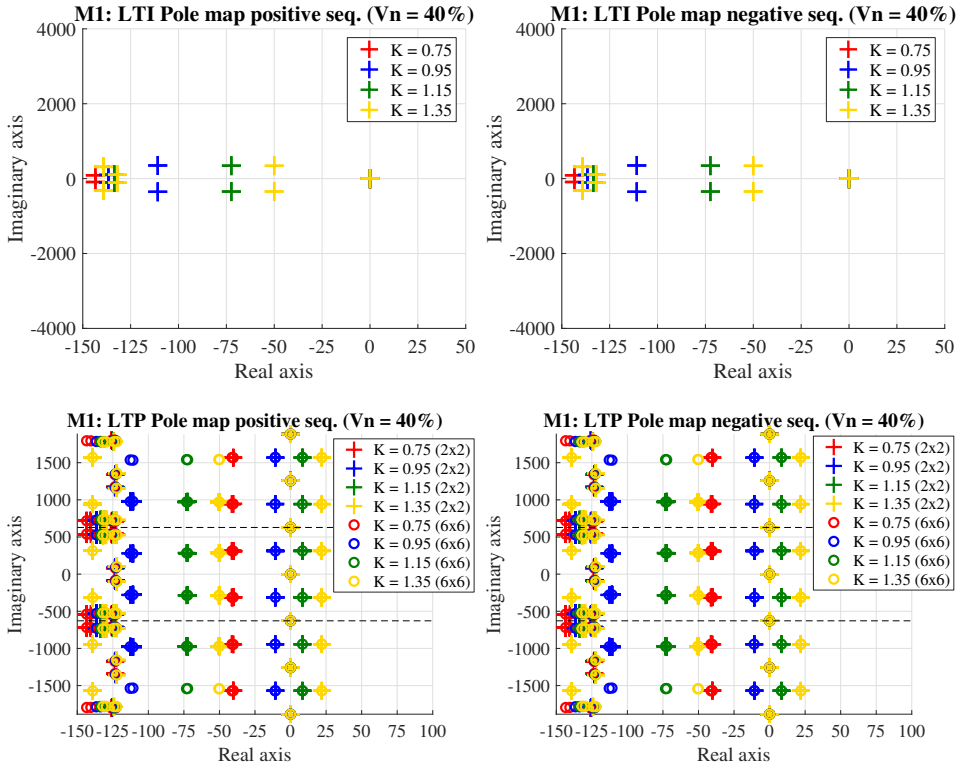

Figure 2.12: Stability results for method 1 ($V_n = 40\%$). The LTP pole map shows the fundamental strip, and two complementary strips (y-axis: $[\frac{-3\omega_p}{2} \frac{3\omega_p}{2}]$ with $\omega_p = 4\omega_1$).

2.10.4 LTI vs LTP stability results: DDSRF-PLL method 2

Here, K is also changed. According to simulations, the DDSRF-PLL method 2 becomes unstable for K values higher than K_{lim}, being:

- $K_{lim} = 2.427$ for $V_n = 5\%$.
- $K_{lim} = 2.089$ for $V_n = 40\%$.

In Fig. 2.13 the pole map from M_{LTI2+} is shown for different K when $V_n = 5\%$. Note that, in method 2, it is only necessary to check the poles of the positive-sequence sub-system, since only θ_{PLL+} is used in the decoupling network. As it can be seen, the LTI method predicts quite accurately the stability boundary, since it predicts that, for the two K values higher than K_{lim}, the system is unstable. In contrast, when the voltage imbalance increases ($V_n = 40\%$), the LTI model becomes inaccurate (Fig. 2.14). The LTP models (2x2 or 6x6) are accurate no matter the V_n level.

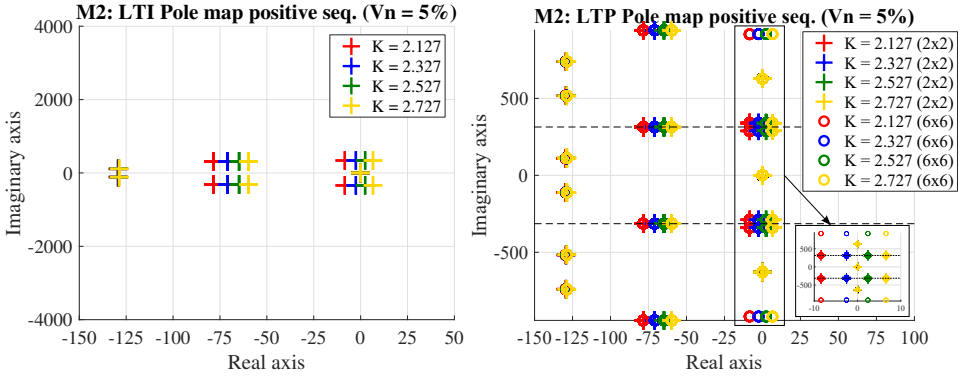

Figure 2.13: Stability results for method 2 ($V_n = 5\%$). The LTP pole map shows the fundamental strip, and two complementary strips (y-axis: $[\frac{-3\omega_p}{2} \frac{3\omega_p}{2}]$ with $\omega_p = 2\omega_1$).

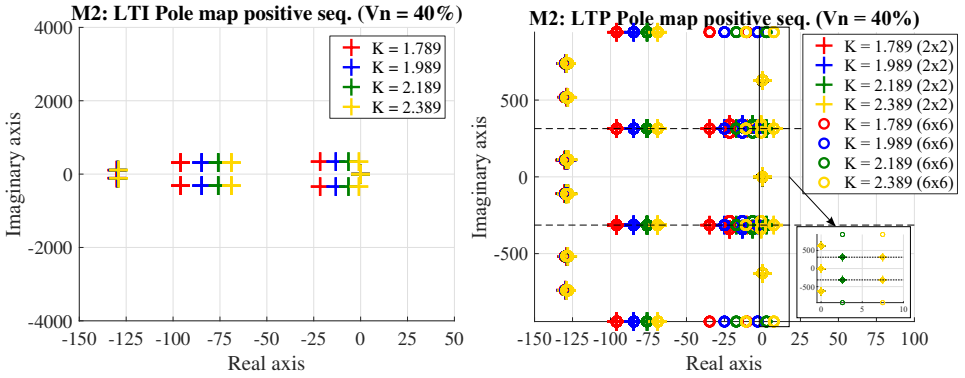

Figure 2.14: Stability results for method 2 ($V_n = 40\%$). The LTP pole map shows the fundamental strip, and two complementary strips (y-axis: $[\frac{-3\omega_p}{2} \frac{3\omega_p}{2}]$ with $\omega_p = 2\omega_1$).

2.10.5 Explanation of the stability results

The results in relation to method 1 are explained first. In this method, it is important to look at the expressions (2.4) and (2.5). The periodic terms in (2.5) depend on V_p and, therefore, the periodic terms in the system are important even if V_n is low. Since the LTI model ignores all periodic terms, the stability of the network is wrongly predicted by the LTI model (see again Fig. 2.11 and Fig. 2.12). In contrast, the LTP model considers the periodic terms, and predicts stability accurately for all imbalance levels. This is clearly summarized in Fig. 2.15.

Thus, the periodic terms explain the inaccuracy of the LTI model shown in Fig. 2.15. Other issues to explain in this figure are: a) why the stability limit is independent on V_n (i.e., why K_{lim} is fixed at 1.05); and b) why the prediction of the LTI model is constant.

The first issue is due to the normalization block. Including the normalization block makes the dynamics to be independent on V_n. In fact, the pole maps of the PLL do not

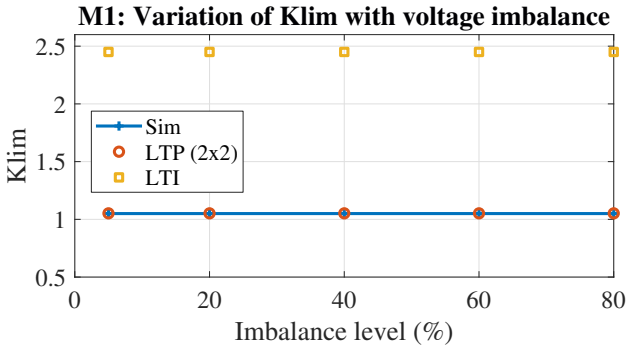

Figure 2.15: Method 1: variation of K_{lim} with the voltage imbalance predicted by simulations, the LTI model and the LTP (2x2) model.

change when V_{n} increases (compare the pole maps shown in Fig. 2.11 and Fig. 2.12). In contrast, if the normalization block is excluded, Fig. 2.16 is obtained. It is seen here that, in this case, K_{lim} depends on V_{n}. Here, note that the LTI model is also always inaccurate, although it is more inaccurate when V_{n} is high.

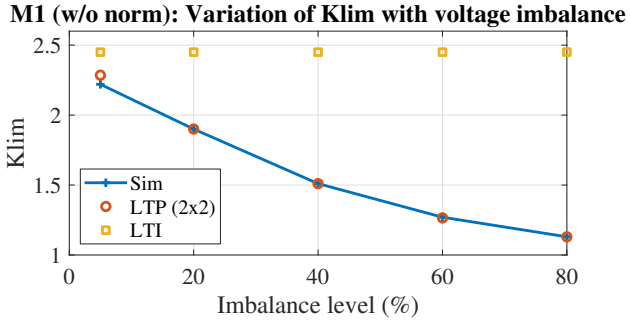

Figure 2.16: Method 1 (w/o normalization): variation of K_{lim} with the voltage imbalance predicted by simulations, the LTI model and the LTP (2x2) model.

The second issue is why the stability prediction of the LTI model for method 1 is always constant no matter V_{n}. The $\overrightarrow{TF_{\text{PLL1+LTI}}}$ in (2.25) does not depend on V_{n} and therefore its poles (and the poles of $M_{\text{LTI1+}}$) do not change with the imbalance level. With respect to $\overrightarrow{TF_{\text{PLL1–LTI}}}$, when the normalization block is included, then $\overrightarrow{TF_{\text{PLL1–LTI}}}$ becomes:

$$\overrightarrow{TF_{\text{PLL1–LTI}}} = \frac{V_{\text{nom}}}{V_{\text{n}}} \frac{H_{\text{PLL–}}(s)\overrightarrow{G^{*}_{\text{dq+}}(s)}}{2j(1 + V_{\text{nom}} H_{\text{PLL–}}(s) G_{\text{re}}(s))}. \tag{2.46}$$

V_{n} appears in (2.46) but only as a gain that cannot modify the poles of the system. Consequently, the LTI model in Fig. 2.15 always predicts a constant stability limit.

With respect to the DDSRF-PLL method 2, only $\theta_{\text{PLL+}}$ is used in the decoupling network. Therefore, the relevant periodic terms in order to determine the stability of the network are those which appear in (2.26) but not the ones which appear in (2.27). It can be

seen that the periodic terms in (2.26) are low when V_n is low, and therefore, in the low-V_n cases the LTI model is accurate for stability calculations (see Fig. 2.13). When V_n increases, however, the periodic terms become relevant and again the LTI model fails to predict the stability boundary (see Fig. 2.14).

This is better summarized in Fig. 2.17. In here, K_{lim} reduces with V_n, and the LTP model perfectly predicts the trend. The LTI model, however, is accurate only when V_n is low. Also, the LTI model predicts a constant $K_{lim} = 2.45$, independent of voltage imbalance. Of course, this is the case for the LTI model, since in method 2 only the M_{LTI1+} matters for stability and the $\overrightarrow{TF_{PLL1+LTI}}$ does not depend on V_n.

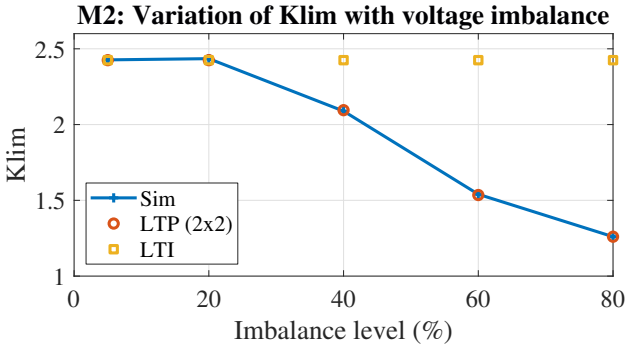

Figure 2.17: Method 2: variation of K_{lim} with the voltage imbalance predicted by simulations, the LTI model and the LTP (2x2) model.

2.10.6 LTP model order truncation

Sections 2.10.3 and 2.10.4 show, both in M1 and M2, that the LTP poles that lay in the fundamental strip do not significantly change when they are calculated with the 2x2 or 6x6 model. With respect to the other strips, the 6x6 model calculates more poles there, which is expected since the 6x6 model has a higher order. However, since the poles in the complementary strips are only reflections of the poles in the fundamental strip, only the poles in the fundamental strip are relevant for stability, and therefore the 2x2 model is considered enough for stability studies. In fact, Fig. 2.15 – 2.17 show that the 2x2 model calculates the stability boundaries accurately; while Fig. 2.8 shows that the $\overrightarrow{TF_{PLL1+}}$ and $\overrightarrow{TF_{PLL2+}}$ alone predict the most relevant oscillations in the PLL response.

2.10.7 Conclusion of the comparison

The LTI and LTP models of two different DDSRF-PLL implementations in the presence of voltage imbalance have been derived. This chapter shows that, when the PLL directly tracks the negative-sequence phase-angle (method 1), the LTP terms depend on both V_p and V_n, separately. Thus, even if the voltage imbalance is low, the LTP dynamics are relevant and influence the stability of the PLL (due to V_p). The main consequence is that the LTI model cannot predict correctly the stability limit at any imbalance level. In contrast, when the PLL indirectly tracks the negative-sequence phase-angle (method 2), the LTP terms depend on

V_n only. Thus, when V_n is low enough (with respect to V_p) the LTI model predicts correctly the stability boundaries, although when V_n is increased, the LTP model is needed.

In general, the only model that can predict accurately the stability limit in all imbalance levels is the LTP model, no matter the DDSRF-PLL implementation. Further, this chapter shows with time domain simulations that, in order to capture the most relevant oscillations that occur in the PLL in the presence of imbalance, it is not necessary to include the coupling terms in the LTP model. In fact, it is shown that a 2x2 HTF matrix is enough for predicting the stability limit, although the order can always be increased to enhance accuracy.

2.11 Comparison of LTI and LTP models for harmonic studies

2.11.1 Interpretation of the models for harmonic analysis

In order to study the harmonic performance of a PLL, one key aspect is to find how distorted is the phase-angle signal as a consequence of a harmonic in the grid voltage. If the PLL models were SISO, the dynamics of each PLL would be defined by only one transfer function, and therefore, one way to assess their harmonic rejection capability would be to look at their transfer functions and their roll-off rates (i.e., their slope at high frequencies).

However, in an LTP model, several transfer functions are defined. The LTP model of method 1 for the positive-sequence phase-angle is copied here for easier reference (this is the same equation as (2.19)):

$$\begin{aligned}\Delta\theta_{1+} \approx\ & \overrightarrow{V_{\text{idealdq+}}}\overrightarrow{TF_{\text{PLL1+}}} + \overrightarrow{V^*_{\text{idealdq+}}}\overrightarrow{TF_{\text{PLL2+}}} \\ &+\overrightarrow{V_{\text{idealdq+}}}\overrightarrow{e^{j4\omega_1 t}}\overrightarrow{TF_{\text{PLL3+}}} + (\overrightarrow{V_{\text{idealdq+}}}\overrightarrow{e^{j4\omega_1 t}})^*\overrightarrow{TF_{\text{PLL4+}}} \\ &+\overrightarrow{V_{\text{idealdq+}}}\overrightarrow{e^{-j4\omega_1 t}}\overrightarrow{TF_{\text{PLL5+}}} + (\overrightarrow{V_{\text{idealdq+}}}\overrightarrow{e^{-j4\omega_1 t}})^*\overrightarrow{TF_{\text{PLL6+}}}\end{aligned} \tag{2.47}$$

where $\overrightarrow{TF_{\text{PLL2+}}(s)} = \overrightarrow{TF^*_{\text{PLL1+}}(s)}$, $\overrightarrow{TF_{\text{PLL4+}}(s)} = \overrightarrow{TF^*_{\text{PLL3+}}(s)}$ and also $\overrightarrow{TF_{\text{PLL6+}}(s)} = \overrightarrow{TF^*_{\text{PLL5+}}(s)}$. Note that $\overrightarrow{V^*_{\text{idealdq+}}}\overrightarrow{TF_{\text{PLL2+}}}$ is the conjugate of $\overrightarrow{V_{\text{idealdq+}}}\overrightarrow{TF_{\text{PLL1+}}}$; that the term $(\overrightarrow{V_{\text{idealdq+}}}\overrightarrow{e^{j4\omega_1 t}})^*\overrightarrow{TF_{\text{PLL4+}}}$ is the conjugate of $\overrightarrow{V_{\text{idealdq+}}}\overrightarrow{e^{j4\omega_1 t}}\overrightarrow{TF_{\text{PLL3+}}}$; and also that the term $(\overrightarrow{V_{\text{idealdq+}}}\overrightarrow{e^{-j4\omega_1 t}})^*\overrightarrow{TF_{\text{PLL6+}}}$ is the conjugate of $\overrightarrow{V_{\text{idealdq+}}}\overrightarrow{e^{-j4\omega_1 t}}\overrightarrow{TF_{\text{PLL5+}}}$.

The way to interpret this equation is as follows: if the grid voltage has a certain harmonic at a frequency ω_p, then the phase-angle will have several components that, expressed with space vectors, have the frequencies $\pm\omega_p$ and $\pm\omega_p \pm 4\omega_1$. These are 3 space vectors with 3 different frequencies, and their conjugates. This means that, in reality, when measuring the phase-angle signal, only 3 frequencies will be captured by the FFT: ω_p, $\omega_p + 4\omega_1$ and $\omega_p - 4\omega_1$.

This is explained subsequently. If there is a space-vector with the generic frequency ω, it can be represented as: $Ae^{j\omega t}$. If that space vector is summed to its conjugate, the result is: $Ae^{j\omega t} + Ae^{-j\omega t} = 2A\cos(\omega t)$. Therefore, if the LTP model gives that the phase-angle has a space-vector component at a frequency ω with an amplitude A, the model shows that the phase-angle will also have the space-vector component conjugate to it, and the end measurable result in the phase-angle will be a cosine with frequency ω and amplitude $2A$.

Similarly to the LTP model, the LTI model is defined by more than one transfer function. The LTI model of the DDSRF-PLL method 1 is repeated below for convenience (this is the same equation as (2.24)):

$$\Delta\theta_{1+} = \overrightarrow{V_{\text{idealdq+}}\overrightarrow{TF_{\text{PLL1+LTI}}}} + \overrightarrow{V^{*}_{\text{idealdq+}}\overrightarrow{TF_{\text{PLL2+LTI}}}} \tag{2.48}$$

Interpreting the space vectors in this model is the same as for the LTP model.

(a) Example

The voltage input to the PLL is:

- $V_{\text{p}} = V_{\text{nom}}$, $\phi_{\text{vp}} = 0°$.
- $V_{\text{n}} = 5\,\%$, $\phi_{\text{vn}} = 0°$.
- harmonic at $f_{\text{h}} = 150\,\text{Hz}$ (defined in the $dq+$ frame) with amplitude $V_{\text{h}} = 1\,\text{V}$, and $\phi_{\text{h}} = 0°$ (in space vector: $\overrightarrow{V_{\text{hdq+}}} = V_{\text{h}} e^{j(2\pi f_{\text{h}} t + \phi_{\text{h}})}$).

For the LTP model, it is necessary to calculate the PLL transfer functions for the specific positive and negative-sequence voltages (Fig. 2.18), and evaluate them at different frequencies. For the DDSRF-PLL method 1:

- $\overrightarrow{TF_{\text{PLL1+}}(s = j2\pi f_{\text{h}})} = \overrightarrow{TF_{\text{PLL1+}}(s = j2\pi 150)} = 0.0008\angle -169.2°$
- $\overrightarrow{TF_{\text{PLL3+}}(s = j2\pi(f_{\text{h}} + 4f_1))} = \overrightarrow{TF_{\text{PLL3+}}(s = j2\pi 350)} = 2.9\text{e}-05\angle -55°$
- $\overrightarrow{TF_{\text{PLL5+}}(s = j2\pi(f_{\text{h}} - 4f_1))} = \overrightarrow{TF_{\text{PLL5+}}(s = -j2\pi 50)} = 0.0005\angle -120.4°$

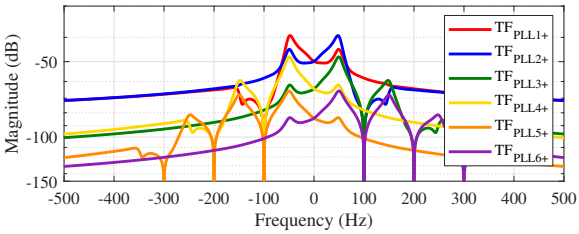

Figure 2.18: LTP transfer functions for method 1 in the example (M1, $V_{\text{n}} = 5\,\%$).

Therefore, according to the LTP model, the harmonics that will appear in $\Delta\theta_{1+}$ are:

- f_{h} (150 Hz): $2\overrightarrow{V_{\text{hdq+}}\overrightarrow{TF_{\text{PLL1+}}(s = j2\pi f_{\text{h}})}} = 0.0016\angle -169.2°$
- $f_{\text{h}} + 4f_1$ (350 Hz): $2\overrightarrow{V_{\text{hdq+}}\overrightarrow{TF_{\text{PLL3+}}(s = j2\pi(f_{\text{h}} + 4f_1))}} = 5.78\text{e}-05\angle -55°$
- $f_{\text{h}} - 4f_1$ (−50 Hz): $2\overrightarrow{V_{\text{hdq+}}\overrightarrow{TF_{\text{PLL5+}}(s = j2\pi(f_{\text{h}} - 4f_1))}} = 0.0011\angle -120.4°$

With respect to the LTI model, the results are:

- f_h (150 Hz): $2\overrightarrow{V_{\mathrm{hdq+}}\overrightarrow{TF_{\mathrm{PLL1+LTI}}(s=j2\pi f_\mathrm{h})}} = 0.0017\angle -167.8°$
- $f_\mathrm{h} + 4f_1$ (350 Hz): 0
- $f_\mathrm{h} - 4f_1$ (−50 Hz): 0

As it can be seen, according to the LTP model, the 150 Hz and the coupling at 50 Hz are expected to be the most visible in $\Delta\theta_{1+}$. These results are checked with time domain simulations, in which a harmonic at $f_{\mathrm{h}\alpha\beta} = 200$ Hz is injected in the voltage (150 Hz in the $dq+$ frame is 200 Hz in the $\alpha\beta$ frame). The results are shown in Fig. 2.19, where the time domain waveform clearly shows that the harmonic created due to f_h is similar in magnitude to one of the couplings. Further, the spectral analysis of the waveform shows that the magnitudes predicted by the LTP model are accurate. With respect to the LTI model, it predicts quite accurately the harmonic at 150 Hz (although not as precisely as the LTP model), but misses to predict the couplings.

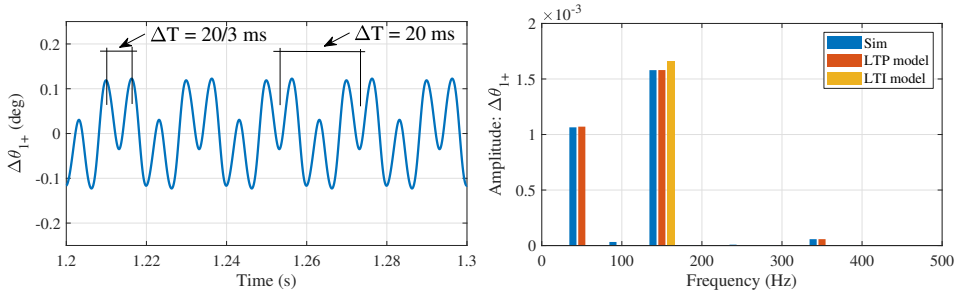

Figure 2.19: Method 1: Positive-sequence phase-angle error created due to a perturbation in the voltage at $f_{\mathrm{h}\alpha\beta} = 200$ Hz ($V_\mathrm{n} = 5\%$). The LTP model predicts the most important harmonics, including the couplings.

The analysis above is focused on $\Delta\theta_{1+}$. For the negative-sequence phase-angle, a similar analysis can be performed. The $f_{\mathrm{h}\alpha\beta} = 200$ Hz is expressed in the negative-sequence dq frame as 250 Hz, and therefore, the main harmonic will appear in $\Delta\theta_{1-}$ at 250 Hz with couplings at 50 Hz and 450 Hz. The calculations are not shown here for brevity, but in this case, the 450 Hz coupling is the one that turns out to be negligible, while the 50 Hz coupling appears with a similar magnitude as the 250 Hz component. In fact, the coupling at 50 Hz is in this case higher than the 250 Hz component. This is shown in Fig. 2.20. In this case, the LTI model predicts correctly the harmonic at the input frequency, but misses to predict the highest harmonic of all, which is due to a coupling.

In this section, the way to use the LTP and LTI models for harmonic analysis is presented. As a summary, the procedure for using the LTP model in this example is represented graphically in Fig. 2.21. In the next section, it is discussed how accurate is the LTI model in finding the component at f_h, and whether the frequency couplings are actually large enough to be included in the model for harmonic calculations.

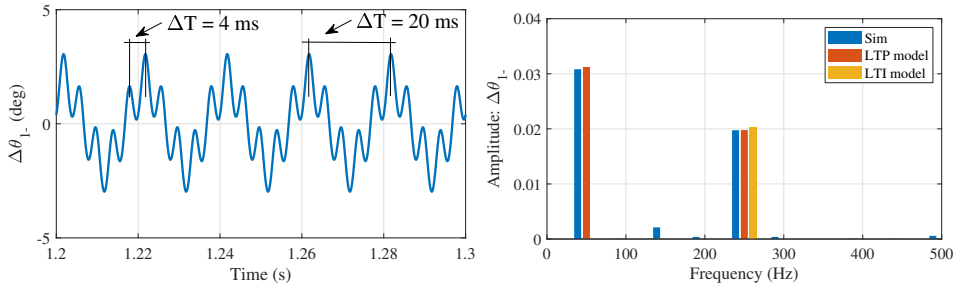

Figure 2.20: Method 1: Negative-sequence phase-angle error created due to a perturbation in the voltage at $f_{h\alpha\beta} = 200$ Hz ($V_n = 5\%$). The LTP model predicts the most important harmonics, including the couplings.

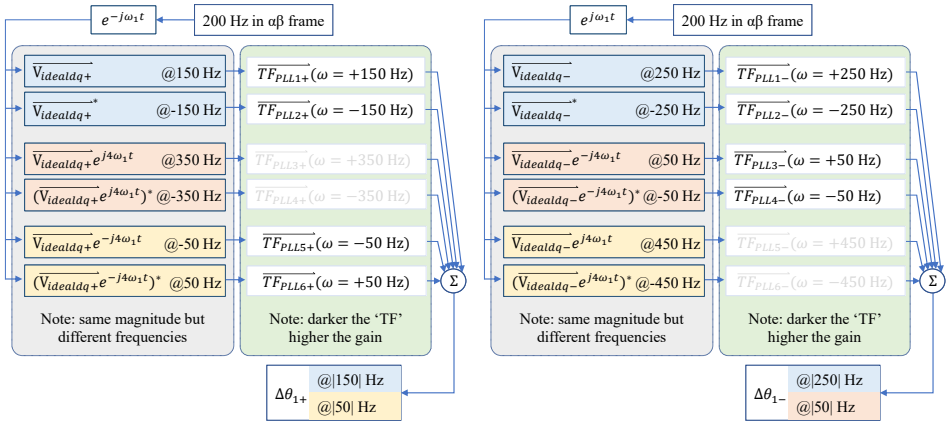

Figure 2.21: Method 1: Explanation of the couplings within the PLL due to a perturbation in the voltage at $f_{h\alpha\beta} = 200$ Hz ($V_n = 5\%$).

2.11.2 Comparison

(a) Accuracy at input harmonic frequency

The accuracy of the LTP model in predicting the harmonic at the input frequency is given by $\overrightarrow{TF}_{\text{PLL1}+}$ and by $\overrightarrow{TF}_{\text{PLL1}-}$. For the LTI model, it is important to look at $\overrightarrow{TF}_{\text{PLL1+LTI}}$ and $\overrightarrow{TF}_{\text{PLL1–LTI}}$. These transfer functions are plotted here for easier reference, although they can also be found in Fig. 2.6 and in Fig. 2.7.

As it can be seen, the LTP model perfectly matches the simulations, whereas the LTI model does not. This means that the LTI model will not be able to perfectly predict the harmonics that appear in the phase-angles at a frequency ω as a consequence of a perturbation in the voltage at a frequency ω. However, it is true that for a large set of frequencies, the LTI model is accurate. Especially, the LTI model can be seen to converge to the simulations specially for frequencies higher than (in absolute value) 200 Hz approximately. Since this is where the majority of the harmonics lay, it could be reasonable to use the LTI model for

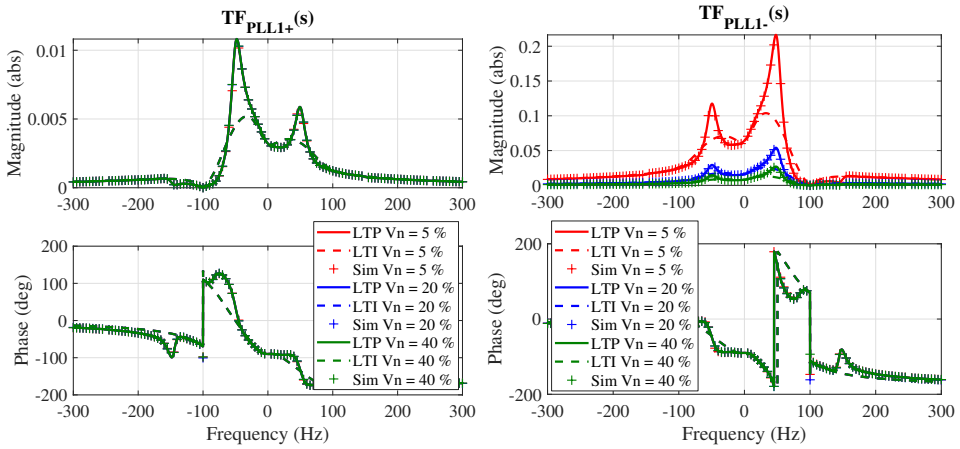

Figure 2.22: Method 1: model predictions of harmonics at input frequency.

harmonic analysis, if only the component at the input frequency is of interest.

(b) Importance of couplings

However, there are some frequencies in which the couplings cannot be ignored. The harmonics shown in Fig. 2.19 and Fig. 2.20 exemplify this. One method to find out if the couplings are relevant is to compare the main transfer function $\overrightarrow{TF_{\text{PLL1+}}}$ to the coupling transfer functions $\overrightarrow{TF_{\text{PLL3+}}}$ and $\overrightarrow{TF_{\text{PLL5+}}}$ at different frequencies (and the same for the negative-sequence transfer functions).

Performing the comparison using Fig. 2.18 is quite burdensome, since the transfer functions need to be evaluated at different frequencies. Therefore, it is more practical to represent the curves with a frequency shift. Additionally, it is very practical to shift the curves to the $\alpha\beta$ frame. The resulting transfer functions are shown in Fig. 2.24. For the particular example discussed before, the transfer functions need to be evaluated at 200 Hz. The same figure can be drawn for the DDSRF-PLL method 2, and it is shown in Fig. 2.25.

It can be seen that, for method 2, the couplings can also be relevant at certain frequencies, although not as much as for method 1. However, note that Fig. 2.24 and Fig. 2.25 only show the transfer functions for $V_{\text{n}} = 5\,\%$. As an example of what can occur if the imbalance is increased, Fig. 2.26 shows the same curves when the imbalance increases to $V_{\text{n}} = 60\,\%$. It can be seen that, depending on the imbalance level, the couplings can be relevant in one DDSRF-PLL method or both. The exact effect of the imbalance on the harmonic generation is assessed in Section 2.13.

2.11.3 Conclusion of the comparison

The above analysis shows that, if the voltage has a harmonic at a frequency ω, the LTI model can predict quite accurately the output harmonic at the same frequency. This is especially true for higher frequencies. However, for lower frequencies, the LTI model can be quite

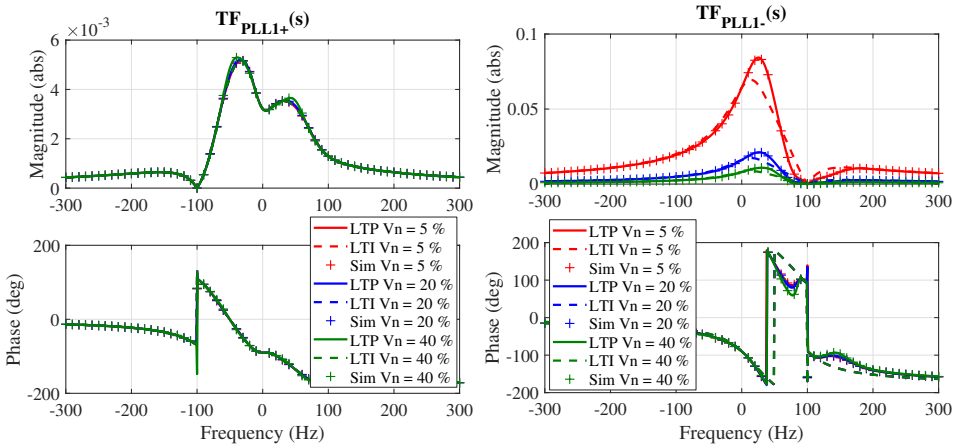

Figure 2.23: Method 2: model predictions of harmonics at input frequency.

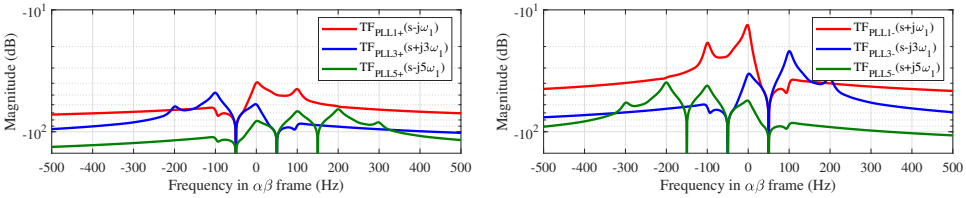

Figure 2.24: LTP functions relevant to the example, with a frequency shift to the $\alpha\beta$ frame (M1, $V_n = 5\,\%$).

inaccurate. Even more important, it has been shown that in certain occasions the coupling frequencies can be be equally high (or higher) than the harmonics at ω. This effect is not captured by the LTI model, but it can be perfectly predicted with the LTP model. In fact, the accuracy for the coupling transfer functions of the LTP model is shown for a whole range of frequencies in the frequency sweeps in Fig. 2.6 and Fig. 2.7.

Another question is whether the next coupling rounds ($\pm\omega \pm 8\omega_1$; etc.) should be considered for harmonic studies. In this thesis, these other rounds are not considered since, for method 1, $\overrightarrow{T_5}$ is always lower than 1 (not shown here for brevity), which means that each round of couplings will be smaller than the previous round (see (2.11) and Fig. 2.3). Similarly, $\overrightarrow{T_6}$ is always lower than 1, which invites to the same conclusion for method 2 (see (2.28)).

Finally, the LTP model is considered valid for harmonic analysis since, even if it is a linearised model (i.e., small-signal), the harmonics present in the grid voltage are expected to be relatively small in real applications, just like the perturbations used in order to create the frequency sweeps shown in Fig. 2.6 and Fig. 2.7.

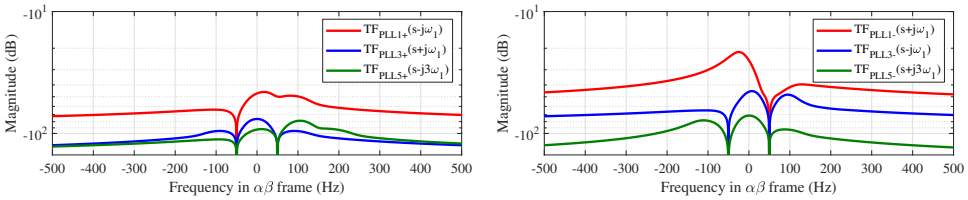

Figure 2.25: LTP functions relevant to the example, with a frequency shift to the $\alpha\beta$ frame (M2, $V_\mathrm{n} = 5\,\%$).

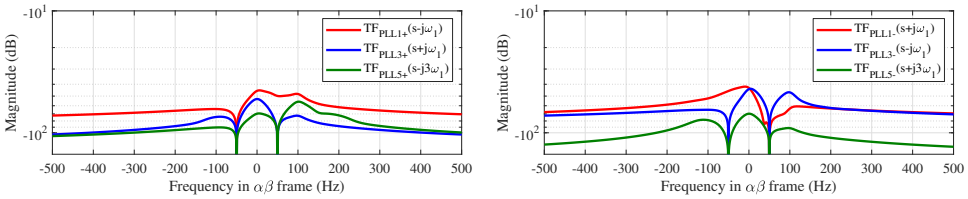

Figure 2.26: LTP functions relevant to the example, with a frequency shift to the $\alpha\beta$ frame (M2, $V_\mathrm{n} = 60\,\%$).

2.12 Effect of grid voltage imbalance on the stability of the DDSRF-PLL

2.12.1 Small-signal analysis

Section 2.10 shows how the LTP model is accurate in predicting the stability limit of both DDSRF-PLL methods for all levels of imbalance. This same model is used in this section to investigate the impact of voltage imbalance on the small-signal stability of the PLL.

The positive- and negative-sequence polemaps of method 1 when $K = 1/\sqrt{2}$ are shown in Fig. 2.27. First, it is noticeable that the pole map of method 1 (M1) does not change with V_n. This is due to the normalization block. If the normalization block is bypassed (in such a way that $v_{\mathrm{q}-}^{\mathrm{dec}}$ is directly fed into the PI), the polemaps vary with V_n, as shown in Fig. 2.28.

Further, when the normalization block is bypassed, the polemaps dangerously approach the $x = 0$ axis for certain values of imbalance (in particular, low values of imbalance). This effect can easily understood if the whole decoupling network is ignored, and only the SRF-PLLs are addressed. A small-signal model of a SRF-PLL is shown in Fig. 2.29. As seen here, the small-signal model depends on the voltage V that is being followed; for the positive-sequence PLL this would be V_p whereas for the negative-sequence PLL, if the normalization block is not used, it would be V_n. The SRF-PLL constants $K_{\mathrm{pPLL}-}$ and $K_{\mathrm{iPLL}-}$, however, are fixed and designed with respect to the nominal voltage of the converter. Therefore, the lower the voltage imbalance, the further that the input of the negative-sequence SRF-PLL is from the voltage value it has been designed for. This supports the fact that, in this DDSRF-PLL method in particular, the normalization block should always be used. In the case of method 2, a normalization block to make the PLL dynamics independent of V_n can also be devised [133], although this is not addressed here.

The eigenvalue plot of method 2 (Fig. 2.30) seems to move closer to $x = 0$ as the

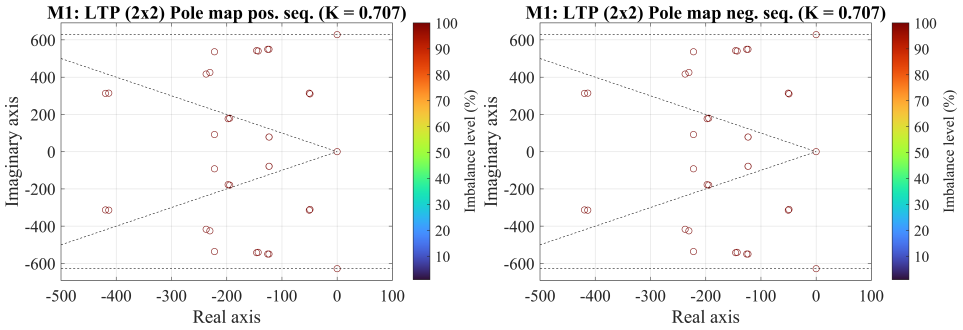

Figure 2.27: Method 1: pole map at different imbalance levels ($K = 1/\sqrt{2}$). The pole map shows the fundamental strip (y-axis: $[\frac{-\omega_p}{2} \frac{\omega_p}{2}]$ with $\omega_p = 2\omega_1$) and the $\zeta = 1/\sqrt{2}$ damping diagonals. The poles appear in one colour since, in this case, they do not vary with the voltage imbalance (i.e., the different colours in the map overlap).

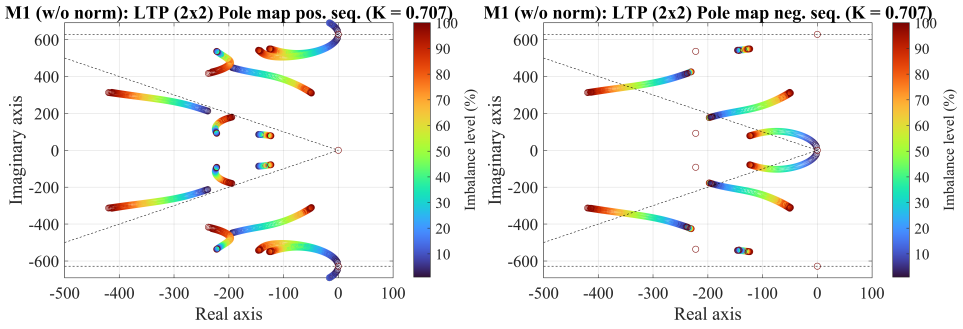

Figure 2.28: Method 1 (w/o norm): pole map at different imbalance levels ($K = 1/\sqrt{2}$). The pole map shows the fundamental strip (y-axis: $[\frac{-\omega_p}{2} \frac{\omega_p}{2}]$ with $\omega_p = 2\omega_1$) and the $\zeta = 1/\sqrt{2}$ damping diagonals.

imbalance level increases. In other words, the stability margin of method 2 depends on the operating point, and worsens with the imbalance.

An interesting issue here is to compare the stability margin of both methods. In this thesis, the property selected to determine how far a system is from instability is the damping ratio, since it is a concept widely used in practice [143]. In particular, for each V_n level, the pole with the worst damping[8] can be located, and the worst-damping ratio can be plotted vs. the imbalance level.

This is done in Fig. 2.31 for method 1 and in Fig. 2.32 for method 2. As expected, the worst pole damping in method 1 is independent of the imbalance level. However, it can be seen that the damping of method 1 is worse than in method 2 for all imbalance levels, except for really high values of imbalance (that seem unrealistic in practical applications).

[8] In [141] it was shown that the concept of pole damping can be generalized to an LTP system, with the only difference that only the poles in the fundamental strip need to be analysed.

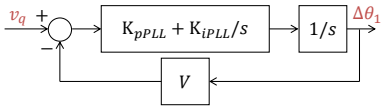

Figure 2.29: Small-signal model of a SRF-PLL when tracking a positive- or a negative-sequence phase-angle.

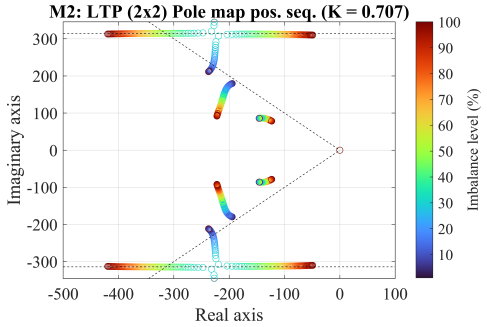

Figure 2.30: Method 2: pole map at different imbalance levels ($K = 1/\sqrt{2}$). The pole map shows the fundamental strip (y-axis: $[\frac{-\omega_p}{2} \frac{\omega_p}{2}]$ with $\omega_p = \omega_1$) and the $\zeta = 1/\sqrt{2}$ damping diagonals.

2.12.2 Large-signal analysis

(a) Limitations of the small-signal model

The DDSRF-PLL is a non-linear system and, therefore, its global stability cannot be guaranteed by assessing the stability around a specific operating point with a linear model. However, an accurate linear model can predict local stability, which is a pre-requisite for global stability. In this sense, the LTP has been shown to be small-signal accurate in Section 2.10 and in the time domain verifications of Test 1 and Test 2 in Section 2.8. In other words, if the LTP model shows instability at a certain operating point, the PLL is expected to be unstable at that operating point, although if the LTP model shows stability, the stability of the PLL is not ensured.

In particular, the LTP model is expected to predict accurately the stability condition if there is a small perturbation around the operating point. Since the objective of this section is to address the effect of imbalance, a question arises as to whether a sudden voltage imbalance (for example, due to a fault) can be considered small-signal. For low voltage imbalance levels, indeed it is believed to be the case; although for large values of V_n, this might not be the case. Indeed, it was shown in Fig. 2.4 and Fig. 2.5 that the LTP model does not perfectly predict the transient behaviour of the PLL when there is a big imbalance step. Nevertheless, this is a common issue with small-signal models, and still they are useful in providing understanding about the stability behaviour of the system and its stability boundaries.

(b) Transient performance against a sudden imbalance

In order to assess the transient performance of the DDSRF-PLL methods against a sudden imbalance, different simulations are performed in which, when the DDSRF-PLL is in

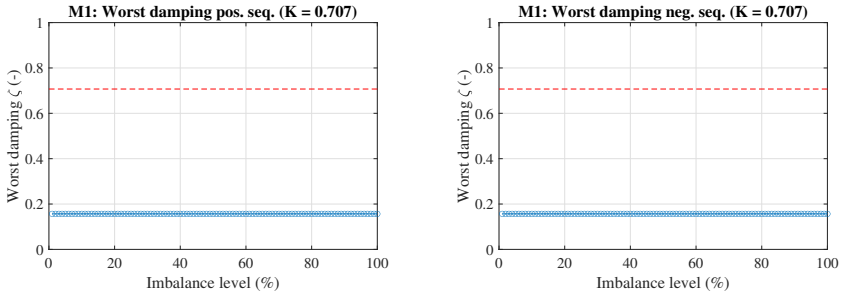

Figure 2.31: Method 1: worst damping ζ at different imbalance levels ($K = 1/\sqrt{2}$). The dotted line shows the $\zeta = 1/\sqrt{2}$ damping.

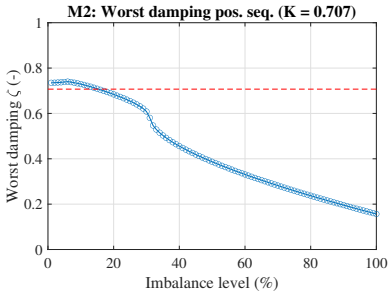

Figure 2.32: Method 2: worst damping ζ at different imbalance levels ($K = 1/\sqrt{2}$). The dotted line shows the $\zeta = 1/\sqrt{2}$ damping.

steady-state and has long converged to the positive-sequence voltage, a specific level of V_{n} is injected as a step. The following variables are monitored:

$$\begin{aligned} \Delta\theta_{1+} &= \theta_{\mathrm{PLL}+} - \theta_{1+} \\ \Delta\theta_{1-} &= \theta_{\mathrm{PLL}-} - \theta_{1-} \\ \Delta V_{\mathrm{p}} &= V_{\mathrm{pPLL}} - V_{\mathrm{p}} \\ \Delta V_{\mathrm{n}} &= V_{\mathrm{nPLL}} - V_{\mathrm{n}} \end{aligned} \tag{2.49}$$

where $\Delta\theta_{1+}$ is the error in the positive-sequence phase-angle, $\Delta\theta_{1-}$ is the error in the negative-sequence phase-angle, ΔV_{p} is the error in positive-sequence magnitude, and ΔV_{n} is the error in negative-sequence magnitude. The time that the PLL takes to converge is stored, being the converging limits for ΔV_{p} and ΔV_{n} defined as 1% of the nominal voltage, and as 1° for $\Delta\theta_{1+}$ and $\Delta\theta_{1-}$. The results for method 1 are shown in Fig. 2.33 and in Fig. 2.34 for method 2.

Fig. 2.33 shows that $\theta_{\mathrm{PLL}-}$ might take longer to converge than $\theta_{\mathrm{PLL}+}$, since the negative-sequence phase angle is independently tracked. This phenomenon is not as strong in method 2, since only θ_{1+} is being followed, and once the PLL converges to this phase angle, all the signals in the network have to eventually converge too.

Also, Fig. 2.34 shows that method 2 takes longer to converge if V_{n} is high than when V_{n}

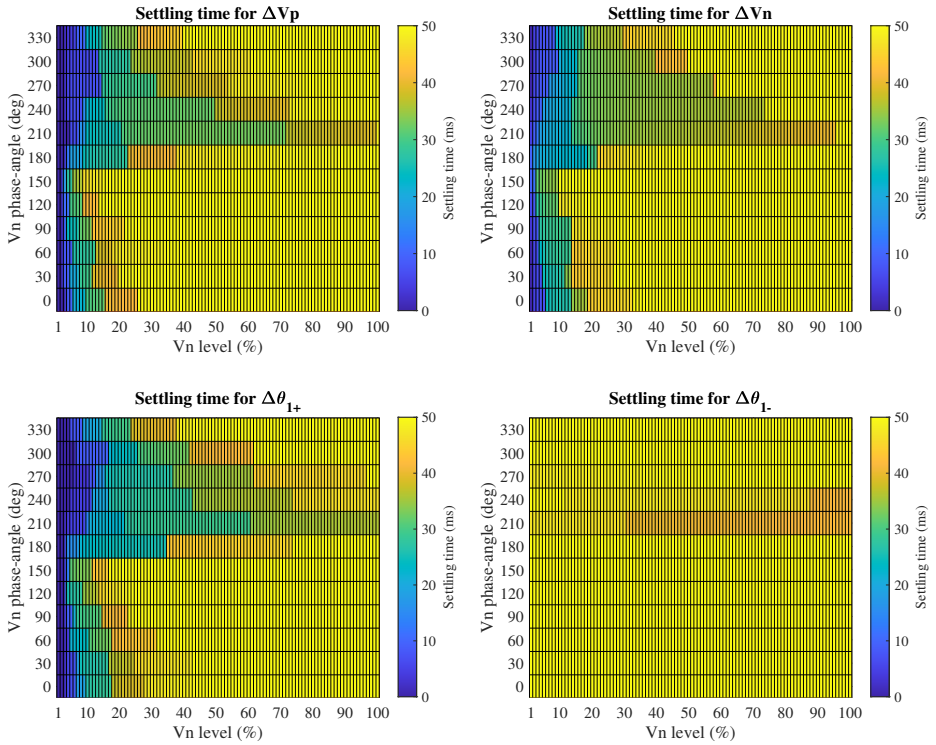

Figure 2.33: Method 1: Transient performance against imbalance ($K = 1/\sqrt{2}$).

is low, which makes sense since in this method V_{n} acts as a disturbance, and therefore, the higher the disturbance the higher the settling time. Another way to see it is that, the higher the V_{n}, the lower the stability margin is (Fig. 2.30 and Fig. 2.32), and therefore the more oscillatory the time response for method 2 is (causing a higher settling time).

The maximum settling time of both methods is shown in Table 2.1 for the cases in which all the imbalance levels are considered ($V_{\mathrm{n}} = 0 - 100\%$), and for the case in which only lower voltage imbalance levels are considered ($V_{\mathrm{n}} = 0 - 60\%$). This table confirms what it is shown with the small-signal stability analysis: method 1 has a consistent performance among imbalance levels, while method 2 is better for lower V_{n} than higher V_{n}.

Finally, when comparing Fig. 2.33 and Fig. 2.34, it appears that method 1 is much slower than method 2. This is not always necessarily the case, as this depends on the parameters design. In order to make a fair comparison, both PLLs should have been designed optimally. This is, however, left out of the scope of this thesis. However, just as an example, Table 2.1 shows that by only lowering the K on method 1 from $K = 1/\sqrt{2}$ to $K = 0.45$, the performance is already considerably improved and it is comparable with such of method 2. In this specific scenario, it is clear that, if all imbalance levels are considered, method 1 performs better. However, if only low imbalance levels are considered, method 2 is faster.

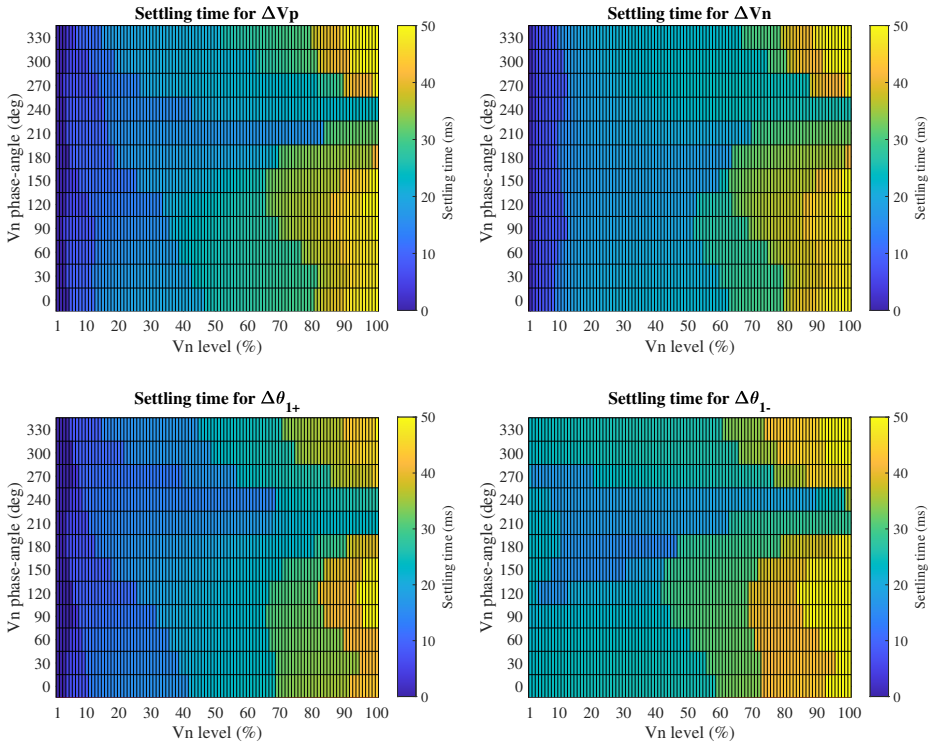

Figure 2.34: Method 2: Transient performance against imbalance ($K = 1/\sqrt{2}$).

Table 2.1: Performance against imbalance: maximum convergence time (ms)

		Until $V_n = 100\%$				Until $V_n = 60\%$			
	K	$\Delta\theta_{1+}$	$\Delta\theta_{1-}$	ΔV_p	ΔV_n	$\Delta\theta_{1+}$	$\Delta\theta_{1-}$	ΔV_p	ΔV_n
Method 1	0.70711	84.4	88.4	87.6	88.0	74.8	88.4	77.7	80.6
Method 1	0.45	44.1	43.2	45.0	53.4	39.2	43.2	41.4	50.6
Method 2	0.70711	53.4	60.2	55.3	55.4	24.8	32.1	27.2	27.6

2.13 Effect of grid voltage imbalance on the harmonic rejection of the DDSRF-PLL

In order to study the harmonic performance of a PLL, one key aspect is to find how distorted is the phase-angle as a result of a harmonic in the voltage. As explained in Section 2.11, for a voltage harmonic at f_h, the magnitude of the harmonics in the positive phase-angle in M1, are given by: $2|\overrightarrow{TF_{PLL1+}(s=j2\pi f_h)}|$, $2|\overrightarrow{TF_{PLL3+}(s=j2\pi(f_h+4f_1))}|$, and $2|\overrightarrow{TF_{PLL5+}(s=j2\pi(f_h-4f_1))}|$. If these frequencies are to be considered in the $\alpha\beta$ frame, a frequency shift is to be performed as well.

The Total Harmonic Distortion (THD) is typically defined in an AC system as the root-mean square of the magnitude of the different harmonics, divided by the magnitude of the fundamental. In the case analysed here, there is no fundamental frequency in the signal $\Delta\theta_{1+}$. However, the root-mean square of the magnitude of the different harmonics can be a good measure of the total distortion of the signal. Therefore, the Total Distortion (TD) is defined in this thesis as such, and it is the quantity that is used in order to assess the effect of the grid voltage imbalance on the output harmonics.

For the DDSRF-PLL method 1, and for an input frequency f_h in the $\alpha\beta$ frame, the TD when tracking $\Delta\theta_{1+}$ can be calculated as:

$$\mathrm{TD}_{M1+}(s) = 2\left(|\overrightarrow{TF_{PLL1+}(s-j\omega_1)}|^2 + |\overrightarrow{TF_{PLL3+}(s+j3\omega_1)}|^2 + |\overrightarrow{TF_{PLL5+}(s-j5\omega_1)}|^2\right)^{0.5}. \quad (2.50)$$

When tracking $\Delta\theta_{1-}$, the TD can be calculated as:

$$\mathrm{TD}_{M1-}(s) = 2\left(|\overrightarrow{TF_{PLL1-}(s+j\omega_1)}|^2 + |\overrightarrow{TF_{PLL3-}(s-j3\omega_1)}|^2 + |\overrightarrow{TF_{PLL5-}(s+j5\omega_1)}|^2\right)^{0.5}. \quad (2.51)$$

For the DDSRF-PLL method 2, the total distortions are calculated as follows:

$$\mathrm{TD}_{M2+}(s) = 2\left(|\overrightarrow{TF_{PLL1+}(s-j\omega_1)}|^2 + |\overrightarrow{TF_{PLL3+}(s+j\omega_1)}|^2 + |\overrightarrow{TF_{PLL5+}(s-j3\omega_1)}|^2\right)^{0.5} \quad (2.52)$$

$$\mathrm{TD}_{M2-}(s) = 2\left(|\overrightarrow{TF_{PLL1-}(s+j\omega_1)}|^2 + |\overrightarrow{TF_{PLL3-}(s-j\omega_1)}|^2 + |\overrightarrow{TF_{PLL5-}(s+j3\omega_1)}|^2\right)^{0.5}. \quad (2.53)$$

The total distortions are plotted for different values of V_n in Fig. 2.35 and Fig. 2.36. For method 1, the distortion that appears in $\Delta\theta_{1+}$ does not depend on V_n. When tracking $\Delta\theta_{1-}$, the lower the imbalance level is, the higher is the distortion in the phase-angle signal when a harmonic appears in the voltage. This is easily explained with the LTI model: when

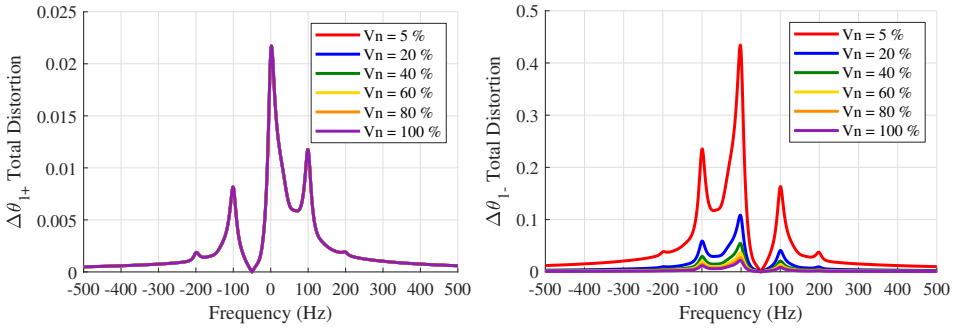

Figure 2.35: Method 1: on the left, Total Distortion (TD) when tracking the positive-sequence phase-angle for different imbalance levels, as in (2.50). On the right, Total Distortion (TD) when tracking the negative-sequence phase-angle for different imbalance levels, as in (2.51).

looking at (2.46) it can be seen that due to the normalization the imbalance does not change the dynamics of the system (pole placement) but it does affect the gain of the system.

With respect to method 2, the voltage imbalance changes the distortion that appears in $\Delta\theta_{1+}$ when there is a harmonic in the voltage. This is mostly due to the frequency couplings: in Fig. 2.7 it can be seen how $\overrightarrow{TF_{\text{PLL}1+}}$ is mostly constant with V_{n}; however, the coupling transfer functions change considerably with it. Still, Fig. 2.36 shows that, for the usual harmonic frequencies, the harmonic distortion is not very dependent on the imbalance. When tracking $\Delta\theta_{1-}$, the distortion is very dependent on V_{n}. Similarly to method 1, this is due to the change in the gain of the system, which can be easily visualized in the LTI model in (2.36).

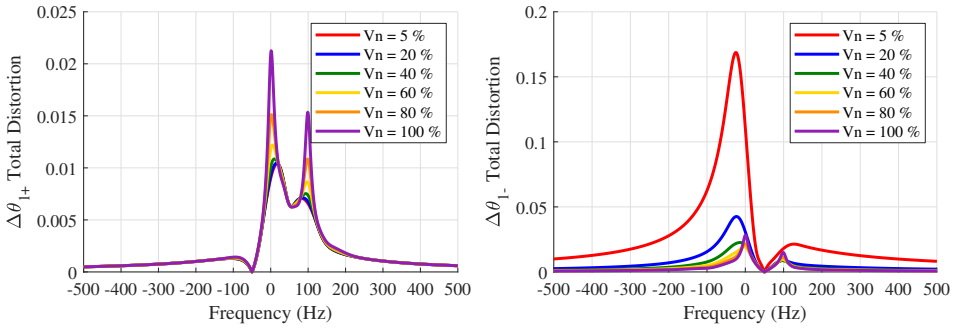

Figure 2.36: Method 2: on the left, Total Distortion (TD) when tracking the positive-sequence phase-angle for different imbalance levels, as in (2.52). On the right, Total Distortion (TD) when tracking the negative-sequence phase-angle for different imbalance levels, as in (2.53).

Finally, by looking at the y-axis limits of Fig. 2.35 and Fig. 2.36 it is shown that, for several imbalance levels, the distortion in $\Delta\theta_{1-}$ is expected to be much higher than in $\Delta\theta_{1+}$.

All these conclusions are clearly shown with time domain simulations in Fig. 2.37 (M1)

Table 2.2: Harmonics injected

Harmonic order	Magnitude[a] (%)
2nd	2%
4th	1%
5th	5%
7th	4%
11th	3%
13th	3%

[a] These values are selected as in [135] and are just indicative.

and in Fig. 2.38 (M2). In this simulations, once the DDSRF-PLL signals have converged to the positive- and negative-sequence voltage, several harmonics are injected at $t = 1\,\text{s}$. The list of the harmonics injected and their magnitude are shown in Table 2.2 and have been selected as it was done in [135]. The harmonics have been injected in their natural sequence. The total THD of the signal is 8%.

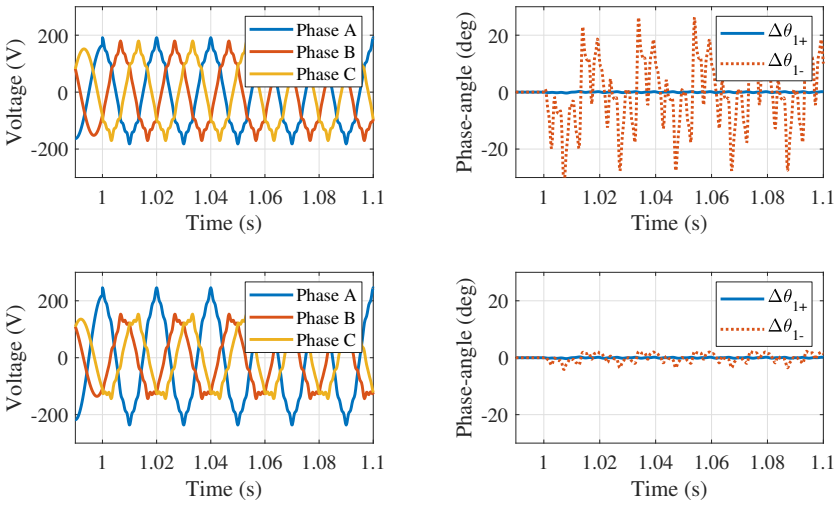

Figure 2.37: Method 1: For the same distorted voltage, the distortion when tracking the negative-sequence phase angle ($\Delta\theta_{1-}$) is higher than when tracking the positive-sequence phase angle ($\Delta\theta_{1+}$) and depends on V_n.

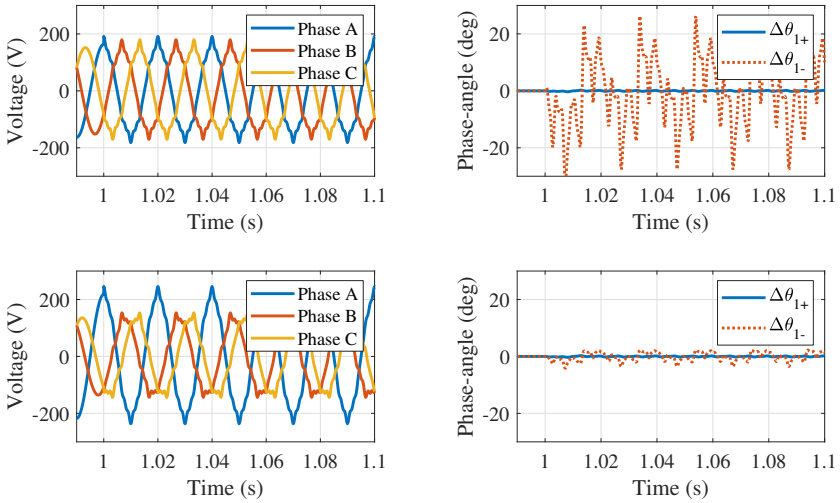

Figure 2.38: Method 2: For the same distorted voltage, the distortion when tracking the negative-sequence phase angle ($\Delta\theta_{1-}$) is higher than when tracking the positive-sequence phase angle ($\Delta\theta_{1+}$) and depends on V_n.

2.14 Conclusions

A significant portion of this chapter has been focused in analysing which type of model (LTI vs LTP) is suitable for studying stability and harmonic emission in two implementations of the DDSRF-PLL. For both purposes, the LTP model gives more accurate results, specially in stability studies where the LTI sometimes misses largely the stability limit. In harmonic studies, the LTI gives realistic results, although it is incapable of modelling the frequency coupling dynamics which in some cases are dominant (e.g. Fig. 2.20).

At the end of the chapter (Section 2.12), the LTP model is used to assess the effect of grid voltage imbalance on the stability of the PLL. For the DDSRF-PLL method 1, it is shown here how the LTP poles move with the changing imbalance level, although this effect can be completely eliminated with the use of voltage normalization. With respect to the DDSRF-PLL method 2, the LTP poles move, in general, closer to instability as the imbalance increases. These small-signal results affect the transient performance of the DDSRF-PLL: the lower the damping of the poles, the more oscillatory the response is, and therefore the longer the DDSRF-PLL takes to converge. As a consequence, method 2 becomes slower as the imbalance increases, although it is overall faster than method 1.

Finally, this chapter has also assessed the effect of grid voltage imbalance on the harmonic generation by the PLL (Section 2.13). For tracking the positive-phase angle the voltage imbalance has not a significant effect. For tracking the negative-sequence, however, the imbalance level acts as an inverse gain in the system, meaning that the lower the imbalance level, the higher the amplification of the harmonics through the PLL.

Chapter 3

Harmonic Stability
Part 2 – Converter Modelling and Analysis

In this chapter, different small-signal models of a wind turbine converter are developed in the presence of voltage and current imbalance. The models are verified with simulations and validated experiments, and are then compared in their suitability to perform accurate harmonic stability studies and distortion calculations. It is found that the influence of the negative-sequence voltage is important not only due to its impact on the PLL dynamics (Chapter 2) but also due to its impact on the currents generated by the converter, which depend on the current-reference strategy. The combination of both the PLL structure and current-reference strategy provokes a very different effect of the negative sequence voltage on the passivity and harmonic stability of the grid-connected converter. This is important in the current context in which different current-reference strategies are being developed to meet the newest grid codes that require very specific responses of the wind turbine converters in the negative and positive sequence in the case of a fault. Finally, the influence of imbalance on the converter model for harmonic studies is also addressed.

This chapter is based on:

- L. Beloqui Larumbe, Z. Qin, L. Wang, and P. Bauer, "Impedance modelling for three-phase inverters with double synchronous reference frame current controller in the presence of imbalance," *IEEE Transactions on Power Electronics*, vol. 37, no. 2, pp. 1461–1475, 2022.

3.1 Introduction

With the rise of renewable energies, distributed-power generation, microgrids and other applications, the penetration of power-electronic converters (PECs) has notably increased in recent years. As a result, PECs have a growing impact on the power quality and stability of power systems [144], having caused several incidents as reported in [16, 19, 26, 145].

In this context, small-signal models of converters and, in particular, impedance models of converters [43, 84, 104, 136, 146, 147], have been proven to be a useful tool for system-wide stability [148, 149], power quality [C6] and resonance studies [113, C1]. When modelling converters, most of the literature assumes a balanced grid (e.g. [84, 104, 136]). However, negative-sequence voltages can appear during transient situations (for example, during faults) and, even, during normal operation [150] due to single-phase or two-phase loads [39, 151–154], single-phase sources [155–157], cables in non-symmetrical arrangements (like flat formation), line asymmetries and lack of line transposition [158], mutual coupling effects between transformer windings, and other causes. In particular, large-scale wind or solar farms are usually connected at remote locations through relatively long untransposed lines [111] (e.g. [36]). Although voltage imbalance is usually relatively high in low voltage or medium voltage grids [159], it may also appear to a certain extent in HV grids due to, for example, railway connectees[1] [39, 151, 160, 161]. Therefore, a small-signal converter model that takes into account the negative-sequence can be useful for stability evaluations and steady-state harmonic calculations in many situations. Specifically, wind turbine converters are required to show adequate performance (which, naturally includes being small-signal stable) in all imbalance levels.

However, developing a converter small-signal model in the presence of imbalance is not a trivial task. Under the balanced-grid assumption, despite being a time-variant AC system, it is possible to find a time-invariant operating point of many converter topologies if the equations are taken to the dq frame[2], where traditional linearisation around an operating point can be undertaken [84]. Nevertheless, when the grid is unbalanced, this is not possible, since the negative-sequence voltage introduces a component at $100\,\text{Hz}$ in the positive-sequence dq frame. In other words, there is no single reference frame in which all the signals remain constant [139]. This posses a challenge when linearising the converter. This chapter belongs to a growing body of literature [139, 162] that addresses the challenge.

In [43], harmonic linearisation is used to assess the impact of voltage imbalance on the converter model; where the imbalance is characterized as a source of coupling between the positive and negative-sequence impedance of the converter. Later, it was found that the coupling essentially appears between two frequencies (e.g. f_p and $2f_1 - f_\text{p}$) [59]. The coupling has been shown to happen due to several reasons, such as control asymmetries in the dq channels [125]. In [162], the Harmonic Transfer Function (HTF) approach is used to model the converter when confronted with imbalance; however, while [162] considers the couplings created due to the asymmetrical grid, the couplings that appear within the PLL due to the Linear Time Periodic (LTP) dynamics created by the negative sequence are ignored. Within this context, this chapter compares different converter models (using an LTP PLL

[1] This is specially relevant due to the electrification trend in train systems in many countries.

[2] This is true, for example, for two-level converters although not necessarily true for all converter topologies; for example, for Modular-Multilevel Converters (MMC).

model, an LTI PLL model, and considering or not the converter coupling admittances) to see which ones are adequate for stability analysis in the presence of imbalance.

Additionally, the current controller also influences the model of the converter. In order to achieve Low Voltage Ride Through (LVRT) capabilities, several current control approaches were developed in the past, and are reviewed in [163]. This thesis is focused in one strategy called double Synchronous Reference Frame (SRF) current controller or dual current control [44], which is based on creating two dq frames, one rotating with the positive-sequence voltage and the other rotating with the negative-sequence voltage. This controller is a common choice by the industry, it is well known and has been extensively implemented [31, 120, 164, 165].

The main attractiveness of the controller is that there is a direct relationship between the active and reactive power with the dq components, for which it is necessary to track the phase-angle of both the positive- and negative sequence voltages [163, C3]. There are several PLL options that can track the positive-sequence voltage [166]. However, merely a few can quickly and accurately track the negative sequence, among which the Decoupled Double SRF-PLL (DDSRF-PLL) [137] is applied in this thesis. In particular, the DDSRF-PLL method 1 and method 2 analysed in Chapter 2 are considered. Some small-signal models of converters with this type of current controller are already available in the literature; however, either the effect of the PLL dynamics is ignored [32] or a simple SRF-PLL design is assumed [167, C4]. Further, the effect of imbalance is overlooked.

Finally, this chapter also addresses the impact of the negative-sequence current. In the past, several works addressed the effect of the positive-sequence current reference [84] and concluded that it has a direct impact on the stability of the converter; however, the impact of the negative-sequence current has not been analysed in the literature before. In this chapter, the current imbalance level is also addressed and it is found to significantly impact the converter harmonic stability. Note that, in the presence of voltage imbalance, it is a common strategy to inject a specific set of unbalanced currents in order to eliminate the 100 Hz ripple in the instantaneous power, achieving a smoother DC voltage [46]. In parallel, a growing tendency is to design the control objectives from the grid point of view, instead of the converter point of view (i.e. in order to provide effective grid support). For this purpose, it has been shown that both sequence currents should be injected during voltage imbalance and, in fact, the injection of dual currents during unbalanced faults is a requirement that is slowly appearing explicitly in grid codes [45]. In short, it is reasonable to assume that current imbalance will accompany voltage imbalance. The analysis in this chapter shows that, the impact of voltage imbalance is not important only because of its influence on the PLL dynamics, but also because it encourages the injection of current imbalance, which significantly impacts the passivity of the converter.

To sum up, in this chapter, a small-signal model is built up for three-phase inverters with double synchronous reference frame current controller. The effect of the PLL dynamics, the grid voltage and current imbalance are all taken into account. This chapter is organized as follows: Section 3.2 describes the converter under study, Section 3.3 models the converter in the frequency domain ignoring the PLL dynamics, and Section 3.4 presents the model of the converter considering the PLL dynamics. Subsequently, this generic converter model is then adapted to include specifically the DDSRF-PLL method 1 and method 2 presented in Chapter 2 (Section 3.5 and Section 3.6, respectively). The model is then verified with

computer-based simulations and validated experiments (Section 3.7 and Section 3.8, respectively). Then, the different converter models are compared in their ability to perform small-signal stability analysis (Section 3.10) and harmonic studies (Section 3.11). Finally, Section 3.12 analyses the effect that the voltage and current imbalance (including different current-reference strategies) have on the passivity and small-signal stability of the grid-connected converter. The effect of imbalance on harmonic performance of the converter is shown in Section 3.13, and conclusions are summarized in Section 3.14.

3.2 Inverter description

The PEC is shown in Fig. 3.1. It consists of a two-level voltage-source inverter controlled by a current loop and a PLL. The PLL follows the phase-angle of the positive-sequence voltage ($\theta_{1+} = \omega_1 t + \phi_{vp}$) and of the negative-sequence voltage ($\theta_{1-} = -\omega_1 t - \phi_{vn}$), defined in (2.1). The outputs of the PLL are θ_{PLL+} and θ_{PLL-}, which, as explained in Chapter 2, in a dynamic situation might not be exactly equal to θ_{1+} and θ_{1-}. Specifically, it is considered here: $\theta_{PLL+} = \theta_{1+} + \Delta\theta_{1+}$ and $\theta_{PLL-} = \theta_{1-} + \Delta\theta_{1-}$.

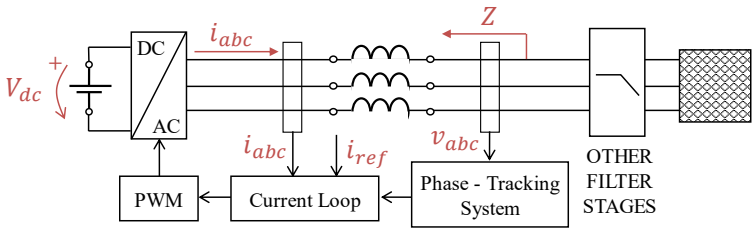

Figure 3.1: Schematic of the inverter under study.

The converter filter is an inductor L with a resistance R_L. The objective is to calculate the impedance of the inverter Z (see Fig. 3.1). Other filter stages can be added a posteriori to Z with linear circuit theory. The reference, i_{ref}, comes either from a user-defined command or from an outer control loop, and depends on the current-reference strategy.

The current controller is shown in Fig. 3.2. The positive and negative-sequence currents, after a low-pass filter (LPF), G_i, and sequence decoupling, are fed to two typical PI controllers ($H_i = K_p + \frac{K_i}{s}$) in their corresponding dq frames, respectively. A dq decoupling constant K_d (which is usually selected as $L\omega_1$) is implemented too. A voltage feed-forward loop is assumed, where an anti-aliasing filter G_v and a LPF, H_{ff}, are used. To prevent the risk of an infinite system gain caused by the voltage feed-forward loop [165], the cut-off frequency of the H_{ff} is limited to 0.5 Hz, as recommended in [168].

The control and modulation delays are modelled as $G_d(s) = e^{-s1.5/f_s}$, where f_s is the sampling frequency. The negative-sequence current can be filtered from the positive-sequence and vice versa through different methods. In here, a Sequence Component Decoupling Network (SCDN) similar to such in [163] is implemented. This network is shown in Fig. 3.3, where $F(s)$ is a LPF with a cut-off frequency ω_f (i.e., $F(s) = \frac{\omega_f}{s+\omega_f}$).

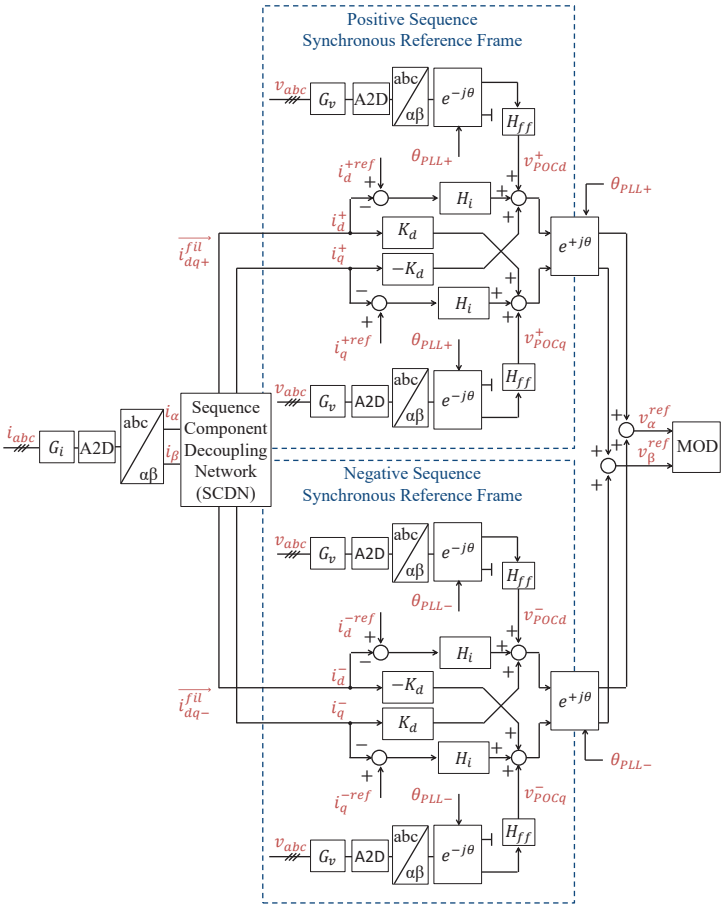

Figure 3.2: Double Synchronous Reference Frame controller.

Literature shows that there are other options in order to achieve positive- and negative-sequence current decoupling, for example by using schemes in the $\alpha\beta$ frame [169]. On the one hand, the SCDN shown in Fig. 3.3 uses different dq transformations that make the SCDN dependent on the phase-tracking dynamics. In comparison, the $\alpha\beta$-frame schemes do not use this type of transformations. However, on the other hand, the $\alpha\beta$-frame schemes usually use SOGI-based algorithms, which require frequency adaptation. Therefore, the comparison in between these two approaches is not straightforward, and it is left out of the scope of this thesis. In fact, the comparison of dq-based or $\alpha\beta$-based approaches for sequence decoupling could also be a subject for debate when implementing the synchronization algorithm.

In this thesis, since the current loop was selected as a double synchronous reference frame control, which requires using the positive- and negative-sequence phase-angles, it was decided to choose a synchronizing structure that follows the phase-angle instead of

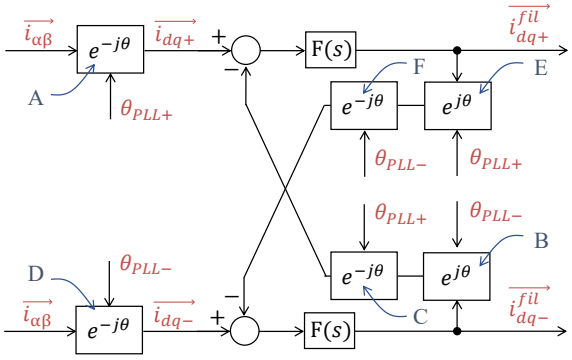

Figure 3.3: Sequence Component Decoupling Network (SCDN).

the frequency (i.e. a PLL instead of a Frequency-Locked Loop or FLL). Literature has shown that the DDSRF-PLL and the SOGI-based PLL present similar performance during imbalance conditions [135]. The former was selected since the approach is more consistent with the current control selected. The decoupling network for the current was chosen analogously, and also due to the fact that this combination of decoupling network with this current control structure has already been proven to present good dynamic performance [163].

3.3 Small-signal model ignoring PLL dynamics

3.3.1 SCDN when ignoring PLL dynamics

As a first approximation, it is assumed that the PLL has perfect tracking (i.e. $\theta_{\text{PLL}+} = \theta_{1+}$ and $\theta_{\text{PLL}-} = \theta_{1-}$). Then, from Fig. 3.3:

$$\begin{aligned}\overrightarrow{i^{\text{fil}}_{\text{dq}+}} &= (\overrightarrow{i_{\text{dq}+}} - \overrightarrow{i^{\text{fil}}_{\text{dq}-}} e^{-j(\theta_{1+}-\theta_{1-})})F(s) \\ \overrightarrow{i^{\text{fil}}_{\text{dq}-}} &= (\overrightarrow{i_{\text{dq}-}} - \overrightarrow{i^{\text{fil}}_{\text{dq}+}} e^{j(\theta_{1+}-\theta_{1-})})F(s).\end{aligned} \tag{3.1}$$

Operating it is possible to obtain:

$$\overrightarrow{i^{\text{fil}}_{\text{dq}+}} = F(s) \underbrace{\frac{1 - F(s + j2\omega_1)}{1 - F(s)F(s + j2\omega_1)}}_{\overrightarrow{G_{\text{dq}+}(s)}} \overrightarrow{i_{\text{dq}+}}. \tag{3.2}$$

The function $\overrightarrow{G_{\text{dec}+}(s)} = F(s)\overrightarrow{G_{\text{dq}+}(s)}$ relates the input current expressed in the positive dq frame, which has positive- and negative-sequence components, with the $\overrightarrow{i^{\text{fil}}_{\text{dq}+}}$ (the positive-sequence current expressed in the positive dq frame which does not contain the negative-sequence component). $\overrightarrow{G_{\text{dq}+}(s)}$ only depends on one parameter, ω_{f}, which is usually set as $\omega_{\text{f}} = K\omega_1 = \omega_1/\sqrt{2}$ or lower, to prevent oscillations. $\overrightarrow{G_{\text{dq}+}(s)}$ has a real and an imaginary part as $\overrightarrow{G_{\text{dq}+}(s)} = G_{\text{re}}(s) + jG_{\text{im}}(s)$ defined in (2.7) and (2.8). Similarly, $\overrightarrow{i^{\text{fil}}_{\text{dq}-}} = \overrightarrow{G_{\text{dec}-}(s)}\overrightarrow{i_{\text{dq}-}} = F(s)\overrightarrow{G_{\text{dq}-}(s)}\overrightarrow{i_{\text{dq}-}}$, where $\overrightarrow{G_{\text{dq}-}(s)} = \overrightarrow{G^*_{\text{dq}+}(s)} = G_{\text{re}}(s) - jG_{\text{im}}(s)$.

3.3.2 Complete model when ignoring PLL dynamics

If the PLL dynamics are neglected, the inverter can be represented by the diagram in Fig. 3.4, where $Y_{\mathrm{L}}(s) = 1/(Ls + R_{\mathrm{L}})$. In this case, taking all the complex transfer functions in the rotating frames into the $\alpha\beta$-frame is an easy procedure, since only a frequency shift has to be applied [125]. For example, the PI controller in the positive-sequence dq frame becomes $H_{\mathrm{i}}(s-j\omega_1)$ in the $\alpha\beta$-frame, and the PI in the negative-sequence dq frame becomes $H_{\mathrm{i}}(s+j\omega_1)$ in the $\alpha\beta$-frame.

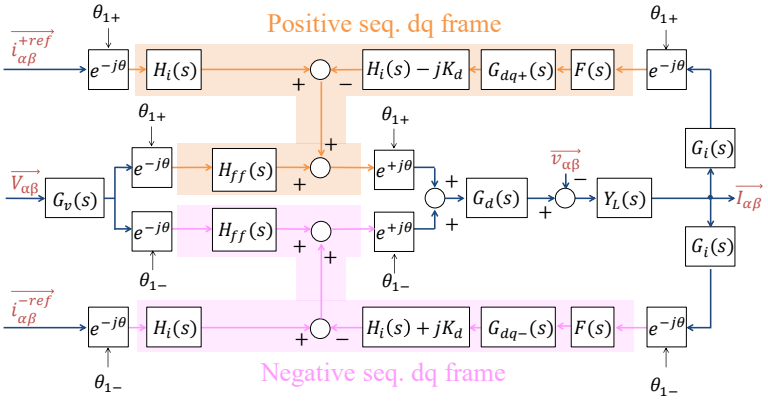

Figure 3.4: Inverter schematic ignoring the PLL dynamics.

The response of the system can be analysed from Fig. 3.4 by finding the transfer function from each input to the output considering that the other inputs are zero. In this case, there are 3 inputs: the two current references (one for the positive SRF and one for the negative SRF) and the voltage. In the analysis below the contribution of the voltage due to the feedforward signal (related to $\overrightarrow{TF_3}$) has been separated from the contribution of the voltage due to the inner characteristics of the plant (related to $\overrightarrow{TF_4}$), leading to:

$$\overrightarrow{I_{\alpha\beta}} = \overrightarrow{TF_1}\overrightarrow{I^{+\mathrm{ref}}_{\alpha\beta}} + \overrightarrow{TF_2}\overrightarrow{I^{-\mathrm{ref}}_{\alpha\beta}} + \overrightarrow{TF_3}\overrightarrow{V_{\alpha\beta}} + \overrightarrow{TF_4}\overrightarrow{V_{\alpha\beta}}. \tag{3.3}$$

It can be seen that $\overrightarrow{TF_1}$ and $\overrightarrow{TF_2}$ are the closed-loop transfer functions of the positive and the negative sequence current; while $-\overrightarrow{TF_4}$ is the output admittance ($\overrightarrow{Y_{\mathrm{p}}}$). Finally, $-\overrightarrow{TF_3}$ is the additional admittance in parallel to $-\overrightarrow{TF_4}$ that is created due to the voltage feed-forward compensation ($\overrightarrow{Y_{\mathrm{ff}}}$). Their expressions are shown (3.4)-(3.7). The impedance of the converter is shown in (3.8) and (3.9). Some of the overhead arrows in (3.4) – (3.9) are omitted for convenience.

$$\begin{aligned}\overrightarrow{TF_1} = \Big\{H_{\mathrm{i}}(s-j\omega_1)G_{\mathrm{d}}(s)\Big\}\Big\{Ls + R_{\mathrm{L}} + \Big([H_{\mathrm{i}}(s-j\omega_1) - jK_{\mathrm{d}}]G_{\mathrm{dec+}}(s-j\omega_1) \\ +[H_{\mathrm{i}}(s+j\omega_1) + jK_{\mathrm{d}}]G_{\mathrm{dec-}}(s+j\omega_1)\Big)G_{\mathrm{i}}(s)G_{\mathrm{d}}(s)\Big\}^{-1}\end{aligned} \tag{3.4}$$

$$\overrightarrow{TF_2} = \Big\{H_\mathrm{i}(s+j\omega_1)G_\mathrm{d}(s)\Big\}\Big\{Ls + R_\mathrm{L} + \Big([H_\mathrm{i}(s-j\omega_1) - jK_\mathrm{d}]G_{\mathrm{dec+}}(s-j\omega_1) + [H_\mathrm{i}(s+j\omega_1) + jK_\mathrm{d}]G_{\mathrm{dec-}}(s+j\omega_1)\Big)G_\mathrm{i}(s)G_\mathrm{d}(s)\Big\}^{-1} \tag{3.5}$$

$$\overrightarrow{Y_\mathrm{p}} = -\overrightarrow{TF_4} = \Big\{Ls + R_\mathrm{L} + \Big([H_\mathrm{i}(s-j\omega_1) - jK_\mathrm{d}]G_{\mathrm{dec+}}(s-j\omega_1) + [H_\mathrm{i}(s+j\omega_1) + jK_\mathrm{d}]G_{\mathrm{dec-}}(s+j\omega_1)\Big)G_\mathrm{i}(s)G_\mathrm{d}(s)\Big\}^{-1} \tag{3.6}$$

$$\overrightarrow{Y_\mathrm{ff}} = -\overrightarrow{TF_3} = \Big\{[H_\mathrm{ff}(s-j\omega_1) + H_\mathrm{ff}(s+j\omega_1)]G_\mathrm{v}(s)G_\mathrm{d}(s)\Big\}\Big\{Ls + R_\mathrm{L} + \Big([H_\mathrm{i}(s-j\omega_1) - jK_\mathrm{d}]G_{\mathrm{dec+}}(s-j\omega_1) + [H_\mathrm{i}(s+j\omega_1) + jK_\mathrm{d}]G_{\mathrm{dec-}}(s+j\omega_1)\Big)G_\mathrm{i}(s)G_\mathrm{d}(s)\Big\}^{-1} \tag{3.7}$$

$$\overrightarrow{Z_{\mathrm{noPLL}}} = \frac{1}{\overrightarrow{Y_{\mathrm{noPLL}}}} = \frac{1}{\overrightarrow{Y_\mathrm{p}} + \overrightarrow{Y_\mathrm{ff}}} \tag{3.8}$$

$$\overrightarrow{Z_{\mathrm{noPLL}}} = \frac{1}{\overrightarrow{Y_{\mathrm{noPLL}}}} = \Big\{Ls + R_\mathrm{L} + \Big([H_\mathrm{i}(s-j\omega_1) - jK_\mathrm{d}]G_{\mathrm{dec+}}(s-j\omega_1) + [H_\mathrm{i}(s+j\omega_1) + jK_\mathrm{d}]G_{\mathrm{dec-}}(s+j\omega_1)\Big)G_\mathrm{i}(s)G_\mathrm{d}(s)\Big\}\Big\{1 + [H_\mathrm{ff}(s-j\omega_1) + H_\mathrm{ff}(s+j\omega_1)]G_\mathrm{v}(s)G_\mathrm{d}(s)\Big\}^{-1} \tag{3.9}$$

In the end, the converter small-signal model when ignoring the PLL dynamics can be found in Fig. 3.5, where the expressions for $G_{\mathrm{cl+}}$ and $G_{\mathrm{cl-}}$ are found in (3.4) and (3.5), and the impedance expression is (3.9).

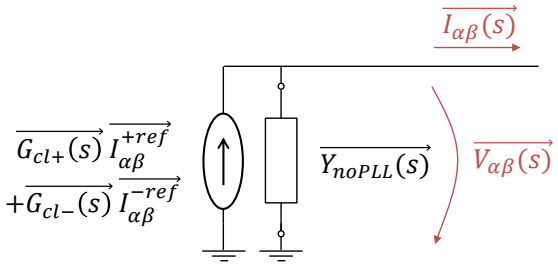

Figure 3.5: Small-signal model of the converter ignoring the PLL dynamics. It considers the closed-loop transfer functions of the current control in both sequences ($G_{\mathrm{cl+}}$ and $G_{\mathrm{cl-}}$) and the main converter impedance/admittance (Y_{noPLL}).

(a) Converter impedance at high frequencies

Whenever there is no voltage feedback loop (i.e. $H_{\mathrm{ff}} = 0$), the impedance of the converter is equal to its output inductor ($Ls + R_{\mathrm{L}}$) plus some additional terms that depend on the control design. These additional terms have a low-pass characteristic, which is directly reinforced by the current anti-aliasing filter $G_{\mathrm{i}}(s)$. Due to this low-pass characteristic, the impedance model will inevitable converge to the impedance of the output inductor for high-enough frequencies.

(b) Converter impedance for the positive and negative sequence

Finally, note that $[H_{\mathrm{i}}(s - j\omega_1) - jK_{\mathrm{d}}]G_{\mathrm{dec+}}(s - j\omega_1)$ is the complex conjugate of $[H_{\mathrm{i}}(s + j\omega_1) + jK_{\mathrm{d}}]G_{\mathrm{dec-}}(s + j\omega_1)$. Since the sum of a complex transfer function and its conjugate leads to a real transfer function, the denominators of (3.4)-(3.7) have real coefficients; and the numerators of (3.6) and (3.7) too. Thus, $\overrightarrow{G_{\mathrm{cl1}}}$ and $\overrightarrow{G_{\mathrm{cl2}}}$ remain complex transfer functions whereas $\overrightarrow{Y_{\mathrm{p}}}$ and $\overrightarrow{Y_{\mathrm{ff}}}$ are real transfer functions (i.e. $\overrightarrow{Y_{\mathrm{p}}} = Y_{\mathrm{p}}$ and $\overrightarrow{Y_{\mathrm{ff}}} = Y_{\mathrm{ff}}$). One important feature of real transfer functions is that their frequency response for negative frequencies is the same as for positive frequencies; which is not true for complex transfer functions.

If the dynamics of the phase-tracking system are ignored, the converter has no inter-sequence couplings and the converter has the same frequency response for the positive and negative sequences. In this case, whenever the whole system is analysed, the sequences can be analysed separately[3] and for both sequences the impedance in (3.9) can be used to represent the converter. This is a clear simplification from the power system's perspective in comparison to using the full 3x3 admittance matrix that is necessary to represent the converter in the abc-frame.

In contrast, if the controller uses only one dq frame, even if the dynamics of the phase-tracking system are ignored, the literature shows that the converter's impedance is a complex transfer function [43], and thus the converter has a different response in both sequences (as seen in the results of [43]).

3.4 Small-signal model including PLL dynamics

This section addresses the impact that the PLL dynamics have on the current control $\alpha\beta$-to-dq transformations (or vice versa). The currents in the time domain are shown in (3.10). As explained in the introduction, in this thesis the negative-sequence currents are considered too, since it is typical to inject I_{n} in the presence of voltage imbalance.

$$\begin{aligned} i_{\mathrm{a}}(t) &= I_{\mathrm{p}}\cos(\omega_1 t + \phi_{\mathrm{ip}}) + I_{\mathrm{n}}\cos(\omega_1 t + \phi_{\mathrm{in}}) \\ i_{\mathrm{b}}(t) &= I_{\mathrm{p}}\cos(\omega_1 t + \phi_{\mathrm{ip}} - \frac{2\pi}{3}) + I_{\mathrm{n}}\cos(\omega_1 t + \phi_{\mathrm{in}} + \frac{2\pi}{3}) \\ i_{\mathrm{c}}(t) &= I_{\mathrm{p}}\cos(\omega_1 t + \phi_{\mathrm{ip}} - \frac{4\pi}{3}) + I_{\mathrm{n}}\cos(\omega_1 t + \phi_{\mathrm{in}} + \frac{4\pi}{3}) \end{aligned} \tag{3.10}$$

[3] Assuming that the rest of the system also does not present inter-sequence couplings.

3.4.1 SCDN when including PLL dynamics

The effect of the DDSRF-PLL on the filtered currents $\overrightarrow{i^{\text{fil}}_{\text{dq+}}}$ and $\overrightarrow{i^{\text{fil}}_{\text{dq−}}}$ has to be addressed. In order to do that, the SCDN needs to be analysed in the same way as it was done for the DDSRF-PLL in Chapter 2. That is to say, the transformations A, B, C, D, E and F in Fig. 3.3 need to be analysed separately. Following this method, this equation is obtained:

$$\overrightarrow{i^{\text{fil}}_{\text{dq+}}} = \overrightarrow{G_{\text{dec+}}(s)}\left(\overrightarrow{I_{\text{idealdq+}}} - jI_{\text{p}}e^{j(\phi_{\text{ip}}-\phi_{\text{vp}})}\Delta\theta_{1+} - jI_{\text{n}}e^{-j(\phi_{\text{in}}+\phi_{\text{vp}})}e^{-2j\omega_1 t}\Delta\theta_{1-}\right). \quad (3.11)$$

$\overrightarrow{i^{\text{fil}}_{\text{dq+}}}$ is the signal injected in the current loop (see Fig. 3.2). Note that this expression is equal to (3.2) but with additional components that show the effect of the phase-tracking error. A similar expression can be found for $\overrightarrow{i^{\text{fil}}_{\text{dq−}}}$. Note in (3.11) that the $\overrightarrow{i^{\text{fil}}_{\text{dq+}}}$ depends on both $\Delta\theta_{1+}$ and $\Delta\theta_{1-}$.

3.4.2 Complete model when including PLL dynamics

The rest of the frame transformations can be modelled using (3.12) (and the negative-sequence version of (3.12)) which leads to the inverter small-signal model shown in Fig. 3.6.

$$\begin{aligned} e^{-j\theta_{\text{PLL+}}} &= e^{-j\theta_{1+}}e^{-j\Delta\theta_{1+}} \approx e^{-j\theta_{1+}}(1 - j\Delta\theta_{1+}) \\ e^{j\theta_{\text{PLL+}}} &= e^{j\theta_{1+}}e^{j\Delta\theta_{1+}} \approx e^{j\theta_{1+}}(1 + j\Delta\theta_{1+}) \end{aligned} \quad (3.12)$$

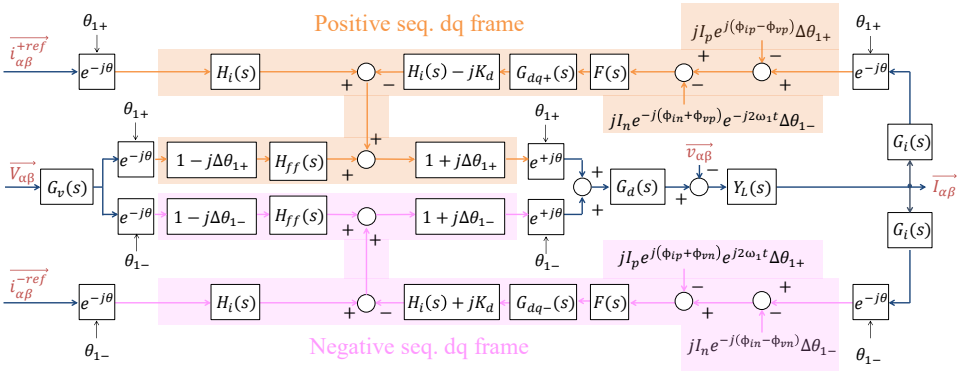

Figure 3.6: Inverter schematic considering the PLL dynamics.

Now, the expressions for $\Delta\theta_{1+}$ and $\Delta\theta_{1-}$ developed in Chapter 2 can be plugged in Fig. 3.6 to obtain the complete model. The specific expressions of $\Delta\theta_{1+}$ and $\Delta\theta_{1-}$ depend on whether the DDSRF-PLL method 1 or method 2 is to be used; and also depending on whether it is desired to use the LTI or LTP PLL model.

3.5 Inverter model using DDSRF-PLL method 1

3.5.1 Using the LTP model of the DDSRF-PLL

In this case, the expressions for $\Delta\theta_{1+}$ and $\Delta\theta_{1-}$ to be plugged in Fig. 3.6 are the LTP expressions derived for method 1, which are (2.19) and (2.20), respectively. By doing this, it can be seen that the PLL dynamics, through $\Delta\theta_{1+}$ and $\Delta\theta_{1-}$, introduce in the current control the voltage vector $\overrightarrow{V_{\alpha\beta}}$ conjugated, frequency shifted or both. This means that, for a single frequency component in $\overrightarrow{V_{\alpha\beta}}$, multiple frequency components will appear in the current, phenomenon that is usually called converter frequency coupling. Some of these frequency couplings, however, may be ignored due to their low magnitude. The detailed reasoning for this is provided in Section 3.9.3. In the end, two main frequency couplings appear in the converter: one through $\overrightarrow{V^*_{\alpha\beta}}e^{j2\omega_1 t}$ and one through $\overrightarrow{V^*_{\alpha\beta}}e^{-j2\omega_1 t}$.

Therefore, from Fig. 3.6, the following equation is obtained:

$$\begin{aligned}\overrightarrow{I_{\alpha\beta}} = \overrightarrow{TF_1}\overrightarrow{I^{+\text{ref}}_{\alpha\beta}} + \overrightarrow{TF_2}\overrightarrow{I^{-\text{ref}}_{\alpha\beta}} + \overrightarrow{TF_3}\overrightarrow{V_{\alpha\beta}} + \overrightarrow{TF_4}\overrightarrow{V_{\alpha\beta}} + \overrightarrow{TF_5}\overrightarrow{V_{\alpha\beta}} + \overrightarrow{TF_6}\overrightarrow{V_{\alpha\beta}} \\ + \overrightarrow{TF_7}\overrightarrow{V^*_{\alpha\beta}}e^{j2\omega_1 t} + \overrightarrow{TF_8}\overrightarrow{V^*_{\alpha\beta}}e^{-j2\omega_1 t}.\end{aligned} \tag{3.13}$$

In Fig. 3.6, it is shown how extra inputs of $\overrightarrow{V_{\alpha\beta}}$ appear due to $\Delta\theta_{1+}$. These contributions are grouped in $\overrightarrow{TF_5}$. Similarly, the extra inputs of $\overrightarrow{V_{\alpha\beta}}$ that appear due to $\Delta\theta_{1-}$ are grouped in $\overrightarrow{TF_6}$. The effect of $\overrightarrow{TF_5}$ and $\overrightarrow{TF_6}$ is to add admittances in parallel to the total admittance of the converter (see (3.14)). Thus, the final impedance of the converter taking into account the phase-tracking system dynamics can be calculated with (3.15). The expressions for $\overrightarrow{TF_5}$ and $\overrightarrow{TF_6}$ are not shown for brevity, but the final expression for the converter impedance is shown in (3.16), where the terms $\overrightarrow{A(s)}$ and $\overrightarrow{B(s)}$ are defined in (3.17) and (3.18).

$$\overrightarrow{Y_{\text{PLL}+}(s)} = -\overrightarrow{TF_5}\,;\ \overrightarrow{Y_{\text{PLL}-}(s)} = -\overrightarrow{TF_6} \tag{3.14}$$

$$\vec{Z} = \frac{1}{\overrightarrow{Y(s)}} = \frac{1}{\overrightarrow{Y_{\text{p}}} + \overrightarrow{Y_{\text{ff}}} + \overrightarrow{Y_{\text{PLL}+}} + \overrightarrow{Y_{\text{PLL}-}}} \tag{3.15}$$

$$\begin{aligned}\vec{Z} = \frac{1}{\overrightarrow{Y(s)}} = \Big\{Ls + R_{\text{L}} + \Big([H_{\text{i}}(s-j\omega_1) - jK_{\text{d}}]G_{\text{dec}+}(s-j\omega_1) \\ + [H_{\text{i}}(s+j\omega_1) + jK_{\text{d}}]G_{\text{dec}-}(s+j\omega_1)\Big)G_{\text{i}}(s)G_{\text{d}}(s)\Big\} \\ \Big\{1 + [H_{\text{ff}}(s-j\omega_1) + H_{\text{ff}}(s+j\omega_1)]G_{\text{v}}(s)G_{\text{d}}(s) \\ -\overrightarrow{A(s)}\overrightarrow{TF_{\text{PLL1}+}(s-j\omega_1)}G_{\text{d}}(s) - \overrightarrow{B(s)}\overrightarrow{TF_{\text{PLL1}-}(s+j\omega_1)}G_{\text{d}}(s)\Big\}^{-1}\end{aligned} \tag{3.16}$$

$$\begin{aligned}\overrightarrow{A(s)} = jI_{\text{p}}e^{j(\phi_{\text{ip}}-\phi_{\text{vp}})}[H_{\text{i}}(s-j\omega_1) - jK_{\text{d}}]G_{\text{dec}+}(s-j\omega_1) \\ + jI_{\text{p}}e^{j(\phi_{\text{ip}}-\phi_{\text{vp}})}[H_{\text{i}}(s+j\omega_1) + jK_{\text{d}}]G_{\text{dec}-}(s+j\omega_1) \\ - jV_{\text{p}}H_{\text{ff}}(s-j\omega_1)G_{\text{v}}(s) + j(I_{\text{p}}e^{j(\phi_{\text{ip}}-\phi_{\text{vp}})}(R_{\text{L}} + jL\omega_1) + V_{\text{p}})\end{aligned} \tag{3.17}$$

$$\begin{aligned}\overrightarrow{B(s)} = {} & jI_{\mathrm{n}}e^{-j(\phi_{\mathrm{in}}-\phi_{\mathrm{vn}})}[H_{\mathrm{i}}(s+j\omega_1)+jK_{\mathrm{d}}]G_{\mathrm{dec-}}(s+j\omega_1) \\ & +jI_{\mathrm{n}}e^{-j(\phi_{\mathrm{in}}-\phi_{\mathrm{vn}})}[H_{\mathrm{i}}(s-j\omega_1)-jK_{\mathrm{d}}]G_{\mathrm{dec+}}(s-j\omega_1) \\ & -jV_{\mathrm{n}}H_{\mathrm{ff}}(s+j\omega_1)G_{\mathrm{v}}(s)+j(I_{\mathrm{n}}e^{-j(\phi_{\mathrm{in}}-\phi_{\mathrm{vn}})}(R_{\mathrm{L}}-jL\omega_1)+V_{\mathrm{n}})\end{aligned} \tag{3.18}$$

Note that the converter impedance when tacking into account the PLL has the same components as in (3.9) and (3.8), plus some additional components that depend on the PLL transfer functions. In (3.13), the vectors $\overrightarrow{V^*_{\alpha\beta}}e^{j2\omega_1 t}$ and $\overrightarrow{V^*_{\alpha\beta}}e^{-j2\omega_1 t}$ are related to the output current through $\overrightarrow{TF_7}$ and $\overrightarrow{TF_8}$, that are the negated version of the coupling admittances, shown in (3.19) and (3.20). Some overhead arrows in (3.16) – (3.20) are omitted for simplicity.

$$\begin{aligned}\overrightarrow{Y_{\mathrm{c1}}} = {} & \Big\{\Big(-\overrightarrow{A(s)TF_{\mathrm{PLL2+}}(s-j\omega_1)}e^{j2\phi_{\mathrm{vp}}} \\ & -\overrightarrow{B(s)TF_{\mathrm{PLL4-}}(s+j\omega_1)}e^{-j2\phi_{\mathrm{vn}}}\Big)G_{\mathrm{d}}(s)\Big\} \\ & \Big\{Ls+R_{\mathrm{L}}+\Big([H_{\mathrm{i}}(s-j\omega_1)-jK_{\mathrm{d}}]G_{\mathrm{dec+}}(s-j\omega_1) \\ & +[H_{\mathrm{i}}(s+j\omega_1)+jK_{\mathrm{d}}]G_{\mathrm{dec-}}(s+j\omega_1)\Big)G_{\mathrm{i}}(s)G_{\mathrm{d}}(s)\Big\}^{-1}\end{aligned} \tag{3.19}$$

$$\begin{aligned}\overrightarrow{Y_{\mathrm{c2}}} = {} & \Big\{\Big(-\overrightarrow{B(s)TF_{\mathrm{PLL2-}}(s+j\omega_1)}e^{-j2\phi_{\mathrm{vn}}} \\ & -\overrightarrow{A(s)TF_{\mathrm{PLL4+}}(s-j\omega_1)}e^{j2\phi_{\mathrm{vp}}}\Big)G_{\mathrm{d}}(s)\Big\} \\ & \Big\{Ls+R_{\mathrm{L}}+\Big([H_{\mathrm{i}}(s-j\omega_1)-jK_{\mathrm{d}}]G_{\mathrm{dec+}}(s-j\omega_1) \\ & +[H_{\mathrm{i}}(s+j\omega_1)+jK_{\mathrm{d}}]G_{\mathrm{dec-}}(s+j\omega_1)\Big)G_{\mathrm{i}}(s)G_{\mathrm{d}}(s)\Big\}^{-1}\end{aligned} \tag{3.20}$$

Therefore, the converter small-signal model when considering the PLL dynamics of the DDSRF-PLL method 1 can be found in Fig. 3.7, where the expressions for $G_{\mathrm{cl+}}$ and $G_{\mathrm{cl-}}$ are found in (3.4) and (3.5), the impedance expression is (3.16) and the coupling admittances are (3.19) and (3.20).

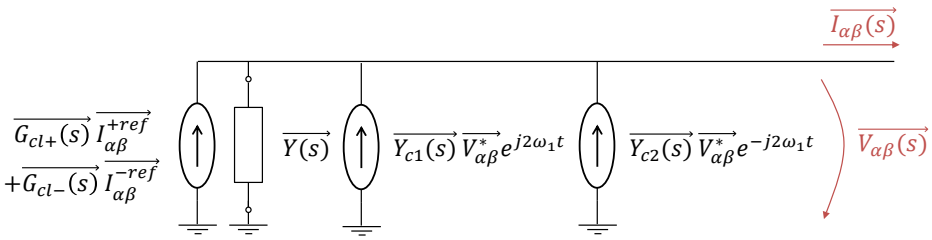

Figure 3.7: Small-signal model of the converter taking into account the PLL dynamics. It considers the closed-loop transfer functions of the current control in both sequences ($G_{\mathrm{cl+}}$ and $G_{\mathrm{cl-}}$), the main converter impedance/admittance (Y) and the two main frequency couplings (Y_{c1} and Y_{c2}).

In previous literature [104], it was already shown how the PLL dynamics may produce a frequency coupling through $\overrightarrow{V^*_{\alpha\beta}}e^{j2\omega_1 t}$ (i.e., for a perturbation in the voltage f_{p} the current

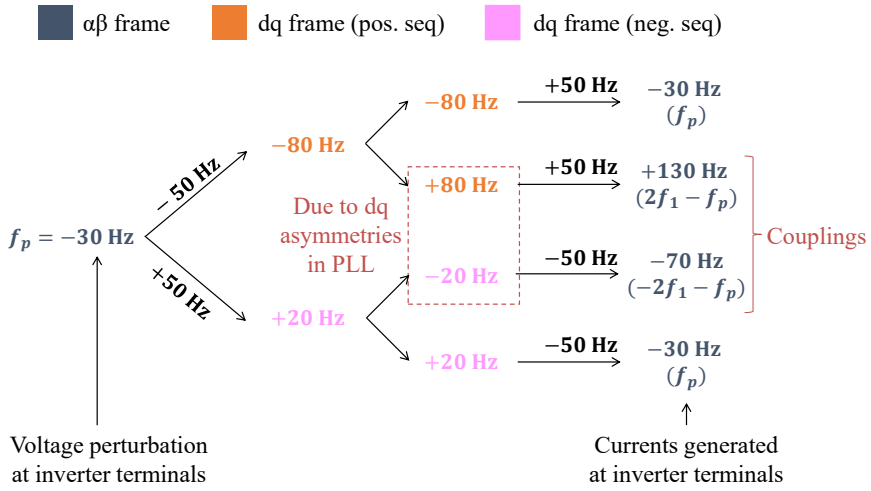

Figure 3.8: Generation process of the first and second frequency couplings. Details on the frequency coupling generation and the reason for the existence of the second frequency coupling are shown in Section 3.9.

has a frequency component at $f_{c1} = 2f_1 - f_p$). What this chapter shows is that, in the cases in which the PLL also tracks the negative-sequence phase-angle, the PLL dynamics produce an extra coupling at $f_{c2} = -2f_1 - f_p$, as illustrated in Fig. 3.8. The existence of this second frequency coupling is validated in Section 3.9.1 and the reasons causing it are explained in detail in Section 3.9.2.

3.5.2 Using the LTI model of the DDSRF-PLL

In this case, the expressions for $\Delta\theta_{1+}$ and $\Delta\theta_{1-}$ to be plugged in Fig. 3.6 are the LTI expressions derived for method 1, which are shown in (2.24). If this is done, the following model is obtained:

$$\begin{aligned}\vec{Z} = \frac{1}{\vec{Y(s)}} = \Big\{ & Ls + R_L + \Big([H_i(s - j\omega_1) - jK_d] G_{dec+}(s - j\omega_1) \\ & + [H_i(s + j\omega_1) + jK_d] G_{dec-}(s + j\omega_1) \Big) G_i(s) G_d(s) \Big\} \\ & \Big\{ 1 + [H_{ff}(s - j\omega_1) + H_{ff}(s + j\omega_1)] G_v(s) G_d(s) \\ & - \overrightarrow{A(s) TF_{PLL1+LTI}(s - j\omega_1)} G_d(s) - \overrightarrow{B(s) TF_{PLL1-LTI}(s + j\omega_1)} G_d(s) \Big\}^{-1}\end{aligned} \tag{3.21}$$

$$\begin{aligned}\overrightarrow{Y_{c1}} = \Big\{ & - \overrightarrow{A(s) TF_{PLL2+LTI}(s - j\omega_1)} e^{j2\phi_{vp}} G_d(s) \Big\} \\ & \Big\{ Ls + R_L + \Big([H_i(s - j\omega_1) - jK_d] G_{dec+}(s - j\omega_1) \\ & + [H_i(s + j\omega_1) + jK_d] G_{dec-}(s + j\omega_1) \Big) G_i(s) G_d(s) \Big\}^{-1}\end{aligned} \tag{3.22}$$

$$\begin{aligned}\overrightarrow{Y_{c2}} = \Big\{ &- \overrightarrow{B(s)}\overrightarrow{TF_{\text{PLL2–LTI}}(s+j\omega_1)}e^{-j2\phi_{vn}}G_d(s)\Big\} \\ &\Big\{Ls + R_L + \Big([H_i(s-j\omega_1) - jK_d]G_{dec+}(s-j\omega_1) \\ &+[H_i(s+j\omega_1) + jK_d]G_{dec-}(s+j\omega_1)\Big)G_i(s)G_d(s)\Big\}^{-1}\end{aligned} \tag{3.23}$$

This means that, when the LTI model for the DDSRF-PLL is used, the schematic in Fig. 3.7 remains valid. However, the expressions to be used for the main impedance and the coupling admittances are different.

3.6 Inverter model using DDSRF-PLL method 2

3.6.1 Using the LTP model of the DDSRF-PLL

In this case, the expressions (2.29) and (2.32) must be plugged for $\Delta\theta_{1+}$ and $\Delta\theta_{1-}$ in Fig. 3.6. When doing this, several frequency couplings appear in the current. Some of these frequency couplings, however, may be ignored due to their low magnitude. The detailed reasoning for this is provided in Section 3.9.3. In the end, just like in the case of using the DDSRF-PLL method 1, two main frequency couplings appear in the converter: one at $f_{c1} = 2f_1 - f_p$ and one at $f_{c2} = -2f_1 - f_p$. This means that, when the DDSRF-PLL method 2 is implemented, the schematic in Fig. 3.7 remains valid.

However, the expressions for the converter impedance and coupling admittances change. The converter impedance when using the DDSRF-PLL method 2 is shown in (3.24), and the coupling admittances are shown in (3.25) and (3.26). Some of the overhead arrows in (3.24) - (3.26) are omitted for simplicity. Also, the transfer functions $\overrightarrow{A(s)}$ and $\overrightarrow{B(s)}$ are defined in (3.17) and (3.18), respectively.

$$\begin{aligned}\vec{Z} = \frac{1}{\overrightarrow{Y(s)}} = \Big\{ &Ls + R_L + \Big([H_i(s-j\omega_1) - jK_d]G_{dec+}(s-j\omega_1) \\ &+[H_i(s+j\omega_1) + jK_d]G_{dec-}(s+j\omega_1)\Big)G_i(s)G_d(s)\Big\} \\ &\Big\{1 + [H_{ff}(s-j\omega_1) + H_{ff}(s+j\omega_1)]G_v(s)G_d(s) \\ &-\overrightarrow{A(s)}\overrightarrow{TF_{\text{PLL1+}}(s-j\omega_1)}G_d(s) - \overrightarrow{B(s)}\overrightarrow{TF_{\text{PLL1–}}(s+j\omega_1)}G_d(s) \\ &+jV_n e^{-j(\phi_{vp}+\phi_{vn})}\overrightarrow{TF_{\text{PLL3+}}(s-j\omega_1)}H_{ff}(s-j\omega_1)G_v(s)G_d(s) \\ &+jV_p e^{j(\phi_{vp}+\phi_{vn})}\overrightarrow{TF_{\text{PLL3–}}(s+j\omega_1)}H_{ff}(s+j\omega_1)G_v(s)G_d(s)\Big\}^{-1}\end{aligned} \tag{3.24}$$

$$\begin{aligned}\overrightarrow{Y_{c1}} = \Big\{\Big(&- \overrightarrow{A(s)TF_{\text{PLL2+}}(s-j\omega_1)}e^{j2\phi_{vp}}G_d(s) \\ &+jV_p e^{j(\phi_{vp}-\phi_{vn})}\overrightarrow{TF_{\text{PLL4-}}(s+j\omega_1)}H_{ff}(s+j\omega_1)G_v(s)G_d(s) \\ &+jV_n e^{j(\phi_{vp}-\phi_{vn})}\overrightarrow{TF_{\text{PLL6+}}(s-j\omega_1)}H_{ff}(s-j\omega_1)G_v(s)G_d(s)\Big\} \\ &\Big\{Ls+R_L+\Big([H_i(s-j\omega_1)-jK_d]G_{\text{dec+}}(s-j\omega_1) \\ &+[H_i(s+j\omega_1)+jK_d]G_{\text{dec-}}(s+j\omega_1)\Big)G_i(s)G_d(s)\Big\}^{-1}\end{aligned} \tag{3.25}$$

$$\begin{aligned}\overrightarrow{Y_{c2}} = \Big\{\Big(&- \overrightarrow{B(s)TF_{\text{PLL2-}}(s+j\omega_1)}e^{-j2\phi_{vn}}G_d(s) \\ &+jV_n e^{j(\phi_{vp}-\phi_{vn})}\overrightarrow{TF_{\text{PLL4+}}(s-j\omega_1)}H_{ff}(s-j\omega_1)G_v(s)G_d(s) \\ &+jV_p e^{j(\phi_{vp}-\phi_{vn})}\overrightarrow{TF_{\text{PLL6-}}(s+j\omega_1)}H_{ff}(s+j\omega_1)G_v(s)G_d(s)\Big\} \\ &\Big\{Ls+R_L+\Big([H_i(s-j\omega_1)-jK_d]G_{\text{dec+}}(s-j\omega_1) \\ &+[H_i(s+j\omega_1)+jK_d]G_{\text{dec-}}(s+j\omega_1)\Big)G_i(s)G_d(s)\Big\}^{-1}\end{aligned} \tag{3.26}$$

3.6.2 Using the LTI model of the DDSRF-PLL

In this case, the expressions for $\Delta\theta_{1+}$ and $\Delta\theta_{1-}$ to be plugged in Fig. 3.6 are the LTI expressions derived for method 2, which are shown in Section 2.6. If this is done, the exact same equations as for method 1 (LTI model) are obtained. That is to say, (3.21), (3.22) and (3.23) apply in this section also, although in this case, the PLL transfer functions derived in Section 2.6 should be used, instead of those derived in Section 2.4.

In this case, the schematic in Fig. 3.7 also remains valid. It is noticeable, then, that no matter the DDSRF-PLL implementation, and no matter the DDSRF-PLL model used (LTI or LTP), the converter model consists of a main admittance and two coupling admittances.

3.7 Simulation-based verification

In order to verify the models, several computer-simulated frequency sweeps are performed with a time-domain model of the converter. At the converter input, there is a grid voltage with a specific level of voltage imbalance. Performing the frequency sweep consists on imposing a harmonic in the grid voltage at a certain perturbation frequency f_p with a certain amplitude and phase-angle, and measuring the current that outputs the converter as a response (at the frequency f_p and the coupling frequencies). With this information, the impedance and coupling admittances can be calculated at each frequency.

The converter parameters are the same in the computer model as in the laboratory prototype[4]. The parameters are discussed in the Appendix A.2 and listed in Table A.1. The intention is to verify the converter models for different PLL parameters and for different voltage and current imbalance situations. In order to do that, several case studies are defined.

[4]The laboratory prototype is described in Section 3.8.

Case studies defined for simulation verification and experimental validation:

- Case A: $\mathrm{BW_{PLL}} = 30\,\mathrm{Hz}$; $V_\mathrm{n} = 5\,\%$; $I_\mathrm{p} = I_\mathrm{n} = 5\,\mathrm{A}$
- Case B: $\mathrm{BW_{PLL}} = 10\,\mathrm{Hz}$; $V_\mathrm{n} = 5\,\%$; $I_\mathrm{p} = I_\mathrm{n} = 5\,\mathrm{A}$
- Case C: $\mathrm{BW_{PLL}} = 30\,\mathrm{Hz}$; $V_\mathrm{n} = 40\,\%$; $I_\mathrm{p} = I_\mathrm{n} = 5\,\mathrm{A}$
- Case D: $\mathrm{BW_{PLL}} = 30\,\mathrm{Hz}$; $V_\mathrm{n} = 5\,\%$; $I_\mathrm{p} = I_\mathrm{n} = 10\,\mathrm{A}$
- Case E: $\mathrm{BW_{PLL}} = 30\,\mathrm{Hz}$; $V_\mathrm{n} = 5\,\%$; $I_\mathrm{p} = 5\,\mathrm{A}$; $I_\mathrm{n} = 0\,\mathrm{A}$

From now on, case A is the base case[5]. In case B, the PLL parameters are modified. In case C, the negative-sequence voltage is increased. In cases A – C the current references are kept constant as $I_{\mathrm{d+ref}} = I_{\mathrm{d-ref}} = 5\,\mathrm{A}$ and $I_{\mathrm{q+ref}} = I_{\mathrm{q-ref}} = 0\,\mathrm{A}$ in order to achieve $I_\mathrm{p} = I_\mathrm{n} = 5\,\mathrm{A}$. In cases D and E these current references are modified. The results of the frequency sweeps are shown in Fig. 3.9 – Fig. 3.13 for the converter using the DDSRF-PLL method 1, and in Fig. 3.14 – Fig. 3.18 for the converter using the DDSRF-PLL method 2.

The results in Fig. 3.9 – Fig. 3.18 show that the proposed LTP model accurately predicts the dynamics of the converter for different PLL methods, PLL tuning, imbalance situations and current references. These figures also show the high impact that all these control designs and operating conditions impose on the converter dynamics in the low frequency range. The impact of all these on the stability of the converter is addressed in Section 3.12.

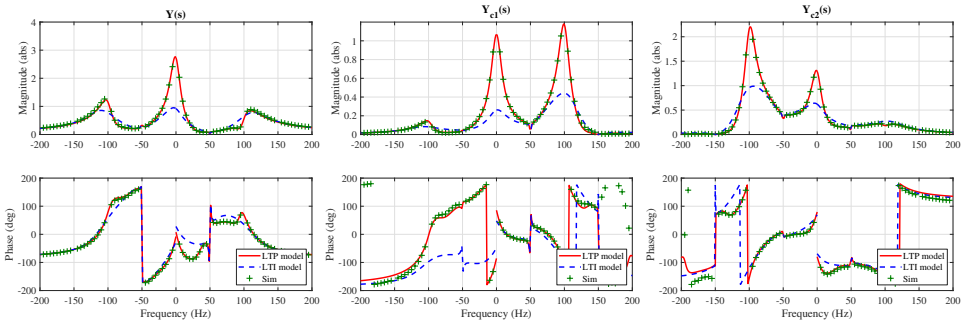

Figure 3.9: Converter model verification showing the converter model with the DDSRF-PLL LTP model, the converter model with the DDSRF-PLL LTI model, and the simulation results. The figure shows the converter using DDSRF-PLL method 1, in the case A conditions: $\mathrm{BW_{PLL}} = 30\,\mathrm{Hz}$; $V_\mathrm{n} = 5\,\%$; $I_\mathrm{p} = I_\mathrm{n} = 5\,\mathrm{A}$.

[5]In case A the PLL constants are: $K = 1/\sqrt{2}$, $K_{\mathrm{pPLL+}} = K_{\mathrm{pPLL-}} = 1.71$, $K_{\mathrm{iPLL+}} = K_{\mathrm{iPLL-}} = 228.4$ (as described in Appendix A). In case B the PLL constants are: $K = 1/2$, $K_{\mathrm{pPLL+}} = K_{\mathrm{pPLL-}} = 0.57$, $K_{\mathrm{iPLL+}} = K_{\mathrm{iPLL-}} = 25.4$ (parameters derived with the formulas in Appendix A but for a different bandwidth). Unless otherwise specified, all the figures in this chapter are derived with the PLL parameters of case A.

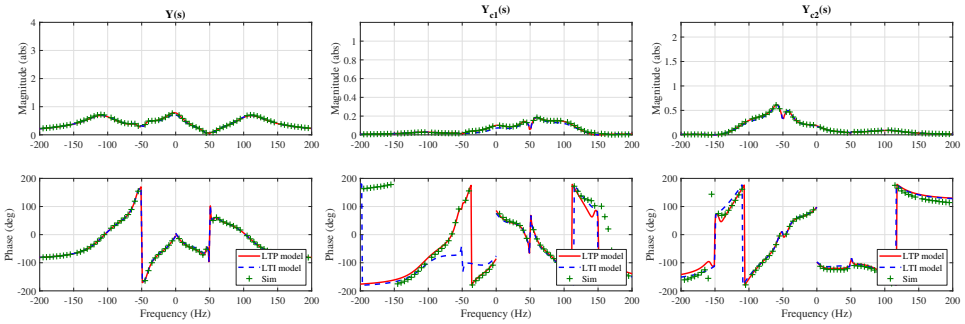

Figure 3.10: Converter model verification showing the converter model with the DDSRF-PLL LTP model, the converter model with the DDSRF-PLL LTI model, and the simulation results. The figure shows the converter using DDSRF-PLL method 1, in the case B conditions: $\mathrm{BW_{PLL}} = 10\,\mathrm{Hz}$; $V_\mathrm{n} = 5\,\%$; $I_\mathrm{p} = I_\mathrm{n} = 5\,\mathrm{A}$.

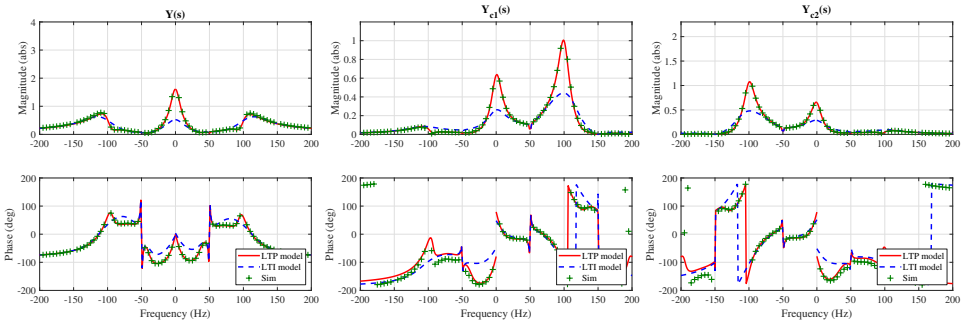

Figure 3.11: Converter model verification showing the converter model with the DDSRF-PLL LTP model, the converter model with the DDSRF-PLL LTI model, and the simulation results. The figure shows the converter using DDSRF-PLL method 1, in the case C conditions: $\mathrm{BW_{PLL}} = 30\,\mathrm{Hz}$; $V_\mathrm{n} = 40\,\%$; $I_\mathrm{p} = I_\mathrm{n} = 5\,\mathrm{A}$.

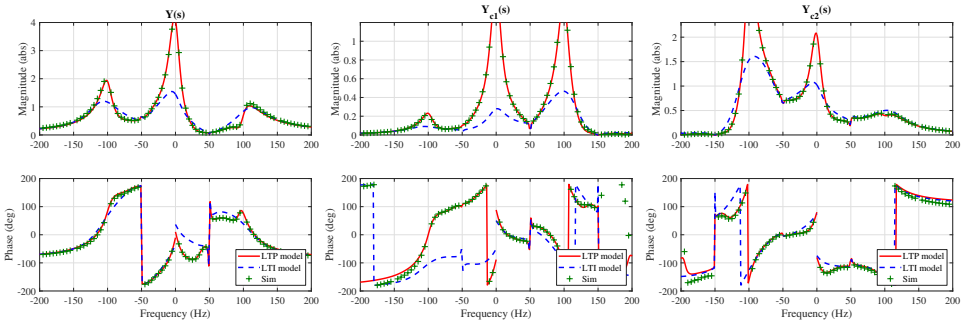

Figure 3.12: Converter model verification showing the converter model with the DDSRF-PLL LTP model, the converter model with the DDSRF-PLL LTI model, and the simulation results. The figure shows the converter using DDSRF-PLL method 1, in the case D conditions: $\mathrm{BW_{PLL}} = 30\,\mathrm{Hz}$; $V_\mathrm{n} = 5\,\%$; $I_\mathrm{p} = I_\mathrm{n} = 10\,\mathrm{A}$.

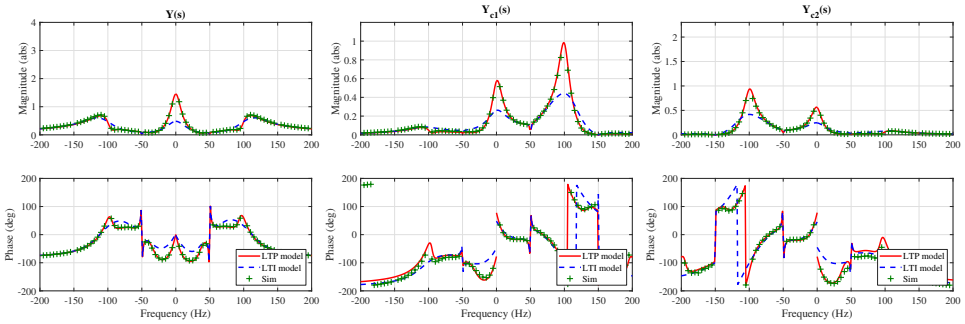

Figure 3.13: Converter model verification showing the converter model with the DDSRF-PLL LTP model, the converter model with the DDSRF-PLL LTI model, and the simulation results. The figure shows the converter using DDSRF-PLL method 1, in the case E conditions: $\mathrm{BW_{PLL}} = 30\,\mathrm{Hz}$; $V_\mathrm{n} = 5\,\%$; $I_\mathrm{p} = 5\,\mathrm{A}$; $I_\mathrm{n} = 0\,\mathrm{A}$.

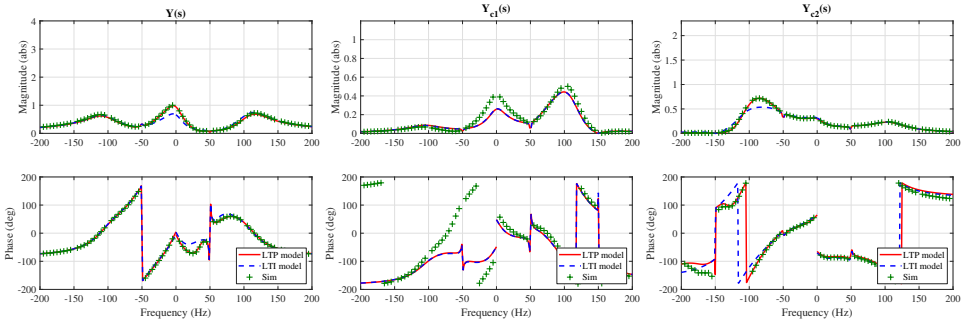

Figure 3.14: Converter model verification showing the converter model with the DDSRF-PLL LTP model, the converter model with the DDSRF-PLL LTI model, and the simulation results. The figure shows the converter using DDSRF-PLL method 2, in the case A conditions: $\mathrm{BW_{PLL}} = 30\,\mathrm{Hz}$; $V_\mathrm{n} = 5\,\%$; $I_\mathrm{p} = I_\mathrm{n} = 5\,\mathrm{A}$.

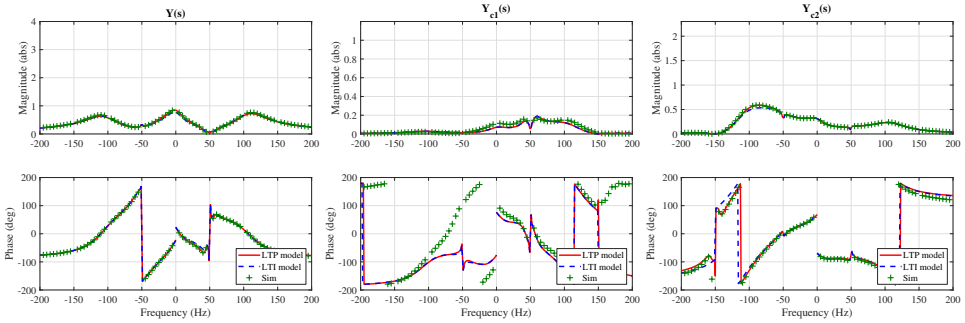

Figure 3.15: Converter model verification showing the converter model with the DDSRF-PLL LTP model, the converter model with the DDSRF-PLL LTI model, and the simulation results. The figure shows the converter using DDSRF-PLL method 2, in the case B conditions: $\mathrm{BW_{PLL}} = 10\,\mathrm{Hz}$; $V_\mathrm{n} = 5\,\%$; $I_\mathrm{p} = I_\mathrm{n} = 5\,\mathrm{A}$.

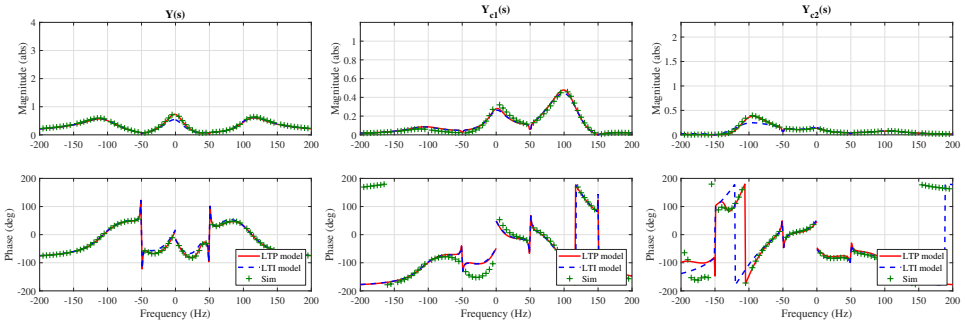

Figure 3.16: Converter model verification showing the converter model with the DDSRF-PLL LTP model, the converter model with the DDSRF-PLL LTI model, and the simulation results. The figure shows the converter using DDSRF-PLL method 2, in the case C conditions: $\mathrm{BW_{PLL}} = 30\,\mathrm{Hz}$; $V_\mathrm{n} = 40\,\%$; $I_\mathrm{p} = I_\mathrm{n} = 5\,\mathrm{A}$.

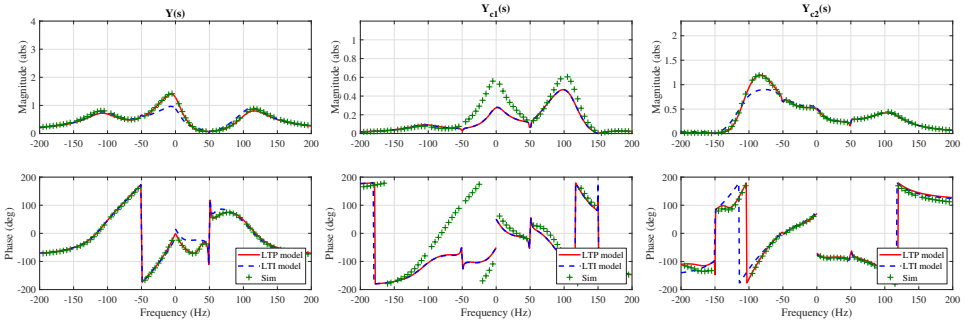

Figure 3.17: Converter model verification showing the converter model with the DDSRF-PLL LTP model, the converter model with the DDSRF-PLL LTI model, and the simulation results. The figure shows the converter using DDSRF-PLL method 2, in the case D conditions: $\mathrm{BW_{PLL}} = 30\,\mathrm{Hz}$; $V_\mathrm{n} = 5\,\%$; $I_\mathrm{p} = I_\mathrm{n} = 10\,\mathrm{A}$.

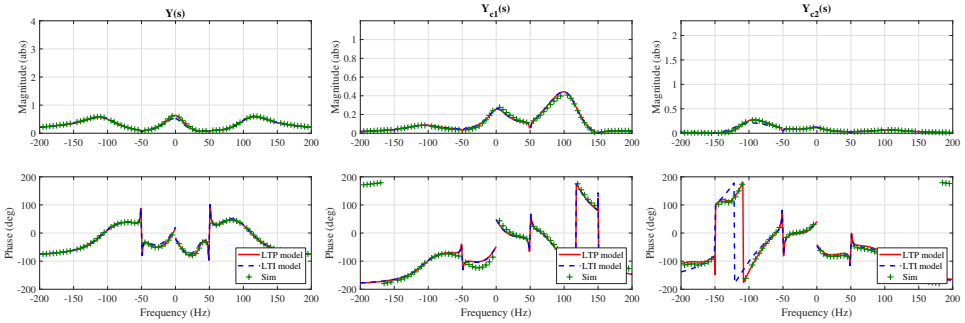

Figure 3.18: Converter model verification showing the converter model with the DDSRF-PLL LTP model, the converter model with the DDSRF-PLL LTI model, and the simulation results. The figure shows the converter using DDSRF-PLL method 2, in the case E conditions: $\mathrm{BW_{PLL}} = 30\,\mathrm{Hz}$; $V_\mathrm{n} = 5\,\%$; $I_\mathrm{p} = 5\,\mathrm{A}$; $I_\mathrm{n} = 0\,\mathrm{A}$.

3.8 Experimental validation

(a) Experiment description

In order to verify the models, experimental frequency sweeps are performed. The converter parameters are discussed in the Appendix A.2 and listed in Table A.1. The laboratory set-up is shown in Fig. 3.19. The grid emulator generates the fundamental voltage with the appropriate imbalance level depending on the case study and also the necessary perturbation for the frequency sweep. The three-phase inverter is controlled with a current loop as described in this section and a DDSRF-PLL method 1 without voltage normalization.

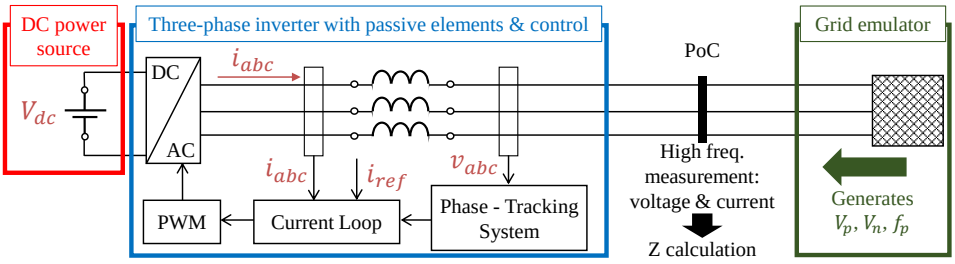

(a)

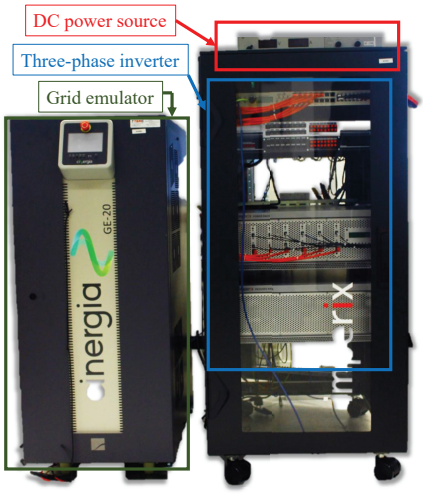

(b)

Figure 3.19: Laboratory set-up; a) schematic representation, and b) experimental hardware.

(b) Results

The same case studies as in the simulation-based verification are performed. These are repeated here for convenience:

- Case A: $\mathrm{BW_{PLL}} = 30\,\mathrm{Hz}$; $V_\mathrm{n} = 5\,\%$; $I_\mathrm{p} = I_\mathrm{n} = 5\,\mathrm{A}$
- Case B: $\mathrm{BW_{PLL}} = 10\,\mathrm{Hz}$; $V_\mathrm{n} = 5\,\%$; $I_\mathrm{p} = I_\mathrm{n} = 5\,\mathrm{A}$
- Case C: $\mathrm{BW_{PLL}} = 30\,\mathrm{Hz}$; $V_\mathrm{n} = 40\,\%$; $I_\mathrm{p} = I_\mathrm{n} = 5\,\mathrm{A}$
- Case D: $\mathrm{BW_{PLL}} = 30\,\mathrm{Hz}$; $V_\mathrm{n} = 5\,\%$; $I_\mathrm{p} = I_\mathrm{n} = 10\,\mathrm{A}$
- Case E: $\mathrm{BW_{PLL}} = 30\,\mathrm{Hz}$; $V_\mathrm{n} = 5\,\%$; $I_\mathrm{p} = 5\,\mathrm{A}$; $I_\mathrm{n} = 0\,\mathrm{A}$

The results of the frequency sweeps are shown in Fig. 3.20 – Fig. 3.24 for the different case studies. In these figures, both the simulation and experimental results are included for easier comparison.

Firstly, Fig. 3.20 shows that the analytical model (line) perfectly matches the simulation results (crosses) for the main admittance and both coupling admittances. This can also be seen in Section 3.7. The experimental results (circles) also match the analytical model and the simulations for the impedance and for both coupling admittances, although, for the coupling admittances, the phase-angle plot of the experiment results shows some deviation. This is mostly due to the limitations of the current probe for low currents (in order to ensure a small-signal perturbation, the harmonic in the voltage was set around $0.5 - 1$ V, and thus the currents to be measured for the coupling admittances were on the range of a few dozens of mA or lower). The difficulty in this measurement lies not only in the low magnitude of the currents to be measured, but also in the fact that they have to be measured in a signal that is dominated by the fundamental, which is several orders of magnitude higher (several A). In fact, note that, when the admittance magnitude is higher, and thus the currents to be measured are higher, the phase-angles obtained in the experiments match perfectly the analytical and simulation results. The experimental results only show some deviations when the admittance value is around or below -30 dB, approximately.

Similar conclusions can be reached in all the other case studies, which means that the model presented in this thesis is accurate for different PLL bandwidths (case B), different levels of voltage imbalance (case C), different output currents (case D) and different levels of current imbalance (case E).

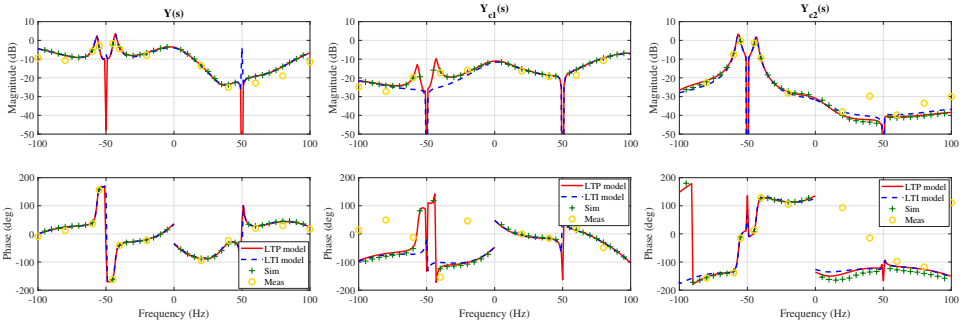

Figure 3.20: Converter model validation. Legend: converter model with LTP model of the PLL, converter model with LTI model of the PLL, simulation results and experimental measurements. Case study: a converter using DDSRF-PLL method 1 w/o normalization, case A conditions ($\mathrm{BW_{PLL}} = 30\,\mathrm{Hz}$; $V_\mathrm{n} = 5\,\%$; $I_\mathrm{p} = I_\mathrm{n} = 5\,\mathrm{A}$).

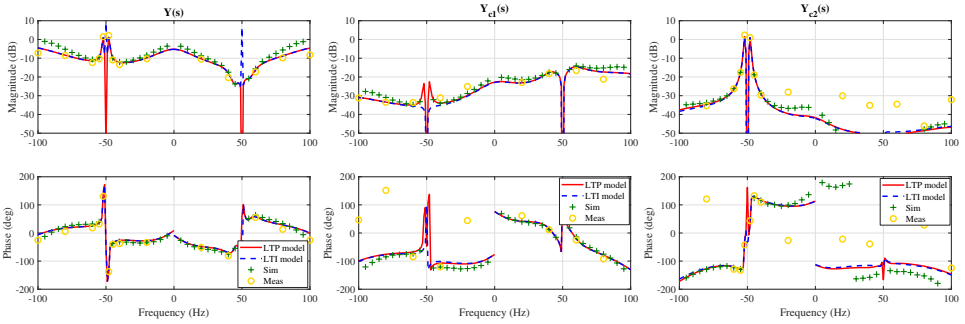

Figure 3.21: Converter model validation. Legend: converter model with LTP model of the PLL, converter model with LTI model of the PLL, simulation results and experimental measurements. Case study: a converter using DDSRF-PLL method 1 w/o normalization, case B conditions ($\mathrm{BW_{PLL}} = 10\,\mathrm{Hz}$; $V_\mathrm{n} = 5\,\%$; $I_\mathrm{p} = I_\mathrm{n} = 5\,\mathrm{A}$).

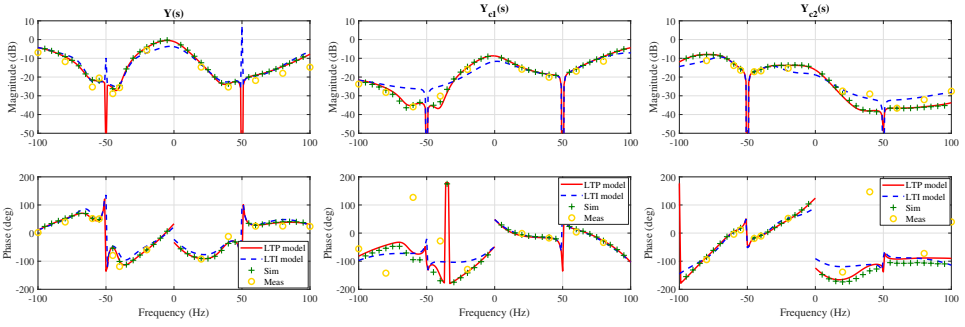

Figure 3.22: Converter model validation. Legend: converter model with LTP model of the PLL, converter model with LTI model of the PLL, simulation results and experimental measurements. Case study: a converter using DDSRF-PLL method 1 w/o normalization, case C conditions ($\mathrm{BW_{PLL}} = 30\,\mathrm{Hz}$; $V_\mathrm{n} = 40\,\%$; $I_\mathrm{p} = I_\mathrm{n} = 5\,\mathrm{A}$).

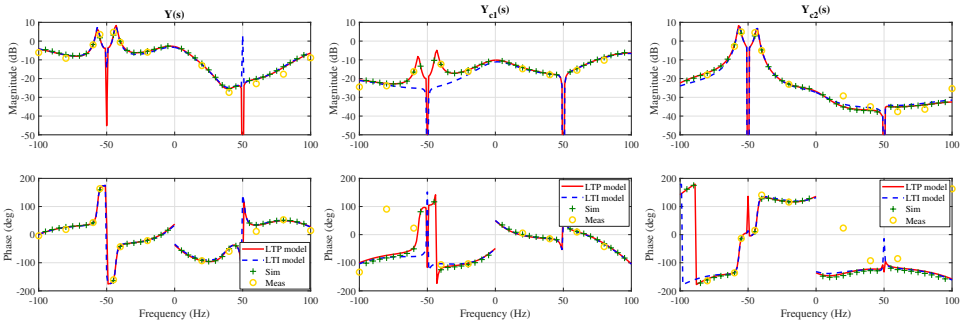

Figure 3.23: Converter model validation. Legend: converter model with LTP model of the PLL, converter model with LTI model of the PLL, simulation results and experimental measurements. Case study: a converter using DDSRF-PLL method 1 w/o normalization, case D conditions ($\text{BW}_{\text{PLL}} = 30\,\text{Hz}$; $V_{\text{n}} = 5\,\%$; $I_{\text{p}} = I_{\text{n}} = 10\,\text{A}$).

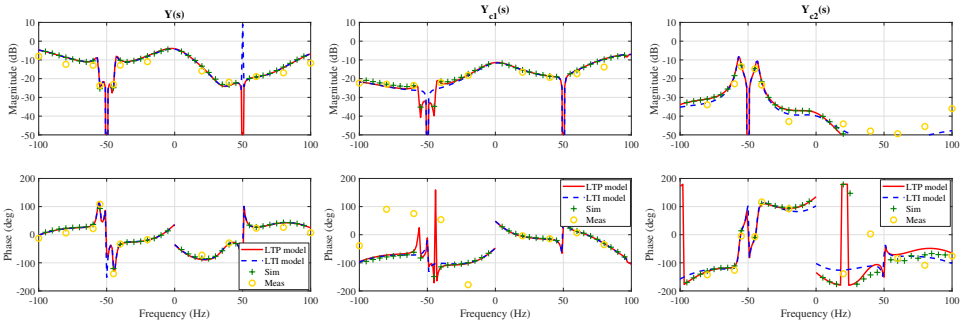

Figure 3.24: Converter model validation. Legend: converter model with LTP model of the PLL, converter model with LTI model of the PLL, simulation results and experimental measurements. Case study: a converter using DDSRF-PLL method 1 w/o normalization, case E conditions ($\text{BW}_{\text{PLL}} = 30\,\text{Hz}$; $V_{\text{n}} = 5\,\%$; $I_{\text{p}} = 5\,\text{A}$; $I_{\text{n}} = 0\,\text{A}$).

3.9 Converter frequency couplings

3.9.1 Existence of the second frequency coupling

In order to clearly show the frequency coupling effect, different simulations are made in which a perturbation is set in the voltage and the current spectrum is acquired. The converter parameters are the same as in the laboratory prototype, and are listed in Table A.1. The DDSRF-PLL used is the method 1 without normalization. The perturbation frequency f_{p} is selected as $-30\,\text{Hz}$ because at this point, for the parameters selected and if $V_{\text{n}} = 5\,\%$ and $I_{\text{p}} = I_{\text{n}} = 5\,\text{A}$, the coupling admittances are approximately equal in magnitude (i.e. $|\overrightarrow{Y_{\text{c1}}(s)}|$ at $2f_1 - f_{\text{p}} = 130\,\text{Hz}$ is approximately equal to $|\overrightarrow{Y_{\text{c2}}(s)}|$ at $-2f_1 - f_{\text{p}} = -70\,\text{Hz}$).[6] The results are shown in Fig. 3.25.

The main conclusion in Fig. 3.25 is that, even in the case where the negative-sequence voltage is relatively low, the second frequency coupling exists. This is due to the fact that

[6]The simulations are performed with a continuous model in the s-domain without switches, in order to have cleaner results and avoid possible switching and modulation couplings.

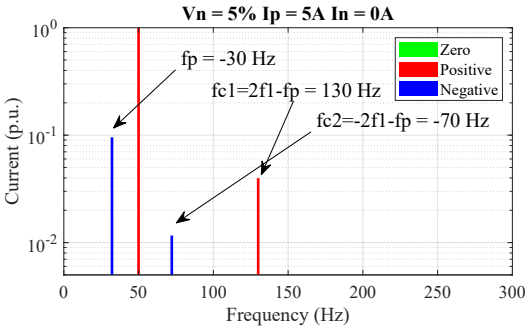

Figure 3.25: Current spectrum as a result of a voltage with perturbation at $f_p = -30$ Hz for $V_n = 5\%$. a) $I_p = 5$ A $I_n = 0$ A; b) $I_p = 5$ A $I_n = 5$ A. These results are from simulation.

this second frequency coupling is not directly due to the presence of V_n, but rather to the use of θ_{PLL-} in the current control loop, as it is explained in detail in Section 3.9.2. Further, the level of the negative-sequence current may affect the magnitude of the coupling, but even when the negative-sequence current is equal to zero the coupling exists. A similar work is performed in the laboratory set-up, and the results are shown in Fig. 3.26.

This figure shows the contrast in the current spectrum when there is a perturbation in the voltage or not. When there is no perturbation, the results are shown in Fig. 3.26 a) and the current only has the fundamental component and a harmonic at 150 Hz, which is probably due to the effect of the voltage imbalance through the DC voltage. This component does not appear in the simulations since in the simulations the effect of the DC voltage is neglected. This effect has been reported in the literature before [139]. When the perturbation is injected, it is shown in Fig. 3.26 b) that two frequency couplings appear, as predicted in this chapter (see Fig. 3.8). Note also that, the magnitude of the harmonics at 70 Hz and 130 Hz are shown at the bottom of the oscilloscope images, where it can be seen quantitatively that the harmonics at these frequencies increase when there is a perturbation at −30 Hz. This validates the frequencies predicted in this thesis. Note that the results in Fig. 3.26 b) are the same as the simulation results in Fig. 3.25 b).

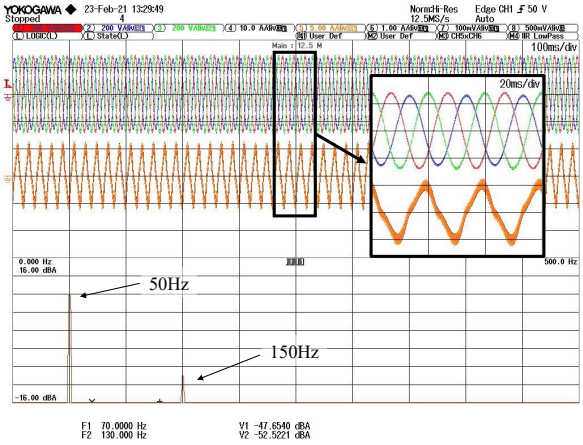

(a)

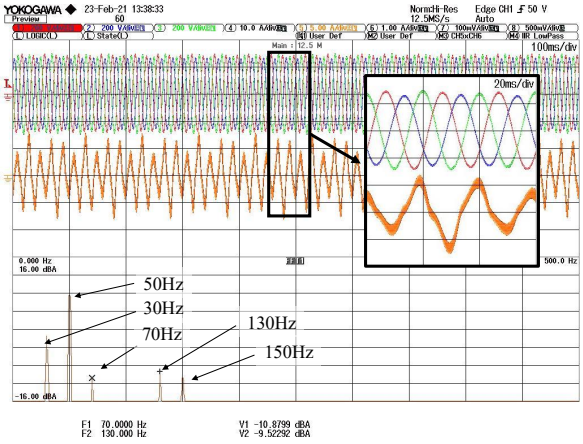

(b)

Figure 3.26: Current spectrum when $I_{\mathrm{p}} = 5$ A $I_{\mathrm{n}} = 5$ A ($V_{\mathrm{n}} = 5\%$). a) No perturbation; b) Perturbation in the voltage at $f_{\mathrm{p}} = -30$ Hz. When a perturbation is introduced, two frequency couplings appear in the current. The x-axis expands from 0 Hz until 500 Hz in increments of 50 Hz. These results are from experiments.

3.9.2 Origin of the second frequency coupling

In comparison to previous literature, one key difference in this thesis is that it considers a PLL structure that also tracks the negative-sequence phase-angle. In particular, it is shown here that, even if the couplings within the PLL are ignored (i.e. $\overrightarrow{TF_{\mathrm{PLL3+}}} - \overrightarrow{TF_{\mathrm{PLL6+}}}$ and $\overrightarrow{TF_{\mathrm{PLL3-}}} - \overrightarrow{TF_{\mathrm{PLL6-}}}$ are neglected), the $\theta_{\mathrm{PLL-}}$ has the frequencies $\pm(f_{\mathrm{p}} + f_1)$. This is due to $\overrightarrow{TF_{\mathrm{PLL1-}}}$ and $\overrightarrow{TF_{\mathrm{PLL2-}}}$. Consequently, if $\theta_{\mathrm{PLL-}}$ is used in the construction of the current control loop, then an additional frequency coupling at $-2f_1 - f_{\mathrm{p}}$ appears (as illustrated in Fig. 3.8). Therefore, the frequency coupling is not directly due to the presence of V_{n}. However, the presence of V_{n} is necessary since otherwise the negative-sequence phase-

angle is undefined and therefore it cannot be used to construct the negative-sequence SRF for the current control, yielding impossible for this second frequency coupling to appear. In a sense, a similar situation happens with the first frequency coupling: the PLL dynamics create the coupling at $2f_1 - f_p$, although it is true that the presence of V_p is a pre-assumed condition so that θ_{1+} is defined.

In order to show more intuitively that the second frequency coupling is due to the use of θ_{PLL-} in the current control loop, another simulation is done with a slightly different DDSRF-PLL. In this case, the DDSRF-PLL tracks only the positive-sequence phase-angle, and the negative-sequence phase-angle is simply calculated by imposing: $\theta_{PLL-} = -\theta_{PLL+}$. In these conditions, the equivalent simulation as the one shown in Fig. 3.25 b) is done. The results are shown in Fig. 3.27.

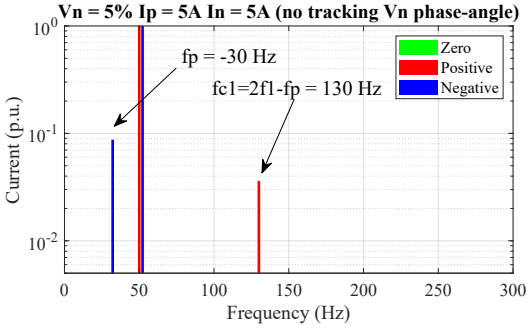

Figure 3.27: Current spectrum as a result of a voltage with perturbation at $f_p = -30$ Hz for $V_n = 5\%$, $I_p = 5$ A $I_n = 5$ A. These results are from simulation. The negative-sequence phase-angle is not tracked.

As it can be seen, the current presents no longer the second frequency coupling. This can be understood by comparing Fig. 2.19 and Fig. 2.20. If the voltage has a perturbation at $f_p = 200$ Hz, even if the PLL couplings are ignored, the distortion in θ_{PLL+} is different from the distortion in θ_{PLL-}. A 150 Hz oscillation can be seen in θ_{PLL+} and a different oscillation (at 250 Hz) can be seen in θ_{PLL-}. This is a different situation from the case in which $\theta_{PLL-} = -\theta_{PLL+}$ since, then, the oscillation at θ_{PLL-} will be seen at 150 Hz. Therefore, it is clear that the second frequency coupling is not due to the use of a negative-sequence dq frame in the current control, but rather due to the use of θ_{PLL-} in the current control.

Finally, it is worth to mention that, for both method 1 and method 2, the first and second couplings are mostly created by $\overrightarrow{TF_{PLL2+}}$ and $\overrightarrow{TF_{PLL2-}}$, and therefore are not due to the frequency coupling dynamics of the DDSRF-PLL. However, since in some instances, some of the couplings within the PLL appear at these exact frequencies ($2f_1 - f_p$ and $-2f_1 - f_p$), then they are considered in the final expression of $\overrightarrow{Y_{c1}}$ and $\overrightarrow{Y_{c2}}$ (in particular, $\overrightarrow{TF_{PLL4+}}$ and $\overrightarrow{TF_{PLL4-}}$ appear in the expression of $\overrightarrow{Y_{c1}}$ and $\overrightarrow{Y_{c2}}$ in method 1, and $\overrightarrow{TF_{PLL4+}}$, $\overrightarrow{TF_{PLL6+}}$, $\overrightarrow{TF_{PLL4-}}$ and $\overrightarrow{TF_{PLL6-}}$ appear in the coupling-admittance expressions in method 2). However, it is worth to note that the contribution of the PLL couplings to $\overrightarrow{Y_{c1}}$ and $\overrightarrow{Y_{c2}}$, respectively, is much smaller than such of $\overrightarrow{TF_{PLL2+}}$ and $\overrightarrow{TF_{PLL2-}}$, respectively. Therefore, it can be concluded, that the first and second coupling are mostly due to tracking the positive and negative phase-angles with a PLL structure that is dq asymmetrical (causing $\overrightarrow{TF_{PLL2+}} \neq 0$ and $\overrightarrow{TF_{PLL2-}} \neq 0$), and then using these phase-angles in the current control.

3.9.3 Number of frequency couplings

(a) Converter couplings when using the DDSRF-PLL method 1

Chapter 2 shows that, when considering only the PLL and for the DDSRF-PLL method 1, the first round of couplings appears at $f_{\mathrm{p}}^{\mathrm{dq}+} \pm 4f_1$ for $\theta_{\mathrm{PLL}+}$ and at $f_{\mathrm{p}}^{\mathrm{dq}-} \pm 4f_1$ for $\theta_{\mathrm{PLL}-}$. Once the whole converter is considered, numerous frequency couplings are predicted in the calculations. In particular, when looking into Fig. 3.6 it can be seen that, in several instances, $\Delta\theta_{1+}$ or $\Delta\theta_{1-}$ appear in the small-signal model of the current control. In total, if the first round of couplings is considered in the PLL, then 13 couplings may appear in the output current of the converter: $f_{\mathrm{c}1} = +2f_1 - f_{\mathrm{p}}$, $f_{\mathrm{c}2} = -2f_1 - f_{\mathrm{p}}$, $f_{\mathrm{c}3} = +4f_1 + f_{\mathrm{p}}$, $f_{\mathrm{c}4} = -4f_1 + f_{\mathrm{p}}$, $f_{\mathrm{c}5} = +6f_1 - f_{\mathrm{p}}$, $f_{\mathrm{c}6} = -6f_1 - f_{\mathrm{p}}$, $f_{\mathrm{c}7} = -2f_1 + f_{\mathrm{p}}$, $f_{\mathrm{c}8} = -f_{\mathrm{p}}$, $f_{\mathrm{c}9} = +2f_1 + f_{\mathrm{p}}$, $f_{\mathrm{c}10} = -4f_1 - f_{\mathrm{p}}$, $f_{\mathrm{c}11} = -6f_1 + f_{\mathrm{p}}$, $f_{\mathrm{c}12} = +4f_1 - f_{\mathrm{p}}$, and $f_{\mathrm{c}13} = +6f_1 + f_{\mathrm{p}}$.

A question arises as to how many of these couplings should be considered in the converter model. When considering the PLL exclusively, it is shown in Chapter 2 that, for stability studies, a 2x2 LTP matrix is enough to achieve accuracy (therefore, ignoring the couplings within the PLL). With respect to harmonic studies, the couplings are very relevant in the low frequency range, but in the range where the majority of harmonics appear, the couplings are quite low. This already points to the direction that, when considering the whole converter, it is probably not necessary to consider the 13 couplings in the current.

In order to address this question, different simulations are done in which a perturbation is imposed in the voltage at different frequencies, and the coupling currents are measured. The results are shown in Fig. 3.28.

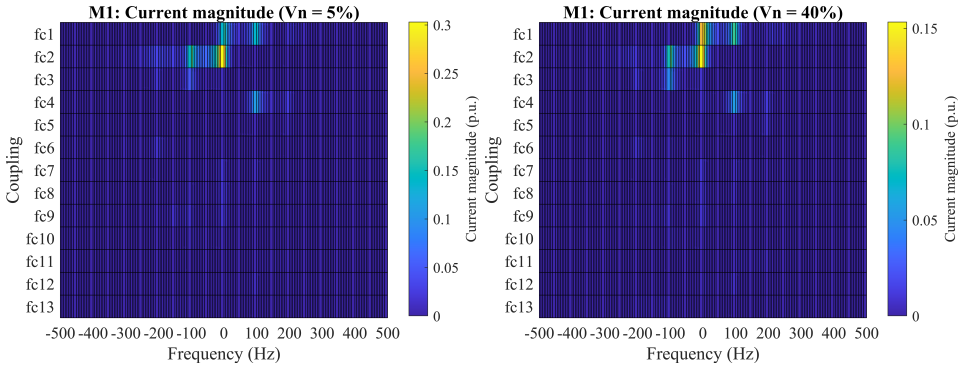

Figure 3.28: M1: Magnitude of the current coupling at different frequencies when $I_{\mathrm{p}} = 5$ A $I_{\mathrm{n}} = 5$ A. a) $V_{\mathrm{n}} = 5\%$; b) $V_{\mathrm{n}} = 40\%$. These results are from simulations.

As it can be seen in Fig. 3.28, no matter the imbalance level, all the frequency couplings are very low in the whole frequency range, except for $f_{\mathrm{c}1} = 2f_1 - f_{\mathrm{p}}$ and $f_{\mathrm{c}2} = -2f_1 - f_{\mathrm{p}}$. Therefore, it is concluded that considering only $f_{\mathrm{c}1}$ and $f_{\mathrm{c}2}$ is sufficient to achieve enough accuracy.

(b) Converter couplings when using the DDSRF-PLL method 2

The first round of couplings for the DDSRF-PLL method 2 appears at $f_{\mathrm{p}}^{\mathrm{dq}+} \pm 2f_1$ for $\theta_{\mathrm{PLL}+}$ and at $f_{\mathrm{p}}^{\mathrm{dq}-} \pm 2f_1$ for $\theta_{\mathrm{PLL}-}$ (Chapter 2). Once the whole converter is considered, numerous frequency couplings are predicted in the calculations. In total, if the first round of couplings is considered in the PLL, then 9 couplings may appear in the output current: $f_{\mathrm{c1}} = +2f_1 - f_{\mathrm{p}}$, $f_{\mathrm{c2}} = -2f_1 - f_{\mathrm{p}}$, $f_{\mathrm{c3}} = +2f_1 + f_{\mathrm{p}}$, $f_{\mathrm{c4}} = -f_{\mathrm{p}}$, $f_{\mathrm{c5}} = -2f_1 + f_{\mathrm{p}}$, $f_{\mathrm{c6}} = +4f_1 - f_{\mathrm{p}}$, $f_{\mathrm{c7}} = -4f_1 - f_{\mathrm{p}}$, $f_{\mathrm{c8}} = -4f_1 + f_{\mathrm{p}}$, and $f_{\mathrm{c9}} = +4f_1 + f_{\mathrm{p}}$. Just like with the DDSRF-PLL method 1, some of these couplings have an insignificant magnitude in comparison with the rest. This is shown in Fig. 3.29.

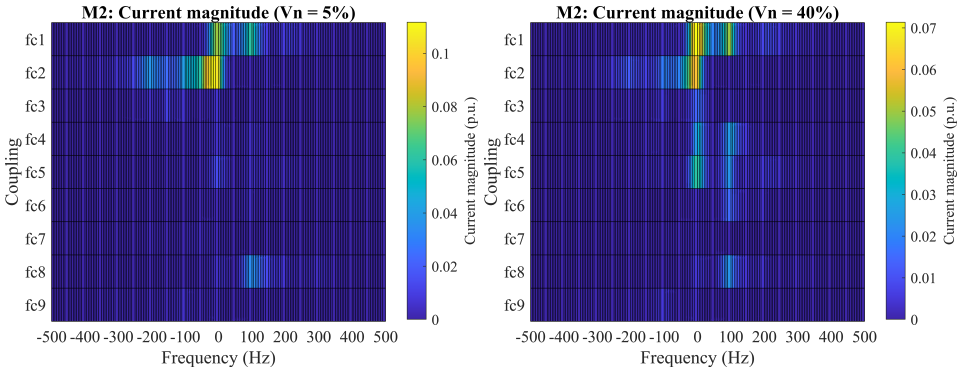

Figure 3.29: M2: Magnitude of the current coupling at different frequencies when $I_{\mathrm{p}} = 5$ A $I_{\mathrm{n}} = 5$ A. a) $V_{\mathrm{n}} = 5\%$; b) $V_{\mathrm{n}} = 40\%$. These results are from simulations.

Based on Fig. 3.29, it is sufficient to include the first two couplings in the model. In any case, if a very accurate model of the converter is desired, other couplings may be included in the analysis, albeit with the drawback of handling a more complex converter model. In the end, depending on the application, a different decision might be made depending on the trade-off between accuracy versus complexity.

3.10 Comparison of converter models for small-signal stability studies

3.10.1 Description of the grid-connected converter case study

The situation under study is shown in Fig. 3.30. It consists of the converter that is modelled in previous sections, together with a CL grid impedance that may represent a resonant point, a cable, or others. The grid impedance is represented by $Z_{\mathrm{g}}(s)$ in the frequency domain, and it is the parallel between the grid capacitor C_{g} and grid inductor L_{g}, each of which have their own parasitic resistance. The parameters for the grid impedance are in Table 3.1.

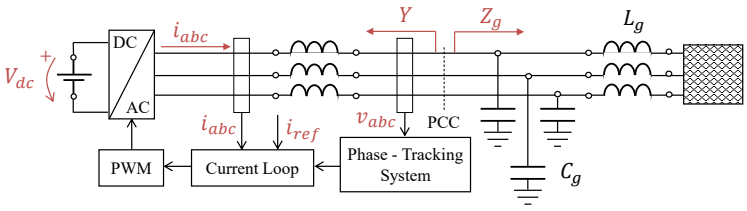

Figure 3.30: Schematic of the grid-connected inverter.

Table 3.1: Grid impedance parameters

	Description	Value	Unit
C_g	Grid Capacitance	10	μF
R_{Cg}	Resistance of Grid Capacitance	0.1	Ω
L_g	Grid Inductance	1	mH
R_{Lg}	Resistance of Grid Inductance	8.8	mΩ

The grid impedance parameters are selected to cause a resonance that can drive the converter to instability for demonstration purposes of the accuracy of different models.

3.10.2 The four types of models

In this section, different models are compared in predicting the stability limit of the converter. In particular, four different small-signal models (SSM) are analysed:

- SSM1: The converter model when the LTI model is used for representing the DDSRF-PLL, and when the coupling admittances of the converter are ignored.
- SSM2: The converter model when the LTI model is used for representing the DDSRF-PLL, and when the coupling admittances of the converter are considered.
- SSM3: The converter model when the LTP model is used for representing the DDSRF-PLL, and when the coupling admittances of the converter are ignored.
- SSM4: The converter model when the LTP model is used for representing the DDSRF-PLL, and when the coupling admittances of the converter are considered.

(a) Evaluating the stability with each model

When the converter coupling admittances are ignored (SSM1 and SSM3), only the main admittance $\overrightarrow{Y(s)}$ is used to represent the converter. Therefore, evaluating the stability of the grid-connected inverter becomes a SISO problem that can be analysed by looking at the Nyquist plot of $Z_g(s)\overrightarrow{Y(s)}$ [148].

If the converter coupling admittances are not neglected (i.e. $\overrightarrow{Y(s)}$, $\overrightarrow{Y_{c1}(s)}$ and $\overrightarrow{Y_{c2}(s)}$ are all considered, as in SSM2 and SSM4), the converter Norton equivalent is shown in Fig. 3.7. In this case, the problem is MIMO, and it can be solved using matrices. The converter admittance matrix is shown in (3.27) and the grid impedance matrix in (3.28).

$$\begin{bmatrix} \overrightarrow{I_{\alpha\beta}} \\ \overrightarrow{I^*_{\alpha\beta}}e^{j2\omega_1 t} \\ \overrightarrow{I^*_{\alpha\beta}}e^{-j2\omega_1 t} \end{bmatrix} = \underbrace{\begin{bmatrix} \overrightarrow{Y(s)} & \overrightarrow{Y_{c1}(s)} & \overrightarrow{Y_{c2}(s)} \\ \overrightarrow{Y^*_{c1}(s-j2\omega_1)} & \overrightarrow{Y^*(s-j2\omega_1)} & 0 \\ \overrightarrow{Y^*_{c2}(s+j2\omega_1)} & 0 & \overrightarrow{Y^*(s+j2\omega_1)} \end{bmatrix}}_{\overrightarrow{Y^M(s)}} \begin{bmatrix} \overrightarrow{V_{\alpha\beta}} \\ \overrightarrow{V^*_{\alpha\beta}}e^{j2\omega_1 t} \\ \overrightarrow{V^*_{\alpha\beta}}e^{-j2\omega_1 t} \end{bmatrix} \tag{3.27}$$

$$\overrightarrow{Z^M_g(s)} = \begin{bmatrix} \overrightarrow{Z_g(s)} & 0 & 0 \\ 0 & \overrightarrow{Z_g(s-j2\omega_1)} & 0 \\ 0 & 0 & \overrightarrow{Z_g(s+j2\omega_1)} \end{bmatrix} \tag{3.28}$$

Note that the grid impedance considered is balanced. The voltage imbalance comes directly from the grid voltage. The Generalized Nyquist Stability Criterion can be applied to the product $\overrightarrow{Z^M_g(s)}\overrightarrow{Y^M(s)}$ in order to analyse the stability of the interconnected system; i.e. the eigenvalues of the matrix $\overrightarrow{Z^M_g(s)}\overrightarrow{Y^M(s)}$ must be calculated in between the frequencies $-\omega_p/2$ and $\omega_p/2$ (with ω_p being the pumping frequency of the LTP system; i.e. $4\omega_1$ in M1 and $2\omega_1$ in M2), and plotted in a Nyquist manner to check whether the eigenloci encircles the point $(-1,0)$.

(b) Sources of LTP behaviour at the converter level

When using the DDSRF-PLL method 2, the source of LTP dynamics at the PLL level is the presence of V_n. For method 1, it was shown in Chapter 2 that, since the negative-sequence is directly tracked, the presence of V_p also causes LTP dynamics. In order to include these LTP dynamics, the PLL has to be linearised directly around a trajectory (i.e. including the periodic terms), and not only around a steady-state operating point. These PLL LTP dynamics get transferred to the converter level. When including the PLL equations in the whole converter model, these equations carry time-periodic terms, provoking LTP dynamics at the converter level.

On top of that, there is another source of LTP dynamics at the converter level. This is due to the dq asymmetries in the PLL. Even if there is no voltage imbalance, it is shown in the literature that LTP dynamics may appear in the converter [103]. Due to the fact that a SRF-PLL (or, in the case of this thesis, a DDSRF-PLL) is not symmetrical in the d and q channels, the relation in between the voltage and the estimated phase-angle is described by using the voltage space-vector multiplied by a complex transfer function, and also the conjugate of the voltage space-vector multiplied by the conjugate of the complex transfer function. When these equations are taken into the $\alpha\beta$ frame, the conjugate of the voltage space-vector appears at a different frequency or, in other words, appears as an extra oscillating term. Therefore, the linearisation must be done around a trajectory, instead of an operating point [170].

In the end, the practical consequence of considering the dq asymmetries in the PLL is that a coupling admittance appears in the converter model. When using a double SRF current control with a DDSRF-PLL method 1 or method 2, it is shown in this thesis that, actually, the dq asymmetries in the PLL cause two couplings at the converter level.

The four models compared in this section, include different levels of LTP dynamics:

- SSM1: This model ignores all sources of LTP dynamics, and it is therefore completely LTI.
- SSM2: This model considers the LTP dynamics caused by the dq asymmetries in the PLL, but not those due to the presence of voltage imbalance in the PLL.
- SSM3: This model considers the LTP dynamics due to the presence of voltage imbalance in the PLL, but not those caused by the dq asymmetries in the PLL.
- SSM4: This model considers both sources of LTP dynamics.

3.10.3 Stability results: DDSRF-PLL method 1

In this section, the stability limit predicted by the models is compared to the stability limit predicted in simulations when changing the K parameter, which defines the cut-off frequency of the Low-Pass Filter that appears within the DDSRF-PLL and the SCDN ($F(s) = \frac{\omega_f}{s+\omega_f}$, where $\omega_f = K\omega_1$). The positive-sequence voltage is always equal to the nominal converter voltage, and the current reference set-points are set as: $I_{d+ref} = 10$ A and $I_{q+ref} = I_{d-ref} = I_{q-ref} = 0$ A in order to achieve $I_p = 10$ A and $I_n = 0$ A.

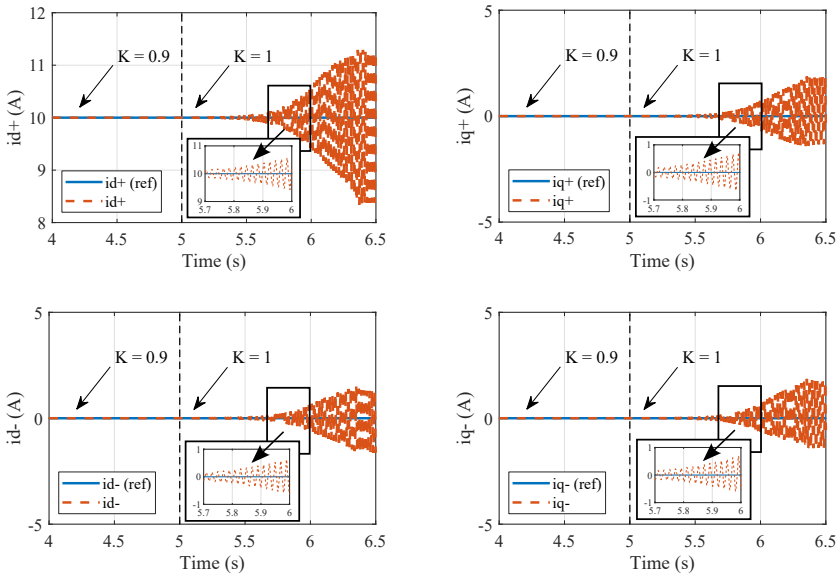

Figure 3.31: Method 1: Instability when changing K from 0.9 to 1 ($V_n = 5\%$).

When using the DDSRF-PLL method 1 and according to simulations (one example is shown in Fig. 3.31), the converter becomes unstable for K values higher than K_{lim}, being:

- $K_{\text{lim}} = 0.94$ for $V_{\text{n}} = 5\%$.
- $K_{\text{lim}} = 0.94$ for $V_{\text{n}} = 40\%$.

Note that these limits are lower than the case in which the DDSRF-PLL is considered alone, without the rest of the converter (see Section 2.10.3). This makes sense since, at the converter level, changing K affects not only the PLL, but also the LPF at the SCDN.

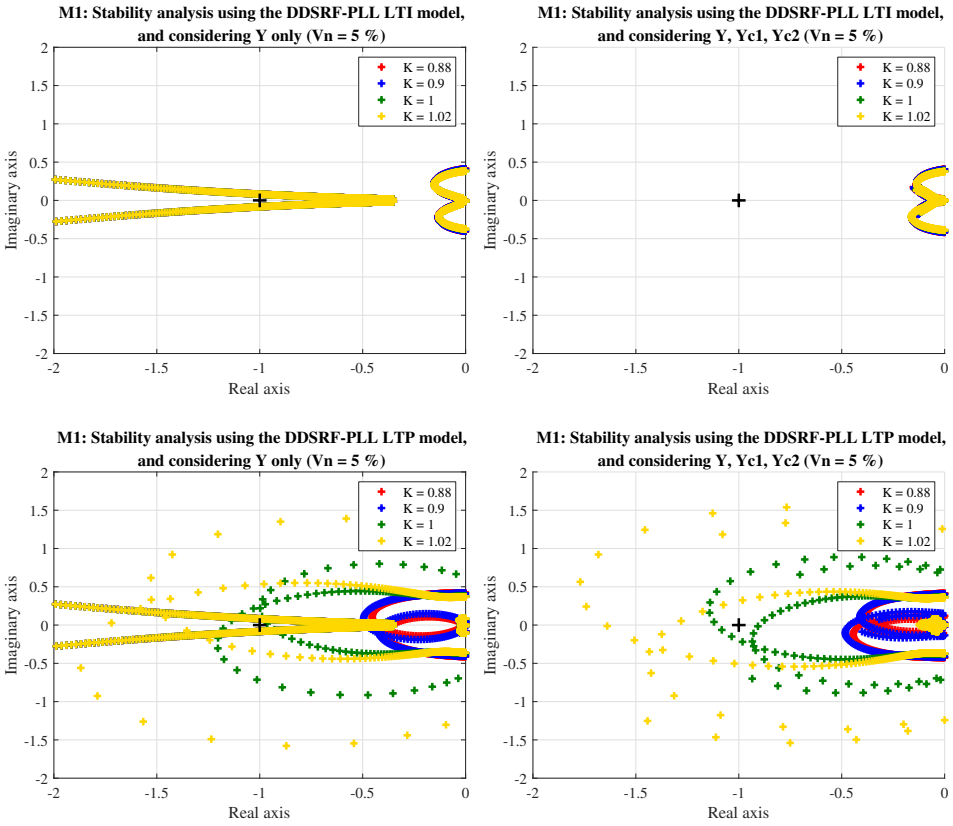

Figure 3.32: Converter stability when using DDSRF-PLL method 1 ($V_{\text{n}} = 5\%$).

In Fig. 3.32, the Nyquist eigenloci are shown for different K when $V_{\text{n}} = 5\%$. As it can be seen, the SSM1 and SSM2 (i.e. the converter models that use the LTI model for the DDSRF-PLL) predict incorrectly the stability boundary, since they predict that, for $K = 1$ and $K = 1.02$, the system is still stable. The K has to be increased until $K = 2.275$ in order to predict instability (not shown in the figure). In contrast, at the bottom of Fig. 3.32, it is shown that the SSM3 and SSM4 converter models (i.e. the converter models that use

the LTP model for the DDSRF-PLL) correctly predict the stability boundary. Note that, no matter that the coupling admittances are considered or not, the stability limit is predicted accurately.

Fig. 3.33 shows the stability predictions of the models for $V_{\mathrm{n}} = 40\%$. Again, the predictions of SSM1 and SSM2 are inaccurate, in contrast to SSM3 and SSM4.

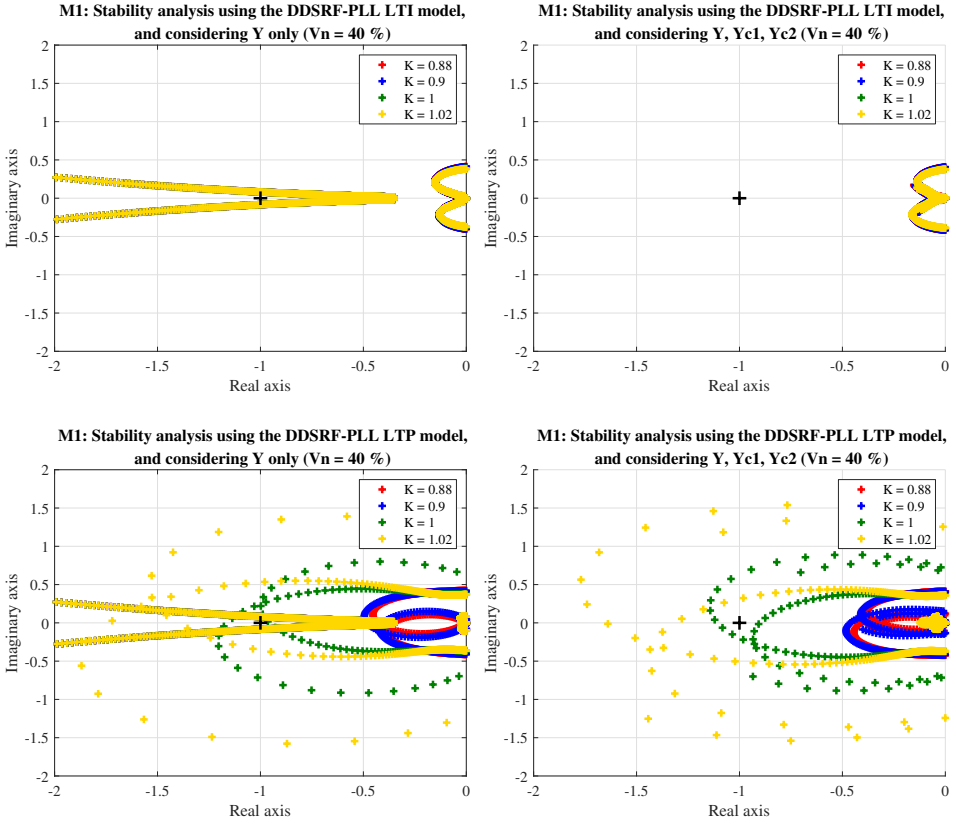

Figure 3.33: Converter stability when using DDSRF-PLL method 1 ($V_{\mathrm{n}} = 40\%$).

3.10.4 Stability results: DDSRF-PLL method 2

When using the DDSRF-PLL method 2 and according to simulations, the converter becomes unstable for K values higher than K_{lim}, being:

- $K_{\mathrm{lim}} = 2.31$ for $V_{\mathrm{n}} = 5\%$.
- $K_{\mathrm{lim}} = 2.02$ for $V_{\mathrm{n}} = 40\%$.

Note that these limits are lower than the case in which the DDSRF-PLL is considered alone, without the rest of the converter (see Section 2.10.4). This is due to the fact that

changing the K parameter affects both the PLL and also the SCDN in the current control loop.

Fig. 3.34 shows that, when $V_{\mathrm{n}} = 5\%$, all converter models predict accurate stability. However, when increasing the imbalance level, this is no longer the case (Fig. 3.35). The SSM1 and SSM2 predict that the converter is stable for K values above K_{lim}. In contrast, SSM3 and SSM4 give correct stability predictions.

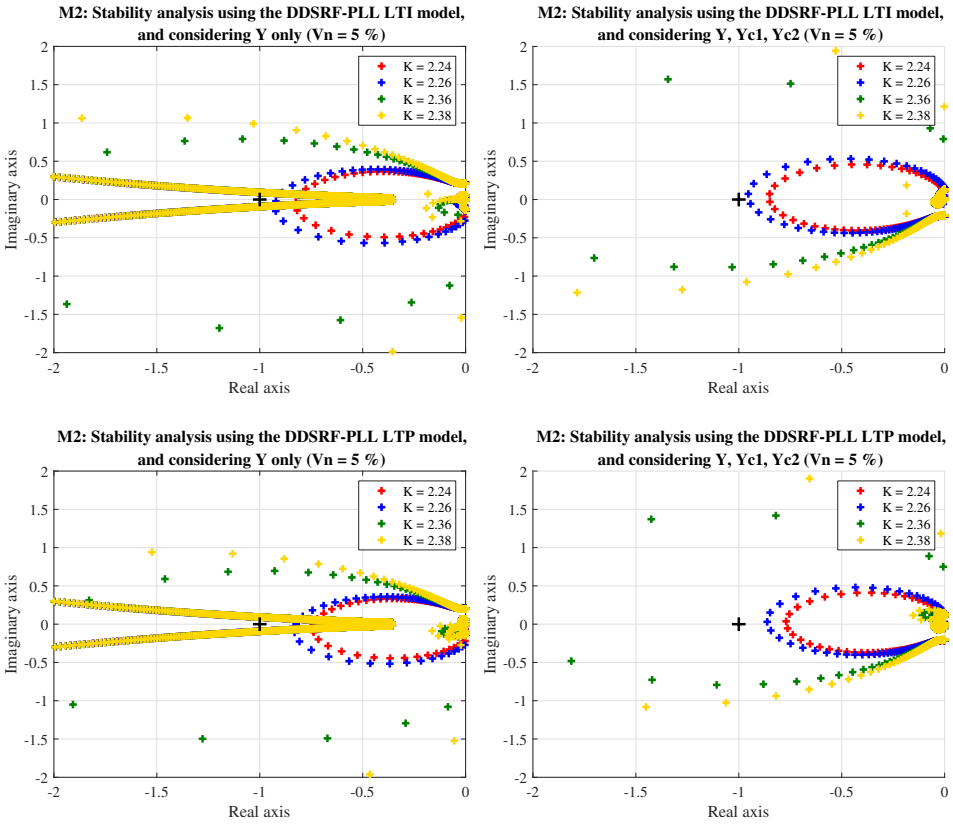

Figure 3.34: Converter stability when using DDSRF-PLL method 2 ($V_{\mathrm{n}} = 5\%$).

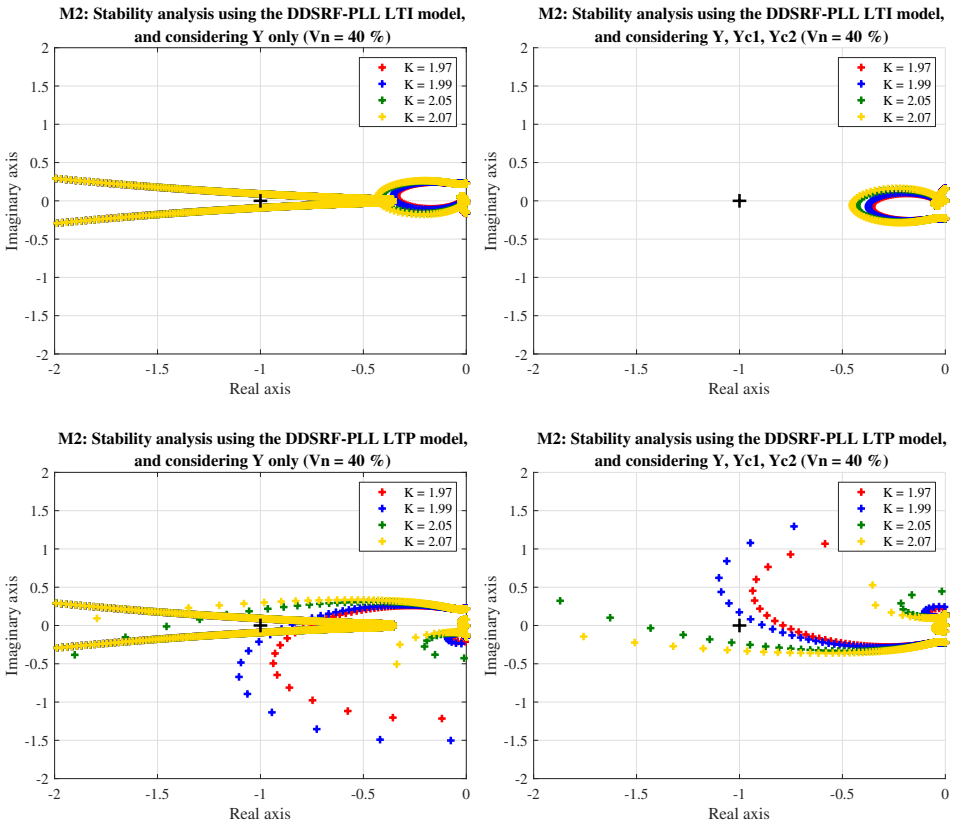

Figure 3.35: Converter stability when using DDSRF-PLL method 2 ($V_{\mathrm{n}} = 40\%$).

3.10.5 Explanation of the stability results

From Chapter 2, it is known that the DDSRF-PLL method 1 has important LTP dynamics even if V_{n} is low. Therefore, when developing the converter model, if the LTI model is used for the PLL, the stability predictions are not expected to be accurate. This is summarized in Fig. 3.36. Just like when analysing the PLL only, the stability limit does not change with the imbalance level. This is due to the normalization in the PLL. If the normalization block is bypassed, K_{lim} varies with V_{n}, as shown in Fig. 3.37.

When the converter uses the DDSRF-PLL method 2, the stability limit changes with the voltage imbalance level, and the models that use the LTI model for the PLL predict accurately the limit only when V_{n} is low. Using the LTP model for the PLL allows accurate stability predictions for all imbalance levels.

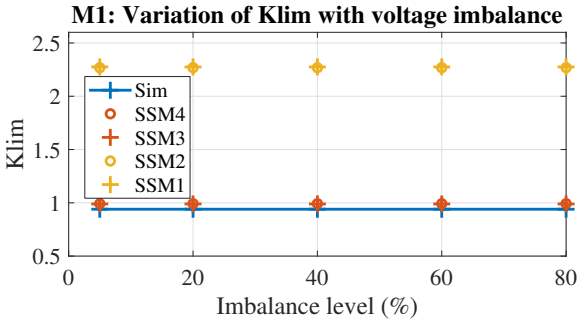

Figure 3.36: Method 1: variation of K_{lim} with V_{n} predicted by simulations, and the converter model that: uses the LTP PLL model and considers Y_{c1} and Y_{c2} (SSM4); uses the LTP PLL model and ignores Y_{c1} and Y_{c2} (SSM3); uses the LTI PLL model and considers Y_{c1} and Y_{c2} (SSM2); and uses the LTI PLL model and ignores Y_{c1} and Y_{c2} (SSM1).

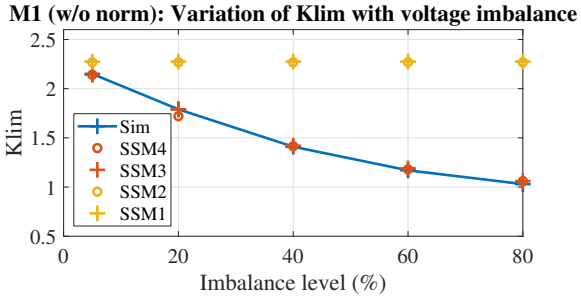

Figure 3.37: Method 1 (w/o norm): variation of K_{lim} with V_{n} predicted by simulations, and the converter model that: uses the LTP PLL model and considers Y_{c1} and Y_{c2} (SSM4); uses the LTP PLL model and ignores Y_{c1} and Y_{c2} (SSM3); uses the LTI PLL model and considers Y_{c1} and Y_{c2} (SSM2); and uses the LTI PLL model and ignores Y_{c1} and Y_{c2} (SSM1).

3.10.6 Importance of the coupling admittances for stability analysis

The fact that Fig. 3.36 – Fig. 3.38 show that the SSM1 has the same stability predictions as SSM2, and that SSM3 achieves the same results as SSM4, does not mean that the coupling admittances are irrelevant. The above examples were specifically chosen to show that, depending on the case study, the LTP dynamics of the PLL due to the presence of imbalance may be equal or more important than the LTP dynamics caused by dq asymmetries in the control. The key lesson is that the importance of the LTP dynamics created by the 100 Hz oscillations in the PLL are not due to the converter coupling admittances. However, this does not mean that the coupling admittances are irrelevant for stability studies.

In particular, the coupling admittances are mostly defined by $\overrightarrow{TF_{\text{PLL2+}}}$ or $\overrightarrow{TF_{\text{PLL2–}}}$ (see (3.19), (3.20), (3.25), and (3.26)) and, therefore, they are limited by the PLL bandwidth. This means that the coupling admittances will have a most notable effect in the low frequency range [171]. However, even if the coupling admittances have an effect with a limited frequency range, this does not mean that they cannot be very relevant in such range. This can be checked by analysing the effect of the couplings on the converter passivity index.

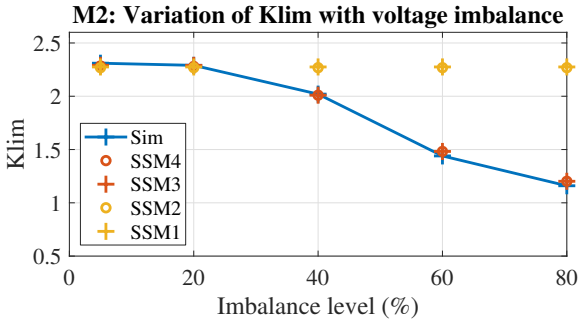

Figure 3.38: Method 2: variation of K_{lim} with V_{n} predicted by simulations, and the converter model that: uses the LTP PLL model and considers Y_{c1} and Y_{c2} (SSM4); uses the LTP PLL model and ignores Y_{c1} and Y_{c2} (SSM3); uses the LTI PLL model and considers Y_{c1} and Y_{c2} (SSM2); and uses the LTI PLL model and ignores Y_{c1} and Y_{c2} (SSM1).

(a) Definition of converter passivity index

Previous literature has already shown that, in the cases where the converter presents no couplings (i.e. its linearised dynamics are completely described by the main impedance or admittance), it is important to look at the real part of the impedance (resistance) or of the admittance (conductance). If $\Re\{\overrightarrow{Z(s)}\} < 0$ (or, alternatively, $\Re\{\overrightarrow{Y(s)}\} < 0$) at a frequency where there is a natural frequency in the system, then the system could go into oscillatory instability [59]. On the one hand, in order for the system to become unstable, what matters is the net damping of the whole system at the natural frequencies and not only the damping provided by the converter; however, on the other hand, if the converter has a negative conductance, its value is measure of how prone the converter is to instability once it is interconnected. That is why a lot of papers have argued that it is convenient to design the converter controls in order to minimize these negative-conductance regions [172]. The $\Re\{\overrightarrow{Y(s)}\}$ is called in this thesis SISO passivity index.

If the converter presents frequency couplings, it is not so straightforward to arrive to an unequivocal conclusion about how prone the converter is to instability (when it is interconnected with the grid and/or other converters) by merely looking at the sign of the main resistance or conductance, since the coupling admittances also influence the converter dynamics. In the literature, different passivity indices have been defined for LTP systems (e.g. [25]) or complex-vector MIMO models (e.g. [173]).

In this thesis, the definition of passivity index from [173] is adopted. According to [173] the passivity (dissipative) properties of a complex-vector MIMO system is quantified by the eigenvalues of $\overrightarrow{A(\omega)}$, being $\overrightarrow{A(\omega)}$:

$$\overrightarrow{A(\omega)} = \frac{1}{2}[\overrightarrow{Y^M(j\omega)} + \overrightarrow{Y^{MH}(j\omega)}] \tag{3.29}$$

where $\overrightarrow{Y^M(j\omega)}$ is the admittance matrix of the converter (defined in (3.27)) and $\overrightarrow{Y^{MH}(j\omega)}$ is its transpose-conjugate (Hermitian conjugate). As such, if the minimum eigenvalue of $\overrightarrow{A(\omega)}$ is non-negative, $\overrightarrow{Y^M(j\omega)}$ is dissipative for that frequency.

Therefore, in this thesis the MIMO passivity index is defined as the minimum eigenvalue of $\overrightarrow{A(\omega)}$, which can be found for each frequency and is desired to be as high as possible to enhance stability. Note that, if $\overrightarrow{Y^M(j\omega)}$ is a 1x1 matrix (i.e. the coupling admittances are ignored) then $\overrightarrow{A(\omega)} = \Re\{\overrightarrow{Y(s)}\}$, and therefore, this definition of passivity index coincides with the traditional SISO definition of passivity index that consists on looking at the converter conductance at each frequency.

(b) Effect of couplings on converter passivity index

Fig. 3.39 shows the passivity index of the converter when using a DDSRF-PLL method 1, and when calculated using two different methods: the first one when considering only $\overrightarrow{Y(s)}$ (SISO approach), and the second one when considering $\overrightarrow{Y(s)}$, $\overrightarrow{Y_{c1}(s)}$ and $\overrightarrow{Y_{c2}(s)}$ (MIMO approach)[7]. As it can be seen, no matter the imbalance level, the coupling admittances have a significant effect on the converter passivity in the low frequency range ($f < 200-300$ Hz approximately). In some frequencies, the passivity index even becomes negative due to the coupling admittances. Similarly occurs when the converter uses the DDSRF-PLL method 2 (Fig. 3.40). Therefore, it is recommended in this thesis to consider the coupling admittances of the converter for stability studies, especially if the frequency range of interest is low.

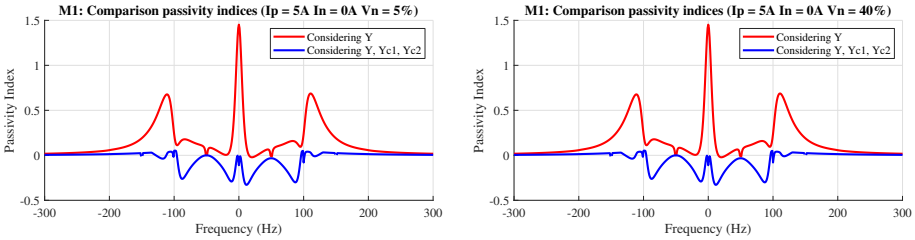

Figure 3.39: M1: Comparison of MIMO vs SISO passivity indices.

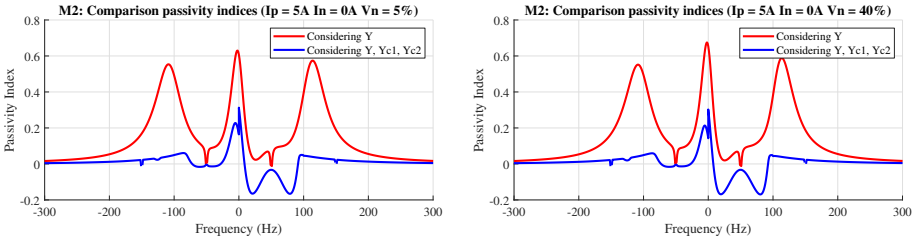

Figure 3.40: M2: Comparison of MIMO vs SISO passivity indices.

[7]This figure is plotted using the LTP model of the DDSRF-PLL, since in this chapter it is shown that this model is very accurate for representing the converter dynamics.

3.11 Comparison of converter models for harmonic studies

(a) Accuracy at input harmonic frequency

In a system-wide harmonic study, it is very important to characterize the harmonics that a converter generates as a result of a distortion in the voltage at its terminals [32]. Usually, this effect is represented by the main impedance or admittance of the converter. This impedance represents the harmonic current that the converter generates at a certain frequency for a harmonic in the voltage at that same frequency. In this section, the different converter models presented in this chapter are compared in their ability to represent this effect.

One direct way of comparing the models for this purpose is to compare the accuracy of the impedance model with a frequency scan. Note that this is a steady-state verification, and is thus correct for steady-state harmonic studies. This is already done in Section 3.7 for different case studies. The results from case A are copied in Fig. 3.41 for easier reference.

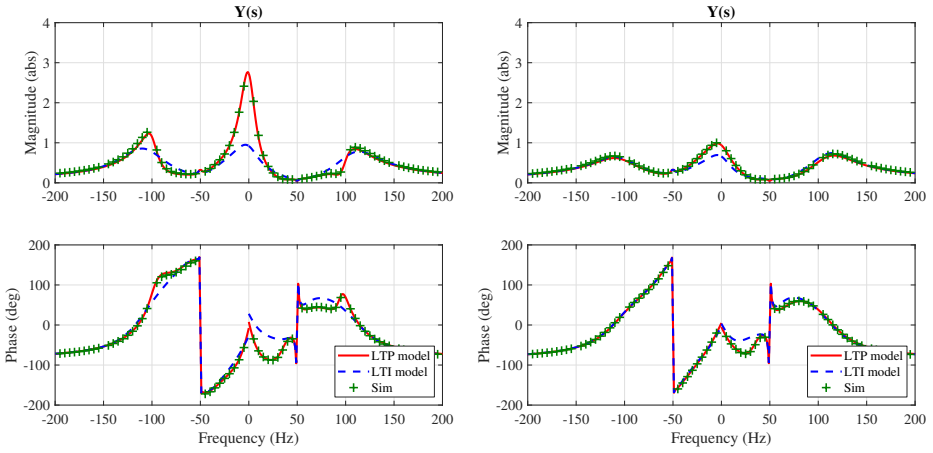

Figure 3.41: Comparison of converter models for predicting the current harmonics at a certain frequency as a result of a voltage harmonic at the same frequency (on the left: using DDSRF-PLL method 1, case A; on the right: using DDSRF-PLL method 2, case A).

As it can be seen in Fig. 3.41, the LTP model is more accurate than the LTI model in the low frequency range ($f < 150$ Hz for M1, and $f < 100$ Hz for M2). However, in high frequencies typical for harmonic distortion, the LTI model delivers accurate predictions. The frequency sweeps in Section 3.7 show that, for other case studies and for both the DDSRF-PLL method 1 or 2, the LTI model delivers accurate predictions in the high frequency range.

(b) Accuracy at coupling frequencies

With respect to the ability of the models to predict the current that the converter generates at a specific frequency, as a result of a harmonic in the voltage at a different frequency, the coupling admittances must be analysed. This is already done in Section 3.7 for different case studies. The results from case A are copied in Fig. 3.42 for the DDSRF-PLL M1, and

in Fig. 3.43 for the DDSRF-PLL M2. Again, it is shown here that, while the LTI model is very inaccurate in the low frequency range, for harmonic frequencies both models converge.

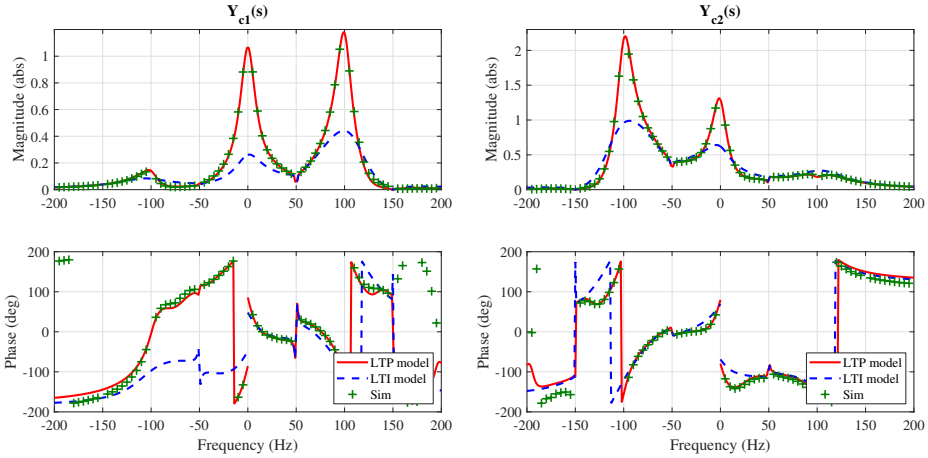

Figure 3.42: Comparison of converter models for predicting the current harmonics at a certain frequency as a result of a voltage harmonic at a different frequency (using DDSRF-PLL method 1, case A).

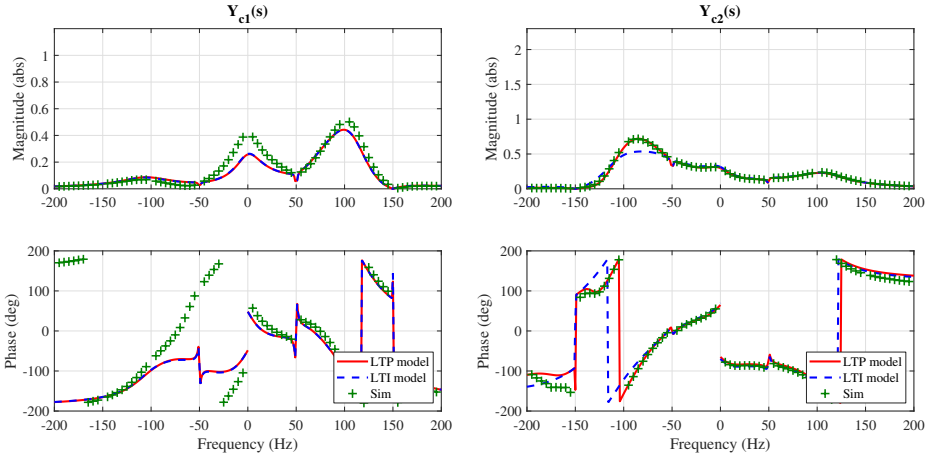

Figure 3.43: Comparison of converter models for predicting the current harmonics at a certain frequency as a result of a voltage harmonic at a different frequency (using DDSRF-PLL method 2, case A).

Therefore, it is concluded here that, for steady-state harmonic studies, using the LTI or the LTP model for the converter is equally valid. Note that this conclusion holds since all other couplings have been considered to be negligible (see Section 3.9.3). If the accuracy requirement for the particular study is very high and other couplings are to be considered, then the accuracy comparison between the LTP and LTI models would need to be re-checked.

3.12 Effect of grid voltage imbalance on the stability of the wind turbine converter

In Section 3.10 it is shown how including the LTP dynamics of the PLL is important for stability analysis in the presence of imbalance. Further, it is argued in Section 3.10.6 that including the coupling admittances in the model is important, especially in the low frequency range. Therefore, in this section, the model SSM4 is used in order to analyse the effect of V_n and I_n on the stability of the converter.

3.12.1 Analysis of the converter admittances

(a) Effect of V_n and I_n

The effect of the negative-sequence voltage on the converter admittances when using the DDSRF-PLL method 1, and when the converter is not injecting negative-sequence current ($I_\mathrm{n} = 0$ A) is shown in Fig. 3.44. As it can be seen, the admittances do not change with voltage imbalance.

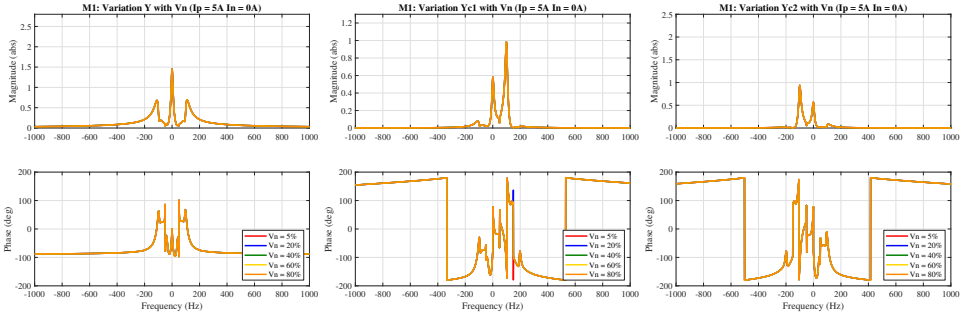

Figure 3.44: Effect of imbalance on the converter admittances when using the DDSRF-PLL method 1 and $I_\mathrm{n} = 0$ A; a) effect on main admittance, b) effect on first coupling admittance, and c) effect on second coupling admittance.

Mathematically, this can be seen in (3.16), (3.19), (3.20) and in the definition of $\overrightarrow{B(s)}$ in (3.18). If $I_\mathrm{n} = 0$, $\overrightarrow{B(s)} = -jV_\mathrm{n}H_\mathrm{ff}(s + j\omega_1)G_\mathrm{v}(s) + jV_\mathrm{n}$ and, since the voltage feed-forward loop has a very limited bandwidth, $\overrightarrow{B(s)} \approx jV_\mathrm{n}$. Also, it is worth to note that, while $\overrightarrow{TF_{\mathrm{PLL1+}}} - \overrightarrow{TF_{\mathrm{PLL6+}}}$ do not vary much with V_n, the $\overrightarrow{TF_{\mathrm{PLL1–}}} - \overrightarrow{TF_{\mathrm{PLL6–}}}$ change their magnitudes inversely to V_n (but not their phase response). For example, this can be seen in Fig. 2.6. Thus, when $\overrightarrow{B(s)}$ multiplies $\overrightarrow{TF_{\mathrm{PLL1–}}}$ in the expression of $\overrightarrow{Y(s)}$, the effect of V_n is cancelled out. Similarly, when $\overrightarrow{B(s)}$ multiplies $\overrightarrow{TF_{\mathrm{PLL4–}}}$ in the expression of $\overrightarrow{Y_{\mathrm{c1}}(s)}$, and when $\overrightarrow{B(s)}$ multiplies $\overrightarrow{TF_{\mathrm{PLL2–}}}$ in the expression of $\overrightarrow{Y_{\mathrm{c2}}(s)}$, the effect of V_n is cancelled out.

Thus, when $I_\mathrm{n} = 0$, the converter admittances remain fairly constant with V_n. Nevertheless, note that, in order for $\overrightarrow{B(s)} \approx jV_\mathrm{n}$, the negative-sequence current must be zero. When it is not, the term $\overrightarrow{B(s)}$ does not cancel out the magnitude variation in $\overrightarrow{TF_{\mathrm{PLL1–}}} - \overrightarrow{TF_{\mathrm{PLL6–}}}$ caused by V_n, and the converter admittances change. This is shown in Fig. 3.45.

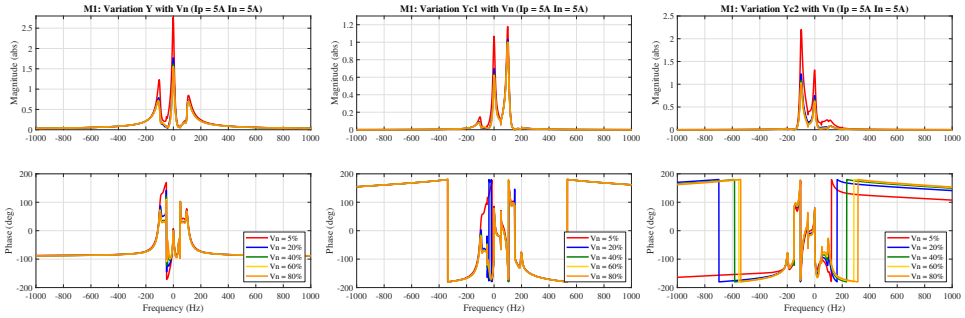

(a) (b) (c)

Figure 3.45: Effect of imbalance on the converter admittances when using the DDSRF-PLL method 1 and $I_n = 5$ A; a) effect on main admittance, b) effect on first coupling admittance, and c) effect on second coupling admittance.

With respect to the converter when using the DDSRF-PLL M2, the effect of V_n on the converter admittances is shown in Fig. 3.46 and Fig. 3.47. In this case, the admittances are also quite constant when $I_n = 0$. For method 2, $\overrightarrow{TF_{PLL1+}}$, $\overrightarrow{TF_{PLL2+}}$ and $\overrightarrow{TF_{PLL3-}} - \overrightarrow{TF_{PLL6-}}$ remain constant with respect to V_n, whereas $\overrightarrow{TF_{PLL1-}}$, $\overrightarrow{TF_{PLL2-}}$ and $\overrightarrow{TF_{PLL3+}} - \overrightarrow{TF_{PLL6+}}$ change inversely proportionally to V_n (see Fig. 2.7). The PLL transfer functions that change with V_n are multiplied by $\overrightarrow{B(s)}$ or directly by V_n in the admittances equations and, thus, the voltage imbalance effect almost perfectly cancels out (see (3.24), (3.25), (3.26)). Just as with the DDSRF-PLL M1, when $I_n \neq 0$, the cancellation does not occur and the converter admittances change more significantly with voltage imbalance (see Fig. 3.47).

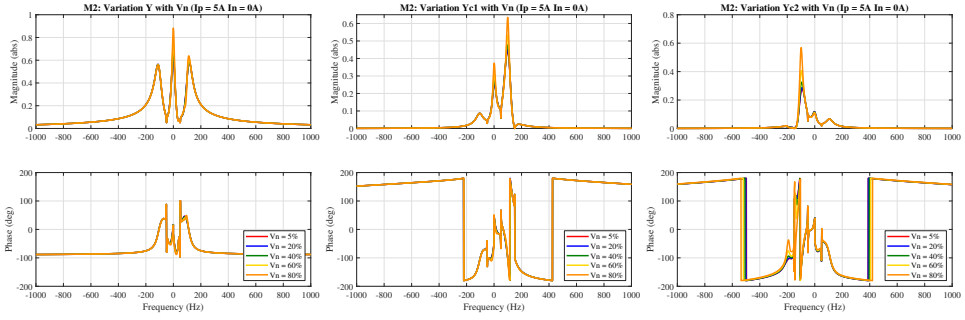

(a) (b) (c)

Figure 3.46: Effect of imbalance on the converter admittances when using the DDSRF-PLL method 2 and $I_n = 0$ A; a) effect on main admittance, b) effect on first coupling admittance, and c) effect on second coupling admittance.

In general, it can be said that, for the converter using either the DDSRF-PLL method 1 or 2, if $\overrightarrow{B(s)}$ is directly proportional to V_n, then $\overrightarrow{B(s)}$ will cancel out the variation that V_n causes in the PLL transfer functions. One way in order to achieve $\overrightarrow{B(s)}$ to be proportional to V_n is when $I_n = 0$; however, this is not the only way. If I_n is selected to be proportional

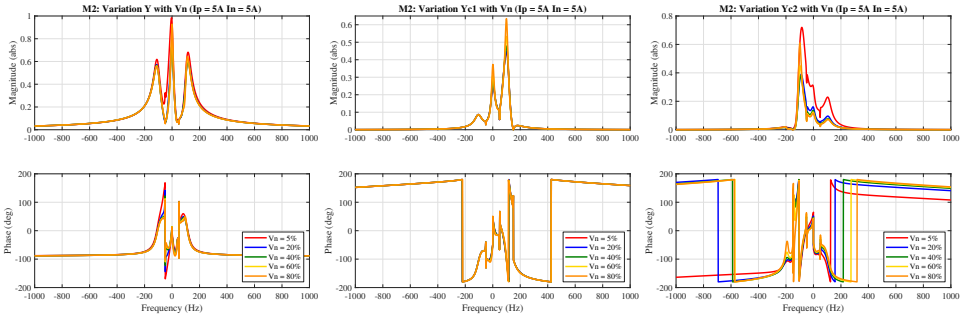

(a) (b) (c)

Figure 3.47: Effect of imbalance on the converter admittances when using the DDSRF-PLL method 2 and $I_{\mathrm{n}} = 5$ A; a) effect on main admittance, b) effect on first coupling admittance, and c) effect on second coupling admittance.

to V_{n}, then it can be seen in (3.18) that $\overrightarrow{B(s)}$ becomes proportional to V_{n}. The question, then, becomes whether it makes sense to inject negative-sequence current at all, or whether it makes sense to inject it proportional to the negative-sequence voltage. The answer to this question depends on the current-reference strategy.

(b) Effect of the current-reference strategy

According to the instantaneous power theory [174], the instantaneous active and reactive powers injected by the converter (p and q, respectively) have oscillating terms in the presence of imbalance and can be described by:

$$\begin{aligned} p &= P_0 + P_{\mathrm{c2}}\cos(2\omega_1 t) + P_{\mathrm{s2}}\sin(2\omega_1 t) \\ q &= Q_0 + Q_{\mathrm{c2}}\cos(2\omega_1 t) + Q_{\mathrm{s2}}\sin(2\omega_1 t) \end{aligned} \tag{3.30}$$

where P_0 and Q_0 are the average values of the instantaneous active and reactive powers, and P_{c2}, P_{s2}, Q_{c2} and Q_{s2} represent the magnitude of the oscillating terms in these instantaneous powers. The expressions of p and q can be expressed in terms of the voltage and current dq components as [44]:

$$\begin{aligned} P_0 &= \frac{3}{2}(V_{\mathrm{d+}}I_{\mathrm{d+}} + V_{\mathrm{q+}}I_{\mathrm{q+}} + V_{\mathrm{d-}}I_{\mathrm{d-}} + V_{\mathrm{q-}}I_{\mathrm{q-}}) \\ P_{\mathrm{c2}} &= \frac{3}{2}(V_{\mathrm{d-}}I_{\mathrm{d+}} + V_{\mathrm{q-}}I_{\mathrm{q+}} + V_{\mathrm{d+}}I_{\mathrm{d-}} + V_{\mathrm{q+}}I_{\mathrm{q-}}) \\ P_{\mathrm{s2}} &= \frac{3}{2}(V_{\mathrm{q-}}I_{\mathrm{d+}} - V_{\mathrm{d-}}I_{\mathrm{q+}} - V_{\mathrm{q+}}I_{\mathrm{d-}} + V_{\mathrm{d+}}I_{\mathrm{q-}}) \\ Q_0 &= \frac{3}{2}(V_{\mathrm{q+}}I_{\mathrm{d+}} - V_{\mathrm{d+}}I_{\mathrm{q+}} + V_{\mathrm{q-}}I_{\mathrm{d-}} - V_{\mathrm{d-}}I_{\mathrm{q-}}) \\ Q_{\mathrm{c2}} &= \frac{3}{2}(V_{\mathrm{q-}}I_{\mathrm{d+}} - V_{\mathrm{d-}}I_{\mathrm{q+}} + V_{\mathrm{q+}}I_{\mathrm{d-}} - V_{\mathrm{d+}}I_{\mathrm{q-}}) \\ Q_{\mathrm{s2}} &= \frac{3}{2}(-V_{\mathrm{d-}}I_{\mathrm{d+}} - V_{\mathrm{q-}}I_{\mathrm{q+}} + V_{\mathrm{d+}}I_{\mathrm{d-}} + V_{\mathrm{q+}}I_{\mathrm{q-}}) \end{aligned} \tag{3.31}$$

Therefore, imposing the instantaneous active and reactive power injected by the converter becomes a problem with 6 variables to control (P_0, Q_0, P_{c2}, P_{s2}, Q_{c2} and Q_{s2}) but only 4 degrees of freedom (I_{d+}, I_{q+}, I_{d-} and I_{q-}). In order to control the average active and reactive powers according to a certain set-point (i.e. in order to impose $P_0 = P_0^{ref}$ and $Q_0 = Q_0^{ref}$) there exist infinite combinations of possible currents to inject into the grid. Choosing the exact currents depends on the control objective, e.g. cancellation of the oscillations in the active or reactive power, injection of sinusoidal and balanced currents into the grid, etc. [175].

One common control objective is to use the 4 degrees of freedom to impose the desired $P_0 = P_0^{ref}$, $Q_0 = Q_0^{ref}$, and to cancel out the oscillations in p (i.e. $P_{c2} = P_{s2} = 0$). The advantage of such an approach is that the average values of active and reactive power can be controlled, and also that, since p is constant, the 100 Hz oscillations in the DC link voltage are minimized. This is beneficial from the hardware point of view (in particular, for the DC link capacitor). Unfortunately, since there are not enough degrees of freedom, in this approach it is not possible to cancel out the oscillations in q[8].

For example, the strategy described in [44] is based on imposing $P_0 = P_0^{ref}$ and $Q_0 = P_{c2} = P_{s2} = 0$. In the case of the current control structure in this thesis, since $V_{q+} = V_{q-} = 0$ in steady-state, this strategy leads to the following current references:

$$\begin{aligned} I_{d+ref} &= f(V_n) = \frac{2}{3} P_0^{ref} \frac{V_p}{V_p^2 - V_n^2} \\ I_{q+ref} &= 0 \\ I_{d-ref} &= g(V_n) = -\frac{2}{3} P_0^{ref} \frac{V_n}{V_p^2 - V_n^2} \\ I_{q-ref} &= 0 \end{aligned} \tag{3.32}$$

Since $I_{q+ref} = 0$, then $I_p = I_{d+ref} = f(V_n)$ and, since $I_{q-ref} = 0$, then $I_n = I_{d-ref} = g(V_n)$. As it can be seen in (3.32), in this current control strategy, I_n does not vary linearly with V_n; however, the variation is almost linear for a significant range of voltage imbalance values ($V_n < 75$ % approximately). This can be seen in Fig. 3.48, where I_{d+ref} and I_{q+ref} are plotted for a $P_0^{ref} = 1.17$ kW[9].

This means that, in this current control strategy, I_n is almost proportional to V_n, and

[8] In reality, it is possible to find current references that allow to control the exact instantaneous value of p and q (for example, to make both constant without any oscillation), no matter the voltage imbalance or the harmonics in the voltage. An example would be the Instantaneous Active-Reactive Control (IARC) strategy summarized in [175]. Nonetheless, even if the voltage has no harmonics, when the voltage is unbalanced, if it is desired to have p and q constant, it is necessary to inject a current with harmonics. This means that the current references in the dq channels are not constant. In a sense, this gives more degrees of freedom (not only the DC values but also the harmonics in the dq current references) that allow to cancel out simultaneously the p and q oscillations. However, having oscillating dq current references means that normal controls implemented in industry (based on PI controllers in the dq frame, like in this thesis) are not sufficient. Furthermore, the current control loop would need to have a high bandwidth to be able to inject such harmonics, which might not be possible in high-power applications where the switching frequency is limited. Finally, the disadvantage of such an approach is that it might affect the voltage distortion at the PCC or trigger resonances in the network. Therefore, this strategy is not considered in this thesis. In this thesis, it is considered that, in order to counteract the effects of voltage imbalance, only currents (in the positive and/or negative sequence) at 50 Hz are to be used. If that is the case, then (3.30) and (3.31) apply. In this case, there is only 4 degrees of freedom given by the d and q (steady-state constant)

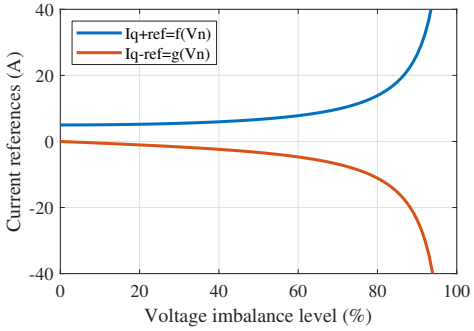

(a)

Figure 3.48: Current-reference strategy following (3.32).

therefore the $\overrightarrow{B(s)}$ becomes almost proportional to V_{n}, making the converter admittances almost independent on V_{n}. This can be seen in Fig. 3.49 for the converter using the DDSRF-PLL method 1, and in Fig. 3.50 for the converter using the DDSRF-PLL method 2.

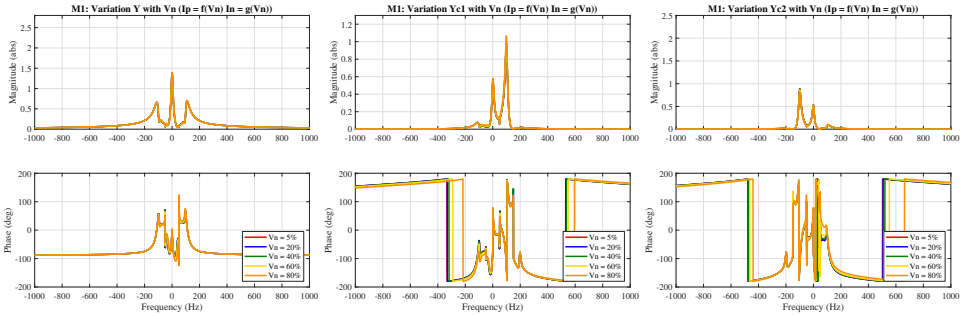

(a) (b) (c)

Figure 3.49: Influence of imbalance on the converter admittances when using the DDSRF-PLL method 1, and when the current-reference strategy follows (3.32); a) effect on main admittance, b) effect on first coupling admittance, and c) effect on second coupling admittance.

Apart from the current-reference strategy used in [44] and outlined in (3.32), there are other current-reference strategies, like the Balanced Positive-Sequence Control (BPSC), which consists in imposing $I_{\mathrm{n}} = 0$ to achieve balanced positive-sequence currents no matter the voltage imbalance level [175]. This strategy also leads to a passivity index independent on V_{n}, as mentioned before.

Furthermore, in recent years, more research has been done in relation to current-reference strategies but, instead of focusing on selecting the current references to influence the constant and oscillatory terms of the instantaneous active and reactive powers, the interest has

references in the positive and negative SRF in the current control.

[9]This is the power that, following (3.32) produces an $I_{\mathrm{d+ref}} = 5$ A when $V_{\mathrm{n}} = 0$ for the V_{p} considered in this thesis.

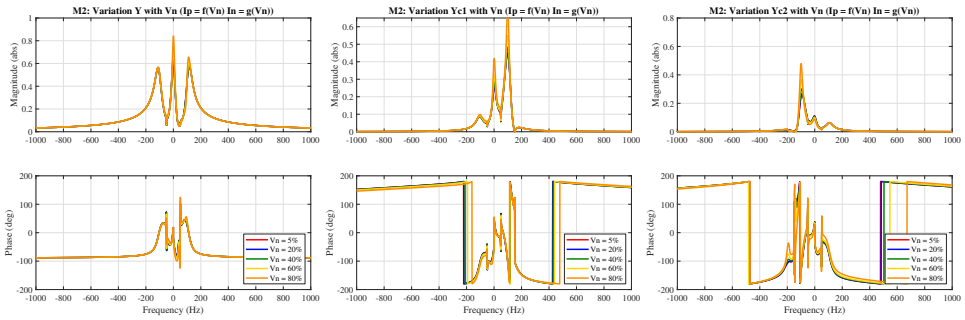

(a) (b) (c)

Figure 3.50: Influence of imbalance on the converter admittances when using the DDSRF-PLL method 2, and when the current-reference strategy follows (3.32); a) effect on main admittance, b) effect on first coupling admittance, and c) effect on second coupling admittance.

shifted into selecting the current references for performing grid support functionalities (typically, voltage support) in the presence of imbalance. Recent literature has shown that optimal grid support is not given when the converter delivers reactive power only in the positive sequence because, among other reasons, this can boost the voltage in non-faulty phases and cause over-voltage problems [45]. Therefore, future grid codes are contemplating to include reactive power requirements during faults in both sequences (typically, to deliver reactive power in the positive sequence to boost the positive sequence voltage, while simultaneously absorbing reactive power in the negative sequence to reduce the negative sequence voltage) [45]. The research into these topics is ongoing although, as pointed out in [45], in future grid codes, in addition to the demand to stay connected, the installed generators should inject positive- and negative-sequence reactive current proportional to the change in positive- and negative-sequence voltage.

If, indeed this is the case and I_{n} is selected proportional to V_{n}, then the passivity index in such a converter would be independent on V_{n}. It is worth to note that, in practice, the current-reference strategies are typically piece-wise functions, in the sense that they might follow a function but saturate at different levels due to grid-code requirements or converter current limits.

3.12.2 Analysis of the converter passivity

Section 3.12.1 shows how the current-reference strategy influences how the admittances change with V_{n}. The admittances changing with voltage imbalance is not necessarily detrimental for the converter stability; in order to analyse the effect of V_{n} on the converter tendency for small-signal instability it is necessary to analyse the converter passivity. The definition of converter passivity is found in Section (a).

(a) Effect of V_n and I_n

The passivity index is plotted for different imbalance levels in Fig. 3.51 for the converter using the DDSRF-PLL method 1 and in Fig. 3.52 when using method 2.

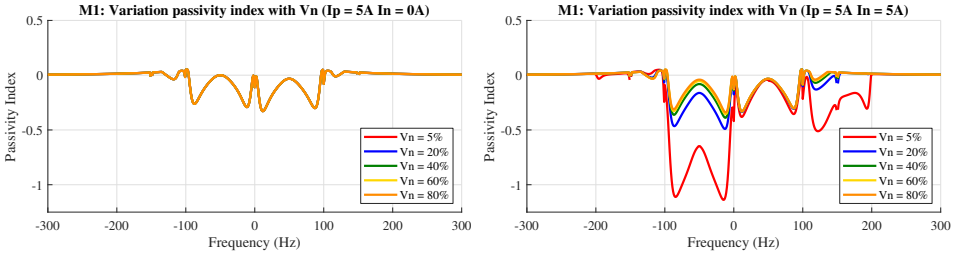

(a) (b)

Figure 3.51: Influence of imbalance on the converter passivity index when using the DDSRF-PLL method 1.

Fig. 3.51 shows that, when $I_n = 0$, the voltage imbalance does not affect the passivity of the converter. This makes sense because, if the admittances are constant with V_n (see Fig. 3.44), then the admittance matrix does not change with V_n, and thus the passivity of the converter becomes independent of V_n (see Section (a)). Fig. 3.51 b) shows that, when $I_n \neq 0$, the passivity of the converter depends on V_n.

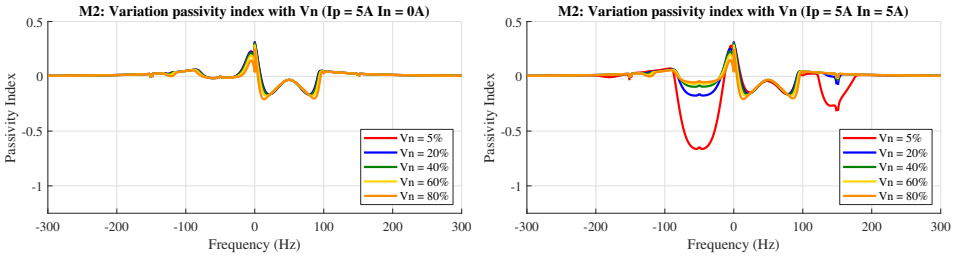

(a) (b)

Figure 3.52: Influence of imbalance on the converter passivity index when using the DDSRF-PLL method 2.

With respect to the converter when using the DDSRF-PLL method 2, the effect of V_n on the passivity index is shown in Fig. 3.52. In this case, the passivity index is also quite constant when $I_n = 0$ but not for $I_n \neq 0$.

(b) Effect of the current-reference strategy

It is argued in Section 3.12.1 that, with the current-reference strategy shown in (3.32), I_n is almost proportional to V_n in a wide range of imbalance levels, which makes the $\overrightarrow{B(s)}$ to become almost proportional to V_n, therefore making the admittances almost independent on V_n. This makes the passivity index almost independent on V_n, as shown in Fig. 3.53 for

the converter using the DDSRF-PLL method 1, and in Fig. 3.54 for the converter using the DDSRF-PLL method 2.

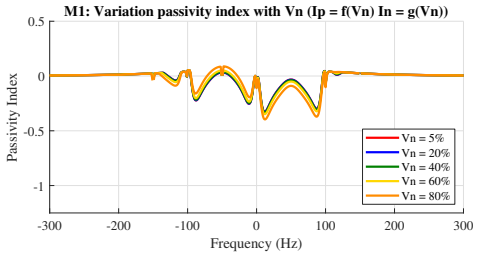

(a)

Figure 3.53: Influence of imbalance on the converter passivity index when using the DDSRF-PLL method 1, and when the current-reference strategy follows (3.32).

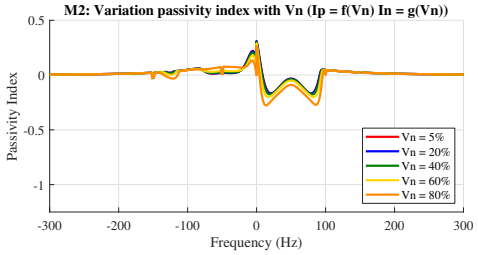

(a)

Figure 3.54: Influence of imbalance on the converter passivity index when using the DDSRF-PLL method 2, and when the current-reference strategy follows (3.32).

Again, there are many other current-reference strategies that could be implemented, which depend on hardware constraints, grid codes, and other factors. The important conclusion that this chapter shows, however, is that the influence of the voltage imbalance on the passivity of the converter occurs not only through the PLL structure, but also through the current-reference strategy. On the other harnd, it can be argued that, in reality, the influence of the PLL structure is double, since the values of V_{n} and V_{p} used to calculate the current references come also from the PLL. In this case, it can be argued that the voltage imbalance always influences the converter dynamics through the PLL, since the PLL-estimated voltage phase-angles affect the dq transformations in the current control, and since the PLL-estimated voltage magnitudes affect the generation of the current references. Indeed, this is a subject that deserves more attention in future work.

3.12.3 Analysis of the grid-connected converter

(a) Effect of V_{n} and I_{n}

The stability analysis of the grid-connected converter can be performed with Nyquist eigenlogi plots for different levels of V_{n}. This is shown for the converter using the DDSRF-PLL

method 1 in Fig. 3.55 and the DDSRF-PLL method 2 in Fig. 3.56. These plots confirm the analysis performed with the passivity index: when $I_{\mathrm{n}} = 0$, the stability of the converter is not affected (or almost not affected in the case of M2) by V_{n}; whereas if $I_{\mathrm{n}} \neq 0$ this is no longer the case.

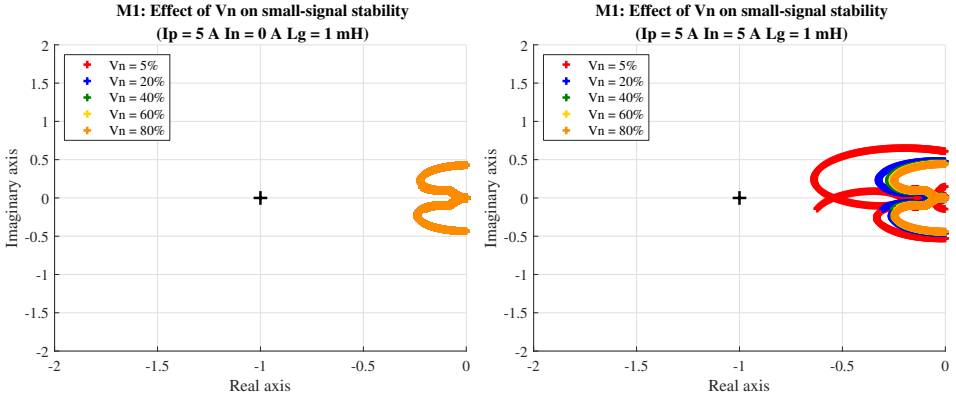

Figure 3.55: Effect of imbalance on the stability of the grid-connected converter (DDSRF-PLL method 1).

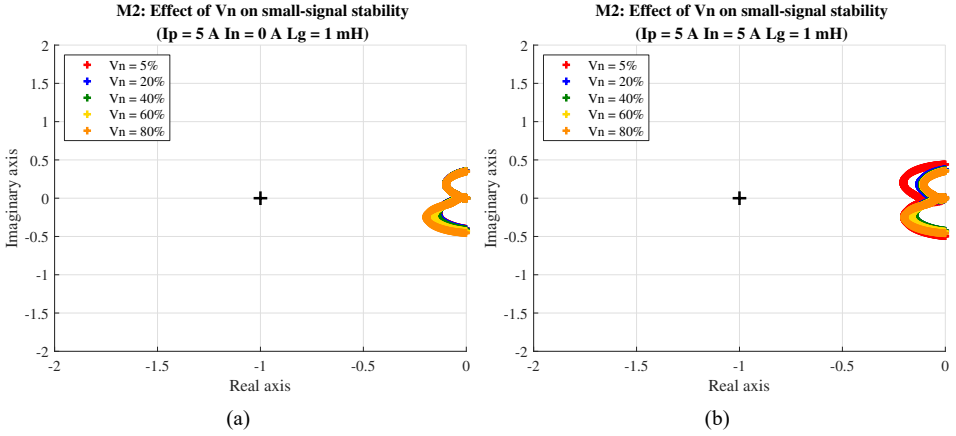

Figure 3.56: Effect of imbalance on the stability of the grid-connected converter (DDSRF-PLL method 2).

(b) Effect of the current-reference strategy

If the current-reference strategy shown in (3.32) is applied, the nyquist plots of the interconnected converter are shown in Fig. 3.57 and Fig. 3.58. These figures confirm the passivity analysis that states that such current-reference strategy makes the small-signal stability of the converter (almost) independent on V_{n}.

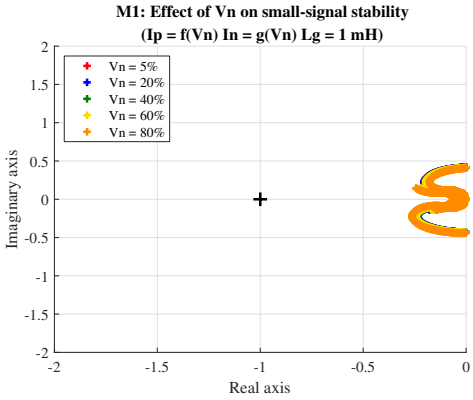

(a)

Figure 3.57: Influence of imbalance on the stability of the grid-connected converter when using the DDSRF-PLL method 1, and when the current-reference strategy follows (3.32).

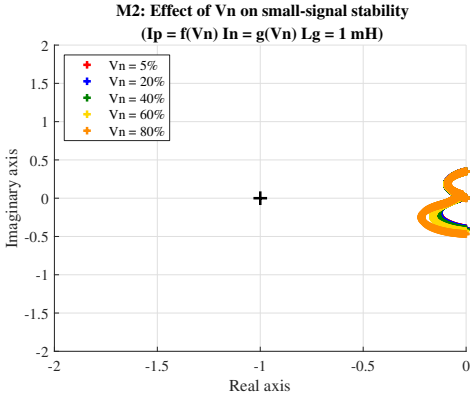

(a)

Figure 3.58: Influence of imbalance on the stability of the grid-connected converter when using the DDSRF-PLL method 2, and when the current-reference strategy follows (3.32).

(c) Effect of grid impedance

In Fig. 3.55 – Fig. 3.58 the converter is far from harmonic instability. This could lead to the thought that the converter will not become small-signal unstable for any imbalance level. However, the stability margin depends also on the grid strength. This is exemplified in Fig. 3.59 and Fig. 3.60. As the grid impedance increases (L_g and its parasitic resistance, as shown in Fig. 3.30) the converter approaches the point $(-1,0)$. This exemplifies the importance of the Short-Circuit Ratio (SCR) for grid-following inverters connected to the grid.

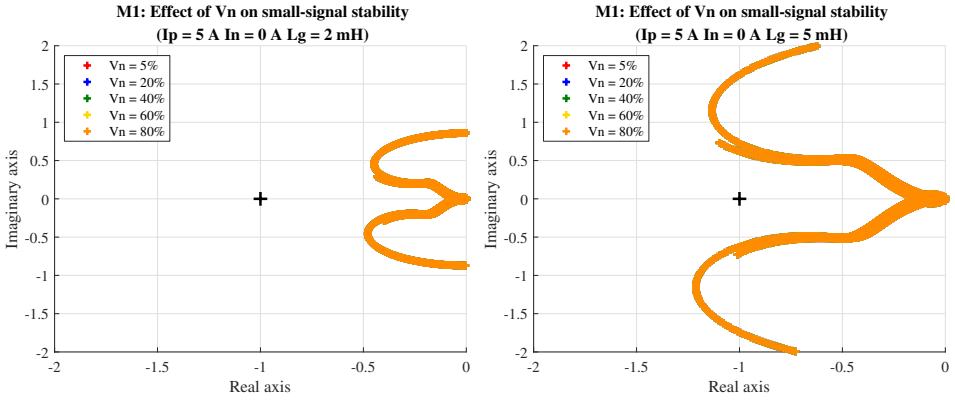

Figure 3.59: Effect of grid strength on the stability of the grid-connected converter (DDSRF-PLL method 1).

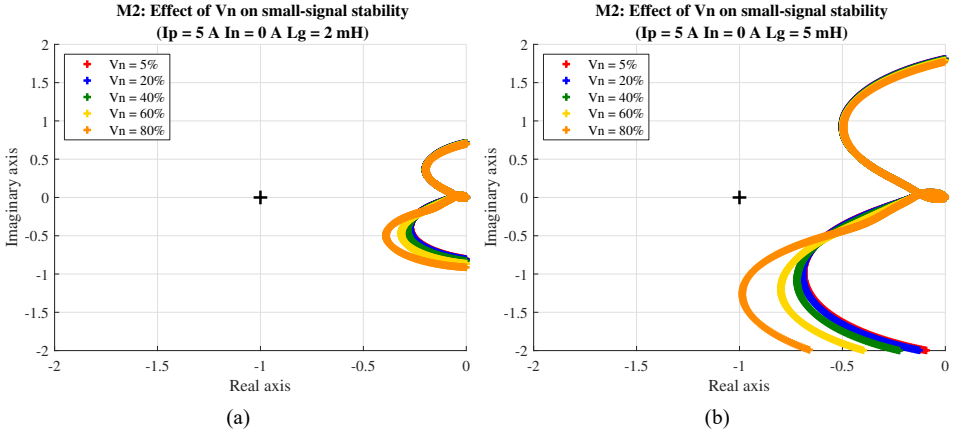

Figure 3.60: Effect of grid strength on the stability of the grid-connected converter (DDSRF-PLL method 2).

3.13 Effect of grid voltage imbalance on the harmonic emission of the wind turbine converter

The harmonic model of a wind turbine converter typically consists of a Norton equivalent containing: a current source, that represents the distortion that the converter generates no matter the grid distortion, and an impedance or admittance, that represents the current the converter generates as a consequence of harmonics in the voltage (more details in Chapter 4).

The Total Harmonic Distortion (THD) is usually defined as the relative signal energy present at non-fundamental frequencies [176], definition which can be applied for both voltage and current. If the THD is to be analysed in the current that comes from a converter

(THD_I), it is possible to separate the distortion that appears due to the current source in the Norton equivalent (I_N) from the distortion that appears due to the admittances in the Norton equivalent (I_Y), as shown in (3.33).

$$\text{THD}_\text{I} = \frac{1}{I_1}\sqrt{\sum I_h^2} = \frac{1}{I_1}\sqrt{\underbrace{\sum I_\text{N}^2}_{\text{Due to current source}} + \underbrace{\sum I_\text{Y}^2}_{\text{Due to admittances}}} \tag{3.33}$$

If there is imbalance in the voltage, both elements in the model (current source and impedance/admittance) could get affected. Nevertheless, the focus of this section is the impedance and coupling admittances. For a voltage harmonic at f_h and magnitude V_h, the magnitude of the harmonics in the current due to the admittances are given by: $|\overrightarrow{Y(s)}|V_\text{h}$ for the current harmonic at f_h, $|\overrightarrow{Y_{c1}^*(s = j2\pi(f_\text{h} - 2f_1))}|V_\text{h}$ for the current harmonic at $2f_1 - f_\text{h}$, and $|\overrightarrow{Y_{c2}^*(s = j2\pi(f_\text{h} + 2f_1))}|V_\text{h}$ for the current harmonic at $-2f_1 - f_\text{h}$.

Therefore, by using the admittance models, it is possible to calculate the I_Y distortion that is generated in the current as a consequence of a harmonic in the voltage, and see if this extra distortion is modified by grid voltage imbalance. For an input frequency f_h in the voltage, the extra distortion in the current is:

$$\sum I_\text{Y}^2(s) = (|\overrightarrow{Y(s)}|^2 + |\overrightarrow{Y_{c1}^*(s - j2\omega_1)}|^2 + |\overrightarrow{Y_{c2}^*(s + j2\omega_1)}|^2)V_\text{h}^2. \tag{3.34}$$

For a voltage harmonic of magnitude $|V_\text{h}| = 1\,\text{V}$, the current distortion $\sum I_\text{Y}^2$ can be plotted for different values of V_n in Fig. 3.61 for the converter that uses the DDSRF-PLL method 1, and in Fig. 3.62 for the converter that uses the DDSRF-PLL method 2.

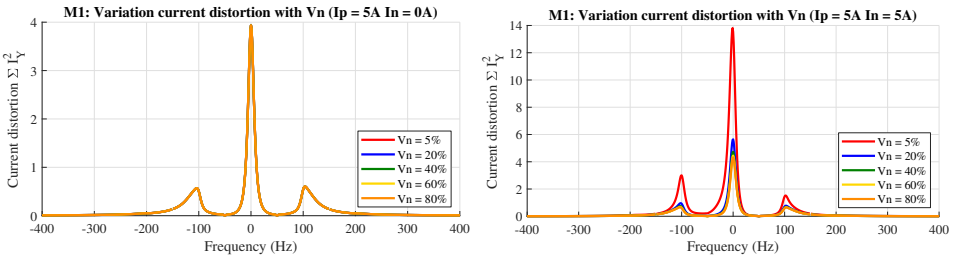

(a) (b)

Figure 3.61: Influence of imbalance on the current distortion when using the DDSRF-PLL method 1.

Section 3.12.1 shows that the negative-sequence voltage might affect the converter admittances depending on the value of I_n. However, it can be seen in Section 3.12.1 that the admittances are modified mostly in the lower frequency range ($f < 150\,\text{Hz}$ or less). In the harmonic frequency range, the converter admittances do not vary as much. What Fig. 3.61 and Fig. 3.62 show is that, indeed, no matter the value of I_n, the distortion that will appear in the current as a consequence of the coupling admittances does not change much with the negative-sequence voltage, no matter the DDSRF-PLL method used.

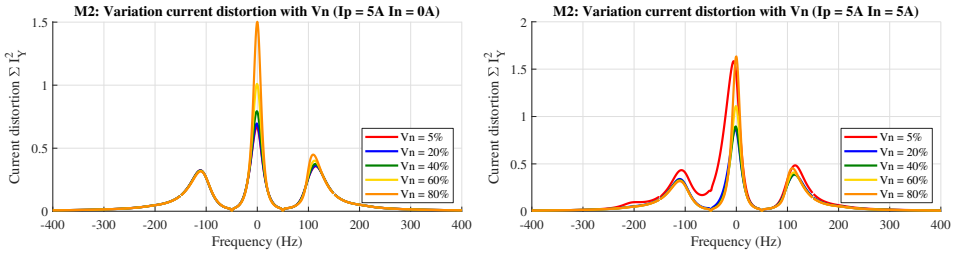

(a) (b)

Figure 3.62: Influence of imbalance on the current distortion when using the DDSRF-PLL method 2.

3.14 Conclusions

The objective of this chapter is to analyse the impact of voltage and current imbalance on the stability and harmonic behaviour of a wind turbine converter. The chapter starts by introducing a common current control strategy in wind turbine converters (the double SRF control structure). Then, the whole converter is modelled and linearised using this current control structure and a DDSRF-PLL. In particular, the two DDSRF-PLL methods introduced in Chapter 2 are considered. The model is verified with simulations and validated with experiments. The model shows that, due to the use of the negative-sequence voltage phase-angle in the current control, an additional frequency coupling at $-2f_1 - f_\mathrm{p}$ (that is not reported in the literature before) appears. This second frequency coupling is mostly due to the fact that the PLL structure is dq asymmetrical, and not that much due to the LTP dynamics of the PLL in the presence of imbalance.

Furthermore, the converter is modelled using two types of PLL models: the LTI and LTP models developed in Chapter 2. This leads to different expressions for the main admittance and coupling admittances of the converter. Then, the chapter performs a small-signal stability analysis to identify which model is accurate in the presence of imbalance. It is shown that it is necessary to use the LTP model of the DDSRF-PLL if the stability analysis is to be performed in a wide-range of voltage imbalance values.

In particular, an example is shown in which the coupling admittances of the converter do not impact significantly the result of the stability analysis, and still, the converter model that uses the LTP PLL model gives more accurate results than the converter model that uses the LTI PLL model. This is due to the fact that the main admittance changes depending on whether the LTP or LTI PLL models are used. Therefore, this chapter shows that considering the LTP dynamics in the presence of imbalance is important not due to the coupling dynamics, but do to the fact that the main dynamics of the converter change.

Since the converter model that uses the LTP dynamics of the PLL is considered accurate for stability analysis, the influence of voltage and current imbalance on the stability of the converter is analysed using this model. The results show that the passivity of the converter depends not only on the V_n level, but also on the I_n level. This means that the current-reference strategy has a considerable influence in determining the passivity of the converter. In particular, it is shown that, for the PLL and current control structures analysed,

if $I_{\mathrm{n}} = 0$ or if I_{n} is selected proportional to V_{n}, the passivity of the converter becomes almost independent on V_{n}. As discussed in this chapter, this occurs for several widely-implemented current-reference strategies.

With respect to harmonic studies, it is shown here that using the LTI model of the PLL already gives accurate frequency sweeps for the converter admittances in the harmonic range. Therefore, using both the LTI or LTP model of the PLL for harmonic analysis is acceptable at the converter level. The voltage imbalance has been shown to not impact significantly the harmonics generated in the converter current as a consequence of a distortion in the voltage (i.e. the distortion due to the converter admittances).

Chapter 4

Harmonic Distortion Enabling Monte Carlo vs Summation Law

Nowadays, the main push for studying steady-state harmonics in Offshore Wind Power Plants (OWPPs) comes from compliance requirements. In essence, when a new installation is planned to be connected to the HV grid, the Transmission System Operator (TSO) has to impose limits on the post-connection voltage harmonics at the Point of Common Coupling (PCC) in order to avoid disturbances to other connectees. As a consequence, the wind farm developer is required to perform harmonic studies to show that these limits are not exceeded.

However, it has been recently reported that certain approaches that are commonly used for these harmonic studies (particularly, those based on the IEC standard and its Summation Law) do not deliver accurate results when compared to actual measurements performed once the wind farm is operational. As a result, new methods for performing harmonic studies are being proposed in the literature. One that has gathered increasing attention is the Monte Carlo method. This thesis investigates different statistical aspects that may affect the results of harmonic studies when performing Monte Carlo simulations. Further, this thesis addresses the impact of the frequency couplings in the wind-turbine generator (WTG) grid-side converter.

4.1 Introduction

The issue of harmonic distortion in wind farms has been thoroughly studied in the past decades [32]. As explained in Chapter 1, the harmonic sources (i.e., the wind turbine generators (WTGs), the grid background distortion, or the possible HVDC converters) in offshore wind farms are not particularly polluting when analysed separately. However, high amplification of these harmonic distortions might occur in the presence of resonances. The resonances depend on the grid and wind farm configuration, so the resonant frequencies and quality factors might vary during the normal operation of the wind farm. On top of the possible amplification/reduction effects, it is possible to see cancellation/summation effects; when two harmonic currents converge in the same busbar, the resulting current might be the algebraic sum of these two harmonic currents if the phase-angles are exactly equal, or might be the subtraction if the phase-angles of the two harmonic currents are exactly opposite. An overview of these phenomena is shown in Fig. 4.1.

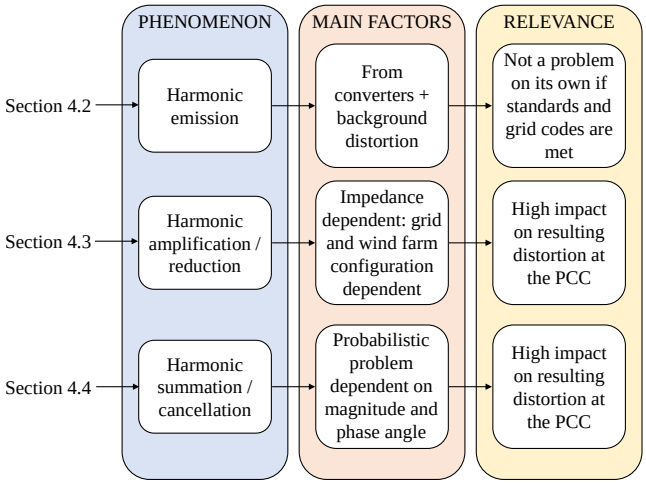

Figure 4.1: Harmonic phenomena in offshore wind power plants.

The process of harmonic generation and propagation in offshore wind farms is already understood in the literature, and remedial measures have already been explored and applied in real systems (a brief review is found in Chapter 1). However, one challenge that still remains is the issue of modelling and prediction. When undergoing the permitting process of an offshore wind farm, different harmonic studies are usually required to prove compliance with grid-code harmonic requirements. Based on these studies, a decision can be made on whether a remedial measure (passive or active) is required. One of the main uncertainties that the industry faces nowadays with respect to harmonic compliance is how well these studies are able to model and predict the real distortion that will eventually appear at the PCC of the wind farm once operation starts. As an example, several studies have shown that the calculation of the harmonic distortion using widely-accepted methods in industry has lead to significantly inaccurate distortion predictions when compared to measurements [177–179].

Consequently, significant efforts have been placed in recent years for improving the

modelling and simulation of harmonics in offshore wind farms. These efforts have been focused in the three phenomena summarized in Fig. 4.1: harmonic emission, harmonic amplification/reduction and harmonic summation/cancellation.

Firstly, in order to improve the modelling of the WTG harmonic emission, investigations on the origin and classification of the WTG distortion have been made [180]. Consequently, the WTG harmonic model has evolved in recent years. Instead of using a simple current source for the WTG representation, nowadays it is a widely accepted practice [181] to consider a more elaborated model consisting on a current or voltage source and an impedance (Norton or Thevenin equivalent), as required in IEC61400-21-3:2019. Further, the statistical variability of the harmonic emission of a WTG has been identified as crucial for accurate WTG modelling as a harmonic source [177]. These topics are addressed in Section 4.2.

Secondly, in order to predict the amplification/reduction of harmonics in the farm it is required to accurately characterize all the other wind farm components (transformers, cable systems, etc.) in a wide frequency range. Thus, several studies have been made on the matter, resulting in tangible recommendations [182, 183]. The topic of harmonic amplification/reduction and its modelling is addressed in Section 4.3.

Nowadays, most efforts are focused on the third aspect in Fig. 4.1: the cancellation or summation effects. One common approach in industry is to use the Summation Law described in IEC61000-3-6 [184], where the probability of the summation or cancellation of a harmonic is simplified by the use of an exponent. An alternative is to use a full statistical representation of the harmonic sources, which requires statistical methods for harmonic assessment like Monte Carlo simulations [185]. Section 4.4 briefly compares the most common methods for harmonic summation studies (IEC Summation Law vs Monte Carlo).

In this chapter, different aspects of the modelling of WTGs as probabilistic harmonic sources are addressed: from correlation of different random variables to the effect of considering converter-generated frequency couplings. The results from the wind-farm level harmonic studies can be found in Section 4.5. Conclusions are summarized in Section 4.6.

4.2 Wind turbine harmonic model and emission

4.2.1 Classification of WTG harmonics due to their origin

The harmonic emission produced by a WTG is mostly due to three sources:

1. The switching and modulation strategy;
2. The switching dead-time;
3. Power hardware effects such as: manufacturing tolerances, different voltage drop characteristics in IGBTs and diodes, PWM command edge resolution, gate driver dynamics, temperature effects, and others.

These sources of emission are usually called “characteristic emissions” of the WTG, since the WTG produces them no matter what is the status of the grid to which it is connected (i.e., this distortion is an intrinsic characteristic of the WTG)[1].

[1] In some classifications, the third item in the list (power hardware effects) are considered as non-characteristic

Additionally to these three harmonic sources, the WTG can produce extra harmonics, usually called "non-characteristic" harmonics, as a consequence of being connected to a non-sinusoidal or unbalanced grid. In this phenomenon, the controls of the WTG grid-side converter play an important role. As illustrated in Fig. 4.2, the background distortion can produce voltage and current harmonics at the Point of Connection (PoC). These harmonics are measured by the WTG, and fed into the WTG software, from where the distortion can cripple through the different control loops until distortion appears on the modulating signal, effectively ensuring that the current produced by the WTG is also distorted.

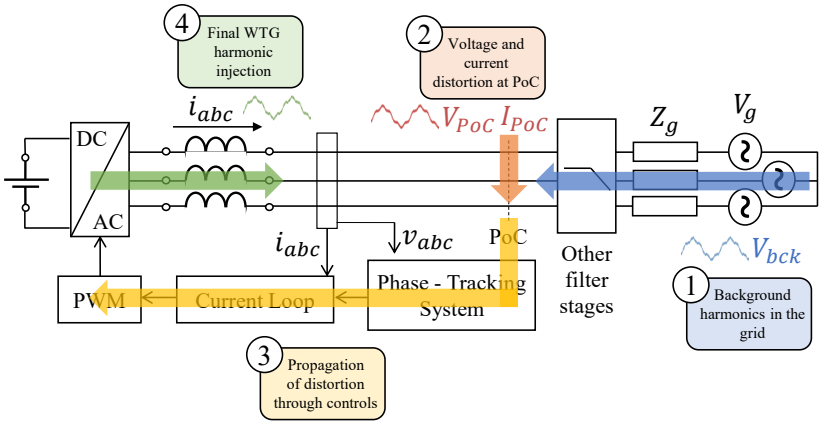

Figure 4.2: Propagation of grid background harmonic distortion to WTG harmonic distortion.

Thus, these non-characteristic harmonics are a consequence of the grid distortion, and are not due to an inner source within the WTG. Consequently, the same WTG can produce different harmonic currents depending on the exact grid point to which is connected, phenomenon that is already acknowledged in the literature. Additionally, the variation of the grid impedance also has an impact. The example shown in [180] (repeated in Fig. 4.3 for convenience) shows that the grid effect is non-negligible.

Nowadays, the most common approach to model this effect is to represent the WTG as a Norton equivalent, in which the current source represents the characteristic emission, while the impedance represents the harmonics that the WTG produces as a consequence of the background distortion. In this sense, the impedance can be interpreted as a linear mapping between the background distortion at the POC and the current response of the WTG. This phenomenon is in reality non-linear, but the linearity assumption (using an impedance) is a common approach in industry.

When measuring the harmonic emission of a WTG, a common issue is how to measure the characteristic emission only, ensuring that the currents measured are not induced by the background distortion in the grid. In order to ensure this, in recent years it has been proposed to measure the voltage and current at the terminals of the connection of the WTG, because, if the impedance is known (this can be measured, calculated analytically, or calculated via

harmonics, e.g., [180]. In [186], the asymmetry in the dead-time error pulses, the non-linearity of the switching devices and the semi-conductor voltage drops are also considered sources of non-characteristic harmonics.

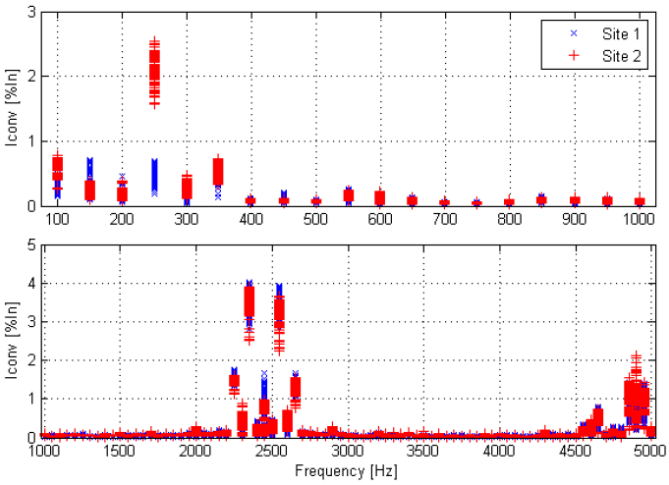

Figure 4.3: Example of the current harmonic spectrum from a commercial wind turbine at different measurement sites [180]. The site-dependence is due to the different local background distortion or grid impedance.

simulation-based frequency sweeps), the characteristic harmonics can be calculated. Looking at the nomenclature in Fig. 4.4, the WTG characteristic harmonics (represented by the current source in the Norton equivalent) can be calculated using (4.1).

$$\mathbf{I_{WT}(\omega) = I_{POC}(\omega) + \frac{V_{POC}(\omega)}{Z_{WT}(\omega)}} \tag{4.1}$$

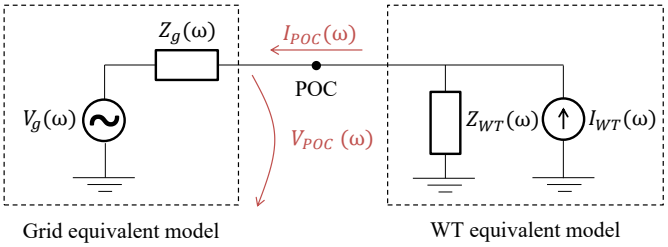

Figure 4.4: Measurement of wind turbine characteristic harmonic emission.

4.2.2 Classification of harmonics due to their frequency

Within the characteristic harmonics enumerated above, the biggest contributor is the switching of the converter semiconductors. Several works have been performed in order to quantify this emission analytically [187]. As an example, for a three-phase two-level voltage source converter with double-edge asymmetrically regular sampled pulse-width modulation (PWM), the phase-to-ground output voltage (at the switching terminals) can be represented as follows (no dead-time considered) [37]:

$$
\begin{aligned}
v_{az}(t) = {} & \frac{2V_{\mathrm{DC}}}{\pi}\sum_{n=1}^{\infty}\frac{1}{n\frac{\omega_0}{\omega_\mathrm{c}}}J_n\Big(n\frac{\omega_0}{\omega_\mathrm{c}}\frac{\pi}{2}M\Big)\sin(n\frac{\pi}{2})\cos(n[\omega_0 t+\theta_0]) \\
& +\frac{2V_{\mathrm{DC}}}{\pi}\sum_{m=1}^{\infty}\frac{1}{m}J_0\Big(m\frac{\pi}{2}M\Big)\sin(m\frac{\pi}{2})\cos(m[\omega_\mathrm{c} t+\theta_\mathrm{c}]) \\
& +\frac{2V_{\mathrm{DC}}}{\pi}\sum_{m=1}^{\infty}\sum_{\substack{n=-\infty \\ n\neq 0}}^{\infty}\frac{1}{[m+n\frac{\omega_0}{\omega_\mathrm{c}}]}\begin{bmatrix}J_n\Big([m+n\frac{\omega_0}{\omega_\mathrm{c}}]\frac{\pi}{2}M\Big)\sin([m+n]\frac{\pi}{2}) \\ \times\cos(m[\omega_\mathrm{c} t+\theta_\mathrm{c}]+n[\omega_0 t+\theta_0])\end{bmatrix}
\end{aligned}
\tag{4.2}
$$

where V_{DC} is the DC voltage, M is the modulation index, ω_0 is the frequency of the modulation signal (which, in steady-state, should be equal to the fundamental frequency), θ_0 is the phase angle of the modulation signal (which might vary depending on the desired active and reactive power injection), ω_c is the carrier frequency, θ_c is the phase angle of the carrier signal, and J_n represents the Bessel function of the n^{th}-kind.

In (4.2), the first line represents the so-called "baseband harmonics", the second one the "carrier harmonics", and the third the "sideband harmonics". The baseband harmonics appear at multiples of the fundamental frequency, and tend to be stronger in the lower frequency range (5^{th}, 7^{th}, etc.). The carrier harmonics appear at multiples of the carrier frequency, and thus appear in the high frequency range (depending on the switching frequency). The sideband harmonics appear around the multiples of the carrier frequency, like bands on the sides that separate from the carrier frequency by multiples of the fundamental frequency.

Harmonics can be classified according to their frequency also into "even harmonics" or "odd harmonics". Even harmonics can only appear in a signal if the positive half-wave is not exactly symmetrical to the negative half-wave. In traditional power systems, even harmonics were traditionally considered very low or zero. Nowadays, however, it is known that power-electronic converters can produce even harmonics (albeit usually smaller than odd harmonics)[2], and thus they are always considered in harmonic studies.

Another common term is "triplen harmonics", which is assigned to harmonics whose order is a multiple of 3 from the fundamental. Sometimes, this term is used interchangeably with "zero sequence harmonics", however, this is misleading. Suppose that a signal has an arbitrary number of harmonics and phase displacements between the harmonics for phase A. Then, for phase B and C the same signal is imposed but shifted 6.67 ms and 13.33 ms, respectively (which correspond to $\frac{2\pi}{3}$ and $\frac{4\pi}{3}$ at 50 Hz). In that case, all the harmonics will appear in their so-called "natural sequence", which is: $+,-,0,+,-,0,+,-$, etc. for the harmonics: 1^{st}, 2^{nd}, 3^{rd}, 4^{th}, 5^{th}, etc. This is shown graphically in Fig. 4.5 and summarized in Table 4.1.

A lot of physical devices connected to the grid follow the phase-shifting pattern between phases A, B and C, and therefore, it is common that harmonics appear in their natural sequence. This situation occurs, for example, in three-phase diode rectifiers when confronted

[2]This can be due, for example, to the asymmetry in the dead-time error pulses [188].

Table 4.1: Natural sequence of harmonics.

Harmonic order	1	2	3	4	5	6	7	8	9
Natural sequence	+	−	0	+	−	0	+	−	0

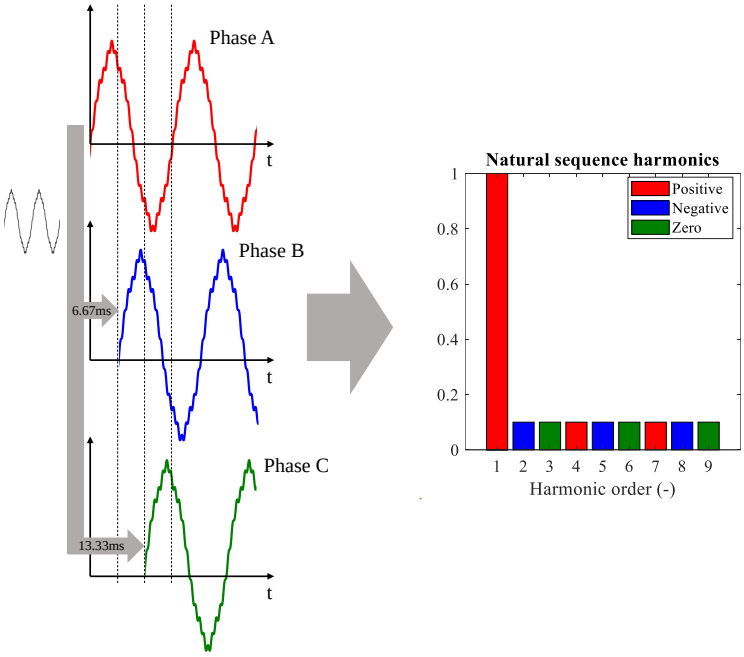

Figure 4.5: Condition to be met to have harmonics exclusively in their natural sequence.

to a perfectly balanced voltage. Since this rectifier is driven by the voltage (which in this case is ideal), it generates exactly the same current in each phase, but shifted in the time domain. However, not all devices follow this same pattern, and thus harmonics appear frequently also in sequences other than their natural sequence. For example, in a three-phase inverter with complex current control this behaviour is not necessarily followed, even if the voltage is ideal. Thus, for many converters, it is possible to generate triplen harmonics that do not appear in the zero sequence and, in general, harmonics that do not appear in their natural sequence. Also, even if the harmonic pollution sources would produce harmonics only in their natural sequence (these harmonics are also usually called “balanced harmonics”), if the impedance network is unbalanced, the harmonics would change their sequence and appear at other sequences (thus the terminology “unbalanced harmonics”).

Finally, note that in a three-wire system, the zero-sequence currents cannot flow. Due to the fact that the triplen harmonics usually appear in the zero sequence, it is usually assumed that triplen harmonic currents cannot appear. However, if the harmonic appears in another sequence, it will be able to flow. Thus, in a converter-based power system, triplen harmonics might propagate.

4.2.3 Statistical variability of the WTG harmonics

As explained in Section 4.2.1, if the output harmonics of a WTG are measured, the values will present some variability due to the background harmonic distortion. However, even if the effect of the background harmonic distortion is decoupled and the characteristic harmonics are calculated, the characteristic harmonics will present some statistical variability. An example can be found in [177] and is repeated in Fig. 4.6, where the voltage and current harmonics at the POC of a WTG have been measured, and the characteristic harmonics have been back-calculated (in this case, [177] models the WTG as a Thevenin equivalent instead of Norton, and thus Fig. 4.6 shows voltage magnitudes and phase angles). Fig. 4.6 shows that both the magnitude and phase angle of the characteristic harmonics have a clear statistical variation.

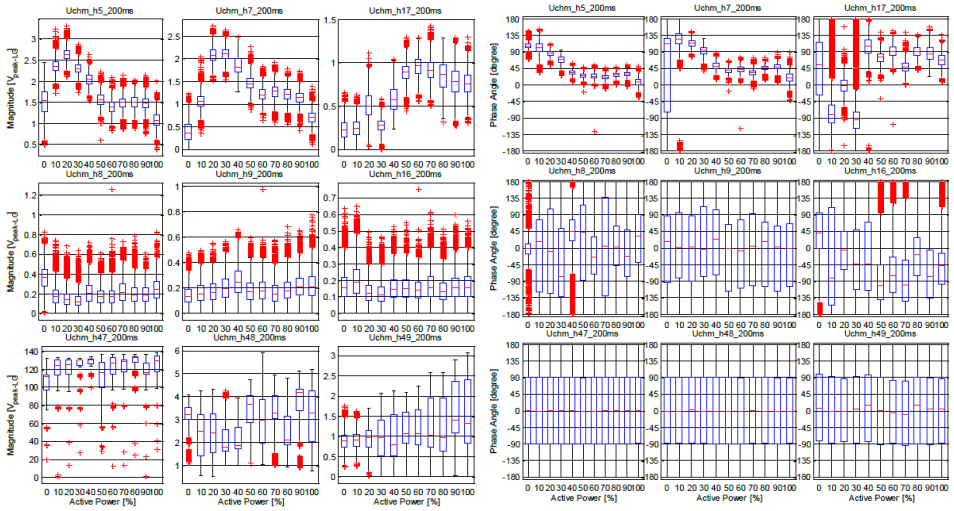

Figure 4.6: Measurement example of the statistical variability of the WTG characteristic harmonics: (a) magnitude variation and (b) phase angle variation [177].

The exact reasons for this statistical variability depend on the modulation strategy used in the WTG, the dead-time implemented, and many other factors. In general, any conclusion about the statistical properties or correlation of the harmonics of a WTG must be device-dependent. Nonetheless, since a significant part of the WTG emission is due to the switching and modulation strategies, a lot of conclusions can be drawn from analytical expressions found in the literature about these strategies. As a generic example, a double-edge asymmetrically regular sampled PWM strategy[3] is briefly analysed here using the expression in (4.2)[4].

[3]For example, PWM is considered for WTGs in [180], although this is not necessarily a true assumption for all commercial units.

[4]Note that, still, a converter has other important emission sources (such as dead-time or manufacturing tolerances) which are not considered in (4.2).

Firstly, it can be seen in (4.2) that the modulation index, M, can modify the magnitude of the harmonics, and that this effect is non-linear: the M appears always inside Bessel functions. This helps to explain why a converter might have a different distortion at different operating points, even if the distortion is expressed as a percent of the fundamental. Further, recent literature has shown that the magnitude of harmonics related to the switching dead-time (which are not considered in (4.2)) also depend on the operating point of the converter [188].

In practice, WTG manufacturers tackle this effect by providing the harmonic emissions of the WTG at different operating points (just as it is done in Fig. 4.6). For example, the emission per harmonic order can be provided for the operating points of $0 - 100\%$ of the rated power in steps of 10%. Of course, in reality, there are variations within the 10% power bin. These variations produce a dispersion in the harmonic measurements for one power bin that can be interpreted in practice as a statistical deviation. This is one source of randomness in WTG emission.

Secondly, it can be seen in (4.2) that the fundamental frequency also has a non-linear effect in the magnitude of the emissions. Thus, with the small but continuous variations of the power system fundamental frequency, the WTG converter produces a different distortion. This effect can also be understood as a driver for statistical deviation in the WTG characteristic emission.

Thirdly, even if the distortion in one WTG would be completely deterministic, the distortion of one WTG with respect to another WTG need not to be. For example, the phase angle of the fundamental at the terminals of all the WTGs is not the same due to the array cables in between them (nowadays, in large offshore wind farms, the distance between WTGs can be $1 - 3$ km). This means that θ_0 is not the same in each WTG. Thus, θ_0 can be considered a deterministic variable that can be found with a load flow simulation for every specific WTG operating point (as done in e.g., [186]); or, otherwise, θ_0 can be considered as an additional source of randomness. Further, θ_c is usually considered a random variable, since the carrier signals of different WTGs are usually not synchronized. In practice, this means that the carrier and sideband harmonics of different WTGs are not synchronized to each other, and that the phase angles of the carrier and sideband emission of different WTGs are not correlated to each other. In fact, some authors propose to model the phase angle of the carrier and sideband harmonics with a circular uniform distribution ($U(0, 2\pi)$) [186], while other distributions (e.g., normal, log-normal, etc.) are considered for the phase angle of the baseband harmonics [185].

In short, statistical considerations are relevant for modelling the characteristic emission of WTGs. Consequently, the statistical modelling of WTG for harmonic studies, as well as different statistical methods like Monte Carlo are gaining ground.

4.3 Wind farm harmonic amplification

In order to analyse the amplification/reduction of harmonics in an offshore wind power plant it is required to accurately model all wind farm components (transformers, cable systems, etc.) in a wide frequency range. This is addressed in this section.

4.3.1 Wind farm model

In this thesis, the example wind farm to showcase the result from different harmonic studies consists on 89 full-converter (type IV) wind turbines rated at 4.2 MW each, making the rated power of the wind farm 374 MW[5]. The wind turbines are connected to the array cables after a passive filter to diminish their distortion, and after a 690 V to 33 kV step-up transformer. The voltage rating of the array cables is, thus, 33 kV. The wind turbines are divided into 12 arrays of 7 to 8 wind turbines. There are two offshore substations that collect the array cables, where two three-winding transformers step up the voltage from 33 kV to 110 kV for the HV transmission. Two parallel circuits take the energy from the wind farm to the grid. The HV transmission has a part offshore that stretches 45 km, and another part onshore of equal length, making a total cable connection of 90 km. Each of the offshore cable circuits is a three-core cable with both-ends bonding. Each of the onshore cable circuits consists of three single-core cables in flat formation with cross-bonding. Due to the length of the AC cable connection, reactive power compensation is a must. Two reactors of 75 MVAr each are installed in the onshore-offshore connection point. A schematic of the wind farm can be found in Fig. 4.7.

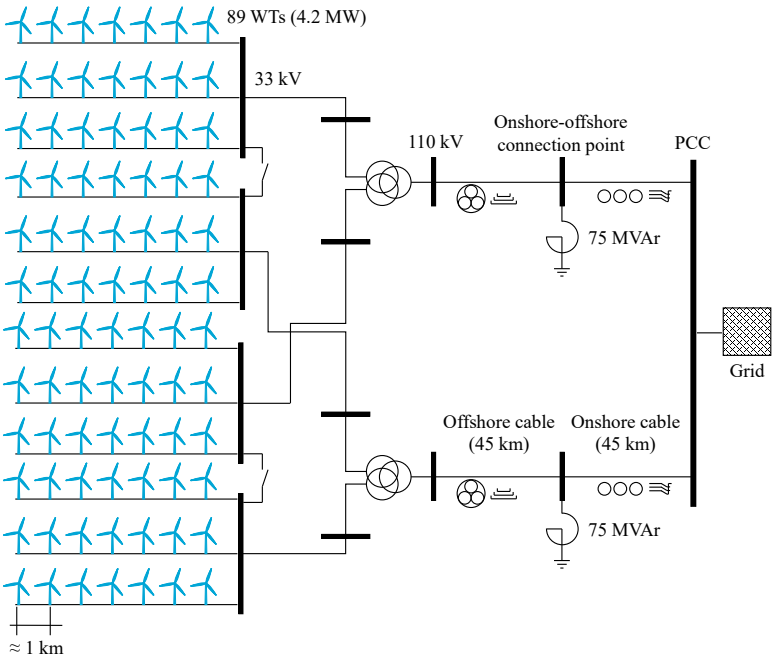

Figure 4.7: Single line diagram of the wind farm under study.

Details of the wind turbine connection are given in Fig. 4.8. Note the difference in notation between PCC (point of common coupling of the whole wind farm with the grid)

[5]It is worth mentioning that the wind farm presented here is just an example, and that the methods and conclusions achieved in this chapter are applicable to other wind farm ratings and configurations.

and the PoC (point of connection of every wind turbine with the rest of the system).

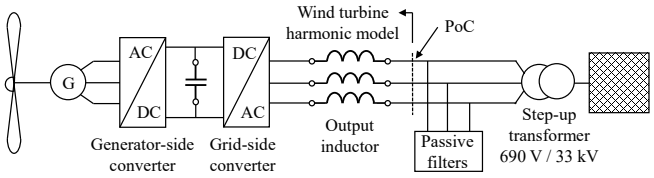

Figure 4.8: Schematic of the full-converter wind turbine connection.

In this thesis, all the elements in the wind farm have been modelled in the software DIgSILENT PowerFactory, due to the readiness of the software for performing harmonic studies (both harmonic power flows and impedance frequency scans). All elements have been modelled following indications from [183]. Details of these models are found subsequently.

(a) Wind farm to grid equivalent representation

In Chapter 1, an equivalent representation of the wind-farm to grid connection was given. This is repeated here for convenience, since this representation and its associated equation are used frequently during this chapter. The grid background distortion is represented in (4.3) as $\mathbf{V_g}$ although $\mathbf{V_{bck}}$ is also common in literature.

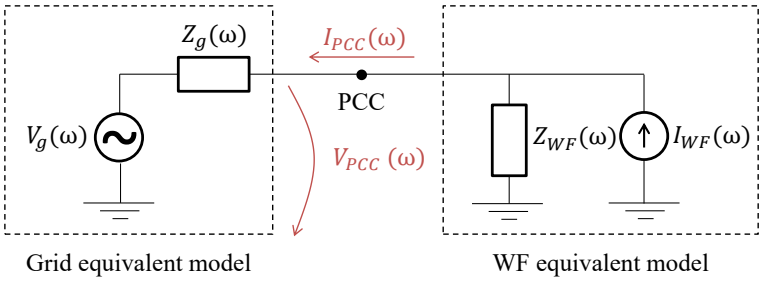

Figure 4.9: Schematic of Wind Farm (WF) to grid connection at the PCC. Same figure as Fig. 1.22.

$$\mathbf{V_{PCC}}(\boldsymbol{\omega}) = \underbrace{\frac{\mathbf{Z_{WF}}(\boldsymbol{\omega})\mathbf{Z_g}(\boldsymbol{\omega})}{\mathbf{Z_{WF}}(\boldsymbol{\omega}) + \mathbf{Z_g}(\boldsymbol{\omega})}}_{\mathbf{Z_{post}}(\boldsymbol{\omega})} \mathbf{I_{WF}}(\boldsymbol{\omega}) + \underbrace{\frac{\mathbf{Z_{WF}}(\boldsymbol{\omega})}{\mathbf{Z_{WF}}(\boldsymbol{\omega}) + \mathbf{Z_g}(\boldsymbol{\omega})}}_{\mathbf{HG}(\boldsymbol{\omega})} \mathbf{V_g}(\boldsymbol{\omega}) \tag{4.3}$$

Some TSOs require the wind farm developers to show compliance with individual emission limits (imposing that $\mathbf{V_{PCC}}(\boldsymbol{\omega})$ must be below a certain limit when $\mathbf{V_g}(\boldsymbol{\omega}) = 0$); some TSOs require to show compliance with the planning levels (imposing that $\mathbf{V_{PCC}}(\boldsymbol{\omega})$ must be below a certain limit when the background distortion is considered); while some TSOs require both. Individual emission limits are always equal or lower than the planning levels;

where the individual emission limits are usually calculated by taking into account the expected number of customers at that grid node and certain assumptions about the summation of harmonic sources [189].

Note that (4.3) calculates $\mathbf{V_{PCC}}$ using four elements: $\mathbf{V_g}$, $\mathbf{Z_g}$, $\mathbf{I_{WF}}$ and $\mathbf{Z_{WF}}$. Note also that $\mathbf{V_{PCC}} \neq \mathbf{V_g}$ and $\mathbf{I_{PCC}} \neq \mathbf{I_{WF}}$. Once a wind farm is connected to the grid, only the PCC voltage and current are accessible for measurement.

(b) Wind turbine harmonic model

The wind turbine harmonic model used in this chapter is a Norton equivalent, as shown in Fig. 4.10. The impedance has been calculated using the formulas derived in Chapter 3. Details of the impedance and the parameters for which it has been calculated can be found in Appendix A.3.

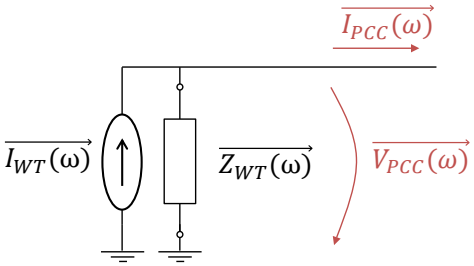

Figure 4.10: Wind turbine harmonic model.

Additionally, in some simulations in this chapter, the first coupling admittance is considered (which, as explained in Chapter 3, relates a voltage at frequency f_p to a generated current at $2f_1 - f_\mathrm{p}$). This coupling admittance is shown in Appendix, in Fig. A.1 (b). Considering the coupling admittance leads to a WTG harmonic model as in Fig. 4.11.

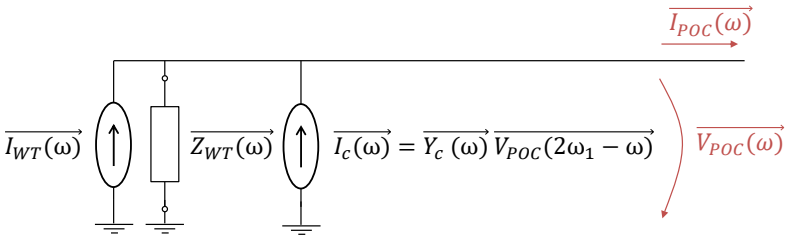

Figure 4.11: Wind turbine harmonic model considering frequency coupling.

In this chapter, one of the modelling uncertainties that is addressed is whether this coupling admittance should be considered or not. In the base case, this coupling admittance is ignored (just as it is done in the literature nowadays) but in other cases it is considered for comparison. Chapter 3 shows that, additionally, the converter can present several other coupling admittances, especially in the presence of voltage imbalance. Indeed, past literature has shown, with simulations and measurements, that commercial MW-scale WTG

converters and PV converters can show several frequency couplings [190–192]. However, for simplification, in this chapter, none of these other coupling admittances are considered. Even the second coupling admittance, which Chapter 3 shows to be significant, is ignored, since it only appears in certain types of control approaches (when the negative-sequence phase-angle is tracked). The method, however, can be extended to include this second coupling and even more couplings that may appear due to voltage imbalance, DC-AC side dynamics [193], control non-linearities, or other considerations.

In this chapter, the focus is applied predominantly to the 5^{th} and 7^{th} harmonic orders. This is done just to show the effect of different calculation assumptions on the final distortion result, although the method can also be applied to other frequencies. Thus, out of all the values calculated for the impedance and coupling admittance (shown in the Appendix in Fig. A.1), in reality only a few are of interest for this chapter, and are shown in Table 4.2 and Table 4.3.

Table 4.2: Relevant impedance values of the WTG converter for the studies herein.

	5^{th} harm	**7^{th} harm**
Mag (ohm)	0,0185	0,00861
Phase (deg)	-12,6	62,6

Table 4.3: Relevant coupling admittance values of the WTG converter for the studies herein.

	5^{th} harm	**7^{th} harm**
Mag (S)	4,64	9,74
Phase (deg)	-132,9	144,3

As for the current source, the values are taken from the WTG harmonic measurements shown in [177]. The values are just taken as a base case, since a sensitivity study about the WTG harmonic model is performed in this chapter. The values from [177] are taken as a base case since, in the paper, the characteristic emission is back-calculated using the impedance of the WTG, which ensures decoupling from the voltage background distortion. Other references give voltage or current harmonic measurements, but it is not clear whether the effect of the background distortion has been compensated or not.

Another reason for using the measurements in [177] is that the WTG in [177] is a type IV WTG with similar power rating to the one studied in this chapter (3.6 MW vs 4.2 MW) and with the same rated output voltage (690 V). Further, [177] gives thorough information of both the magnitude and phase angle of the harmonics (see Fig. 4.6), divided per power bin. In addition, [177] shows some statistical properties of the harmonic emission (percentiles) and not just one emission value per harmonic. Finally, measurements in [177] are reliable since the post-processing of the harmonic measurements is rigorous[6]. Therefore, the measurements from [177] are considered a reliable and relevant source of information for modelling the characteristic emission of the WTG in this chapter.

[6]This is due to: 1) the measured voltages and currents are post-processed according to IEC 61000-4-7, which specifies that 10 consecutive cycles shall be used for the time window of frequency analysis in a 50 Hz power system (as a result 5 Hz-resolution harmonics are obtained); and 2) the phase angles are directly extracted from raw FFT results using a 200 ms rectangular time window without any averaging (thus, avoiding introducing a misleading picture by using averaging methods)

However, the values in [177] cannot be directly used in this chapter, since [177] assumes a Thevenin equivalent instead of a Norton equivalent. Thus, the Thevenin equivalent values have been translated into Norton equivalent values by using the impedance. Further, the values have been scaled to the exact power rating of the WTG considered in this chapter. Finally, the measurements reported in [177] are the mean value, the 25th percentile and the 75th percentile, but the exact probability distribution function (PDF) followed by the harmonic magnitudes and phase angles is not clarified. In this chapter, it is assumed that the PDFs follow a normal distribution, although in reality, the methods used in this chapter can be adapted to any distribution. If normality is assumed, the mean and standard deviation of the current characteristic emission can be derived from the data shown in [177]. The data from the rated-power operating point is used in this chapter, although the method may be applied to any operating point.

The final results of this process are shown in Fig. 4.12 (a) for the magnitude PDF of the harmonics; and (b) for the phase-angle PDF of the harmonics[7]. Note that, in this chapter, several sensitivities on the WTG model are considered. The wind turbine impedance is considered fixed but the coupling admittance may be considered or not depending on the case study. The magnitude and phase angle of the wind turbine emission are always considered normally-distributed statistical variables, but the effect of changing the mean and standard deviation of these variables is investigated.

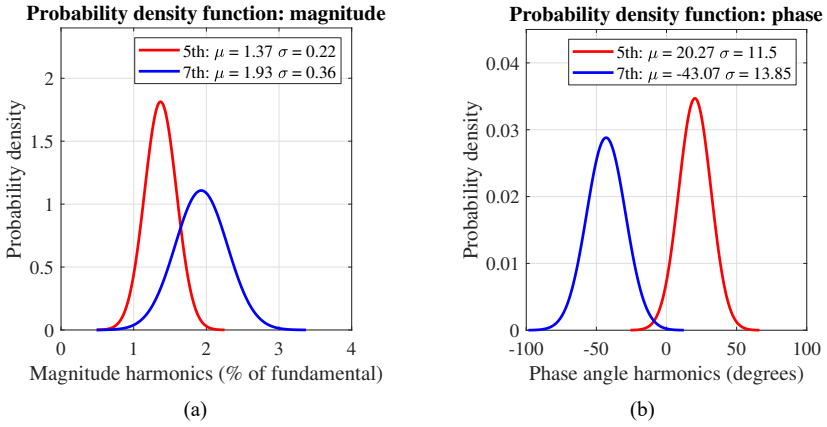

Figure 4.12: WTG converter probability density function (PDF) of the harmonics: (a) magnitude and (b) phase angle. This is a base case derived from [177].

[7]In this chapter, the wind-turbine emission phase-angle is the phase-angle of the current harmonic injected by the converter expressed relative to the voltage fundamental at the PoC. This is due to the fact that, when measuring harmonics, it is needed to decide at which moment the FFT window starts, which is usually synchronized with the voltage fundamental. Thus, when reported, harmonic emission phase-angles are typically expressed as relative to the voltage fundamental.

(c) Transformers

The wind farm has two types of transformers: the wind turbine step-up transformers (690 V / 33 kV) and the three-winding offshore transformers (110 kV / 33 kV / 33 kV). According to [183], it is not necessary to consider the transformer stray capacitances for studies below 4 kHz (approximately). Further, according to [183], it is not necessary to consider the magnetizing branch of the transformers for usual harmonic studies, as long as the transformer operates in its linear region. Therefore, for harmonic studies, the transformers can be modelled as having only an impedance connected in series between its terminals. In this thesis, both types of transformers are modelled with a frequency-dependent impedance to account for skin effect and other losses. In particular, the recommendation in [183] is to account for the increase of the resistance with frequency, while the inductance can be considered constant over the frequency range of interest.

(d) Reactors

Two reactors of 75 MVAr each are installed at the onshore-offshore connection point, as shown in Fig. 4.7. The reactors are modelled as shunt inductors with a resistance, determined by the quality factor of the inductor. The frequency dependency is considered by increasing the resistance with frequency, while leaving the inductance value constant.

(e) Passive filters

In between the wind turbine harmonic model and the step-up transformer, a set of shunt passive filters has been considered, as shown in Fig. 4.8. The passive filters consist on a set of resistive, capacitive and inductive components designed to attenuate the emission of the wind turbine. In particular, two trap-filters are used to attenuate the emission at the first and second switching harmonic groups, combined with a high-pass filter. The filter model can be more accurate in the high frequency range by adding a frequency-dependent impedance, however this is not considered here since it is not widely performed in the literature [183].

(f) Grid

For 50 Hz, the grid impedance has been assumed[8] to have a Short-Circuit Ratio (SCR) of 10, with a reactance-to-resistance proportion of X/R = 5. For other frequencies, the grid impedance can present a completely different behaviour other than inductive-resistive; in fact, at other frequencies the grid impedance might even be capacitive (negative reactance).

Further, it is known that the grid impedance can considerably change depending on the grid configuration (exact number of high power consumers connected to the grid, N-1 or N-2 contingencies, etc.). In order to deal with the variations of the grid impedance, a lot of TSOs provide so-called "grid-impedance loci" to perform harmonic studies. The TSOs usually provide several loci (one per frequency). In order to construct a grid-impedance locus, the TSO performs a number of impedance frequency scans at the PCC (without the wind farm connected) considering different grid configuration scenarios. After that, for each harmonic order it is possible to check the range of R and X values that can be expected for the grid impedance, $\mathbf{Z_g}$, at the PCC. These values can be plotted in a 2D plane, the

[8] Note that the methods presented in this thesis are applicable to other wind farms or grid data assumed.

RX-plane (one RX plane per frequency, where each point in the plane represents one grid scenario). Finally, the TSOs build a boundary around all these possible RX combinations, due to the fact that the grid might have a wider range of RX combinations in the future due to possible grid expansions and other considerations. Finally, the TSOs usually provide these boundaries (the grid-impedance loci), expecting the wind farm developer to prove compliance for the grid-impedance points in the boundaries. This is done due to the fact that the equivalent post-connection impedance, $\mathbf{Z_{post}}$ (see definition (4.3), and Fig. 4.9), is maximum when the grid impedance is at the boundary [194]. Thus, the highest harmonic amplification of the wind-farm harmonics are expected when the grid impedance is at the boundary of the locus. Therefore, when providing the grid-impedance loci, TSOs take a conservative approach that assumes a worst-case amplification.

The grid-impedance locus considered here is taken from [C6], since [C6] also analyses a wind farm with a 110 kV connection. Mathematically speaking, a contour has an infinity number of points. Usually, a key question is how many grid-impedance points should be considered in the boundary. In this chapter, only 20 points have been considered, for simplicity. The nomenclature of the points and their position in the boundary are shown in Fig. 4.13. The exact value of these points is listed in Table 4.4.

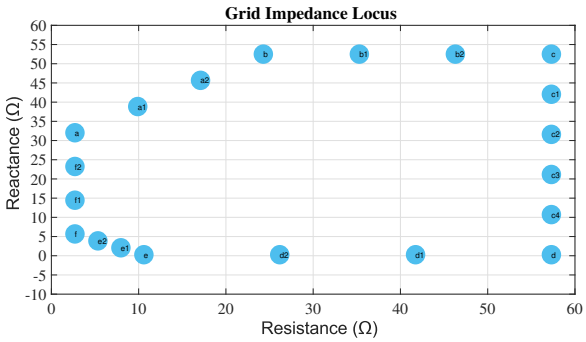

Figure 4.13: Grid impedance locus both for the 5^{th} and 7^{th} harmonics.

Table 4.4: Grid impedance points.

Z_g	R (Ω)	X (Ω)	Z_g	R (Ω)	X (Ω)
a	2.70	32.03	c4	57.30	10.72
a1	9.90	38.85	d	57.30	0.27
a2	17.09	45.68	d1	41.73	0.27
b	24.29	52.50	d2	26.17	0.27
b1	35.29	52.50	e	10.60	0.27
b2	46.30	52.50	e1	7.97	2.07
c	57.30	52.50	e2	5.33	3.88
c1	57.30	42.05	f	2.70	5.68
c2	57.30	31.61	f1	2.70	14.46
c3	57.30	21.16	f2	2.70	23.25

Unless otherwise specified, if in any simulation only one impedance point is considered,

this is the point a. In this sense, point a is considered the grid impedance base case ($\mathbf{Z_g} = 2.7+j32.03$). Note that the locus (Fig. 4.13) is valid for both the 5^{th} and 7^{th} harmonics [C6]. This is normal practice; instead of providing one locus per frequency under study, very often the TSOs provide one locus per group of frequencies (e.g., sometimes a locus defines the possible RX values of the grid impedance in a certain harmonic range, e.g. $5^{th} - 8^{th}$ harmonics).

(g) Cables

In the wind farm case study considered, there are three main types of cables:

1. MV array cables: rated at 33 kV, with three different cross-sections, depending on the position within the array.
2. HV offshore export cables: rated at 110 kV, and modelled as three-core submarine cables with double bonding.
3. HV onshore export cables: rated at 110 kV, and modelled as single-core land cables in flat formation with cross bonding.

The cables are modelled in PowerFactory including their geometry (the cable layers and their properties). The cable data has been extracted from different manufacturer brochures. These type of models are considered accurate for harmonic studies, since PowerFactory uses the geometrical information to calculate the impedance and admittance matrix of the complete cable system considering frequency dependencies (e.g., skin effect and proximity effect). Further, the cable bonding has been explicitly modelled, as this is very influential in harmonic studies [195].

It is worth to repeat that the onshore export cables are in flat-formation, which is an unbalanced formation. By performing a frequency sweep at the PCC, it is possible to find the equivalent post-connection impedance, $\mathbf{Z_{post}}$ (see definition in (4.3), and Fig. 4.9), which is the measurable impedance at the PCC after the wind farm has already been connected. In practice, it is the parallel between the grid equivalent impedance $\mathbf{Z_g}$ and the wind farm equivalent impedance $\mathbf{Z_{WF}}$. For illustration purposes, $\mathbf{Z_{post}}$ is shown in Fig. 4.14, in which it has been assumed that the grid impedance is simply an inductor with a resistor (calculating such values from the SCR and X/R ratio).

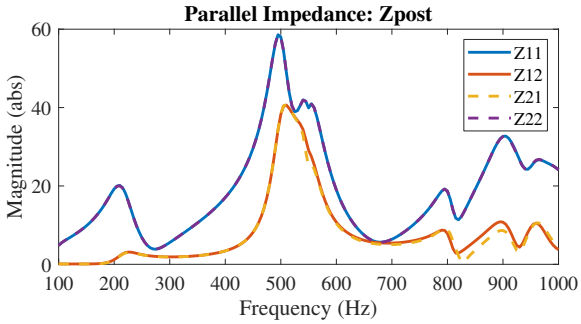

Figure 4.14: Z_{post}: Parallel impedance of Z_g and Z_{WF} calculated with a frequency sweep.

Fig. 4.14 shows four curves. That is because the impedance can be represented as an impedance matrix in the sequence domain with the following elements:

$$\begin{bmatrix} \mathbf{V_1} \\ \mathbf{V_2} \end{bmatrix} = \begin{bmatrix} \mathbf{Z_{11}} & \mathbf{Z_{12}} \\ \mathbf{Z_{21}} & \mathbf{Z_{22}} \end{bmatrix} \begin{bmatrix} \mathbf{I_1} \\ \mathbf{I_2} \end{bmatrix} \tag{4.4}$$

As it can be seen, in the notation here, $\mathbf{Z_{11}}$ and $\mathbf{Z_{22}}$ are the sequence impedances in the positive and negative sequence (respectively), and $\mathbf{Z_{12}}$ and $\mathbf{Z_{21}}$ are the sequence-coupling impedances. Fig. 4.14 shows a strong coupling between the two sequences, which is due to the long onshore cable laid in flat formation. Note that, even if the coupling is small in the low frequency range, still it can produce some sequence coupling at 50 Hz, as it is shown in Chapter 1, Fig. 1.13. Further, the coupling can be even stronger at higher frequencies, especially around resonant points (see Fig. 4.14 at $200-300$ Hz and at $500-700$ Hz). This stronger network imbalance around resonant frequencies is a phenomenon already reported in the literature [36], and which requires unbalanced harmonic power flows to be performed in the case of asymmetrical transmission components.

From $\mathbf{Z_{post}}$, knowing the grid impedance, it is possible to derive the wind farm impedance, which is shown in Fig. 4.15.

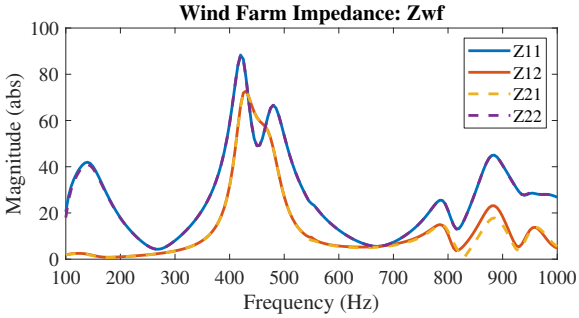

Figure 4.15: Z_{WF}: Equivalent wind farm impedance at the PCC.

4.4 Wind farm harmonic summation

4.4.1 The statistical problem of harmonic summation

In this section, the complexity of the statistical problem of harmonic summation is explained by using a simple wind-farm model consisting in only 2 WTGs, as shown in Fig. 4.16. If the background harmonic distortion is ignored, the voltage distortion appearing at the PCC can be calculated as[9]:

$$\mathbf{V_{PCC}}(\boldsymbol{\omega}) = \mathbf{Z_{total1}}(\boldsymbol{\omega})\mathbf{I_{WT1}}(\boldsymbol{\omega}) + \mathbf{Z_{total2}}(\boldsymbol{\omega})\mathbf{I_{WT2}}(\boldsymbol{\omega}). \tag{4.5}$$

In the general case, $\mathbf{Z_{total1}} \neq \mathbf{Z_{total2}}$; however, if $\mathbf{Z_{a1}} = \mathbf{Z_{a2}} = \mathbf{Z_a}$ and $\mathbf{Z_{b1}} = \mathbf{Z_{b2}} = \mathbf{Z_b}$, then $\mathbf{Z_{total1}} = \mathbf{Z_{total2}} = \mathbf{Z_{total}}$, with $\mathbf{Z_{total}}$ being:

[9]Note the bold font indicating phasor notation.

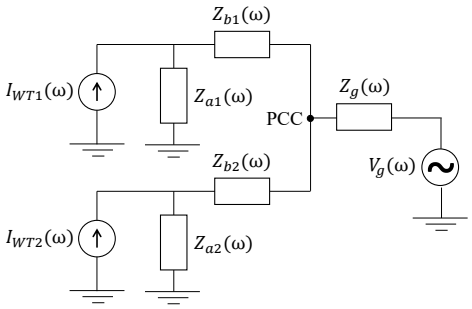

Figure 4.16: Example case study to show differences between IEC method and Monte Carlo method.

$$\mathbf{V_{PCC}}(\boldsymbol{\omega}) = \underbrace{\frac{\mathbf{Z_a}(\boldsymbol{\omega})\mathbf{Z_g}(\boldsymbol{\omega})}{\mathbf{Z_a}(\boldsymbol{\omega}) + \mathbf{Z_b}(\boldsymbol{\omega}) + 2\mathbf{Z_g}(\boldsymbol{\omega})}}_{\mathbf{Z_{total}}(\boldsymbol{\omega})} \left[\mathbf{I_{WT1}}(\boldsymbol{\omega}) + \mathbf{I_{WT2}}(\boldsymbol{\omega})\right]. \tag{4.6}$$

Note that, irrespectively of the amplification or reduction that may happen to the harmonics due to the impedance network (i.e., due to possible resonances in $\mathbf{Z_{total}}$), the resulting voltage harmonics at the PCC are very dependent on the phase angle with which both WTGs inject their harmonics[10]. If the phase angle of $\mathbf{I_{WT1}}$ at a certain harmonic is the opposite to the phase angle of $\mathbf{I_{WT2}}$ at that same harmonic[11], then that would lead to the highest cancellation; whereas if the phase angle is the same, then that would lead to the highest addition. In the specific case in which the magnitudes of the harmonics are the same in both WTGs, then $180°$ difference would mean complete cancellation, and $0°$ difference would mean that $\mathbf{I_{WT1}}(\boldsymbol{\omega}) + \mathbf{I_{WT2}}(\boldsymbol{\omega}) = 2\mathbf{I_{WT1}}(\boldsymbol{\omega})$.

Even in the case that the impedance network is simplified and it is considered that $\mathbf{Z_{total1}} = \mathbf{Z_{total2}} = \mathbf{Z_{total}}$, (4.6) represents a complex statistical problem, since the the WTG harmonic emission is random (this is substantiated in Section 4.2.3; for an example of the statistical variability of measured WTG harmonics, see Fig. 4.6).

The phasor $\mathbf{I_{WT1}}$ is defined by two random variables: its magnitude A_1 and its phase angle P_1 as in $\mathbf{I_{WT1}} = A_1 e^{jP_1}$; or its real part X_1 and its imaginary part Y_1 as in $\mathbf{I_{WT1}} = X_1 + jY_1$. The phasor $\mathbf{I_{WT2}}$ is also defined by another two random variables. The phasor that results from summing $\mathbf{I_{WT1}}$ and $\mathbf{I_{WT2}}$ is defined as $\mathbf{I_{WF}}$:

$$\mathbf{I_{WF}} = X_1 + jY_1 + X_2 + jY_2 = X + jY \tag{4.7}$$

The real part of $\mathbf{I_{WF}}$, X, and its imaginary part, Y, are both random variables that have statistical properties such as mean (μ_X and μ_Y) and standard deviation (σ_X and σ_Y), and which might have a certain correlation factor between them (r_{XY}). The magnitude of the harmonic resulting from the summation is given by the following formula:

[10] This is true even in the general case of $\mathbf{Z_{total1}} \neq \mathbf{Z_{total2}}$.

[11] In this case, opposition is defined in a phasor sense; that is to say, $180°$ apart.

$$|\mathbf{I_{WF}}| = A_{\mathrm{WF}} = \sqrt{[X_1 + X_2]^2 + [Y_1 + Y_2]^2} \\ = \sqrt{[A_1 \cos(P_1) + A_2 \cos(P_2)]^2 + [A_1 \sin(P_1) + A_2 \sin(P_2)]^2} \tag{4.8}$$

As it can be seen, A_{WF} is a random variable that depends on other random variables (either A_1, P_1, A_2 and P_2; or X_1, Y_1, X_2 and Y_2) in a non-linear manner. Solving this non-linear equation analytically, and achieving a closed-form expression for the Probability Distribution Function (PDF) of A_{WF}, $f_{A_{\mathrm{WF}}}$, is a complex mathematical endeavour.

If certain assumptions and approximations are considered about the random variables and their relationships (e.g., about the harmonic injections or about μ_X, μ_Y, σ_X, σ_Y and r_{XY}) then analytical solutions can be achieved (e.g., [196, 197]). Usually, a common assumption is that the injected currents must be independent and have uniform or Gaussian distributions [198]. However, previous literature has reported measurements in real wind farms showing that some of the conditions that are typically assumed when deriving analytical solutions do not always hold (e.g., [196]).

4.4.2 The IEC method: application of the Summation Law

The IEC method, described in IEC61000-3-6 [184], consists of two steps:

1. Calculate the voltage distortion that is created at the PCC by each harmonic source (this can be done by turning iteratively all the harmonic sources to zero except one, and performing as many harmonic power flows as sources there are in the network). In this case, the value for the magnitude typically used is the 95^{th} percentile, although other percentiles may be used.

2. Sum the voltage distortion contribution of all the harmonic sources according to the Summation Law.

The Summation Law is defined in [184] as:

$$U_h = \sqrt[\alpha]{\sum_i U_{hi}^{\alpha}} \tag{4.9}$$

where U_h is the magnitude of the h-th order voltage harmonic of the i-th emission unit to be aggregated; and α is an exponent that is recommended to be taken as in Table 4.5.

Table 4.5: Exponents for the Summation Law

Harmonic Order	$\boldsymbol{\alpha}$
h <5	1
5 ≤ h ≤ 10	1.4
h >10	2

Sometimes all the injections are considered in phase by selecting the factor $\alpha = 1$. However, considering all harmonics in phase is a very conservative approach, so typically the coefficients in IEC61000-3-6 are used.

The Summation Law is sometimes expressed in terms of currents as in (4.10). Both expressions are interchangeable; solving the statistical problem of current harmonic summation is equivalent to solving the statistical problem of voltage summation, since they are related by a linear impedance.

$$I_h = \sqrt[\alpha]{\sum_i I_{hi}^{\alpha}} \tag{4.10}$$

(a) Mathematical background to the Summation Law

The expression (4.10) is not arbitrary. In [197] it is shown that, under the assumptions that: a) the Central Limit Theorem is applicable (i.e., enough harmonic sources are considered); b) $r_{XY} = 0$; c) $\mu_X = \mu_Y = 0$ (the mean value of the real and imaginary parts of the resulting summation are zero); and d) $\sigma_X = \sigma_Y = \sigma$ (the standard deviation is the same for the real and imaginary parts of the resulting summation); then the magnitude of the harmonic that results from the summation of harmonics follows a Rayleigh distribution, as in (4.11) (where $c = \sigma$ and A is the magnitude of the harmonic injection by the polluting sources). This is also shown in [198].

$$f_{A_{\mathrm{WF}}} = \left(\frac{A}{c^2}\right) \exp\left(-\frac{A^2}{2c^2}\right) \tag{4.11}$$

These mathematical assumptions can be met in different cases; for example, when the harmonic injections are statistically independent, with their phase-angles being uniformly distributed over the interval $(0, 2\pi)$ [197].

Further, [199] shows extra analysis considering a case study of a wind farm with N_{WT} WTGs, taking into account the magnitude of the harmonic injection by each WTG (A in (4.11)). If A is considered a fixed variable, then [199] shows that the 95^{th} percentile of $f_{A_{\mathrm{WF}}}$ (normalized) can be approximated by $\sqrt{3N_{\mathrm{WT}}}$. Further, if A is considered a random variable following a uniform distribution from zero to its maximum value, then [199] shows that the 95^{th} percentile of $f_{A_{\mathrm{WF}}}$ can be approximated by $\sqrt{N_{\mathrm{WT}}}$. Note that this is equivalent to (4.10) if $\alpha = 2$.

Thus, [199] shows that the Summation Law in (4.10) can be derived mathematically, but only if certain assumptions are met. These mathematical assumptions are met, for example, when:

1. $\alpha = 2$;
2. enough harmonic sources are considered so as to apply the Central Limit Theorem;
3. the harmonic injections are statistically independent;
4. the harmonic injections have their phase-angles uniformly distributed over the interval $(0, 2\pi)$;
5. the harmonic injections have their magnitudes following a uniform distribution; or, alternatively, if the magnitudes of the emission are fixed, then the Summation Law calculations must be multiplied by $\sqrt{3}$.

(b) Advantages and disadvantages of the Summation Law

From a practical perspective, the Summation Law has the clear advantage that it can be applied without knowledge of the phase angles of the harmonic emission. In a sense, the Summation Law helps to make assumptions about the phase angle through a summation factor or exponent. However, two main problems appear with the application of the Summation Law in modern power systems.

Firstly, the alpha exponents to be assigned to each harmonic, shown in Table 4.5, were found taking into account the typical distorting equipment at the time of publication (mostly rectifier bridges) [200], which seem to not be suitable any more for characterizing the behaviour of the emission of modern-day power electronic devices [183]. In order to keep applying the Summation Law, new exponents would have to be proposed. Even though some proposals have been presented in the literature (e.g., [200, 201]), the exact exponent selection would depend enormously on the exact power-electronic converter topology considered, its modulation and switching strategies, and other factors.

Secondly, as explained here, if the harmonic sources in a system meet different conditions about their magnitude and phase-angle, then the Summation Law has a strong mathematical foundation. However, power-electronic converters have intricate emission profiles whose statistical properties might comply or not with the mathematical assumptions of the Summation Law. The measurements in [196] are an example of a wind farm in which these assumptions are not met. The measured phase angles of the 5^{th} and 7^{th} harmonic currents injected by this wind farm are taken from [196] and plotted in Fig. 4.17 for convenience[12]. It is shown here that the typical assumption that the wind farm emission has a random phase angle uniformly distributed in the range $0 - 360\,^{\circ}$ is not met. Thus, the uncertainty in the application of the Summation Law does not only derive from the chosen exponents, but also from the possible inaccuracies in the assumptions that form the mathematical basis of the method.

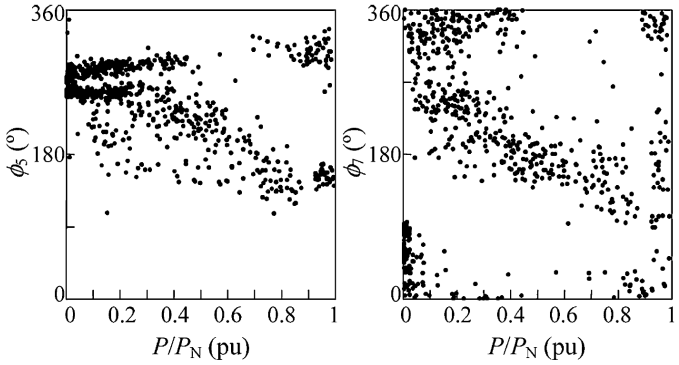

Figure 4.17: Measured phase angles of the 5^{th} and 7^{th} harmonic currents injected by a wind farm [196].

[12] It is worth noting that the possible influence of the background distortion on the measurements presented in [196] is not clarified.

4.4.3 Monte Carlo method

Due to the disadvantages of the Summation Law, industry and academia are making increasing efforts to develop a solid alternative. The harmonic analysis methodology that is gathering most attention nowadays is the Monte Carlo method [186].

In this alternative, the probability density function of the magnitude and phase-angle of the harmonics emitted by the wind turbine are considered. For each harmonic order, a series of power flow calculations are performed to calculate the harmonic voltage at the PCC. In each iteration, the magnitude and phase-angle of the wind turbine harmonic emission is modified according to its probability distribution function. After performing a considerable number of simulations (in the order of hundreds to thousands) the histogram of the harmonic voltage at the PCC can be built, and thus the 95^{th} percentile obtained. This is illustrated in Fig. 4.18.

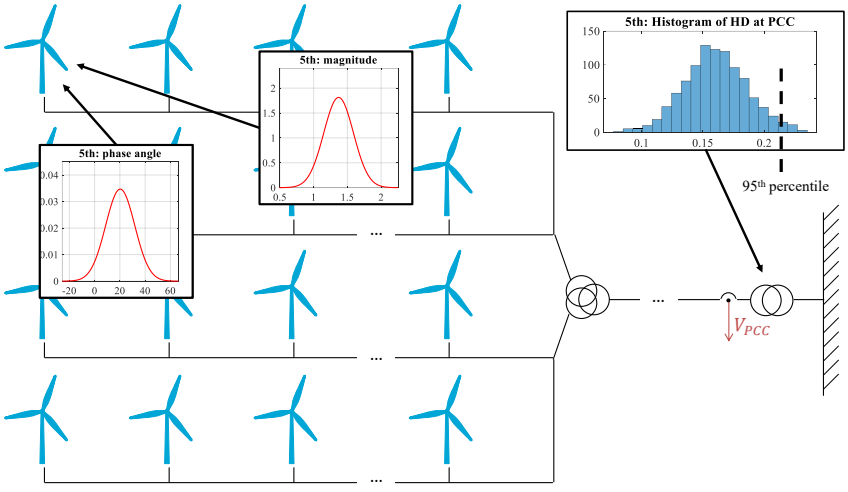

Figure 4.18: Monte Carlo method for harmonic calculations in offshore wind farms.

(a) Advantages and disadvantages of the Monte Carlo method

The main disadvantage of this method is that it requires more data to be applied than the IEC method. With the IEC method, only the 95^{th} percentile of the magnitude of the harmonics is needed. In contrast, with the Monte Carlo method, the Probability Distribution Functions (PDFs) of both the magnitude and phase angle of the emission are needed.

Nowadays, most WT manufacturers only provide static emission levels (e.g., only the 95^{th} percentile of the magnitude for each harmonic). One of the reasons for this lack of data might be the fact that accurately measuring the phase angle for harmonics in the presence of noise is not an easy procedure [202], and due to the fact that standard Power Quality (PQ) analysers only sometimes have an angle measurement option (note that angles are not covered by the IEC 61000-4-7 standard for measurements).

However, despite these difficulties, some WTG manufacturers do provide a more sophisticated WTG harmonic model including statistical information, phase angles and LV filter. Thus, the Monte Carlo method is applicable in industry nowadays, albeit not being widespread.

4.4.4 Comparison of IEC method and Monte Carlo method

In this section, a small comparison of both methods is made. The objective is to show the differences in the predictions of both methods and to draw general conclusions. For this purpose, several example networks are used. The small 2-WTG network shown in Fig. 4.16 is used as a first example. In this case study, it is considered that $\mathbf{Z_{a1}} = \mathbf{Z_{a2}} = \mathbf{Z_a} = 1\,\Omega$, $\mathbf{Z_{b1}} = \mathbf{Z_{b2}} = \mathbf{Z_b} = 1\,\Omega$, and $\mathbf{Z_g} = 1\,\Omega$ (i.e., all the impedances in the network are simply resistors of value $1\,\Omega$). Also, the background distortion is zero. On the one hand, the Summation Law can be applied. This entails that the following must be calculated:

$$|\mathbf{V_{PCC}}(\omega)| = \sqrt[\alpha]{(\mathbf{Z_{total}}(\omega)\mathbf{I_{WT1}}(\omega))^{\alpha} + (\mathbf{Z_{total}}(\omega)\mathbf{I_{WT2}}(\omega))^{\alpha}} \tag{4.12}$$

where $\mathbf{Z_{total}}$ can be calculated using (4.6). The result is $\mathbf{Z_{total}} = 0.25\,\Omega$ at all frequencies due to the resistive value assumed for all impedances (resistances have no frequency dependency). If, also, the magnitude of the emission of both WTGs is assumed to be $|\mathbf{I_{WT1}}| = |\mathbf{I_{WT2}}| = 1$ A, then:

$$|\mathbf{V_{PCC}}| = \sqrt[\alpha]{(0.25 \times 1)^{\alpha} + (0.25 \times 1)^{\alpha}} \tag{4.13}$$

Note that many α exponents can be assumed. The dependence of the distortion prediction of the IEC method on the α exponent is shown in Fig. 4.19.

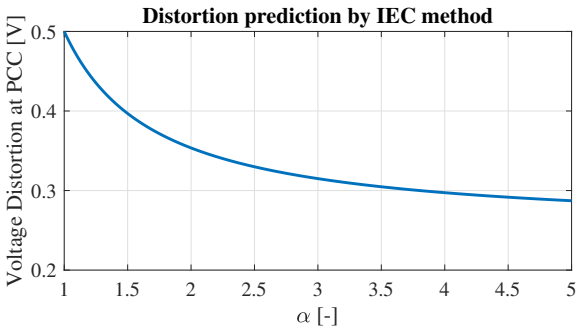

Figure 4.19: Voltage harmonic distortion prediction at the PCC by IEC method for the 2-WTG case study.

On the other hand, the Monte Carlo method can be applied. The Monte Carlo method can be applied for different Probability Distribution Functions (PDFs). In here, a constant magnitude of 1 A is used, while different PDFs are assumed for the phase angles. A fixed number of runs of $R = 1000$ is assumed for simplicity. Once these runs have been made, a histogram of the distortion at the PCC can be built, out of which the 95^{th} percentile can be calculated. The results of performing a Monte Carlo study for different PDFs are shown in Fig. 4.20. The PDFs assumed for the phase angles are different versions of a normal

distribution $N(\mu, \sigma^2)$ with μ being the mean (in all cases $\mu = 0$), and σ being the standard deviation[13]; and also a uniform distribution $U(0, 2\pi)$[14].

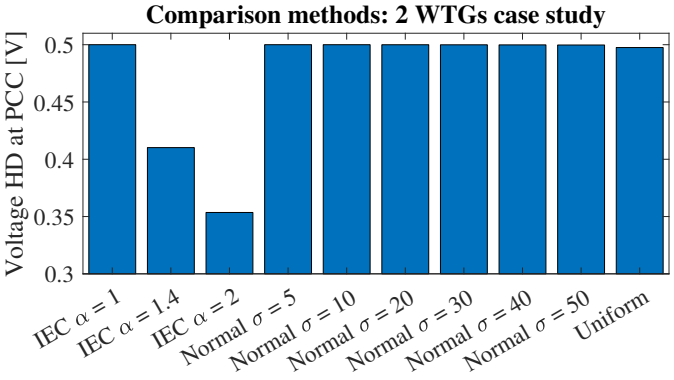

Figure 4.20: Comparison of results with the IEC method and the Monte Carlo method for the 2-WTG case study.

As explained in Section 4.4.2 (a), the equation of the Summation Law can be derived mathematically when $\alpha = 2$. However, Fig. 4.20 shows that the results for $\alpha = 2$ are inaccurate. That is because, on top of using $\alpha = 2$, additionally, certain assumptions about the harmonic injections must be met. One of these assumptions is that the number of harmonic sources must be high enough so that the Central Limit Theorem can be applied. If 10 WTGs are considered instead, the results are shown in Fig. 4.21.

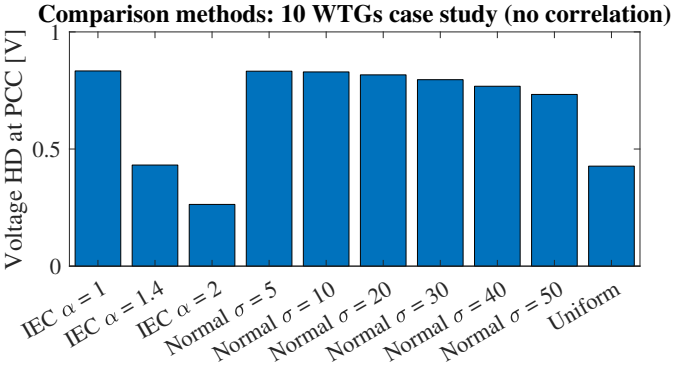

Figure 4.21: Comparison of results with the IEC method and the Monte Carlo method for the 10-WTG case study.

Fig. 4.21 shows that, if the phase angle follows a uniform distribution, if the number of WTGs is high enough (in the example herein, 10 WTGs seems already high enough) and

[13] In this thesis, the standard deviation is reported instead of the variance. The choice is deliberate. The standard deviation of the phase-angle has the same units as the phase-angle (degrees) and has easy interpretation: for a normal distribution, the 95^{th} confidence interval is delimited by $\pm \sim 2\sigma$ around the mean, and the 99^{th} confidence interval is delimited by $\pm \sim 3\sigma$ around the mean. For example, if $\mu = 0°$ and $\sigma = 20°$, 95 % of the values are expected to fall between $[-40°, +40°]$.

[14] Note that phase-angle uniformity is one of the assumptions listed in Section 4.4.2 (a).

$\alpha = 2$, then the results of the Summation Law improve considerably and match approximately those of the Monte Carlo method. However, still the column of Summation Law for $\alpha = 2$ (HD $= 0.26$ V) does not match perfectly the results for the uniform distribution (HD $= 0.43$ V). The difference is approximately $\sqrt{3}$. This is because the results shown in Fig. 4.21 are drawn considering a constant magnitude for the harmonic injections. In order for the results to perfectly match the Summation Law predictions, then the magnitude of the emission must also be a uniform random variable (see Section 4.4.2 (a)).

Additionally, one more assumption considered when deriving Fig. 4.21 is that the harmonic injections must be statistically independent. Simulations are performed when this assumption is not met (in this case, when all the harmonic sources are 100 % correlated) and the Fig. 4.22 is obtained.

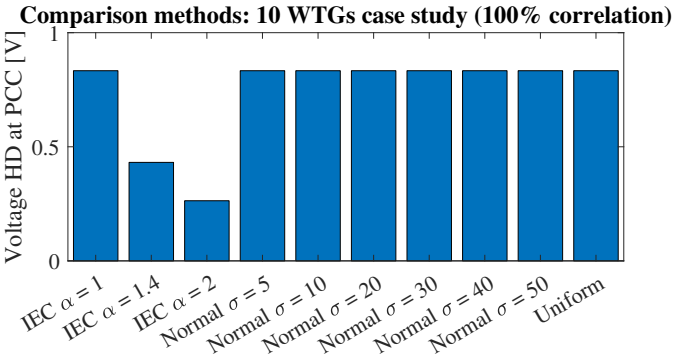

Figure 4.22: Comparison of results with the IEC method and the Monte Carlo method for the 10-WTG case study.

Fig. 4.22 shows that, when the harmonic sources are statistically dependent, the Summation Law is inaccurate again. This makes sense, as statistical independence is one of the 5 assumptions listed in Section 4.4.2 (a).

(a) Discussion

It has been shown that the Summation Law provides a strong mathematical foundation if the 5 conditions listed in Section 4.4.2 (a) are met, but if one or several are not met, the results may be very misleading.

Further, it can be argued that the Summation Law is accurate in other set of conditions other than those described in Section 4.4.2 (a). For example, the Summation Law is quite accurate in Fig. 4.20 and Fig. 4.22, if $\alpha = 1$ is assumed. This makes sense, since $\alpha = 1$ implies the geometric summation of the harmonic injections with no cancellation effects. In Fig. 4.20, the cancellation effects are low due to the low number of WTGs, and in Fig. 4.22 the cancellation effects are low due to the correlation of the phase angles in the WTGs.

In this sense, it can be argued that the Summation Law can always be applied if different α exponents are assumed for each harmonic, if one has an estimation of the cancellation effects to be expected in a certain system for that specific harmonic order. However, estimating these cancellation effects is a difficult task. Note that the cancellation effects depend strongly on the randomness of the phase angle of the harmonic injections. For example,

Fig. 4.21 shows that, the more statistically random that the phase angle is (higher σ), the more cancellation effect is achieved.

In practice, this means that, if the 5^{th} or 7^{th} harmonic emission in a wind farm would have a very low statistical variation, the α exponent recommended by the IEC Summation Law for these harmonics (which is $\alpha = 1.4$) would probably lead to an underestimation of these harmonics; whereas if the 5^{th} or 7^{th} harmonic would be very random for a particular WTG model, then the IEC Summation Law would probably lead to an overestimation of the distortion.

Indeed, it has been reported in literature before that the Summation Law is not able to predict the aggregated emission of wind farms, resulting very often in an overestimation of the harmonics [177, 178]. What is worse, in some studies it has been shown that the Summation Law produces an overestimation only in some harmonics (typically, low-order even harmonics and high-order ones around the switching frequency), whereas in some others it underestimates their amplitude at the PCC (e.g. 5^{th}, 7^{th}, 11^{th}, etc.) [179].

To sum up, this section shows that the Summation Law can achieve accurate predictions of the PCC harmonic distortion, but only if the theoretical assumptions upon which it is based are met. Numerous references have shown that these assumptions are not met in wind farms [196] and, further, numerous papers have shown that, when comparing the IEC method predictions with actual wind farm measurements, the IEC method can both overestimate and underestimate harmonics. On the contrary, the Monte Carlo method offers the flexibility to consider different PDFs for the magnitude and phase angle of the emissions, including the hypothetical case of having different WTG vendors in the same wind farm. The Monte Carlo method requires more data to be provided by the WTG manufacturer, but an increasing number of vendors provide the information needed for the application of Monte Carlo. Thus, in the rest of this chapter, only the Monte Carlo method is used for harmonic studies.

4.5 Application and analysis of the Monte Carlo method

In this thesis, different factors that affect the calculations of harmonic studies performed with the Monte Carlo method are analysed. The results of these efforts are shown in this section.

4.5.1 Effect of the wind farm impedance network and grid impedance

This section shows the importance of the impedance network frequency characteristics within the wind farm, and the importance of the grid impedance point considered in the locus.

The following study considers, for both the 5^{th} and 7^{th} harmonic, the current magnitude of the wind turbine emission to be 1 % of the fundamental. The phase angles of the wind turbine emission are zero degrees (thus, each WTG injects the harmonics in phase with respect to the voltage fundamental at its terminals). There is no statistical variation considered, and the coupling admittance is not considered. Meanwhile, the grid background emission is set to zero. The resulting Harmonic Distortion (HD) at the PCC is shown in Fig. 4.23.

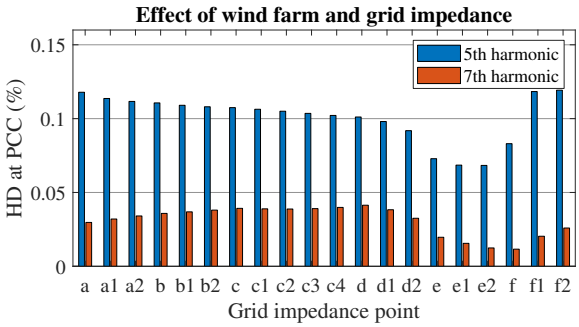

Figure 4.23: Effect of the wind farm impedance network and grid impedance.

For the same grid impedance (e.g., look at the base case point a in Fig. 4.23), the distortion created at the PCC by the WTG emission is higher when injected in the 5th harmonic than in the 7th harmonic. Note that, in both harmonics, the emission is the same (1 % of the fundamental). The only thing that changes is the fact that the impedances in the wind farm have a frequency characteristic, and thus a 5th harmonic propagates differently than a 7th harmonic. The wind farm shows higher amplification of the WTG harmonics for the 5th frequency. Thus, this figure shows the impact of the wind farm frequency-dependent impedance.

Further, Fig. 4.23 shows that changing the grid impedance is very relevant as well, as this also affects the amplification of harmonics. For both the 5th and the 7th harmonics, the lowest distortion appears when the grid impedance is around the point e-f. However, this is only true if the background distortion is disregarded.

4.5.2 Effect of background distortion (magnitude and phase angle)

Fig. 4.24 shows the 5th harmonic distortion at the PCC caused when injecting both: a) 1 % of the fundamental in the WT emission; and b) different levels of voltage background distortion. The chosen levels of $\mathbf{V_{bck}}$ are up until 2 % (in particular, 0 %, 1 % and 2 %) since, in IEC61000-3-6, the planning level for the 5th and 7th harmonic is 2 % (HV systems).

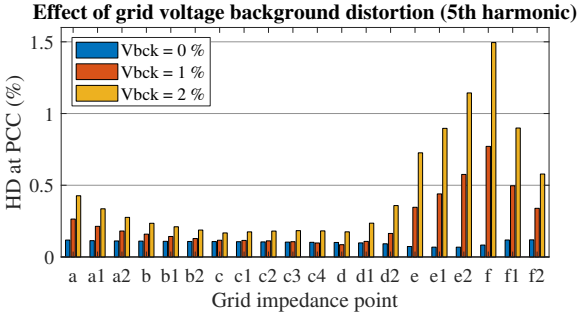

Figure 4.24: Effect of the magnitude of the voltage background distortion.

It can be seen that the background distortion in the grid can have a big impact in the distortion at the PCC of the wind farm. When looking at the blue columns, the lowest distortion appears around the grid points e-f. This is due to the fact that the distortion only depends on the harmonics produced by the wind turbines. When the background distortion increases, the amplification of background harmonics becomes more relevant, and actually the point f becomes the point with highest distortion.

This can be explained by looking at (4.3) and Fig. 4.9. When the background distortion is zero, $\mathbf{V_{PCC}(\omega)}$ depends only on $\mathbf{I_{WF}(\omega)}$, and the total impedance after the connection of the farm, $\mathbf{Z_{post}}$, determines how much the wind farm distortion is amplified or reduced. Fig. 4.25 shows that $\mathbf{Z_{post}}$ at 250 Hz is lowest when the grid impedance is at point e in the grid locus, which confirms the results in Fig. 4.23. However, when the background distortion is present, the harmonic gain (**HG**) also plays a role. Fig. 4.26 shows that the **HG** is actually very high when the grid impedance is e-f, which explains the results in Fig. 4.24.

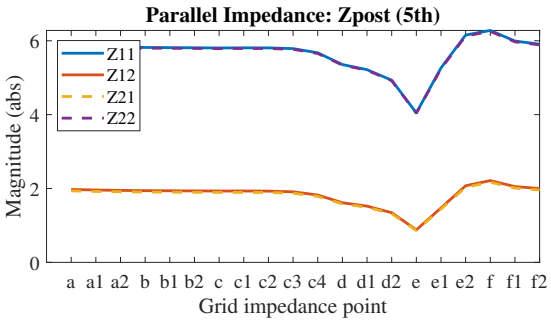

Figure 4.25: Variation of Z_{post} at the 5$^{\text{th}}$ harmonic with the grid impedance.

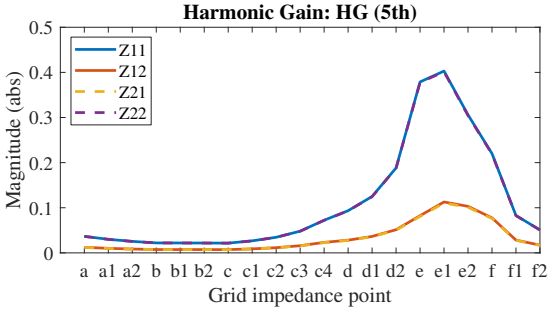

Figure 4.26: Variation of HG at the 5$^{\text{th}}$ harmonic with the grid impedance.

In the case of considering the background distortion, the phase angles also become relevant. When $|\mathbf{V_{bck}}| = 0$, it does not matter with which phase angle the wind turbine injects its distortion, as shown for different phase-angles in Fig. 4.27 (for the 5$^{\text{th}}$ harmonic)[15].

[15]This is only true because all the wind turbines are injecting with the same phase angle. The phase angle differences between wind turbines is addressed in the next section.

However, when the background distortion is non-zero, the phase-angle with which the wind turbine injects the harmonics matters, since this can cause higher or lower cancellation with the grid background harmonics.

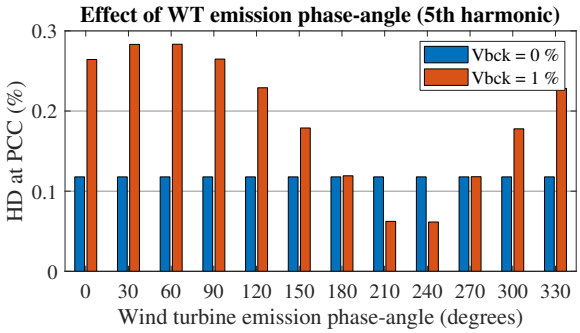

Figure 4.27: Effect of the WTG emission phase angle (5^{th} harmonic).

This means that the phase-angle with which the grid background harmonics are modelled also influences the results, as seen in Fig. 4.28 (5^{th} harmonic). If not specified otherwise, in this chapter the phase-angle of $\mathbf{V_{bck}}$ is assumed to be zero.

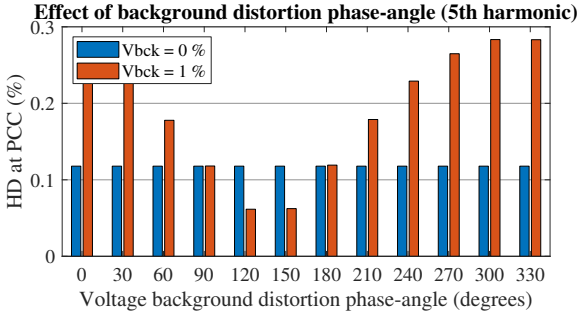

Figure 4.28: Effect of the background distortion phase angle (5^{th} harmonic).

4.5.3 Effect of the statistical variation and correlation between random variables

Fig. 4.27 and Fig. 4.28 show that, when the background distortion is zero, the phase-angle with which the wind turbines inject the emission has no impact on the HD at the PCC. This is true as long as all the wind turbines inject their harmonics with the same phase-angle. If the wind turbines inject the emission with different phase-angles, the phase-angles matter, as some phase-angle combinations might induce higher or lower harmonic cancellation at the PCC.

This is very relevant when modelling the statistical information of the phase-angles (and the magnitudes). In this chapter, the statistical aspects of the wind turbine emission are considered by performing Monte Carlo simulations. The process is described in Fig. 4.29.

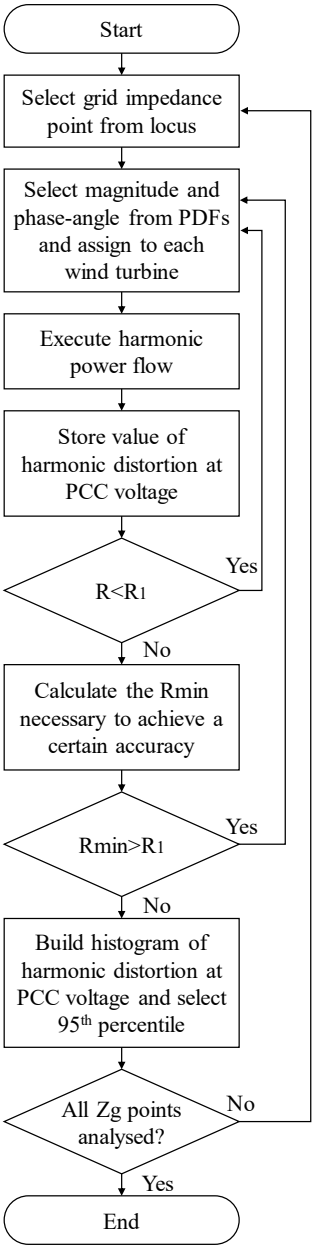

Figure 4.29: Flow chart for performing Monte Carlo simulation. R, R_1 and $R_{\min}$ relate to the number of runs.

In every Monte Carlo run, a magnitude and a phase angle is extracted from the normal

distributions and assigned to the wind turbines. Then, a harmonic power flow is performed, from which one value of HD at the PCC is extracted. After performing the required number of runs R to ensure statistical significance (this is further discussed later) a histogram can be built for the HD at the PCC, from which the mean, standard deviation, 95th percentile, and other characteristics can be withdrawn.

When assigning the magnitude and phase-angle value for each wind turbine, one approach is to assign the same value to all wind turbines. In this case, the emission between the wind turbines is 100 % correlated. When the harmonics increase or decrease in one wind turbine, it is assumed that the same happens in the other wind turbines. Another approach is to independently extract one different magnitude and phase angle for each wind turbine, which is the equivalent to assuming that the wind turbines are 0 % correlated.

The results obtained when assuming 100 % correlation or 0 % correlation are very different. This is shown in Fig. 4.30 and Fig. 4.31.

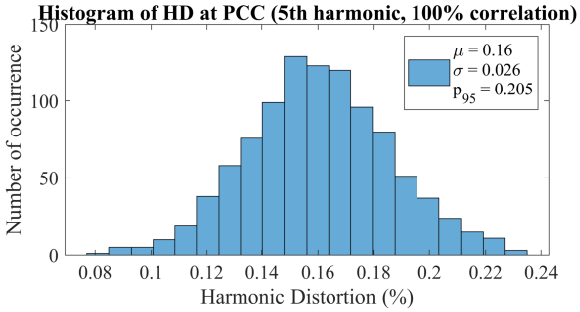

Figure 4.30: Histogram of the 5th harmonic distortion at the PCC when considering 100 % correlation.

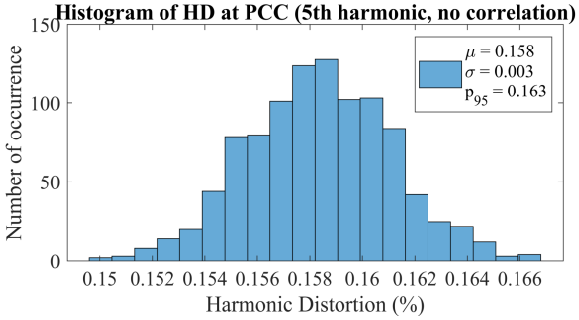

Figure 4.31: Histogram of the 5th harmonic distortion at the PCC when considering 0 % correlation.

When considering the emission parameters as independent random variables between turbines (i.e., no correlation), the harmonic cancellation is higher, which can be seen, mostly, in the standard deviation. Even if the average remains fairly similar, due to the reduction in the standard deviation when there is no correlation, the 95th percentile is significantly affected. This can be seen in Fig. 4.32 for different impedance points.

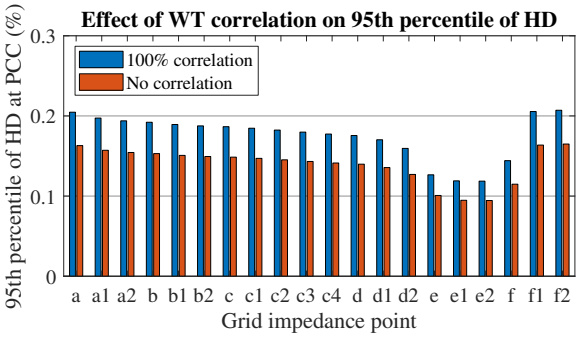

Figure 4.32: Effect of considering correlation or not between the emission of different WTGs (95^{th} percentile of the 5^{th} harmonic distortion at the PCC).

In general, when dealing with random variables and Monte Carlo simulations, correlation is an important factor. In the wind farm case study, there are three possible correlation relationships to consider:

1. The correlation between wind turbines (when picking a magnitude and phase angle from the probability distribution in each Monte Carlo run, whether the same value is assigned to all the wind turbines or not);

2. The possible correlation in between the magnitude and phase angle in one same wind turbine (whether a certain phase angle tends to appear more when the magnitude is high, and vice-versa);

3. The possible correlation between grid impedance (which could be considered a random variable as well) and the grid background harmonic voltage.

(a) Correlation between WTGs

When considering the possible correlation between the random harmonic emission of different WTGs, one key question is to address what are the drivers for such randomness. On the one hand, as it is discussed in Section 4.2.3, the frequency is one of the drivers for the statistical variation of the WTG characteristic emission. If it is considered that the frequency is the same in the whole wind farm, then it can be considered that every time that the emission increases or decreases in WTG, it will occur the same in all the other generators. This will be the case of having a perfect correlation between the WTGs. However, on the other hand, the operating point is also one of the drivers for statistical variation, and it is only an approximation to consider that all the WTGs will function at the same operating point – wake effects are prominent in offshore wind farms. In this sense, 100 % correlation might not be a realistic assumption. Further, there are other sources of harmonic emission other than switching effects (as discussed in Section 4.2.1) that might be different in each WTG (e.g., component tolerances).

(b) Correlation between magnitude and phase angle of WTG emission

With respect to the relation between the magnitude and phase-angle of a same harmonic in a same WTG, some correlation may exist. In (4.2), it can be seen that the phase angle of the baseband harmonics depends on the phase angle of the fundamental voltage at the terminals of the WTG. In a strong grid scenario, this voltage would not depend on the active and reactive power injected by the WTG. However, in a weak grid scenario, the wind turbine generator changing its own operating point can have an effect on the fundamental voltage at its terminals. In this sense, the modulation index M can be a source for modifying the phase-angle of the harmonic emission of the WTG. Since the modulation index can also change the magnitude of the emissions, M can be interpreted as a source of correlation between the magnitude and phase angle of the WTG characteristic emission. However, quantifying this correlation in an analytical way is very challenging and very case dependent, as it would depend on the specific operating point and grid scenario.

(c) Correlation between grid impedance and background distortion

Finally, the relationship between the background distortion and the grid impedance is a complex one. It can be argued that, whenever there is a topology change in the grid (grid equivalent impedance change) the propagation of the harmonics through the grid transmission lines might change as well, therefore generating a correlation with the background harmonic distortion. This relationship becomes more complex since, in practice, the equivalent grid impedance used for harmonic studies is obtained from a grid locus. Since the grid impedance is obtained from the envelope, establishing a correlation between the grid impedance and the background distortion seems challenging, if not impossible to achieve.

In any case, this thesis shows that considering different types of correlation between the statistical variables can affect significantly the results of a Monte Carlo harmonic study. Other than the possible correlation between WTGs, other possible sources of correlation between different variables are discussed. Quantifying these correlations is, however, considered out of the scope of this thesis. The correlations are expected to be very converter-dependent (i.e., depending on each WTG manufacturer) and very system dependent. Nonetheless, it is shown here that this is an issue that deserves the attention of the power system engineers in charge of harmonic studies, and thus exploring this (perhaps through thorough statistical analysis of the data obtained in a measurement campaign) is recommended.

4.5.4 Ensuring statistical significance in Monte Carlo simulations

When performing a Monte Carlo simulation, one variable to decide is the number of runs to perform. Every run of a harmonic power flow can be considered an estimation of the Harmonic Distortion (HD) at the PCC. From the Law of Large Numbers, it is know that, if the number of runs R is big enough, the average of all these estimations should approach the true average. In fact, the Law of Large Numbers establishes that the probably distribution should approximate the true distribution, so for a large enough R, other probability characteristics (95^{th} percentile, standard deviation, etc.) should also approach the true value.

One key issue is to find what is a large enough value for R to achieve a desired level of statistical significance. From the Central Limit Theorem, it is know that, if the number

of runs R is big enough, the average of a certain number of draws (μ_R) should approach a normal distribution of the kind: $N(\mu_t, (\sigma_t^2)/R)$ where μ_t is the true average of the estimated variable, and σ_t is the true standard deviation. Therefore, the interval $[\mu_R - 1.96 \times \sigma_t/\sqrt{R}, \mu_R + 1.96 \times \sigma_t/\sqrt{R}]$ is the 95 % confidence interval for the mean.

When performing a Monte Carlo simulation, μ_t and σ_t are not known, but a common approach is to perform a first number of runs R_1 with which the mean and standard deviation of the target variable can be estimated. After that, the 95 % confidence interval can be built and it can be checked if this interval is accurate enough for the purpose of the calculation.

That is to say, after performing a first number of runs R_1, it can be said with 95 % confidence that the error in estimating the average of the harmonic distortion is:

$$E = 2 \times 1.96 \times \frac{\sigma_{\mathrm{HD}}}{\sqrt{R}} \tag{4.14}$$

Thus, a tolerance can be imposed as:

$$E = 2 \times 1.96 \times \frac{\sigma_{\mathrm{HD}}}{\sqrt{R}} < \mathrm{tol} \times \mu_{\mathrm{HD}} \tag{4.15}$$

$$R > \left(2 \times 1.96 \times \frac{\sigma_{\mathrm{HD}}}{\mathrm{tol} \times \mu_{\mathrm{HD}}}\right)^2 \tag{4.16}$$

Thus, a minimum number of runs $R_{\min} = \left(2 \times 1.96 \times \frac{\sigma_{\mathrm{HD}}}{\mathrm{tol} \times \mu_{\mathrm{HD}}}\right)^2$ can be calculated to achieve a certain tolerance in the 95 % confidence interval.

Note that this would allow to produce an estimation of the average of the HD with a certain confidence, but not necessarily of other statistical variables. In this chapter, however, the main interest is on the 95$^{\mathrm{th}}$ percentile of the HD, since a lot of standards require limits to be met during 95 % of the time. From here onwards, different approaches can be taken.

One approach would be to assume that the 95$^{\mathrm{th}}$ percentile is also accurate to a certain tolerance with high confidence, due to the fact that this can be said about the average. In a sense, this approach relies on the fact that, for a large enough R, the estimated 95$^{\mathrm{th}}$ percentile should approximate the true value; the approximation is to assume that the R value that is large enough for estimating μ_{HD} with a certain statistical significance is the same as when estimating the 95$^{\mathrm{th}}$ percentile.

A second approach would be to perform a number of harmonic power flows, and then to calculate the 95$^{\mathrm{th}}$ percentile. This process can be repeated several times, so in a sense each one of these times that the process is repeated can be considered a draw. If the number of times that this process is repeated is high enough, it is known that the average of the draws (the average of the 95$^{\mathrm{th}}$ percentile estimations) will approximate the true value; and just like before, a minimum number of runs can be calculated in order to achieve a certain tolerance in the 95 % confidence interval.

This second method is, in practice, repeating the first method several times (i.e., it can be seen as repeating the Monte Carlo study several times). Fig. 4.33 shows the results when this is done. For obtaining this figure, the following assumptions have been made: the grid impedance is the base case grid impedance, 100 % correlation is considered between wind turbines, and in each Monte Carlo study 200 runs are performed.

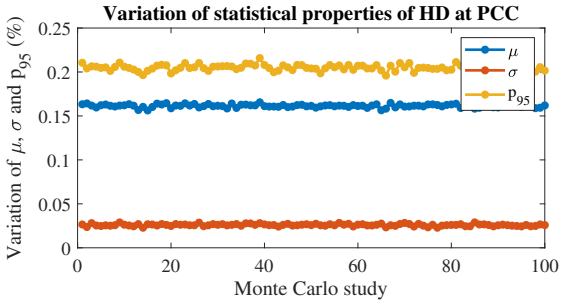

Figure 4.33: Variation of statistical properties of the HD at the PCC with different MC studies (5th harmonic).

It can be seen that, despite repeating the study 100 times, the statistical properties of the harmonic distortion (the average μ, the standard deviation σ, and the 95th percentile p_{95}) do not vary significantly. Therefore, this second method, even though it provides a way of ensuring a certain tolerance when estimating the 95 % confidence interval of the 95th percentile, is considered unnecessary in this thesis.

For the rest of the chapter, the first method is adopted: a first amount of runs is performed ($R_1 = 1000$) with which the average and standard deviation are estimated, and the minimum number of runs in order to achieve certain statistical significance is calculated. If this number is lower than R_1, the results are considered valid. If $R_{\text{min}} > R_1$, then the extra necessary simulations to achieve statistical significance are performed. In this thesis, the tolerance considered when calculating R_{min} is 0.05 (i.e., the error should be lower than 5 % of μ_{HD}), although this can be customized depending on the requirements of the application. For the majority of the Monte Carlo studies presented here, $R_1 = 1000$ is enough. However, if other PDFs are considered (in particular, PDFs with higher standard deviations) it is very possible that $R_{\text{min}} > R_1$. Fig. 4.29 shows a flow chart with the process.

4.5.5 Effect of statistical properties of the WTG emission

The effect of the mean of the magnitude of the WTG harmonic injection is shown in Fig. 4.34 (for the 5th harmonic). As expected, higher mean magnitude of the injection, leads to higher distortion at the PCC.

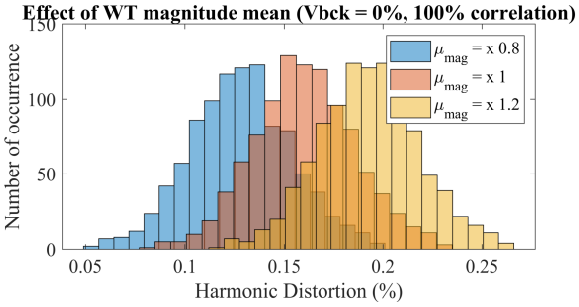

Figure 4.34: Effect of the WTG statistic properties: mean of the magnitude (5th harmonic).

The effect of the standard deviation (std) of the magnitude of the WT harmonic injection is shown in Fig. 4.35 (for the 5th harmonic). It can be seen that, for higher levels of standard deviation in the magnitude of the injection, the standard deviation of the final result (HD at the PCC) also increases.

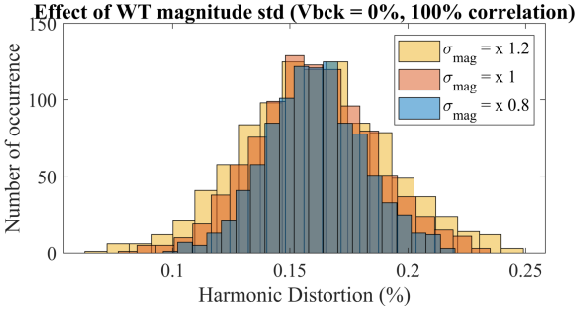

Figure 4.35: Effect of the WTG statistic properties: standard deviation of the magnitude (5th harmonic).

The effect of the mean of the phase angle of the wind turbine harmonic injection is shown in Fig. 4.36 and the effect of the standard deviation (std) of the phase angle of the wind turbine harmonic injection is shown in Fig. 4.37 (for the 5th harmonic). As it can be seen, neither of these two variables have any effect on the result. The reason for this is explained previously. If $|\mathbf{V_{bck}}| = 0$, then the exact phase-angle of the wind turbine emission is irrelevant if the wind turbine emission is 100 % correlated (see Fig. 4.27 and Fig. 4.28).

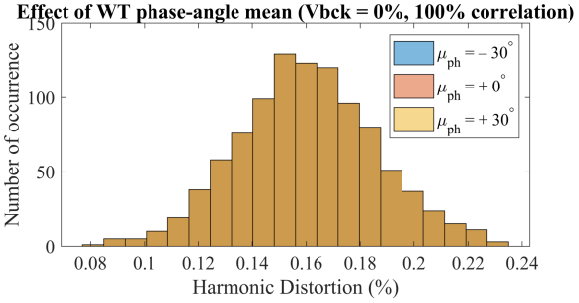

Figure 4.36: Effect of the WTG statistic properties: mean of the phase angle (5th harmonic).

However, this is not necessarily true if $\mathbf{V_{bck}} \neq 0$, or if the correlation is not 100 %. Fig. 4.38 shows that the mean of the phase-angle has an effect on the results if the background harmonic magnitude is 1 %, since changing the phase-angle may increase or decrease the harmonic cancellation with the background distortion. Still, Fig. 4.39 shows that the standard deviation of the phase-angle injection has no significant effect, since the wind turbines are still 100 % correlated.

There are two main conclusions: first, the statistical properties of the magnitude of the WTG harmonic injection are always influential on the final 95th percentile of HD at the PCC. Second, the statistical properties of the phase angle of the WTG harmonic injection are

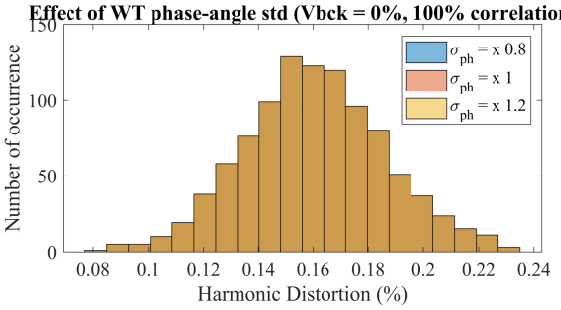

Figure 4.37: Effect of the WTG statistic properties: standard deviation of the phase angle (5th harmonic).

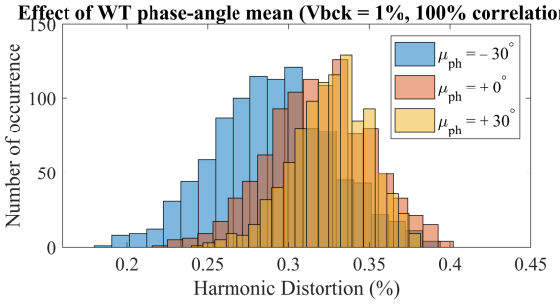

Figure 4.38: Effect of the WTG statistic properties: mean of the phase angle (5th harmonic, $\mathbf{V_{bck}} = 1\,\%$).

relevant only if the background harmonic distortion is to be taken into account in the study, or if the WTGs are not 100 % correlated. On the one hand, some TSOs require harmonic studies in which only the wind farm distortion is taken into account ($|\mathbf{V_{bck}}| = 0$), which might render irrelevant the phase angle of the WTG emission. However, on the other hand, the emission of the different WTGs is known to not be completely correlated (especially for carrier and sideband harmonics, as explained in Section 4.2.3). Thus, the phase angle of the WTG emission also needs to be properly represented in the statistical domain, especially in cases of low correlation between harmonic sources.

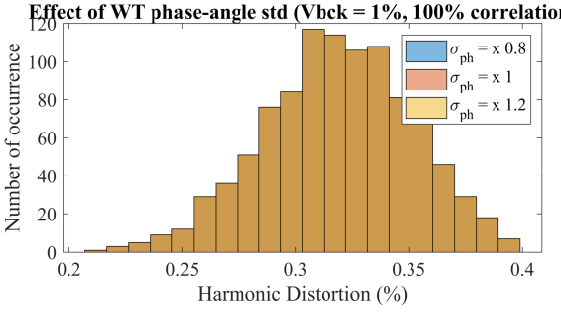

Figure 4.39: Effect of the WTG statistic properties: standard deviation of phase angle (5th harmonic, $\mathbf{V_{bck}} = 1\,\%$).

4.5.6 Effect of the WTG frequency coupling dynamics

(a) Coupled frequencies

In this section, only the 5th and 7th harmonics are studied. The 5th and 7th harmonics are coupled to each other, as explained in Section 4.3.1 (b). In particular, it is explained there that a harmonic in the voltage at a frequency f_p induces the converter to create a harmonic in the current at the frequency f_p (through the converter impedance) and also a harmonic at the frequency $2f_1 - f_p$ (through the converter coupling admittance). Therefore, a 5th harmonic in the negative-sequence in the voltage ($f_p = -250\,\text{Hz}$[16]) produces a harmonic in the current at $f_p = -250\,\text{Hz}$ and also at the coupled frequency $2f_1 - f_p = +350\,\text{Hz}$ (i.e., a 7th harmonic in the positive sequence).

Even if only these two harmonics are analysed here, the method shown here can be applied to other harmonics. However, it is worth to note that, the magnitude of the converter coupling admittance reduces very fast with increasing frequency and, therefore, this frequency-coupling effect is not expected to be relevant in the high frequency range.

(b) The influence of the grid impedance in the harmonic studies with coupled frequencies

When considering the frequency coupling dynamics of the converter, the WTG model to be used is shown in Fig. 4.11. In this model, the converter impedance represents the fact that, for a harmonic in the voltage at the frequency f_p, the converter generates a harmonic in the current at the frequency f_p. The coupling admittance represents the fact that, for a harmonic in the voltage at the frequency f_p, the converter also generates a harmonic in the current at the frequency $2f_1 - f_p$. The coupling in between these two frequencies, however, is more intense due to $\mathbf{Z_g}$. This can be seen by looking at the grid-connected WTG model in Fig. 4.40.

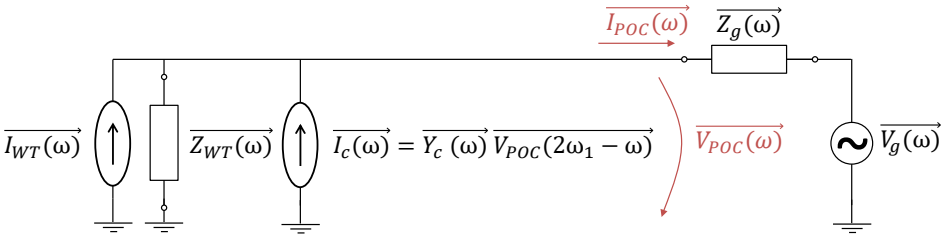

Figure 4.40: Wind turbine harmonic model connected to the grid while considering frequency coupling.

When the coupled current (at $2f_1 - f_p$) is injected into the grid, the current produces a voltage drop through the grid impedance that essentially creates a voltage distortion at $2f_1 - f_p$ at the terminals of the converter. The voltage distortion at $2f_1 - f_p$ induces the

[16] A harmonic in the negative sequence produces a space vector that rotates in the opposite direction, i.e., with negative frequency. Since the formula for the coupling frequency $2f_1 - f_p$ is obtained using space vector notation, it is necessary to use a negative frequency for the negative-sequence harmonics. Strictly, a harmonic with negative frequency does not exist in the physical system, although it is correct to use this notation if space vectors are considered.

converter to create current at $2f_1 - f_p$ and also at its coupled frequency, which is f_p. This closes the loop in which two frequencies f_p and $2f_1 - f_p$ (i.e., 5th and 7th harmonic as considered here) mutually create each other. This can be seen by analysing the equations of the grid-connected wind turbine, shown in a schematic way in Fig. 4.41.

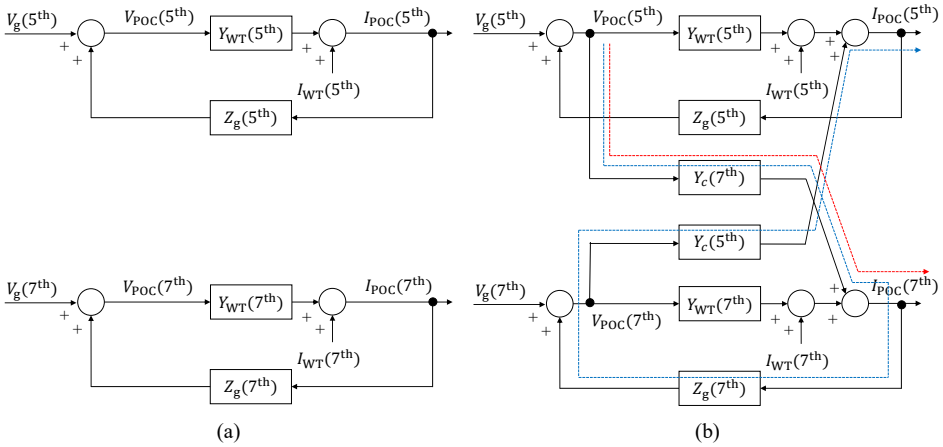

Figure 4.41: Schematic of the equations ruling a wind turbine connection with the grid: a) independent frequencies; and b) coupled frequencies.

As seen in Fig. 4.41, which exemplifies the case of the 5th and 7th harmonics, the coupling admittance makes both frequencies to be coupled. Further, the coupling exists not only because a 5th harmonic in the voltage produces a current in the 7th harmonic (red path) but also because, due to $\mathbf{Z_g}$, in the end this process creates extra 5th harmonic current (blue path). If $\mathbf{Z_g} = 0$, then only the red path exists.

(c) Method for harmonic studies in the presence of coupled frequencies

The network influence on the resulting harmonic currents at the POC of each WTG has an impact in the procedure for system-wide harmonic studies. For the case in which there are no frequency couplings, the network is solved by performing a harmonic power flow.

The nomenclature around harmonic power flow studies can be misleading in the literature. In this thesis, the harmonic power flow method consists in directly solving the voltages and currents in the system using the network admittance matrix defined at different frequencies. Thus, in this thesis, the harmonic power flow method used is the one that in [183] is called Direct Harmonic Penetration Method.

In the Direct Harmonic Penetration Method, the network is solved directly. In contrast, when couplings are considered, the harmonics 5th and 7th are coupled, and therefore have to be solved simultaneously. In here, an iterative procedure is proposed for solving the network (summarized in in Fig. 4.42).

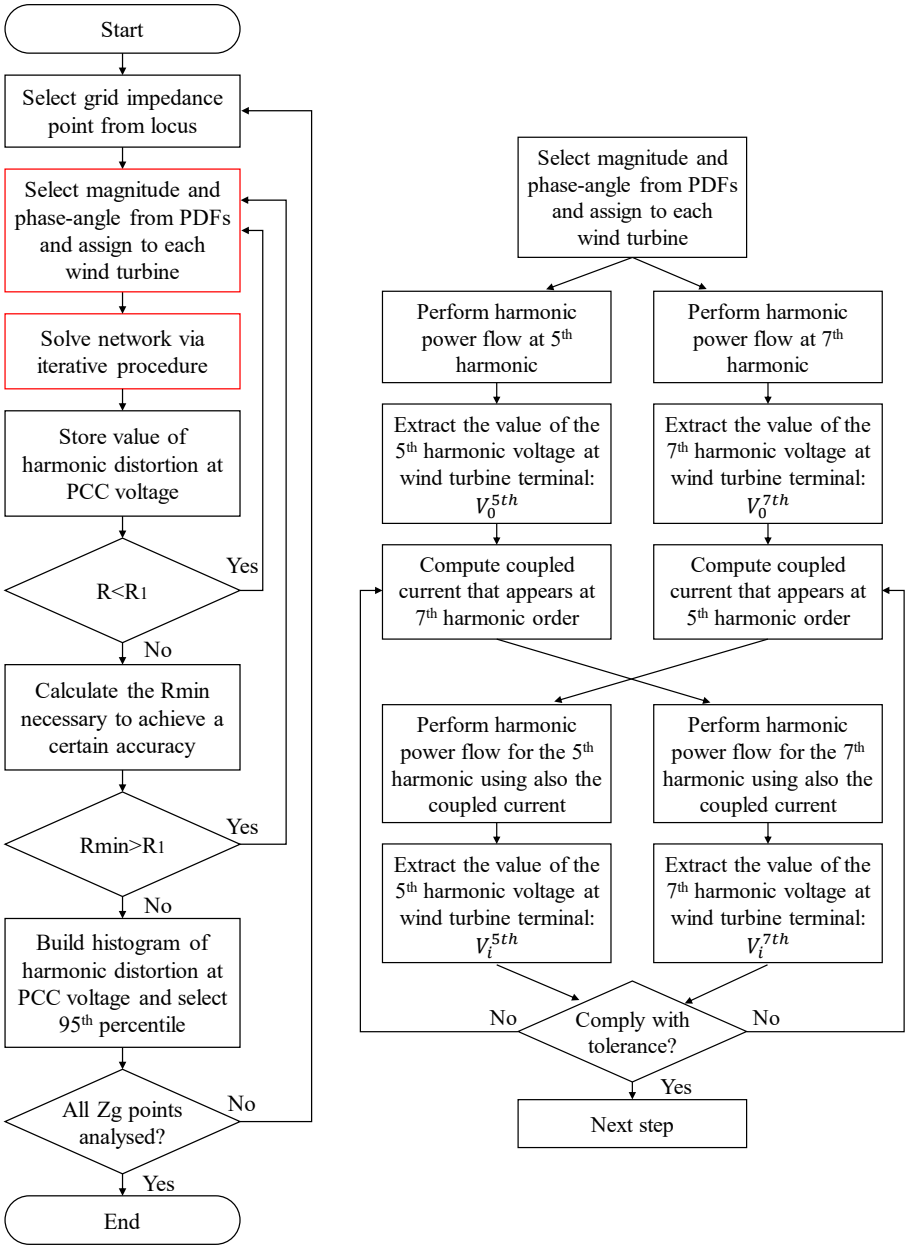

Figure 4.42: Flow chart for a harmonic study with coupled frequencies: a) general flow chart; b) detailed steps for solving the network via iterative procedure. R, R_1 and $R_{\min}$ relate to the number of runs.

Once a value has been selected for the magnitude and phase-angle of the 5^{th} and 7^{th} harmonics, instead of simply running two separate power flows at those frequencies, a more detailed process is carried out. First, two harmonic power flows are run in order to get the value of the 5^{th} and 7^{th} harmonic distortion in the voltage at the terminals of the wind turbines (called here $\mathbf{V_0^{5th}}$ and $\mathbf{V_0^{7th}}$, respectively). These values are not the correct values of the actual 5^{th} and 7^{th} harmonics in the voltage at the terminals of the wind turbine, since the coupling currents still have not been taken into account. However, they can be considered a first iteration to find their true value. With these values, the coupling currents can be calculated, and another two power flows can be computed. From such power flows, the next iteration of harmonics at the wind turbine terminals can be obtained: $\mathbf{V_i^{5th}}$ and $\mathbf{V_i^{7th}}$. The process is repeated until these computed values converge. That is to say, until the following tolerance is met:

$$\begin{aligned} \left| \frac{\mathbf{V_i^{5th}} - \mathbf{V_{i-1}^{5th}}}{\mathbf{V_{i-1}^{5th}}} \right| \leq \text{tolerance; and} \\ \left| \frac{\mathbf{V_i^{7th}} - \mathbf{V_{i-1}^{7th}}}{\mathbf{V_{i-1}^{7th}}} \right| \leq \text{tolerance} \end{aligned} \tag{4.17}$$

In this thesis, the tolerance used is 0.001. The tolerance must be met for both harmonics, and in the voltages defined at the terminals of all the wind turbines in the wind farm. After the tolerance is met, it is considered that the iteration procedure has converged, and therefore the value of the harmonic distortion at the PCC voltage is stored, and the same steps as for the uncoupled-frequencies case can be performed.

In a sense, the method proposed here is a version of the so-called "Iterative Harmonic Penetration Method" briefly mentioned in [183], but adapted to the reality of the frequency couplings present in wind farms. It is worth to mention that, in Chapter 3, it is shown that the phase-angle of the voltage fundamental might appear in the expression for the coupling admittances. With a few simplifications, it can be shown by looking at the equations shown in Chapter 3, that the phase-angle of the voltage fundamental produces only a phase-shift on the coupling admittance. This effect is usually called "phase dependence" in the literature [170]. This effect has been considered in the calculations by considering the appropriate phase-shift (different in each WTG) to the coupling admittance shown in Fig. A.1 (b).

(d) Results

The effect of considering or ignoring the frequency coupling in the wind turbine model is shown in Fig. 4.43.

The results here show that, for the case study considered, the impact of the frequency coupling is negligible. However, as shown here it is possible to include its effects by slightly modifying the flow chart for performing a Monte Carlo study and including only a few more steps in the calculation. From the data-acquisition perspective, the wind turbine manufacturers are already required in many countries to provide the equivalent impedance. Therefore, it is not considered that obtaining the coupling admittance could be problematic, since it can be obtained in similar ways as the main converter impedance. Also, the coupling admittance is also black-box, which allows manufacturers to keep protected their proprietary

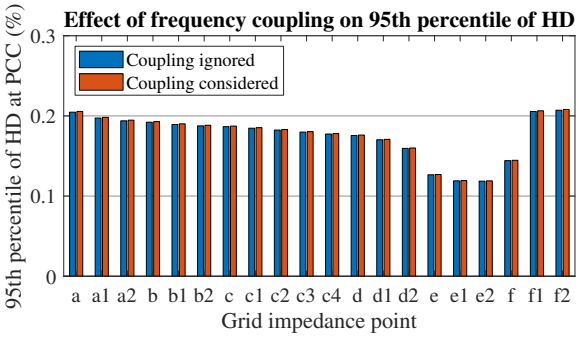

Figure 4.43: Effect of the WTG frequency coupling dynamics (5^{th} harmonic).

data. However, the indication here is that the frequency coupling is probably negligible for harmonic studies. Further case studies should be performed to determine if the frequency coupling could be relevant in other wind farm architectures, work in which the methodology presented here is still applicable.

4.6 Conclusions

In this chapter, the typical method used in industry for harmonic studies, the IEC method, is compared with the Monte Carlo method. The IEC method provides robust results if the mathematical assumptions on which the method is based are met. However, as it is discussed in this chapter, in many wind farms these assumptions are not met, and thus a lot of measurement campaigns shown in literature portray the inaccuracy of the IEC-method estimations.

Alternatively, if enough data is gathered from the WTG manufacturer, the Monte Carlo method can be applied. This chapter discusses that, when applying this method, several assumptions on the correlations between variables must be done, which are often overlooked in previous works. For example, [196] and [197] mention correlation, but only referring to the magnitude and phase angle of a specific harmonic (or, alternatively, its real and imaginary part in its Cartesian representation). In contrast, other correlations, like the possible correlation between harmonics in between different WTGs, or the lack thereof, is not directly addressed in the literature. Usually, when applying the Monte Carlo method, as it is done when deriving the theoretical basis for the IEC Summation Law, the emission sources are considered completely uncorrelated. However, this chapter shows that the assumption of statistical independence between WTGs is not necessarily true. For example, the baseband harmonics in certain modulation strategies are dependent on the fundamental frequency variation, which is common to all WTGs. The correlation between WTGs, thus, must be studied in detail in real applications, as this thesis shows that it may have strong impact in the results when applying Monte Carlo simulation. Further, this chapter shows the strong impact that background harmonic distortion can have in the final distortion levels at the PCC. A more accurate background harmonic representation, perhaps using probability distributions, is recommended.

Finally, the effect of WTG converter frequency couplings on the harmonic compliance is addressed. A methodology is presented for the study of such phenomenon and, according to the results in the specific case study considered, the effect seems to be insignificant. Further studies should be performed to determine if the frequency couplings could be relevant in other wind farm architectures or under different assumptions (e.g., including a higher number of couplings).

Chapter 5

Conclusions

The main objective of this thesis is to investigate the effect of voltage imbalance on the stability and harmonic generation of wind turbine converters in offshore wind farms. Within the scope of this thesis is voltage imbalance that appears in steady-state (typically, a low value limited by grid codes and international power quality standards) and also voltage imbalance that appears during transient situations (typically, a higher value due to temporary conditions like faults). In this chapter, the main conclusions for each research question and some recommendations for future research are given.

How does the grid voltage imbalance affect the stability and harmonic rejection capability of the PLL?

First, with respect to stability, it is concluded that the effect of voltage imbalance on the stability margins of the PLL depends strongly on the PLL design. In this thesis, the focus is the widely known Double Decoupled Synchronous Reference Frame PLL (DDSRF-PLL) and some variants. For a typical DDSRF-PLL design, increasing the voltage imbalance worsens the stability margin of the PLL; however, the imbalance increase must be large so that the stability margin is significantly affected. In particular, the pole damping of the PLL remains at high levels and nearly unchanged up until imbalance levels of around 20%. This includes, by far, the voltage imbalance that may appear in steady-state conditions (e.g., IEC 61000-3-13 suggests a planning level limit of 1.4% for HV networks) and even some fault conditions. For the transients that induce a higher imbalance, the stability margin decreases.

Secondly, for a given distorted voltage, it is important to quantify the amount of harmonics that appears in the phase-angle calculated by the PLL. In this thesis, this is called the analysis of the harmonic rejection capability of the PLL, which must be done in the frequency range in which harmonics typically appear in the voltage. This thesis concludes that, when tracking the positive-sequence voltage phase angle, the harmonic rejection capability of the PLL is high for any imbalance level (i.e., the PLL acts as a low-pass filter).

The output of a typical PLL algorithm is the phase angle of the positive-sequence voltage. Additionally, in this thesis, it is also explored the possibility of tracking the phase angle of the negative-sequence voltage. Tracking the negative-sequence voltage phase angle could be useful in the design of certain unbalanced current control loops; however,

this thesis shows that it is a challenge. Two methods for tracking the negative-sequence voltage phase angle are explored. In the direct-tracking method (called method 1 in this thesis), an extra loop is added to the PLL architecture whose objective is to lock its dq frame to the negative-sequence voltage. In the indirect-tracking method (called method 2 in this thesis), the negative-sequence voltage phase-angle is mathematically derived from the positive-sequence phase angle. When comparing them, the direct-tracking method has the disadvantage that it is challenging to design the control parameters to track a certain signal (the negative-sequence voltage) that has a wide range of possible amplitudes. However, in any case, both methods suffer from the problem that, even if the poles of the PLL are independent from the imbalance (e.g., due to the use of normalization blocks), the gain of the system is not. This causes that, depending on the voltage imbalance level and control parameters design, the harmonics present in the voltage may cause very high distortion in the negative-sequence voltage phase-angle signal. This problem should be addressed if the negative-sequence voltage phase angle would ever be used in converter control.

In order to achieve these conclusions, this thesis devotes a significant effort into quantifying with equations the changes that the negative-sequence voltage introduces in the dynamics of the PLL. Both Linear Time Periodic (LTP) and Linear Time Invariant (LTI) models have been developed and compared to check their accuracy in the presence of imbalance. With the LTP model it is possible to analyse small-signal stability at all imbalance levels, which is not possible with the LTI model. For harmonic rejection capability analysis, both models are accurate enough in the majority of the frequency range of interest.

The considerations shown here are not directly useful to system operators or plant developers. However, they should provide some guidance for engineers and manufacturers working on PLL design in the presence of imbalance.

How does the grid voltage imbalance affect the stability and harmonic generation of the wind-turbine converter?

Firstly, with respect to stability, this thesis shows that the effect of the voltage imbalance on the passivity of the converter depends significantly on the control design. The current control structure used here is based on the double Synchronous Reference Frame (SRF) control, with a sequence-component decoupling network, and with the use of both the positive and negative sequence phase angle.

In this thesis, the current-reference strategy is defined as the amount of active and reactive current in the positive and negative sequence that the converter is trying to inject as a result of an imbalance in the voltage. For low imbalance levels, the converter typically will inject no negative-sequence current, whereas for high imbalance levels, the behaviour of the converter is typically driven by Fault-Ride Through (FRT) requirements. This thesis shows that the passivity of the converter not only depends on the imbalance in the voltage, but also on the negative-sequence current that the converter injects in the presence of voltage imbalance. Therefore, the passivity of the converter depends on the current-reference strategy that the converter follows. This thesis shows that, if the negative-sequence current reference is zero or is selected proportional to the voltage imbalance level, the passivity of the converter becomes almost independent of the voltage imbalance. This is the case for several widely-implemented current-reference strategies. In any case, conclusions on the effect of

current-reference strategies and FRT requirements on the stability of the converter shall not be generalized, since they are very dependent on the control design of the converter.

Secondly, with respect to harmonic studies, it is important to address the effect that voltage imbalance may have on the harmonic model by the converter (which typically consists on one emission source and one impedance). Due to the high influence that a vendor-specific modulation strategy may have on the harmonic emission, this is not addressed here. Instead, this thesis shows that the voltage imbalance does not impact significantly the harmonics generated in the converter current as a consequence of a distortion in the voltage (i.e., the distortion due to the converter admittances).

In order to achieve these conclusions, this thesis develops a purely LTI model of the converter, and another three LTP models of the converter with different levels of complexity. For stability studies, LTP model is always recommended, whereas for harmonic studies, the LTI model is accurate enough in the relevant frequency range.

The results at the converter level are not considered to be widely applicable due to the variability in converter-control design; however, the method and the considerations shown here could be useful to system operators, plant developers, grid code regulators, and manufacturers that look for a robust design of wind-turbine converters.

How do the converter frequency couplings affect the harmonic compliance of the wind farm?

A wind farm case study has been designed and modelled for harmonic analyses. Studies have been performed using a Monte Carlo approach to take into account the statistical variability of the magnitude and phase angle of the harmonic emission by the wind turbine converter. The final voltage distortion at the PCC can be obtained. A method has been proposed to include the effect of the converter frequency couplings in harmonic studies. The results show that the difference in between considering or not the frequency coupling is not decisive. However, further studies should be performed including a higher number of couplings and different wind farm architectures.

In contrast, the statistical correlation between the emissions of different Wind Turbine Generators (WTGs) has been found to have a significant impact. Usually, when applying the Monte Carlo method, the emission sources are considered completely uncorrelated. However, this thesis shows that the assumption of statistical independence between WTGs is not necessarily true. For example, the baseband harmonics in certain modulation strategies are dependent on the fundamental frequency variation, which is common to all WTGs. It is recommended that future work is carried out taking into account other WTG model assumptions and wind farm designs.

These considerations are relevant to the stakeholders involved in grid-code compliance of wind farms, e.g, vendors, plant developers, or system operators. This thesis shows that correlation has an impact on the results of a harmonic study; however, a discussion shall be had about the level of complexity really required on the WTG harmonic models, given that other uncertainties in the wind farm harmonic studies (e.g., future grid developments) may have a more significant role. Further, quantifying correlation may prove to be a challenge, which is an important consideration given that the quality of the prediction in a harmonic study does not depend only on the method applied, but also on the quality of the input data.

5.1 Future work

During fault conditions, apart from the possible appearance of negative-sequence voltage, the positive sequence voltage may also change. This thesis has focused on analysing the effect of the negative-sequence voltage, but similar efforts can be performed to study the effect of positive-sequence voltage variation. Different normalization schemes within the PLL can also be studied to address the variation in the voltage in both sequences.

Further, the effect of the current-reference strategy on the passivity of the converter has been emphasized in this thesis. The conclusions reached about the impact of the negative-sequence current on the passivity of the inverter should be generalized to other converter control architectures. Also, this phenomenon has been modelled in a static way, without considering that the values used to generate the current references (e.g. the values of the positive and negative sequence voltage magnitude) come from the PLL and therefore are also subject to their own dynamics. This should be studied in future work to get a complete picture of the dynamic behaviour of the converter under faulty conditions.

When performing harmonic studies at the wind farm level, a Monte Carlo method has been applied. The random variables in this study are the magnitude and phase angle of the harmonic at each wind turbine, and therefore twice as many random variables as number of wind turbines have been considered. First of all, the exact correlation between these variables must be studied, including the possible correlation between the magnitude and phase-angle of a harmonic in a specific WTG, and the relationship between the emission of different WTGs. As explained in this thesis, the statistical characteristics of the emission (including correlation effects) are very device dependent and, therefore, it is recommended the use of real WTG measurement data. Second, it might be possible to consider the variability of the grid background harmonics (magnitude, and phase angle) in future harmonic studies if the information is available. The conclusions in this thesis shall be generalized for other WTG assumptions and wind farm designs. This future work is only possible if more power quality measurements from future or operating wind farms are available.

With respect to wind-farm level studies, the use of grid impedance loci is common. Despite that the grid impedance loci is a powerful way to ensure that the distortion at the PCC remains low even if there is grid topology changes or expansions, it provides a conservative assessment about the harmonic distortion at the PCC. In the end, harmonic studies become risk assessment studies. Future work should be devoted into trying to quantify such risk, with respect to the grid impedance considered from the loci, other variables considered in the study, and the modelling uncertainties in the wind farm.

Finally, the analysis in this thesis is based on grid-following technology, while grid-forming converters are expected to be increasingly present in future power systems. Certain grid-forming converters have similar low-level control loops as grid-following converters. In particular, the current control loop and the switching and modulation strategy, might be similar in both types of converters. However, grid-forming converters typically use power-synchronization loops, instead of voltage synchronization strategies. Other upper-level control loops are also very different in grid-forming technology. Thus, the modelling and analysis performed in this thesis is only partially applicable to grid-forming converters, so further work needs to be undertaken in order to assess the effect of grid voltage imbalance in the stability and harmonics of grid-forming converters.

Appendix A

Control design and parameters

A.1 DDSRF-PLL parameters

In this Appendix, the design for the DDSRF-PLL constants is discussed. The first design choice is the cut-off frequency of the Low-Pass Filter (LPF) $F(s) = \frac{\omega_f}{s+\omega_f}$. This frequency is usually set as $\omega_f = K\omega_1$, where K is the parameter changed in Section 2.10 to test the LTI and LTP methods at the PLL level. Further, this is the parameter changed in Section 3.10 to test the different converter models. Except for these sections, the rest of the thesis uses a $K = 1/\sqrt{2}$ as recommended in [137].

The second design choice is the proportional and integral constants in the PI regulators. In this paper, the same strategy as in [137] is followed, which consists in ignoring the decoupling network and analysing the SRF-PLL separately. If that is performed, the SRF-PLL is a second-order small-signal model with two poles whose locations depend on K_{pPLL} and K_{iPLL}. It is possible to impose the damping and frequency of the poles (in this paper, $\omega_c = 2\pi 30$ rad/s and $\xi = 1/\sqrt{2}$) as follows:

$$K_{\text{iPLL}} = \frac{\omega_c^2}{V_{\text{nom}}}\,;\; K_{\text{pPLL}} = \frac{2\xi\omega_c}{V_{\text{nom}}}. \tag{A.1}$$

In the previous equation V_{nom} is the nominal voltage of the converter, which is selected as $V_{\text{nom}} = 110\sqrt{2}$ V for chapter 2 and 3 (unless otherwise specified). These PI constants can be used in the positive-sequence SRF-PLL in both DDSRF-PLL methods. With respect to the negative-sequence SRF in method 1, these constants can be used too, since the negative-sequence voltage is normalized and scaled to V_{nom}.

A.2 Inverter parameters

In this Appendix, the inverter parameters are discussed. The phase-voltage for the laboratory set-up is equal to the nominal voltage V_{nom} with which the PLL constants are designed (in RMS). The output inductor and its parasitic resistance were chosen according to the availability in the laboratory. The switching frequency was chosen as high as it was possible with the available equipment, while still maintaining performance. This was done in order to make sure that the distortion due to the switching action happened as far as possible from

the distortion that is under study in this thesis: i.e. the distortion due to the PLL and current control dynamics that happen as a reaction of the voltage distortion.

The PI constants for the current control were chosen based on a common simplified technique for current control design that consists on analysing the current control loop without considering the rest of the loops nor the modulation and switching delay. If that is done and, in the case of using a single SRF, the current control loop becomes a simple loop consisting on a transfer-function defined by the PI controller $H_{\mathrm{i}}(s) = K_{\mathrm{p}} + K_{\mathrm{i}}/s = (K_{\mathrm{p}}s + K_{\mathrm{i}})/s$, and a transfer function that represents the plant, which is simply $Y_{\mathrm{L}}(s) = 1/(Ls + R_{\mathrm{L}})$. Under all these assumptions, then, the only pole in the loop (from the plant) can be cancelled out with the only zero in the loop (from the PI controller) if the following constants are selected:

$$\begin{aligned} K_{\mathrm{p}} &= \omega_{\mathrm{c}} L \\ K_{\mathrm{i}} &= K_{\mathrm{p}} \frac{R_{\mathrm{L}}}{L} \end{aligned} \tag{A.2}$$

where the ω_{c} will represent, approximately, the desired cross-over frequency of the loop. In reality, the above simplifications do not take into account that the PI controller is in a different frame than the plant (dq vs $\alpha\beta$), nor the switching and modulation delays, which will provoke a different cross-over frequency for the current-control loop (other than the one specified by ω_{c}). This method, however, was used for its simplicity and since, in reality, the parameter selection is not a fundamental issue in this thesis. If, for example, the objective of the thesis was to compare different ways of implementing the converter control, the parameter selection would be fundamental, since it would affect the result of the comparison. However, in this thesis, the focus lies more in the method to study the impact of different items in the stability and harmonics of the converter, and the method must be applicable irrespective of the parameter selection.

Finally, the voltage feed-forward loop uses a LPF (H_{ff}). In order to prevent the risk of an infinite system gain caused by this loop [165], the cut-off frequency of the H_{ff} is limited to 0.5 Hz, as recommended in [168].

Table A.1: Inverter parameters

	Description	**Value**	**Unit**
V_{dc}	DC Voltage	500	V
V_{phase}	Phase Voltage	110	V
L	Output Inductor	5	mH
R_{L}	Resistance of Output Inductor	44	mΩ
f_{sw}	Switching Frequency	20	kHz
f_{s}	Sampling Frequency	20	kHz
K_{p}	Proportional Constant PI Current	4.7	Ω
K_{i}	Integral Constant PI Current	41.5	Ω/s

A.3 WTG parameters

In Chapter 4, a WTG for harmonic studies is modelled. The impedance for the Norton harmonic model has been calculated using the formulas derived in Chapter 3, and is compared

against simulation results in Fig. A.1 (a). More specifically, the control method used is M2 (see Chapter 3) and the control parameters used are shown in Table A.2 for an operating point defined as: positive-sequence voltage equal to the rated voltage, low negative-sequence voltage (2%), positive-sequence current equal to its rated value, and negative-sequence current equal to zero. The PLL and inverter parameters of the WTG shown in Table A.2 are derived following indications in this Appendix.

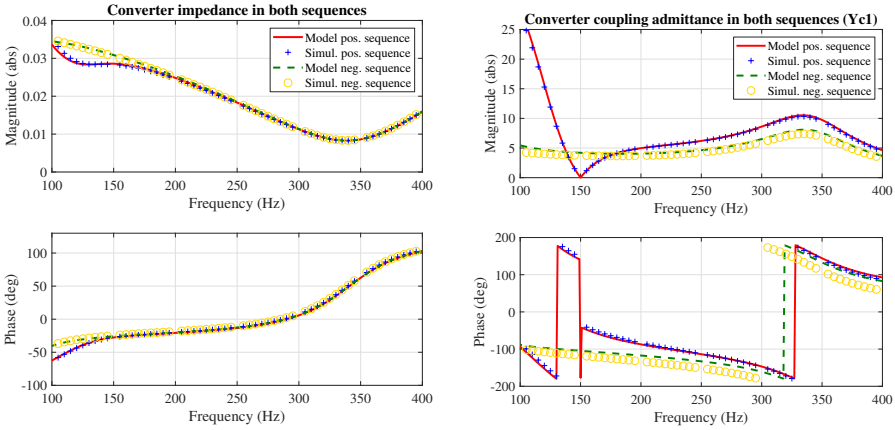

(a) (b)

Figure A.1: WTG converter (a) impedance and (b) coupling admittance.

Table A.2: WTG converter parameters

	Description	**Value**	**Unit**
V_{dc}	DC Voltage[a]	1500	V
V_{ll}	Line-to-line Voltage	690	V
P_{rated}	Rated Power	4.2	MW
L	Output Inductor	21	μH
R_L	Resistance of Output Inductor	5.7	mΩ
f_{sw}	Switching Frequency	2.5	kHz
f_s	Sampling Frequency	2.5	kHz
K_p	Proportional Constant PI Current	0.02	-
K_i	Integral Constant PI Current	5.34	-
K_{pPLL}	Proportional Constant PI PLL	0.47	-
K_{iPLL}	Integral Constant PI PLL	63.1	-
K_{PLL}	Low-Pass Filter Constant PLL	0.707	-
ω_{ff}	Voltage Feed-forward Bandwidth	3.14	rad/s

[a] Third harmonic injection is not applied. Thus, the DC bus is over-rated compared to usual values.

References

[1] Wind Europe, "Wind energy in Europe: 2021 statistics and the outlook for 2022-2026," Feb 2022.

[2] European Commission, "European green deal," https://ec.europa.eu/clima/eu-action/european-green-deal_en, accessed: 2022-02-06.

[3] ——, "A clean planet for all: A European long-term strategic vision for a prosperous, modern, competitive and climate neutral economy," 2018, Commission Communication COM(2018) 773.

[4] Wind Europe, "Our energy, our future: How offshore wind will help Europe go carbon-neutral," Nov 2019.

[5] European Commission, "An EU strategy to harness the potential of offshore renewable energy for a climate neutral future," 2020, Commission Communication COM(2020) 741.

[6] International Energy Agency (IEA), "Offshore wind outlook 2019," Nov 2019.

[7] International Renewable Energy Agency (IRENA), "Offshore renewables: An action agenda for deployment," Jul 2021.

[8] F. Blaabjerg and K. Ma, "Wind energy systems," *Proceedings of the IEEE*, vol. 105, no. 11, pp. 2116–2131, 2017.

[9] J. Sun, C. Buchlagen, and M. Greve, "Impedance modelling and simulation of wind turbines for power system harmonic analysis," in *16th International Workshop on Large-Scale Integration of Wind Power into Power Systems as well as Transmission Networks for Offshore Wind Power Plants (16th Wind Integration Workshop), Berlin, Germany*, Oct 2017.

[10] D. Elliott, K. R. W. Bell, S. J. Finney, R. Adapa, C. Brozio, J. Yu, and K. Hussain, "A comparison of AC and HVDC options for the connection of offshore wind generation in Great Britain," *IEEE Transactions on Power Delivery*, vol. 31, no. 2, pp. 798–809, 2016.

[11] J. Dakic, M. Cheah-Mane, O. Gomis-Bellmunt, and E. Prieto-Araujo, "HVAC transmission system for offshore wind power plants including mid-cable reactive power compensation: Optimal design and comparison to VSC-HVDC transmission," *IEEE Transactions on Power Delivery*, vol. 36, no. 5, pp. 2814–2824, 2021.

[12] Gemini Wind Park website, [Online]. Available: https://www.geminiwindpark.nl/details-cables.html#c1.

[13] W. Wiechowski and P. B. Eriksen, "Selected studies on offshore wind farm cable connections - challenges and experience of the Danish TSO," in *2008 IEEE Power and Energy Society General Meeting - Conversion and Delivery of Electrical Energy in the 21st Century*, July 2008, pp. 1–8.

[14] Ørsted, "Hornsea project one-project overview," Presentation for Ofgem OFTO. [Online]. Available: https://www.ofgem.gov.uk/sites/default/files/docs/2018/10/hornsea_one_project_presentation.pdf.

[15] Cigre WG B4.62, "Connection of wind farms to weak AC networks," Cigre Report 671, Dec 2016.

[16] J. L. Agorreta, M. Borrega, J. López, and L. Marroyo, "Modeling and control of N-paralleled grid-connected inverters with LCL filter coupled due to grid impedance in PV plants," *IEEE Transactions on Power Electronics*, vol. 26, no. 3, pp. 770–785, March 2011.

[17] M. K. Bakhshizadeh, J. Hjerrild, Ł. Kocewiak, B. Hesselbæk, T. Sørensen, F. Blaabjerg, C. L. Bak, and F. F. da Silva, "Harmonic modelling, propagation and mitigation for large wind power plants connected via long HVAC cables: Review and outlook of current research," in *2016 IEEE International Energy Conference (ENERGYCON)*, April 2016, pp. 1–5.

[18] H. Liu, X. Xie, J. He, T. Xu, Z. Yu, C. Wang, and C. Zhang, "Subsynchronous interaction between direct-drive PMSG based wind farms and weak AC networks," *IEEE Transactions on Power Systems*, vol. 32, no. 6, pp. 4708–4720, 2017.

[19] C. Li, "Unstable operation of photovoltaic inverter from field experiences," *IEEE Transactions on Power Delivery*, vol. 33, no. 2, pp. 1013–1015, April 2018.

[20] J. Sun, M. Xu, M. Cespedes, and M. Kauffman, "Data center power system stability — part I: Power supply impedance modeling," *CSEE Journal of Power and Energy Systems*, vol. 8, no. 2, pp. 403–419, 2022.

[21] C. Zou, H. Rao, S. Xu, Y. Li, W. Li, J. Chen, X. Zhao, Y. Yang, and B. Lei, "Analysis of resonance between a vsc-hvdc converter and the ac grid," *IEEE Transactions on Power Electronics*, vol. 33, no. 12, pp. 10 157–10 168, 2018.

[22] S. Dennetiere, H. Saad, Y. Vernay, P. Rault, C. Martin, and B. Clerc, "Supporting energy transition in transmission systems: An operator's experience using electromagnetic transient simulation," *IEEE Power and Energy Magazine*, vol. 17, no. 3, pp. 48–60, May 2019.

[23] D. Shu, X. Xie, H. Rao, X. Gao, Q. Jiang, and Y. Huang, "Sub- and super-synchronous interactions between STATCOMs and weak AC/DC transmissions with series compensations," *IEEE Transactions on Power Electronics*, vol. 33, no. 9, pp. 7424–7437, 2018.

[24] H. Hu, H. Tao, F. Blaabjerg, X. Wang, Z. He, and S. Gao, "Train–network interactions and stability evaluation in high-speed railways–part I: Phenomena and modeling," *IEEE Transactions on Power Electronics*, vol. 33, no. 6, pp. 4627–4642, 2018.

[25] E. Mollerstedt and B. Bernhardsson, "Out of control because of harmonics — an analysis of the harmonic response of an inverter locomotive," *IEEE Control Systems*, vol. 20, no. 4, pp. 70–81, Aug 2000.

[26] C. Buchhagen, C. Rauscher, A. Menze, and J. Jung, "Borwin1 — first experiences with harmonic interactions in converter dominated grids," in *International ETG Congress 2015; Die Energiewende - Blueprints for the new energy age*, Nov 2015, pp. 1–7.

[27] S. Shah, P. Koralewicz, V. Gevorgian, H. Liu, and J. Fu, "Impedance methods for analyzing stability impacts of inverter-based resources: Stability analysis tools for modern power systems," *IEEE Electrification Magazine*, vol. 9, no. 1, pp. 53–65, 2021.

[28] A. M. C. Buchhagen, M. Greve and J. Jung, "Harmonic stability – practical experience of a TSO," in *Proc. The 15th International Workshop on Large-Scale Integration of Wind Power into Power Systems as well as Transmission Networks for Offshore Wind Farms*, Nov 2016.

[29] National Grid Electricity Transmission (NGET), "Report into the power interruption following generator trips and frequency excursion on 9th August 2019," 2019.

[30] National Grid ESO, "Technical report on the events of 9 august 2019," London, Sep 2019.

[31] L. Shuai, R. Sharma, K. H. Jensen, J. N. Nielsen, D. Murcia, S. Pirzada, P. Brogan, and P. Godridge, "Eigenvalue-based stability analysis of sub-synchronous oscillation in an offshore wind power plant," in *17th Wind Integration Workshop, Stockholm, Sweden*, Oct 2018.

[32] Ł. Kocewiak, "Harmonics in large offshore wind farms," Ph.D. dissertation, Aalborg University, 2012.

[33] M. Bollen and K. Yang, "Harmonics — another aspect of the interaction between windpower installations and the grid," in *22nd International Conference and Exhibition on Electricity Distribution (CIRED 2013)*, 2013, pp. 1–4.

[34] D. O. Brasil, Z. Emin, L. S. Cano, C. Buchhagen, C. F. Jensen, and M. V. Escudero, "International comparison of harmonic assessment approaches and implications," C4-111 CIGRE 2018.

[35] M. Val Escudero, "Power quality and grid codes in view of massive integration of power electronic devices (migrate project)," Presentation at the 17th International Workshop on Large-Scale Integration of Wind Power into Power Systems as well as Transmission Networks for Offshore Wind Power Plants (17th Wind Integration Workshop), Stockholm, Sweden, Oct 2018.

[36] C. F. Jensen, Ł. H. Kocewiak, and Z. Emin, "Amplification of harmonic background distortion in wind power plants with long high voltage connections," in *CIGRE Biennial Session, CIGRÉ, Paris, France, C4-112*, Aug 2016.

[37] C. F. Flytkjær and Ł. H. Kocewiak, "Harmonics in power electronic power systems," PhD and Industry Course, Aalborg University, Denmark, Oct 2018.

[38] P. Sørensen, P. H. Madsen, A. Vikkelsø, K. K. Jensen, K. A. Fathima, A. K. Unnikrishnan, and Z. V. Lakaparampil, "Power quality and integration of wind farms in weak grids in India," Risø National Laboratory, Roskilde, Apr 2000.

[39] A. Stamatopoulos, H. Vikelgaard, F. F. da Silva, and C. L. Bak, "Power system unbalance due to railway electrification: Review of challenges and outlook of the danish case," in *2016 IEEE International Energy Conference (ENERGYCON)*, 2016, pp. 1–6.

[40] A. Stamatopoulos, F. Faria da Silva, C. L. Bak, and H. Vikelgaard, "On-site measurements for voltage unbalance studies associated with the AC railway operation: Objectives, methodology and monitoring results," in *2017 52nd International Universities Power Engineering Conference (UPEC)*, 2017, pp. 1–6.

[41] M. M. Kiani, "Effects of voltage unbalance and system harmonics on the performance of doubly fed induction wind generators," Ph.D. dissertation, The University of Texas at Arlington, 2009.

[42] ABB, "Windstar transformers," Company website. [Online]. Available: https://www.hitachienergy.com/offering/product-and-system/transformers/special-application-transformers/windstar-transformers.

[43] M. Cespedes and J. Sun, "Impedance modeling and analysis of grid-connected voltage-source converters," *IEEE Transactions on Power Electronics*, vol. 29, no. 3, pp. 1254–1261, March 2014.

[44] Hong-Seok Song and Kwanghee Nam, "Dual current control scheme for PWM converter under unbalanced input voltage conditions," *IEEE Transactions on Industrial Electronics*, vol. 46, no. 5, pp. 953–959, Oct 1999.

[45] M. Graungaard Taul, X. Wang, P. Davari, and F. Blaabjerg, "Current reference generation based on next-generation grid code requirements of grid-tied converters during asymmetrical faults," *IEEE Journal of Emerging and Selected Topics in Power Electronics*, vol. 8, no. 4, pp. 3784–3797, 2020.

[46] C. H. Ng, L. Ran, and J. Bumby, "Unbalanced-grid-fault ride-through control for a wind turbine inverter," *IEEE Transactions on Industry Applications*, vol. 44, no. 3, pp. 845–856, May 2008.

[47] H. Wu, X. Wang, J. Hjerrild, Ł. Kocewiak and L. Zeni, "Sequence current controllability analysis of offshore MMC-HVDC during asymmetrical faults," Presentation at the 18th International Workshop on Large-Scale Integration of Wind Power into Power Systems as well as Transmission Networks for Offshore Wind Power Plants, Oct 2019.

[48] Y. Chen, M. Chen, Z. Tian, Y. Liu, and S. Hillmansen, "VU limit pre-assessment for high-speed railway considering a grid connection scheme," *IET Generation, Transmission and Distribution*, vol. 13, no. 7, pp. 1121–1131, 2019.

[49] F. Ding, D. Zhang, J. He, H. Liu, and Y. Li, "Evaluation of the influence of electrified railway on wind farm," in *2017 IEEE Transportation Electrification Conference and Expo, Asia-Pacific (ITEC Asia-Pacific)*, 2017, pp. 1–6.

[50] Q. Zhou, L. Zhao, X. Han, Y. Ma, Y. Zhang, and S. Yang, "The impact of high-speed heavy electric railway load on wind farms," in *2020 IEEE 4th Conference on Energy Internet and Energy System Integration (EI2)*, 2020, pp. 1539–1542.

[51] Y. Chen, M. Chen, Z. Tian, and Y. Liu, "Voltage unbalance management for high-speed railway considering the impact of large-scale dfig-based wind farm," *IEEE Transactions on Power Delivery*, vol. 35, no. 4, pp. 1667–1677, 2020.

[52] Y. Chen, M. Chen, Y. Liu, and L. Chen, "Analysing the voltage unbalance impact of wind farm on traction power supply system," in *2019 14th IEEE Conference on Industrial Electronics and Applications (ICIEA)*, 2019, pp. 1557–1561.

[53] Y.-q. Xiao, W.-L. Fan, X.-f. He, Q.-y. Li, and D.-y. Luan, "Vulnerability analysis of power system with wind farm integrated considering high-speed rail loads," in *2021 IEEE 16th Conference on Industrial Electronics and Applications (ICIEA)*, 2021, pp. 345–350.

[54] G. Zhang, S. Li, F. Sun, X. Bai, and X. Cheng, "Power quality evaluation of electrified railway's impact on wind farm electric and its engineering application," *Journal of Physics: Conference Series*, vol. 1087, p. 042066, 09 2018.

[55] J. Kearney, "Grid voltage unbalance and the integration of DFIG's," Ph.D. dissertation, Technological University Dublin, 2013.

[56] P. Kundur, J. Paserba, V. Ajjarapu, G. Andersson, A. Bose, C. Cañizares, N. Hatziargyriou, D. Hill, A. Stankovic, C. Taylor, T. Van Cutsem, and V. Vittal, "Definition and classification of power system stability IEEE/CIGRE joint task force on stability terms and definitions," *IEEE Transactions on Power Systems*, vol. 19, no. 3, pp. 1387–1401, 2004.

[57] Task force on stability definitions and characterization of dynamic behavior in systems with high penetration of power electronic interfaced technologies, "Stability definitions and characterization of dynamic behavior in systems with high penetration of power electronic interfaced technologies," IEEE Power and Energy Society, PES-TR77, Apr 2020.

[58] N. Hatziargyriou, J. Milanovic, C. Rahmann, V. Ajjarapu, C. Cañizares, I. Erlich, D. Hill, I. Hiskens, I. Kamwa, B. Pal, P. Pourbeik, J. Sanchez-Gasca, A. Stankovic, T. Van Cutsem, V. Vittal, and C. Vournas, "Definition and classification of power system stability – revisited & extended," *IEEE Transactions on Power Systems*, vol. 36, no. 4, pp. 3271–3281, 2021.

[59] X. Wang and F. Blaabjerg, "Harmonic stability in power electronic based power systems: Concept, modeling, and analysis," *IEEE Transactions on Smart Grid*, pp. 1–1, 2018.

[60] P. M. Anderson, B. L. Agrawal and J. E. Van Ness, *Subsynchronous Resonance in Power Systems*. Wiley-IEEE Press, 1990.

[61] L. Harnefors, "Analysis of subsynchronous torsional interaction with power electronic converters," *IEEE Transactions on Power Systems*, vol. 22, no. 1, pp. 305–313, 2007.

[62] J. Adams, V. A. Pappu, and A. Dixit, "Ercot experience screening for sub-synchronous control interaction in the vicinity of series capacitor banks," in *2012 IEEE Power and Energy Society General Meeting*, 2012, pp. 1–5.

[63] K. Narendra, D. Fedirchuk, R. Midence, N. Zhang, A. Mulawarman, P. Mysore, and V. Sood, "New microprocessor based relay to monitor and protect power systems against sub-harmonics," in *2011 IEEE Electrical Power and Energy Conference*, 2011, pp. 438–443.

[64] L. Wang, X. Xie, Q. Jiang, H. Liu, Y. Li, and H. Liu, "Investigation of SSR in practical DFIG-based wind farms connected to a series-compensated power system," *IEEE Transactions on Power Systems*, vol. 30, no. 5, pp. 2772–2779, 2015.

[65] Task Force on Wind SSO, "Wind energy systems sub-synchronous oscillations: Events and modeling," IEEE Power and Energy Society, PES-TR80, Jul 2020.

[66] X. He, H. Geng, J. Xi, and J. M. Guerrero, "Resynchronization analysis and improvement of grid-connected VSCs during grid faults," *IEEE Journal of Emerging and Selected Topics in Power Electronics*, vol. 9, no. 1, pp. 438–450, 2021.

[67] N. Bottrell and T. C. Green, "Comparison of current-limiting strategies during fault ride-through of inverters to prevent latch-up and wind-up," *IEEE Transactions on Power Electronics*, vol. 29, no. 7, pp. 3786–3797, 2014.

[68] X. Wang, F. Blaabjerg, and W. Wu, "Modeling and analysis of harmonic stability in an ac power-electronics-based power system," *IEEE Transactions on Power Electronics*, vol. 29, no. 12, pp. 6421–6432, Dec 2014.

[69] J. Arrillaga and N. R. Watson, *Power System Harmonics (2nd Edition)*. John Wiley & Sons, 2003.

[70] J. Sun, M. Xu, M. Cespedes, and M. Kauffman, "Low-frequency input impedance modeling of single-phase PFC converters for data center power system stability studies," in *2019 IEEE Energy Conversion Congress and Exposition (ECCE)*, 2019, pp. 97–106.

[71] J. Sun, M. Xu, M. Cespedes, D. Wong, and M. Kauffman, "Modeling and analysis of data center power system stability by impedance methods," in *2019 IEEE Energy Conversion Congress and Exposition (ECCE)*, 2019, pp. 107–116.

[72] H. Wang, W. Mingli, and J. Sun, “Analysis of low-frequency oscillation in electric railways based on small-signal modeling of vehicle-grid system in <italic>dq</italic> frame,” *IEEE Transactions on Power Electronics*, vol. 30, no. 9, pp. 5318–5330, 2015.

[73] S.-H. Huang, J. Schmall, J. Conto, J. Adams, Y. Zhang, and C. Carter, “Voltage control challenges on weak grids with high penetration of wind generation: ERCOT experience,” in *2012 IEEE Power and Energy Society General Meeting*, 2012, pp. 1–7.

[74] Y. Cheng, L. Fan, J. Rose, F. Huang, J. Schmall, X. Wang, X. Xie, J. Shair, J. Ramamurthy, N. Modi, C. Li, C. Wang, S. Shah, B. C. Pal, Z. Miao, A. Isaacs, J. Mahseredjian, and Z. J. Zhou, “Real-world subsynchronous oscillation events in power grids with high penetrations of inverter-based resources,” *IEEE Transactions on Power Systems*, pp. 1–1, 2022.

[75] J. Sun, G. Wang, X. Du, and H. Wang, “A theory for harmonics created by resonance in converter-grid systems,” *IEEE Transactions on Power Electronics*, vol. 34, no. 4, pp. 3025–3029, 2019.

[76] G. De Carne, M. Langwasser, M. Ndreko, R. Bachmann, R. W. De Doncker, R. Dimitrovski, B. J. Mortimer, A. Neufeld, F. Rojas, and M. Liserre, “Which deepness class is suited for modeling power electronics?: A guide for choosing the right model for grid-integration studies,” *IEEE Industrial Electronics Magazine*, vol. 13, no. 2, pp. 41–55, 2019.

[77] J. Sun, “Two-port characterization and transfer immittances of AC-DC converters part I: Modeling,” *IEEE Open Journal of Power Electronics*, vol. 2, pp. 1–1, 08 2021.

[78] ——, “Two-port characterization and transfer immittances of ac-dc converters part ii: Applications,” *IEEE Open Journal of Power Electronics*, vol. 2, pp. 1–1, 08 2021.

[79] Y. Sun, “The impact of voltage-source-converters’ control on the power system : the stability analysis of a power electronics dominant grid,” Ph.D. dissertation, Technische Universiteit Eindhoven, 2018.

[80] Z. Xin, X. Wang, P. C. Loh, and F. Blaabjerg, “Grid-current-feedback control for lcl-filtered grid converters with enhanced stability,” *IEEE Transactions on Power Electronics*, vol. 32, no. 4, pp. 3216–3228, April 2017.

[81] X. Wang, F. Blaabjerg, and P. C. Loh, “Passivity-based stability analysis and damping injection for multiparalleled vscs with lcl filters,” *IEEE Transactions on Power Electronics*, vol. 32, no. 11, pp. 8922–8935, 2017.

[82] S. Zhang, S. Jiang, X. Lu, B. Ge, and F. Z. Peng, “Resonance issues and damping techniques for grid-connected inverters with long transmission cable,” *IEEE Transactions on Power Electronics*, vol. 29, no. 1, pp. 110–120, Jan 2014.

[83] J. Z. Zhou, H. Ding, S. Fan, Y. Zhang, and A. M. Gole, “Impact of short-circuit ratio and phase-locked-loop parameters on the small-signal behavior of a VSC-HVDC converter,” *IEEE Transactions on Power Delivery*, vol. 29, no. 5, pp. 2287–2296, 2014.

[84] B. Wen, D. Boroyevich, R. Burgos, P. Mattavelli, and Z. Shen, "Analysis of D-Q Small-Signal Impedance of Grid-Tied Inverters," *IEEE Transactions on Power Electronics*, vol. 31, no. 1, pp. 675–687, Jan 2016.

[85] T. Messo, J. Jokipii, A. Mäkinen, and T. Suntio, "Modeling the grid synchronization induced negative-resistor-like behavior in the output impedance of a three-phase photovoltaic inverter," in *2013 4th IEEE International Symposium on Power Electronics for Distributed Generation Systems (PEDG)*, 2013, pp. 1–7.

[86] B. Wen, D. Dong, D. Boroyevich, R. Burgos, P. Mattavelli, and Z. Shen, "Impedance-based analysis of grid-synchronization stability for three-phase paralleled converters," *IEEE Transactions on Power Electronics*, vol. 31, no. 1, pp. 26–38, 2016.

[87] N. Bottrell, M. Prodanovic, and T. C. Green, "Dynamic stability of a microgrid with an active load," *IEEE Transactions on Power Electronics*, vol. 28, no. 11, pp. 5107–5119, 2013.

[88] Y. Huang, X. Yuan, J. Hu, and P. Zhou, "Modeling of VSC connected to weak grid for stability analysis of DC-link voltage control," *IEEE Journal of Emerging and Selected Topics in Power Electronics*, vol. 3, no. 4, pp. 1193–1204, 2015.

[89] D. Yang, X. Wang, and F. Blaabjerg, "Sideband-harmonic instability of paralleled inverters with asynchronous carriers," *IEEE Transactions on Power Electronics*, vol. PP, no. 99, pp. 1–1, 2017.

[90] C. Yu, X. Zhang, F. Liu, F. Li, H. Xu, R. Cao, and H. Ni, "Modeling and resonance analysis of multiparallel inverters system under asynchronous carriers conditions," *IEEE Transactions on Power Electronics*, vol. 32, no. 4, pp. 3192–3205, 2017.

[91] L. Harnefors, R. Finger, X. Wang, H. Bai, and F. Blaabjerg, "Vsc input-admittance modeling and analysis above the nyquist frequency for passivity-based stability assessment," *IEEE Transactions on Industrial Electronics*, vol. 64, no. 8, pp. 6362–6370, 2017.

[92] X. Wang, M. G. Taul, H. Wu, Y. Liao, F. Blaabjerg, and L. Harnefors, "Grid-synchronization stability of converter-based resources—an overview," *IEEE Open Journal of Industry Applications*, vol. 1, pp. 115–134, 2020.

[93] P. Rodriguez, "Modelling and stability analysis of a electrical networks dominated by grid-connected power converters," Webinar, Jul 2020.

[94] Ł. Kocewiak, R. Blasco-Giménez, C. Buchhagen, J. B. Kwon, M. Larsson, A. Schwanka Trevisan, Y. Sun, and X. Wang, "Instability mitigation methods in modern converter-based power systems," Presentation at the 20th International Workshop on Large-Scale Integration of Wind Power into Power Systems as well as Transmission Networks for Offshore Wind Power Plants, Sep 2021.

[95] M. Amin and M. Molinas, "Small-signal stability assessment of power electronics based power systems: A discussion of impedance- and eigenvalue-based methods," *IEEE Transactions on Industry Applications*, vol. 53, no. 5, pp. 5014–5030, 2017.

[96] M. K. Bakhshizadeh, J. Hjerrild, L. H. Kocewiak, F. Blaabjerg, and C. L. Bak, "On aggregation requirements for harmonic stability analysis in wind power plants," in *16th International Workshop on Large-Scale Integration of Wind Power into Power Systems as well as Transmission Networks for Offshore Wind Power Plants (16th Wind Integration Workshop), Berlin, Germany*, Oct 2017.

[97] Y. Liao, X. Wang, and X. Wang, "Frequency-domain participation analysis for electronic power systems," *IEEE Transactions on Power Electronics*, vol. 37, no. 3, pp. 2531–2537, 2022.

[98] D. Yang and Y. Sun, "Siso impedance-based stability analysis for system-level small-signal stability assessment of large-scale power electronics-dominated power systems," *IEEE Transactions on Sustainable Energy*, vol. 13, no. 1, pp. 537–550, 2022.

[99] L. Fan and Z. Miao, "Admittance-based stability analysis: Bode plots, nyquist diagrams or eigenvalue analysis?" *IEEE Transactions on Power Systems*, vol. 35, no. 4, pp. 3312–3315, 2020.

[100] D. Lumbreras, E. L. Barrios, A. Urtasun, A. Ursúa, L. Marroyo, and P. Sanchis, "On the stability of advanced power electronic converters: The generalized bode criterion," *IEEE Transactions on Power Electronics*, vol. 34, no. 9, pp. 9247–9262, 2019.

[101] J. Samanes, A. Urtasun, E. L. Barrios, D. Lumbreras, J. López, E. Gubia, and P. Sanchis, "Control design and stability analysis of power converters: The mimo generalized bode criterion," *IEEE Journal of Emerging and Selected Topics in Power Electronics*, vol. 8, no. 2, pp. 1880–1893, 2020.

[102] A. Urtasun, J. Samanes, E. L. Barrios, and P. Sanchis, "Control design and stability analysis of power converters: The discrete generalized bode criterion," *IEEE Access*, vol. 9, pp. 37 840–37 854, 2021.

[103] M. Kazem Bakhshizadeh, X. Wang, F. Blaabjerg, J. Hjerrild, Ł. Kocewiak, C. L. Bak, and B. Hesselbæk, "Couplings in phase domain impedance modeling of grid-connected converters," *IEEE Transactions on Power Electronics*, vol. 31, no. 10, pp. 6792–6796, Oct 2016.

[104] X. Wang, L. Harnefors, and F. Blaabjerg, "Unified impedance model of grid-connected voltage-source converters," *IEEE Transactions on Power Electronics*, vol. 33, no. 2, pp. 1775–1787, Feb 2018.

[105] I. Vieto, G. Li, and J. Sun, "Behavior, modeling and damping of a new type of resonance involving type-III wind turbines," in *2018 IEEE 19th Workshop on Control and Modeling for Power Electronics (COMPEL)*, 2018, pp. 1–8.

[106] J. Sun and I. Vieto, "Development and application of type-iii turbine impedance models including dc bus dynamics," *IEEE Open Journal of Power Electronics*, vol. 1, pp. 513–528, 2020.

[107] O. Can Sakinci and J. Beerten, "Comparison of linear time-invariant and linear time-periodic models for small-signal stability analysis of power electronic converters," in *Young Researchers Symposium*, 2018.

[108] R. de Groot, F, van Erp, K. Jansen, J. van Waes, M. Hap, L. Thielman, "Method for harmonic and tov connection impact assessment of offshore wind power plants - part i: Harmonic distortion," in *17th International Workshop on Large-Scale Integration of Wind Power into Power Systems as well as Transmission Networks for Offshore Wind Power Plants (17th Wind Integration Workshop), Stockholm, Sweden*, Oct 2018.

[109] K. Jansen, R. de Groot, B. van Hulst, K. Velitsikakis, C. Engelbrecht, "Method for harmonic and tov connection impact assessment of offshore wind power plants - part ii: Tov impact assessment," in *17th International Workshop on Large-Scale Integration of Wind Power into Power Systems as well as Transmission Networks for Offshore Wind Power Plants (17th Wind Integration Workshop), Stockholm, Sweden*, Oct 2018.

[110] Ł. Kocewiak, I. Arana Aristi, B. Gustavsen, and A. Hołdyk, "Modelling of wind power plant transmission system for harmonic propagation and small-signal stability studies," *IET Renewable Power Generation*, vol. 13, no. 5, pp. 717–724, 2019.

[111] C. F. Flytkjaer, B. Badrzadeh, M. Bollen, Z. Emin, L. Kocewiak, G. Lietz, S. Perera, F. F. Da Silva, and M. Val Escudero, "Power quality trends in the transition to carbon-free electrical energy systems," Cigre Science and Engineering Journal, CSE 017, February 2020.

[112] Ł. H. Kocewiak, S. K. Chaudhary, and B. Hesselbæk, "Harmonic mitigation methods in large offshore wind power plants," Presentation at the 12th International Workshop on Large-Scale Integration of Wind Power into Power Systems as well as Transmission Networks for Offshore Wind Power Plants, Oct 2013.

[113] F. D. Freijedo, S. K. Chaudhary, R. Teodorescu, J. M. Guerrero, C. L. Bak, Ł. H. Kocewiak, and C. F. Jensen, "Harmonic resonances in wind power plants: Modeling, analysis and active mitigation methods," in *2015 IEEE Eindhoven PowerTech*, 2015, pp. 1–6.

[114] B. Andresen, P. B. Brogan, and N. M. Goldenbaum, "Decomposition and mitigation of a disturbance being present at an electric connection between an electric power generating system and a power grid," Europe Patent EP2630510 A1, Apr 2012.

[115] Ł. H. Kocewiak, B. L. Øhlenschlæger Kramer, O. Holmstrøm, K. H. Jensen and L. Shuai, "Active filtering application in large offshore wind farms," Presentation at the 13th International Workshop on Large-Scale Integration of Wind Power into Power Systems as well as Transmission Networks for Offshore Wind Power Plants, Nov 2014.

[116] Ł. H. Kocewiak, B. Laudal Øhlenschlæger Kramer, O. Holmstrøm, K. Høj Jensen, L. Shuai, "Resonance damping in array cable systems by wind turbine active filtering in large offshore wind power plants," *IET Renewable Power Generation*, vol. 11, no. 7, pp. 1069–1077, July 2017.

[117] Ł. Kocewiak, M. Gautschi, L. Zeni, B. Hesselbæk, N. Barberis Negra, T. Stybe Sørensen, B. Blaumeiser and S. Vogelsanger, "Power quality improvement of wind power plants by active filters embedded in STATCOMs," Presentation at the 15th International Workshop on Large-Scale Integration of Wind Power into Power Systems as well as Transmission Networks for Offshore Wind Power Plants, Nov 2016.

[118] M. Lehmann, M. Pieschel, Ł. H. Kocewiak, M. Juamperez, S. Sahukari and K. Kabel, "Active filtering with large-scale STATCOM for the integration of offshore wind power," Presentation at the 17th International Workshop on Large-Scale Integration of Wind Power into Power Systems as well as Transmission Networks for Offshore Wind Power Plants, Oct 2018.

[119] E. Kontos, G. Tsolaridis, R. Teodorescu, and P. Bauer, "High order voltage and current harmonic mitigation using the modular multilevel converter statcom," *IEEE Access*, vol. 5, pp. 16 684–16 692, 2017.

[120] Ł. H. Kocewiak, J. Hjerrild and C. L. Bak, "Wind turbine converter control interaction with complex wind farm systems," *IET Renewable Power Generation*, vol. 7, no. 4, pp. 380–389, July 2013.

[121] S. K. Chaudhary, F. D. Freijedo, J. M. Guerrero, R. Teodorescu, C. L. Bak, Ł. Kocewiak and C. F. Jensen, "Harmonic analysis and active filtering in offshore wind power plants," Presentation at the 14th International Workshop on Large-Scale Integration of Wind Power into Power Systems as well as Transmission Networks for Offshore Wind Power Plants, Oct 2015.

[122] J. Bærholm Glasdam, Ł. H. Kocewiak, J. Hjerrild and C. L. Bak, "Control system interaction in the VSC-HVDC grid connected offshore wind power plant," Cigré Symposium, CIGRÉ, May 2015.

[123] S. K. Chaudhary, Ö. Göksu, R. Teodorescu, and P. C. Kjaer, "Impact of negative sequence current injection by wind power plants," in *2013 IEEE Power Energy Society General Meeting*, 2013, pp. 1–5.

[124] O. Troeng, B. Bernhardsson, and C. Rivetta, "Complex-coefficient systems in control," in *2017 American Control Conference (ACC)*, 2017, pp. 1721–1727.

[125] L. Harnefors, "Modeling of three-phase dynamic systems using complex transfer functions and transfer matrices," *IEEE Transactions on Industrial Electronics*, vol. 54, no. 4, pp. 2239–2248, Aug 2007.

[126] S. Golestan, J. M. Guerrero, and J. C. Vasquez, "Ltp modeling of single-phase $t/4$ delay-based plls," *IEEE Transactions on Industrial Electronics*, vol. 68, no. 9, pp. 9003–9008, 2021.

[127] ——, "Modeling and stability assessment of single-phase grid synchronization techniques: Linear time-periodic versus linear time-invariant frameworks," *IEEE Transactions on Power Electronics*, vol. 34, no. 1, pp. 20–27, 2019.

[128] S. Golestan, J. M. Guerrero, J. C. Vasquez, A. M. Abusorrah, and Y. Al-Turki, "Standard sogi-fll and its close variants: Precise modeling in ltp framework and determining stability region/robustness metrics," *IEEE Transactions on Power Electronics*, vol. 36, no. 1, pp. 409–422, 2021.

[129] C. Zhang, S. Føyen, J. A. Suul, and M. Molinas, "Modeling and analysis of SOGI-PLL/FLL-based synchronization units: Stability impacts of different frequency-feedback paths," *IEEE Transactions on Energy Conversion*, vol. 36, no. 3, pp. 2047–2058, 2021.

[130] S. Shah, P. Koralewicz, V. Gevorgian, and L. Parsa, "Small-signal modeling and design of phase-locked loops using harmonic signal-flow graphs," *IEEE Transactions on Energy Conversion*, vol. 35, no. 2, pp. 600–610, 2020.

[131] S. Golestan, J. M. Guerrero, J. C. Vasquez, A. M. Abusorrah, and Y. Al-Turki, "Linear time-periodic modeling, examination, and performance enhancement of grid synchronization systems with dc component rejection/estimation capability," *IEEE Transactions on Power Electronics*, vol. 36, no. 4, pp. 4237–4253, 2021.

[132] Y. Liao, X. Wang, X. Yue, and H. Gong, "Harmonic transfer-function model of three-phase synchronous reference frame pll under unbalanced grid conditions," in *2019 IEEE Applied Power Electronics Conference and Exposition (APEC)*, 2019, pp. 58–65.

[133] P. D. Achlerkar and B. K. Panigrahi, "New perspectives on stability of decoupled double synchronous reference frame pll," *IEEE Transactions on Power Electronics*, vol. 37, no. 1, pp. 285–302, 2022.

[134] S. R. Hall and N. M. Wereley, "Generalized nyquist stability criterion for linear time periodic systems," in *1990 American Control Conference*, 1990, pp. 1518–1525.

[135] A. Luna, J. Rocabert, J. I. Candela, J. R. Hermoso, R. Teodorescu, F. Blaabjerg, and P. Rodríguez, "Grid voltage synchronization for distributed generation systems under grid fault conditions," *IEEE Transactions on Industry Applications*, vol. 51, no. 4, pp. 3414–3425, 2015.

[136] L. Harnefors, M. Bongiorno, and S. Lundberg, "Input-admittance calculation and shaping for controlled voltage-source converters," *IEEE Transactions on Industrial Electronics*, vol. 54, no. 6, pp. 3323–3334, Dec 2007.

[137] P. Rodriguez, J. Pou, J. Bergas, J. I. Candela, R. P. Burgos, and D. Boroyevich, "Decoupled Double Synchronous Reference Frame PLL for Power Converters Control," *IEEE Transactions on Power Electronics*, vol. 22, no. 2, pp. 584–592, 2007.

[138] J. B. Kwon, "Harmonic state space (hss) modeling for power electronic based power systems," Ph.D. dissertation, Aalborg University, 2017.

[139] Y. Liao, X. Wang, X. Yue, and L. Harnefors, "Complex-valued multifrequency admittance model of three-phase VSCs in unbalanced grids," *IEEE Journal of Emerging and Selected Topics in Power Electronics*, vol. 8, no. 2, pp. 1934–1946, 2020.

[140] J. M. Maciejowski, *Multivariable feedback design*. Addison Wesley, 1989.

[141] N. M. Wereley and S. R. Hall, "Linear time periodic systems: Transfer function, poles, transmission zeroes and directional properties," in *1991 American Control Conference*, 1991, pp. 1179–1184.

[142] J. Lyu, X. Cai, X. Zhang, and M. Molinas, "Harmonic state space modeling and analysis of modular multilevel converter," in *2018 IEEE International Power Electronics and Application Conference and Exposition (PEAC)*, 2018, pp. 1–6.

[143] *Power System Stability And Control*, ser. EPRI power system engineering series. McGraw-Hill, 1994.

[144] B. Ferreira, "Understanding the Challenges of Converter Networks and Systems: Better opportunities in the future," *IEEE Power Electronics Magazine*, vol. 3, no. 2, pp. 46–49, June 2016.

[145] J. H. R. Enslin and P. J. M. Heskes, "Harmonic interaction between a large number of distributed power inverters and the distribution network," *IEEE Transactions on Power Electronics*, vol. 19, no. 6, pp. 1586–1593, Nov 2004.

[146] F. D. Freijedo, M. Ferrer, and D. Dujic, "Multivariable high-frequency input-admittance of grid-connected converters: Modeling, validation, and implications on stability," *IEEE Transactions on Industrial Electronics*, vol. 66, no. 8, pp. 6505–6515, 2019.

[147] A. Rygg, M. Molinas, C. Zhang, and X. Cai, "A modified sequence-domain impedance definition and its equivalence to the dq-domain impedance definition for the stability analysis of AC power electronic systems," *IEEE Journal of Emerging and Selected Topics in Power Electronics*, vol. 4, no. 4, pp. 1383–1396, 2016.

[148] J. Sun, "Impedance-based stability criterion for grid-connected inverters," *IEEE Transactions on Power Electronics*, vol. 26, no. 11, pp. 3075–3078, Nov 2011.

[149] C. Zhang, M. Molinas, A. Rygg, and X. Cai, "Impedance-based analysis of interconnected power electronics systems: Impedance network modeling and comparative studies of stability criteria," *IEEE Journal of Emerging and Selected Topics in Power Electronics*, vol. 8, no. 3, pp. 2520–2533, 2020.

[150] A. von Jouanne and B. Banerjee, "Assessment of voltage unbalance," *IEEE Transactions on Power Delivery*, vol. 16, no. 4, pp. 782–790, 2001.

[151] A. Stamatopoulos, F. Faria da Silva, C. L. Bak and H. Vikelgaard, "Investigation into the transmission system modeling for the effective assessment of voltage unbalance due to AC railway operation: Evaluation using on-site measurement data," Cigre Session C4-113, 2018.

[152] Tsai-Hsiang Chen, "Criteria to Estimate the Voltage Unbalances due to High-Speed Railway Demands," *IEEE Transactions on Power Systems*, vol. 9, no. 3, pp. 1672–1678, 1994.

[153] A. Bueno, J. M. Aller, J. A. Restrepo, R. Harley, and T. G. Habetler, "Harmonic and Unbalance Compensation Based on Direct Power Control for Electric Railway Systems," *IEEE Transactions on Power Electronics*, vol. 28, no. 12, pp. 5823–5831, 2013.

[154] J. Meyer, S. Hähle, P. Schegner, and C. Wald, "Impact of electrical car charging on unbalance in public low voltage grids," in *11th International Conference on Electrical Power Quality and Utilisation*, 2011, pp. 1–6.

[155] D. Schwanz, F. Möller, S. K. Rönnberg, J. Meyer, and M. H. J. Bollen, "Stochastic Assessment of Voltage Unbalance Due to Single-Phase-Connected Solar Power," *IEEE Transactions on Power Delivery*, vol. 32, no. 2, pp. 852–861, 2017.

[156] R. Yan and T. K. Saha, "Voltage variation sensitivity analysis for unbalanced distribution networks due to photovoltaic power fluctuations," *IEEE Transactions on Power Systems*, vol. 27, no. 2, pp. 1078–1089, 2012.

[157] Ł. Topolski, "Mitigation of voltage swells and unbalance caused by photovoltaic installations using a balancing transformer and an automatic voltage regulator in low-voltage networks," in *2020 12th International Conference and Exhibition on Electrical Power Quality and Utilisation- (EPQU)*, 2020, pp. 1–5.

[158] P. Paranavithana, S. Perera, R. Koch, and Z. Emin, "Global voltage unbalance in MV networks due to line asymmetries," *IEEE Transactions on Power Delivery*, vol. 24, no. 4, pp. 2353–2360, 2009.

[159] R. Yan and T. K. Saha, "Investigation of Voltage Imbalance Due to Distribution Network Unbalanced Line Configurations and Load Levels," *IEEE Transactions on Power Systems*, vol. 28, no. 2, pp. 1829–1838, 2013.

[160] H. Hu, Z. He, K. Wang, X. Ma, and S. Gao, "Power-quality impact assessment for high-speed railway associated with high-speed trains using train timetable—part ii: Verifications, estimations and applications," *IEEE Transactions on Power Delivery*, vol. 31, no. 4, pp. 1482–1492, 2016.

[161] S. M. Mousavi Gazafrudi, A. Tabakhpour Langerudy, E. F. Fuchs, and K. Al-Haddad, "Power quality issues in railway electrification: A comprehensive perspective," *IEEE Transactions on Industrial Electronics*, vol. 62, no. 5, pp. 3081–3090, 2015.

[162] C. Zhang, M. Molinas, A. Rygg, J. Lyu, and X. Cai, "Harmonic transfer-function-based impedance modeling of a three-phase VSC for asymmetric AC grid stability analysis," *IEEE Transactions on Power Electronics*, vol. 34, no. 12, pp. 12 552–12 566, 2019.

[163] M. Reyes, P. Rodriguez, S. Vazquez, A. Luna, R. Teodorescu, and J. M. Carrasco, "Enhanced decoupled double synchronous reference frame current controller for unbalanced grid-voltage conditions," *IEEE Transactions on Power Electronics*, vol. 27, no. 9, pp. 3934–3943, 2012.

[164] M. Bollen, J. Meyer, H. Amaris, A. M. Blanco, A. Gil de Castro, J. Desmet, M. Klatt, Ł. Kocewiak, S. Rönnberg, and K. Yang, "Future work on harmonics - some expert opinions part i - wind and solar power," in *2014 16th Int. Conf. on Harmonics and Quality of Power*, May 2014, pp. 904–908.

[165] P. Brogan, "The stability of multiple, high power, active front end voltage sourced converters when connected to wind farm collector systems," in *2010 Electrical Power and Energy Conference (EPEC)*, 2010.

[166] S. Golestan, J. M. Guerrero, and J. C. Vasquez, "Three-phase PLLs: A review of recent advances," *IEEE Trans. on Power El.*, no. 3, 2017.

[167] G. Amico, A. Egea-Àlvarez, P. Brogan, and S. Zhang, "Small-signal converter admittance in the pn-frame: Systematic derivation and analysis of the cross-coupling terms," *IEEE Transactions on Energy Conversion*, vol. 34, no. 4, pp. 1829–1838, 2019.

[168] P. B. Brogan, N. Goldenbaum, and J. Thisted, "Wind turbine operation based on a frequency of an AC output voltage signal provided by a power converter of the wind turbine," US Patent US10072633B2, 2015.

[169] H. Wu, X. Wang, K. Wang, G. Li, B. Zhang, and Y. Lu, "Passivity-based harmonic stability analysis of voltage source converters considering the impact of sequence decomposition algorithms," in *2020 IEEE 9th International Power Electronics and Motion Control Conference (IPEMC2020-ECCE Asia)*, 2020, pp. 1930–1934.

[170] Y. Liao and X. Wang, "Stationary-frame complex-valued frequency-domain modeling of three-phase power converters," *IEEE Journal of Emerging and Selected Topics in Power Electronics*, vol. 8, no. 2, pp. 1922–1933, 2020.

[171] I. Vieto, X. Du, H. Nian, and J. Sun, "Frequency-domain coupling in two-level vsc small-signal dynamics," in *2017 IEEE 18th Workshop on Control and Modeling for Power Electronics (COMPEL)*, 2017, pp. 1–8.

[172] L. Harnefors, X. Wang, A. G. Yepes, and F. Blaabjerg, "Passivity-based stability assessment of grid-connected VSCs—an overview," *IEEE Journal of Emerging and Selected Topics in Power Electronics*, vol. 4, no. 1, pp. 116–125, 2016.

[173] L. Harnefors, X. Wang, S. Chou, M. Bongiorno, M. Hinkkanen, and M. Routimo, "Asymmetric complex-vector models with application to VSC–grid interaction," *IEEE Journal of Emerging and Selected Topics in Power Electronics*, vol. 8, no. 2, pp. 1911–1921, 2020.

[174] H. Akagi, E. Hirokazu Watanabe, and M. Aredes, *Instantaneous Power Theory and Its Applications to Power Conditioning*. John Wiley & Sons, 2007.

[175] R. Teodorescu, M. Liserre, and P. Rodriguez, *Grid Converters for Photovoltaic and Wind Power Systems*. Wiley-IEEE Press, 2007.

[176] Math H. Bollen and Irene Gu, *Signal Processing of Power Quality Disturbances*. Wiley-IEEE Press, 2006.

[177] L. Shuai, L. H. Kocewiak, and K. H. Jensen, "Application of type iv wind turbine harmonic model for wind power plant harmonic study," in *15th International Workshop on Large-Scale Integration of Wind Power into Power Systems as well as Transmission Networks for Offshore Wind Power Plants (15th Wind Integration Workshop), Vienna, Austria*, Nov 2016.

[178] K. Redondo, I. Azcarate, J. J. Gutierrez, P. Saiz, L. A. Leturiondo, and S. Lodetti, "Case study: Reliability of the summation method to assess the harmonic current due to a wind power plant," in *17th International Workshop on Large-Scale Integration of Wind Power into Power Systems as well as Transmission Networks for Offshore Wind Power Plants (17th Wind Integration Workshop), Stockholm, Sweden*, Oct 2018.

[179] M. Eltouki, T. W. Rasmussen, E. Guest, L. Shuai and Ł. Kocewiak, "Analysis of harmonic summation in wind power plants based on harmonic phase modelling and measurements," in *17th International Workshop on Large-Scale Integration of Wind Power into Power Systems as well as Transmission Networks for Offshore Wind Power Plants (17th Wind Integration Workshop), Stockholm, Sweden*, Oct 2018.

[180] P. Brogan and N. Goldenbaum, "Harmonic model of the network bridge power converter for wind turbine harmonic studies," in *11th International Workshop on Large-Scale Integration of Wind Power into Power Systems as well as Transmission Networks for Offshore Wind Power Plants (11th Wind Integration Workshop), Lisbon, Portugal*, Nov 2012.

[181] Ł. H. Kocewiak, C. Álvarez, P. Muszynski, J. Cassoli and L. Shuai, "Wind turbine harmonic model and its application – overview, status and outline of the new IEC technical report," in *14th International Workshop on Large-Scale Integration of Wind Power into Power Systems as well as Transmission Networks for Offshore Wind Power Plants (14th Wind Integration Workshop), Brussels, Belgium*, Oct 2015.

[182] L. Kocewiak, B. Gustavsen, and A. Holdyk, "Wind power plant transmission system modelling for harmonic propagation and small-signal stability analysis," in *16th Wind Integration Workshop*, Oct 2017.

[183] CIGRE JWG C4/B4.38, "Network modelling for harmonic studies," CIGRE Brochure, C4/B4 766, Apr 2019.

[184] "IEC61000-3-6: Electromagnetic compatibility (EMC) - Part 3-6: Limits - assessment of emission limits for the connection of distorting installations to MV, HV and EHV power systems," International Electrotechnical Commission, Standard, 2008.

[185] C. Jensen, C. Bak, L. H. Kocewiak, J. Hjerrild, and K. Berthelsen, "Probabilistic aspects of harmonic emission of large offshore wind farms," in *10th International Workshop on Large-Scale Integration of Wind Power into Power Systems as well as on Transmission Networks for OffshoreWind Power Plants (10th Wind Integration Workshop), Aarhus, Denmark*, Oct 2011.

[186] E. Guest, K. H. Jensen and T. W. Rasmussen, "Probabilistic harmonic modeling of wind power plants," in *16th International Workshop on Large-Scale Integration of Wind*

Power into Power Systems as well as Transmission Networks for Offshore Wind Power Plants (16th Wind Integration Workshop), Berlin, Germany, Oct 2017.

[187] D. G. Holmes and T. A. Lipo, *Pulse Width Modulation for Power Converters: Principles and Practice*. Wiley-IEEE Press, 2003. [Online]. Available: https://ieeexplore.ieee.org/document/5311978

[188] E. Guest, K. H. Jensen, and T. W. Rasmussen, "Sequence domain harmonic modeling of type-iv wind turbines," *IEEE Transactions on Power Electronics*, vol. 33, no. 6, pp. 4934–4943, 2018.

[189] M. Bollen, M. Häger and M. Olofsson, "Allocation of emission limits for individual emitters at different voltage levels: flicker and harmonics," CIGRE C4-106, 2010.

[190] B. Nouri, Ł. Kocewiak and P. E. Sørensen, "Frequency and sequence couplings in type 4 and type 3 wind turbines," in *19th International Workshop on Large-Scale Integration of Wind Power into Power Systems as well as Transmission Networks for Offshore Wind Power Plants (19th Wind Integration Workshop), Online*, Nov 2020.

[191] B. Nouri, Ł. Kocewiak, S. Shah, P. Koralewicz, V. Gevorgian, and P. Sørensen, "Generic multi-frequency modelling of converter-connected renewable energy generators considering frequency and sequence couplings," *IEEE Transactions on Energy Conversion*, vol. 37, no. 1, pp. 547–559, 2022.

[192] S. Shah, P. Koralewicz, V. Gevorgian and R. Wallen, "Impedance measurement of wind turbines using a multi-megawatt grid simulator," in *18th International Workshop on Large-Scale Integration of Wind Power into Power Systems as well as Transmission Networks for Offshore Wind Power Plants (18th Wind Integration Workshop), Dublin, Ireland*, Oct 2019.

[193] Y. Jiang and A. Ekstrom, "General analysis of harmonic transfer through converters," *IEEE Transactions on Power Electronics*, vol. 12, no. 2, pp. 287–293, 1997.

[194] L. Petersen, S. Buruchaga Laza, V. Myagkov, F. Iov and Ł. H. Kocewiak, "Parametric variation for detailed model of external grid in offshore wind farms," in *13th International Workshop on Large-Scale Integration of Wind Power into Power Systems as well as Transmission Networks for Offshore Wind Power Plants (13th Wind Integration Workshop), Berlin, Germany*, Nov 2014.

[195] F. Faria da Silva, C. L. Bak and P. B. Holst, "Study of harmonics in cable-based transmission networks," CIGRE C4-108, 2012.

[196] L. Sainz, J. J. Mesas, R. Teodorescu, and P. Rodriguez, "Deterministic and stochastic study of wind farm harmonic currents," *IEEE Transactions on Energy Conversion*, vol. 25, no. 4, pp. 1071–1080, 2010.

[197] A. Cavallini, R. Langella, A. Testa, and F. Ruggiero, "Gaussian modeling of harmonic vectors in power systems," in *8th International Conference on Harmonics and Quality of Power. Proceedings (Cat. No.98EX227)*, vol. 2, 1998, pp. 1010–1017 vol.2.

[198] Y. Baghzouz, R. Burch, A. Capasso, A. Cavallini, A. Emanuel, M. Halpin, R. Langella, G. Montanari, K. Olejniczak, P. Ribeiro, S. Rios-Marcuello, F. Ruggiero, R. Thallam, A. Testa, and P. Verde, "Time-varying harmonics. ii. harmonic summation and propagation," *IEEE Transactions on Power Delivery*, vol. 17, no. 1, pp. 279–285, 2002.

[199] S. Papathanassiou and M. Papadopoulos, "Harmonic analysis in a power system with wind generation," *IEEE Transactions on Power Delivery*, vol. 21, no. 4, pp. 2006–2016, 2006.

[200] Y. Xiao and X. Yang, "Harmonic summation and assessment based on probability distribution," *IEEE Transactions on Power Delivery*, vol. 27, no. 2, pp. 1030–1032, 2012.

[201] H. Ghanavati, Ł. Kocewiak and A. Jalilian, "Updated harmonic and interharmonic current summation rule in wind power plants with type III wind turbines," in *18th International Workshop on Large-Scale Integration of Wind Power into Power Systems as well as Transmission Networks for Offshore Wind Power Plants (18th Wind Integration Workshop), Dublin, Ireland*, Oct 2019.

[202] H. Xue and P. Zhang, "Subspace-least mean square method for accurate harmonic and interharmonic measurement in power systems," *IEEE Transactions on Power Delivery*, vol. 27, no. 3, pp. 1260–1267, 2012.

List of publications

Journal Publications

[J1] L. Beloqui Larumbe, Z. Qin, and P. Bauer, "Guidelines for stability analysis of the DDSRF-PLL using LTI and LTP modelling in the presence of imbalance," *IEEE Open Journal of the Industrial Electronics Society*, vol. 3, pp. 339–352, 2022.

[J2] L. Beloqui Larumbe, Z. Qin, L. Wang, and P. Bauer, "Impedance modelling for three-phase inverters with double synchronous reference frame current controller in the presence of imbalance," *IEEE Transactions on Power Electronics*, vol. 37, no. 2, pp. 1461–1475, 2022.

[J3] L. Wang, Z. Qin, L. Beloqui Larumbe, and P. Bauer, "Python supervised co-simulation for a day-long harmonic evaluation of EV charging," *Chinese Journal of Electrical Engineering*, vol. 7, no. 4, pp. 15–24, 2021.

Conference Publications

[C1] L. Beloqui Larumbe, Z. Qin, and P. Bauer, "Introduction to the analysis of harmonics and resonances in large offshore wind power plants," in *2018 IEEE 18th International Power Electronics and Motion Control Conference (PEMC)*, 2018, pp. 393–400.

[C2] ——, "Type iv wind turbine system impedance modelling for harmonic analysis: On the use of a double synchronous reference frame and notch filter," in *The 17th International Workshop on Large-Scale Integration of Wind Power into Power Systems as well as on Transmission Networks for Offshore Wind Power Plants (17th Wind Integration Workshop), Stockholm, Sweden*, 2018.

[C3] ——, "On the importance of tracking the negative-sequence phase-angle in three-phase inverters with double synchronous reference frame current control," in *29th IEEE International Symposium on Industrial Electronics (ISIE)*, 2019.

[C4] ——, “Output impedance modelling and sensitivity study of grid-feeding inverters with dual current control,” in *IECON 2019 - 45th Annual Conf. of the IEEE Ind. El. Soc.*, 2019.

[C5] A. Shekhar, L. Beloqui Larumbe, T. B. Soeiro, Y. Wu, and P. Bauer, “Number of levels, arm inductance and modulation trade-offs for high power medium voltage grid-connected modular multilevel converters,” in *2019 10th International Conference on Power Electronics and ECCE Asia (ICPE 2019 - ECCE Asia)*, 2019, pp. 1–8.

[C6] D. Vree, L. Beloqui Larumbe, Z. Qin, P. Bauer, and B. C. Ummels, “Impact of WTG converter impedance model on harmonic amplification factor of the Dutch 110 kV transmission network using a 383 MW wind farm case study,” in *CIGRE C4-302*, 2020.

[C7] L. Wang, Z. Qin, L. Beloqui Larumbe, and P. Bauer, “Multi-timescale modeling of fast charging stations for power quality analysis,” in *2021 23rd European Conference on Power Electronics and Applications (EPE’21 ECCE Europe)*, 2021, pp. P.1–P.9.

Errata for

“Harmonic Stability and Distortion in Offshore Wind Farms”

Lucia Beloqui Larumbe

30th October 2024

Chapter 5 – Conclusions

The thesis states:

> “First, with respect to stability, it is concluded that the effect of voltage imbalance on the stability margins of the PLL depends strongly on the PLL design. In this thesis, the focus is the widely known Double Decoupled Synchronous Reference Frame PLL (DDSRF-PLL) and some variants. For a typical DDSRF-PLL design, increasing the voltage imbalance worsens the stability margin of the PLL; however, the imbalance increase must be large so that the stability margin is significantly affected. In particular, the pole damping of the PLL remains at high levels and nearly unchanged up until imbalance levels of around 20%. This includes, by far, the voltage imbalance that may appear in steady-state conditions (e.g., IEC 61000-3-13 suggests a planning level limit of 1.4% for HV networks) and even some fault conditions. For the transients that induce a higher imbalance, the stability margin decreases.”

Clarification:

This document is to clarify that, since the PLL pole damping has been found to be high until imbalance levels of around 20%, the PLL is expected to have a good stability margin for the imbalance levels indicated in many standards across the world, not only IEC 61000-3-13. For example, the imbalance level indicated in EN50160 is 2%, and thus it is also included in this range.

To summarize, in this thesis, the effect of voltage unbalance is analysed for a number of topics using different values of voltage unbalance. An outcome is that, if the (indicative) values for voltage unbalance from EN50160 are met, no problems are to be expected for the considered topics.